The transverse mechanical behaviour of glass fibre reinforced plastics

Wells, Garry Michael

Award date:
1987

Awarding institution:
University of Bath

THE TRANSVERSE MECHANICAL

BEHAVIOUR OF

GLASS FIBRE REINFORCED PLASTICS

Submitted by Garry Michael Wells for the
degree of Ph.D of the University of Bath
1987

COPYRIGHT

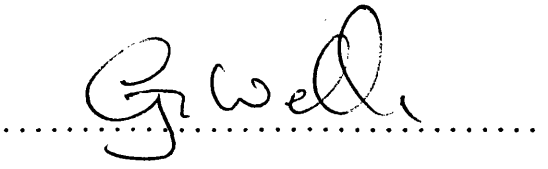

ProQuest LLC
789 East Eisenhower Parkway
P.O. Box 1346
Ann Arbor, MI 48106-1346

SUMMARY

The Transverse Mechanical Behaviour of Glass Fibre Reinforced Plastics

G M Wells

The importance of transverse cracking in composites technology is highlighted by the use of classical lamination theory to predict the sequential damage process in cross-plied laminates.

The literature on transverse fibre composite behaviour is comprehensively reviewed, with particular emphasis on papers which present quantitative theoretical models. No work reviewed has measured the full range of mechanical properties on a single material necessary to allow a complete assessment of all the models of transverse failure.

A resin system, based on epoxy/urethane blends, has been identified which allows production of high quality unidirectional composites with a systematic variation in flexibility. A preliminary experimental programme has identified those test specimens which can provide the necessary stress/strain and toughness properties of the range of flexibilised materials and thereby allow a validation of the theoretical models reviewed.

In the preliminary experimental programme, transverse cracks are shown to extend with an increasing fracture toughness due to the formation of a 'tied zone' of fracture face bridging 'stringers' behind the crack tip. The influence of this effect on crack stability is discussed. By modelling the balance between fracture and strain energies, the equilibrium state of individual stringers is predicted. Direct observations of equilibrium stringer angles are seen to correspond with these predictions.

A quite general model is developed which predicts, with reasonble accuracy, the observed increase of fracture toughness with crack extension and the geometry dependence of this increase.

The literature models of stiffness, strength and failure strain are seen to display a dissappointing lack of agreement with the experimental results over the full range of material flexibilities. The influence of matrix Poisson constraint on these properties is discussed.

Fracture toughness results indicate that very large critical defects control transverse strength. It is suggested that such defects develop by sub-critical debond or microcrack coalescence.

CONTENTS

1. INTRODUCTION

1.1 Objectives and Scope

The objective of this work was to gain a greater understanding of the way in which composite transverse mechanical behaviour is controlled by the microstructure and properties of the constituent fibre and matrix.

In the course of the study the programme split into two parallel tasks: (i) the measurement of transverse modulus, strength, failure strain and toughness which enabled the available theories which attempt to describe this behaviour to be tested; and (ii) development and validation of a model of transverse crack propagation.

Chapter I highlights the importance of transverse cracking by showing, through classical lamination theory, how for some laminates, this is the first stage in their failure. In Chapter 2 previous theories of transverse mechanical behaviour are reviewed and the key experimental parameters required to test these theories defined. Chapter 3 outlines the experimental approach, which was to fabricate composites with a gradation in matrix flexibility and which would therefore display a systematic variation in the key mechanical properties highlighted in Chapter 2. Chapter 4 describes the selection of a suitable resin system together with its physical and chemical characterisation. In Chapter 5 a preliminary experimental programme is described within which particular test specimen geometries were selected for evaluating the stress/strain and toughness properties of the flexibilised materials. The results of

these tests are summarised in Chapter 6. A theoretical model of transverse crack propagation is developed in Chapter 7 which agrees quite well with experimental observations. Also presented in Chapter 7 are comparisons of the literature theoretical models of mechanical behaviour with the experimental results. Explanations are put forward for the lack of correspondence of theory and experiment in certain cases. In the conclusion, Chapter 8, the regimes of flexibility within which particular theoretical models may successfully apply are outlined, and a suggestion is made as to how the apparently opposing theoretical models based on micromechanics and fracture mechanics may be reconciled.

1.2 Fibre Composites

Most materials in common use today are, in fact, composite materials of one form or another. The concept of a useful composite implies that two or more phases are combined to produce a material which has a combination of properties which are advantageous, and which neither phase alone could display [1,2,3]. The materials properties may include strength, stiffness, cost, corrosion resistance, wear resistance, appearance, etc., and the intention, for an efficient engineering application of the material, is to optimise the combination of properties which are considered important. The composite concept has been exploited in nature and by man. Examples of composites in the natural world are bone, teeth, wood and muscle, and in the artificial world are metal alloys, concrete, toughened plastics and of course fibre composites such as alumina fibre reinforced aluminium and glass fibre reinforced polyester resin. The concept of fibre reinforcement is certainly not new, but relatively

recent developments in the production of strong fibres, and matrices with which they are compatible, has resulted in a rapid expansion in the technology and exploitation of these materials over the past few years. Hitherto, most of this development has been in the field of fibre reinforced plastics primarily because of the relatively straightforward technology of investing fibres with low viscosity thermosetting resins and producing useful structures after solidification of the resin matrix. However, it is clear that the field of fibre reinforced metals and fine ceramics (in which the production technology is more difficult, but the performance rewards greater) represents an area which is receiving considerable attention and which will, eventually produce materials of great utility to the engineer.

The area of the present study is centred, at a practical level, on fibre reinforced plastics although some of the more theoretical aspects explored may be of more general applicability. Fibre reinforced plastics themselves represent a broad class of materials in which variations in the matrix type and the fibre type, form, orientation, volume fraction and surface characteristics have critical implications for the properties of the composite which result. The term fibre reinforced plastic is something of a misnomer since it is the fibre which is the major load bearing component and one of the vital functions of the plastic matrix is to enable the fibres to carry the applied loads efficiently in tension and compression. Other functions of the matrix are to protect the fibres from mechanical damage and environmental degradation, and to enable the (usually brittle) fibres to act separately so that a single crack cannot run directly through both fibre and matrix,

thereby conferring a degree of toughness to the system.

Since it is the fibre which principally confers strength and stiffness to the composite; the greater the fibre volume fraction, in general, the better the material properties. The highest packing density of fibre is achieved by aligning continuous fibre unidirectionally. In this way fibre volume fractions of approximately 70% can be routinely achieved in practice. Intuitively it would be expected that the behaviour of such a material would be highly anisotropic, and indeed the strength and stiffness of such unidirectional composite can be orders of magnitude higher in the fibre direction than transverse to it. This anisotropy represents one of the major difficulties of designing with composites, but, conversely it also represents a unique design opportunity since the fibre orientation can be specified with regard to the applied stress system and intended function of the structure allowing a tailoring of the material to the application. In Table 1 approximate property data on various 60% volume fraction unidirectional composites are presented together with corresponding data for some metals. A comparison of the specific strengths and stiffnesses indicates one of the major reasons why fibre composites are used: to produce low mass, high performance structures. However, a comparison of the longitudinal and the transverse properties, particularly strength, for a given class of composite material graphically highlights why correct choice of fibre orientation is vital when attempting to design composite structures which will operate satisfactorily. Essential to any discussion on the selection of optimum fibre angles is an outline of the concept of lamination.

1.3 Lamination

A method of predicting the mechanical properties of candidate laminate constructions is a prerequisite for the design of optimum composite structures. Fortunately, a branch of elasticity theory originally developed by crystallographers at the turn of the century has been adapted into an invaluable theoretical framework in which the stiffness and strengths of arbitrary assemblies of laminae can be understood and predicted. This framework, commonly called classical lamination theory[4,5] is based upon several rigid assumptions; the most restricting perhaps being that the analysis is applicable only to thin plies in which out-of-plane stresses and deformations can be neglected. Further assumptions are that individual laminae can be treated as macroscopically homogeneous, but orthotropic in their elastic properties, and that material constants such as stiffnesses and thermal expansion coefficients are truly constant and do not vary with strain or temperature. Within these, and other assumptions it is possible to predict the macroscopic thermo-elastic properties of the laminate from a knowledge of the individual lamina properties, and conversely to subsequently calculate the individual stress system within each lamina when the laminate is subjected to an applied loading or a temperature change.

A general lamination analysis for prediction of both stiffness and strength requires a considerable amount of calculation. Appendix 1 summarises, in matrix notation, the mathematics of classical lamination theory. The approach provides a prediction of the in-plane stresses acting in the fibre direction, transversely and

in shear for each lamina when the laminate is subjected to in-plane mechanical stress and/or a temperature change (which gives rise to residual thermal stresses due to thermo-elastic anisotropy). A failure criterion is used in order to decide whether this combination of stresses is sufficient to cause failure of the particular lamina under consideration. The concept of failure criteria will be expanded in later sections, but in brief, they are equations, or sets of equations, which attempt to describe the stress states that the material can withstand without failure. The most simple failure criterion is the maximum stress failure criterion which simply states that a unidirectional lamina will fail longitudinally, transversely or in shear when the applied stress in the appropriate direction exceeds the maximum value measured in a uniaxial test. Other failure criteria are interactive in predicting that simultaneously applying different stress components can bring a lamina closer to failure than applying the stresses independently. If, for a given laminate stress condition, none of the individual laminae have been observed to exceed the relevant failure criterion, the notional applied stress system can be incrementally increased and the process repeated until any one of the laminae are predicted to fail. Failure of any one lamina may not necessarily precipitate failure of the whole laminate, which may well be capable of sustaining further load. If a prediction of laminate performance beyond first ply failure is required it is necessary to make an assessment of the mode of failure of the initial lamina fracture and to reduce the appropriate elastic constants of the lamina (a conservative estimation is a reduction to zero). The reduced overall laminate stiffness can then be recalculated and the whole process repeated until all the laminae in

all directions have been predicted to fail. In this way a sequential damage development process can be predicted for any laminate under an arbitrary in-plane stress system.

The iterative procedure which has been described is ideally suited to a computer solution and a laminate analysis program has been written, in Basic, to run on Apple and Commodore PET micro-computers. Appendix 2 presents a sequential failure process predicted using this laminate analysis for a simple 0°/90° symmetrical glass reinforced epoxide laminate, with and without residual thermal curing stresses. These results show that for this material, transverse cracking is predicted to occur at a stress level which is only 12% of the final failure stress of the laminate as a whole, and that the predicted initial failure stress is even lower if thermal stresses are taken into account. An insight into the controlling influence of transverse strain to failure can be gained if the lamina material properties used as input to the program are modified so that the transverse strength remains constant, but the transverse modulus is halved, resulting in a doubling of the transverse strain to failure. This might be obtained by the use of a more flexible matrix. A rerun of the laminate analysis program with this notional, flexiblised material shows that the stress for the onset of damage has increased by approximately 70%. Figure 1 shows the predicted stress-strain response and sequential damage process in notional 0°/90° laminates of the conventional and flexibilised composites outlined above.

1.4 Lamina Moduli and Failure Modes

A unidirectional lamina can fail in a number of different modes depending on the applied loading conditions. Longitudinal tensile fracture is primarily controlled by the fibre properties while transverse fracture, in tension and compression, and shear fracture are primarily controlled by the properties of the resin matrix. While it is possible to attach names to these different failure modes, in practice, under complex loading conditions, it is often difficult (and indeed pointless) to distinguish between transverse and shear fracture modes. In these circumstances it is more appropriate to use the term 'resin cracking' to describe shear and transverse fracture. This effect of interaction between failure modes is exemplified by many of failure criteria which will be outlined later.

The geometry of thin, continuous fibres in a unidirectional array ensures that, when loaded in the fibre direction, the strain in the fibre and resin matrix are equivalent. For this reason the 'rule of mixtures' can be used with reasonable accuracy to predict the longitudinal modulus and tensile strength, i.e.

$$E_{11} = E_f V_f + E_m (1-V_f) \qquad (1.1)$$

and

$$\sigma_1 = \sigma_f V_f + \sigma_m' (1-V_f) \qquad (1.2)$$

where E_{11} = composite longitudinal modulus

E_f = fibre longitudinal modulus

E_m = matrix modulus

V_f = fibre volume fraction

σ_1 = composite longitudinal tensile strength

σ_m' = matrix stress at fibre failure strain

σ_f = fibre strength

Strictly, the rule of mixtures strength prediction above is valid only where the matrix failure strain is greater than the fibre failure strain. This is the case for most practical polymer matrix composites.

That the rule of mixtures strength prediction is found experimentaly to be a good approximation is somewhat surprising in view of the complex nature of the failure process. For example, the above approach neglects the statistical nature of fibre strength which results from the distribution of flaws of varying severity within fibres. This means that all the fibres do not fail at a single stress level, but that progressively greater numbers of fibres fail as the stress increases until a stress is reached at which separation occurs. The statistical distribution of fibre flaws leads to a marked dependence of measured average strength on the length of fibre tested; the longer the fibre the greater the probability of encountering a severe flaw and the lower the average strength. This implies a fundamental difficulty in identifying the appropriate fibre strength, from single fibre tests, to use in equation 1.1 above. In practice, the fibre strength is usually calculated using equation 1.1 from measurements on known fibre volume fraction composites.

Longitudinal compressive failure is less well understood than tensile failure, and there does not exist, at present, a completely satisfactory model of compression behaviour. What is clear is that the resin has a vital role to play in supporting the fibres in compression. Failure seems to involve microbuckling of the fibres probably in a co-operative fashion which leads to the formation of kink bands. Reductions in matrix modulus, by increasing temperature or by using flexibilisers, encourage microbuckling and reduce compressive strength. Reliable measurements of the compressive strength are notoriously difficult to make since the test specimens must be short and fat to avoid macroscopic Euler buckling and at the

same time the end fittings must allow a smooth introduction of stress and discourage 'brooming' and longitudinal splitting.

In contrast to the longitudinal tensile properties the transverse and shear properties are dominated by the resin matrix. The geometrical arrangement under longitudinal loading ensures continuity of strain (the Voigt model) which gives rise to the law of mixtures for longitudinal modulus. The geometry of transverse and shear loading approximates more closely to a continuity of stress; the Reuss model, for which the appropriate equation for transverse modulus (E_{22}) is:

$$\frac{1}{E_{22}} = \frac{V_f}{E_f} + \frac{(1-V_f)}{E_m} \qquad (1.3)$$

In practice the transverse modulus is greater than equation 1.3 would predict by an amount which depends on the connectivity or 'contiguity' of fibres which increases with increasing fibre volume fraction[1]. Many more sophisticated models exist for transverse modulus prediction which will be outlined in more detail later. Unlike the longitudinal tensile strength which is primarily controlled by only two parameters (the fibre strength and fibre volume fraction) the transverse tensile strength depends on several factors including the resin and fibre properties, the fibre volume fraction, the nature of the fibre/matrix interface and the presence of voids or other defects. In general, it has usually been found that the strength of a transverse composite is less than the strength of the neat resin, so that the fibres have a weakening, rather than a reinforcing, effect. An understanding of the way in which the resin

and fibre properties interact to control transverse strength and strain to failure is the intention of a greater part of the present study.

Which of the fracture modes outlined above occurs at failure depends on the relative magnitudes of the applied stresses in relation to the material strengths. Since it would be an impossible task to characterise the failure level for every complex state of stress that a particular fibre composite may encounter, the concept of a failure criterion has been introduced to allow prediction of the failure level of a lamina under complex loading states using strength values measured under (usually) uniaxial conditions[6]. The following discussion on failure criteria relates only to plane stress, an approach consistent with a classical lamination theory analysis. For isotropic materials the values of the principal stresses (σ_1 and σ_2) provides a complete description. For composite materials a knowledge of the principal stresses alone is inadequate as a basis for a failure criterion. For a composite material, under plane stress, the normal and shear stresses (σ_1, σ_2 and τ_{12}) in the material directions must be known. Unidirectional composite failure envelopes then are necessarily expressed in three-dimensional stress space, forming a surface, or set of surfaces, outside of which fracture is predicted. Of the 20 or more failure criteria available in the literature a few representative ones are described below.

The Maximum Stress theory is one of the simplest failure criteria and states that when any of the stress components in the material directions exceeds the corresponding strength measured in a uniaxial test then the lamina will fail in the corresponding mode,

i.e.

$$\sigma_1 = \sigma_{1T\ ult} \text{ or } \sigma_{1C\ ult}$$

$$\sigma_2 = \sigma_{2T\ ult} \text{ or } \sigma_{2C\ ult}$$

or $$\tau_{12} = \tau_{12\ ult}$$

where subscripts T and C denote tensile and compressive strengths.

In 3-dimensional stress space the criterion is represented by six planes intersecting orthogonally (i.e. a rectangular box). The criterion has no interaction between applied stresses and allows unambiguous determination of the failure mode.

The Maximum Strain theory is similar to the Maximum Stress theory but predicts failure when any of the applied strains in the material directions exceeds the corresponding ultimate value, i.e.

$$\epsilon_1 = \epsilon_{1T\ ult} \text{ or } \epsilon_{1C\ ult}$$

$$\epsilon_2 = \epsilon_{2T\ ult} \text{ or } \epsilon_{2C\ ult}$$

$$\gamma_{12} = \gamma_{12\ ult}$$

The failure mode is again unambiguously described, but some interaction between applied stresses occurs via the Poisson effect.

The Puck-Schneider Theory[7] considers interaction between shear and transverse tensile and compressive stresses to cause resin cracking, but considers longitudinal stresses and consequent fibre failure independently, i.e.

$$\sigma_2 \left[\frac{\sigma_{2C\ ult} + \sigma_{2T\ ult}}{\sigma_{2C\ ult}\ \sigma_{2T\ ult}} \right] - \frac{\sigma_2^2}{\sigma_{2C\ ult}\ \sigma_{2T\ ult}}$$

$$+ \left[\frac{\tau_{12}}{\tau_{12\ ult}} \right]^2 = 1 \quad \text{for resin cracking.}$$

and $\sigma_1 = \sigma_{1T\ ult}$ or $\sigma_{1C\ ult}$ for longitudinal failure.

This criterion is intuitively appealing since it considers interaction between shear and transverse stresses to cause resin cracking, which is supported by experimental evidence, yet by predicting independent fibre failure the criterion is able to differentiate between the fibre and resin failure modes. This is useful when attempting to predict the fracture sequence of a laminate beyond first ply failure. The failure envelope is represented by an ellipsoid in the σ_2, τ_{12} plane which extends with constant section along the σ_1 axis between the $\sigma_{1\ ult}$ values.

There are many criteria which model fully interactive failure between all three applied stresses σ_1, σ_2 and τ_{12}[6]. One of the most useful is the Hoffman criterion which is a generalisation of the Azzi- Tsai criterion taking into account differences between tensile and compressive strengths. The Azzi-Tsai criterion is based on the Hill criterion which itself is a generalisation of the Von Mises-Hencky maximum distortional energy theory modified for anisotropic materials. Since it is fully interactive the Hoffman criterion is described by a single equation:

$$\frac{\sigma_1^2 - \sigma_1\sigma_2}{\sigma_{1T\ ult}\ \sigma_{1C\ ult}} + \frac{\sigma_2^2}{\sigma_{2T\ ult}\ \sigma_{2C\ ult}} + \sigma_1\left[\frac{\sigma_{1C\ ult} - \sigma_{1T\ ult}}{\sigma_{1C\ ult}\ \sigma_{1T\ ult}}\right]$$

$$+ \sigma_2\left[\frac{\sigma_{2C\ ult} - \sigma_{2T\ ult}}{\sigma_{2C\ ult}\ \sigma_{2T\ ult}}\right] + \frac{\tau_{12}^2}{\tau_{12\ ult}^2} = 1$$

The failure envelope gives rise to ellipsoidal sections at each of the σ_1/σ_2, σ_1/τ_{12} and σ_2/τ_{12} planes, and since it is fully interactive does not allow easy determination of the failure mode.

The Tsai-Wu criterion has been proposed as the general theory of strength for anisotropic materials[6]. It is a tensor polynomial theory which requires measurement of strength tensors determined from biaxial tests, and for this reason has been little used. It can be written:

$$F_1\sigma_1 + F_2\sigma_2 + F_6\tau_{12} + F_{11}\sigma_1^2 + F_{22}\sigma_2^2$$

$$+ 2F_{12}\sigma_1\sigma_2 + F_{66}\tau_{12}^2 = 1$$

where:

$$F_{11} = \frac{1}{X\,X'} \qquad F_{22} = \frac{1}{Y\,Y'} \qquad F_{66} = \frac{1}{S^2}$$

$$F_1 = \frac{1}{X} - \frac{1}{X'} \qquad F_2 = \frac{1}{Y} - \frac{1}{Y'}$$

in which X, Y and S are the tensile longitudinal, transverse and shear strengths and the prime denotes the corresponding compressive values. Within certain limits of stability the equation represents a closed surface of the second degree[8]. The coefficient F_{12} is determined from combined loading tests and controls the level of 'tilt' of the surface in the σ_x, σ_y plane such that the greatest value of longitudinal tensile strength is only achieved with simultaneous transverse compression.

Several other failure criteria are available which have been applied to laminates as a whole. Since these criteria require experimental strength data which are valid only for the specific laminate under consideration they are of limited use in gaining an understanding of laminate fracture processes or for designing optimised laminate constructions.

The above discussion on failure criteria has been presented to emphasise the complex and interactive nature of composite failure processes and to provide a background against which the much more specific phenomenon of transverse cracking can be explored.

2. LITERATURE REVIEW

Transverse cracking was recognised early on as an important feature of the mechanical behaviour of unidirectional composites. Consequently the phenomenon has been broadly explored in a wide range of fibre and resin combinations but with varying degrees of effort towards gaining a fundamental understanding of the process.

In order to provide a framework in which to present this somewhat disparate body of work, the literature will be reviewed under the headings of those theoretical approaches which have attempted to develop a quantitative understanding of the transverse cracking process. Papers which present purely experimental results will be reviewed under the heading of the theoretical approach to which the results are most relevant.

The transverse failure theories divide themselves roughly into two groups[9]. In the first, more or less sophisticated continuum mechanics approaches attempt to deduce interfibre stresses or strains and thereby predict failure stresses or strains in the transverse ply as a whole. These will be termed the micromechanics theories. In the second group, termed the fracture mechanics theories, the energetics of crack growth are considered and transverse cracking is assumed to be controlled by matrix (or interfacial) toughness. Within this second group can sensibly be gathered the attempts, based on fracture mechanics, to explain the influence of ply thickness on transverse cracking strain in multidirectional laminates. While these approaches are applicable only to laminates and this is a study

primarily of unidirectional material, it is considered that a discussion of this work is relevant since transverse cracking in multidirectional laminates is of great practical importance.

2.1 Micromechanics Approaches

Many micromechanics theories attempt to derive the distribution of stresses and strains within a loaded composite from a knowledge of the fibre and matrix elastic properties and the geometric disposition of the fibres. The assumptions normally made in these analyses are:

(i) that the fibre and matrix are perfectly elastic (though one approach does consider matrix plasticity),

(ii) the fibres are arranged in idealised, regular repeating arrays (though one approach does consider 'random arrays'), and

(iii) the fibres are perfectly bonded to the matrix (though several approaches consider the case of complete fibre debonding).

Knowing the interfibre stresses or strains the micromechanics theories can then be used to predict the overall composite transverse strength or strain to failure by assuming that fracture occurs when the stress or strain at any point exceeds the matrix strength or strain to failure.

2.1.1 Transverse Modulus Prediction

Some micromechanics theories predict interfibre stress and strain distributions but the same approach has been used by several workers to predict transverse composite modulus as a function of fibre and matrix moduli and fibre volume fraction. Accurate prediction of composite elastic properties is of considerable importance for design purposes and a wide variety of models to enable this have been proposed[10]. Theories which require numerical solution based on finite difference[11] or finite element[12] techniques, or approaches based on variational methods[13] have been little used because of their inherent complexity. More convenient solutions are available which are supported by reasonable experimental corroboration. Several of the models are reviewed below.

The Reuss theory is based on the assumption of continuity of stress through a series arrangement of fibre and matrix. The strain contribution from each component being proportional to the volume fraction of that component and inversely proportional to its modulus. It is embodied in the equation[1, 14]:

$$E_{22} = \frac{E_f E_m}{V_f E_m + V_m E_f}$$

where E_{22} = transverse composite modulus

E_f = fibre modulus

E_m = matrix modulus

V_f = fibre volume fraction

V_m = matrix volume fraction.

Poisson effects are neglected. Data on glass/polyester with a range of volume fractions have been shown to be described quite well by this equation[2].

The longitudinal Poisson constraint theory modifies the Reuss model by considering that, due to their considerably higher modulus, the fibres can prevent all the Poisson contraction in the matrix in the fibre direction[2]. This increases the effective modulus of the matrix by an amount which depends on the Poisson's ratio, i.e.

$$E'_m = \frac{E_m}{1 - \nu^2_m}$$

where E'_m = effective matrix modulus

and ν_m = matrix Poisson's ratio.

The Reuss model therefore becomes

$$E_{22} = \frac{E_f \quad E_m'}{V_f E'_m + V_m E_f}$$

The Ekvall model[15] represents a further modification to the Reuss approach by considering the Poisson constraint giving rise to a triaxial stress state in the matrix such that:

$$\sigma_2 = \sigma_3 = \nu_m \sigma_1$$

where the subscripts 1, 2 and 3 refer to the longitudinal, transverse and through-thickness directions respectively.

Allred and Gerstle[14] conclude that the assumption of the existence of this particular triaxial stress state has little physical justification. However, within this assumption the effective matrix modulus becomes:

$$E_m' = \frac{E_m}{1 - 2\nu_m^2}$$

and the transverse modulus is given by the equation:

$$E_{22} = \frac{E_f E_m'}{V_f E_m' + V_m E_f (1 - \nu_m^2)}$$

A more physically realistic representation of Poisson's constraint has been suggested[14] as the plane strain bulk modulus:

$$E_m^* = \frac{E_m}{2(1 + \nu_m)(1 - 2\nu_m)}$$

For $\nu_m = 0.37$, which is close to actual values for typical epoxy resins, E_m^* and E_m' are identical.

The appropriate value of fibre modulus to use in many micromechanics models which predict composite transverse modulus is, of course, the fibre transverse modulus. For isotropic fibres such as glass this can be assumed to be the same as the longitudinal modulus, which is easily measurable. However, carbon and aramid fibres have anisotropic structures which give rise to a longitudinal modulus which can be 60 times greater than the transverse modulus[16]. Values for fibre transverse moduli of carbon fibres measured by ultrasonic techniques are quoted by Smith[17]. In fact, the measurements of elastic constants were made on composites and the fibre moduli inferred using the Halpin-Tsai model (reviewed later). It would therefore seem possible that several subsequent attempts to validate the Halpin-Tsai model using these fibre data would force good agreement with experiment[14,18].

The Hashin model[19] would seem to be one of the few analytical approaches able to accommodate true fibre anisotropy. The original equations, based on a composite cylinder assemblage model[13], allow both the matrix and fibre to be transversely isotropic with five independent elastic constants for each phase. A subsequent modification by Hahn[20] rewrote the equations for the case of matrix isotropy to give:

$$E_{22} = \frac{4\ K_T\ G_T}{K_T + m\ G_T}$$

where

$$m = \frac{1 + 4\ K_T\ \nu_{12}}{E_{11}}$$

$$\frac{1}{K_T} = \frac{1}{V_f + n_K\ V_m} \left[\frac{V_f}{K_{2f}} + \frac{n_K\ V_m}{K_m} \right]$$

and

$$\frac{1}{G_T} = \frac{1}{V_f + n_G\ V_m} \left[\frac{V_f}{G_{2f}} + \frac{n_G\ V_m}{G_m} \right]$$

in which

$$n_K = \frac{1}{2(1 - \nu_m)} \left[1 + \frac{G_m}{K_{2f}} \right]$$

and

$$n_G = \frac{1}{4(1 - \nu_m)} \left[3 - 4\ \nu_m + \frac{G_m}{G_{2f}} \right]$$

The materials properties are represented by the symbols:

E_{11} = composite longitudinal modulus

ν_{12} = composite major Poisson's ratio

ν_m = matrix Poisson's ratio

K_m = matrix bulk modulus

G_m = matrix shear modulus

G_{2f} = fibre shear modulus

K_{2f} = fibre plane strain bulk modulus

with V_f = fibre volume fraction

and V_m = matrix volume fraction, as previously defined.

These (and the Halpin-Tsai) equations have been used by Kowalski[21] to infer the transverse moduli of a range of carbon fibres. It is unfortunate that a direct method of determining fibre transverse modulus is unavailable at the present time.

By using an analytical approach which considered an idealised rectangular array of circular filaments embedded in matrix containing an idealised distribution of voids (such as seen in Figure 2) Greszczuk[22] was able to generate simple closed form expressions for the transverse modulus:

$$E_{22} = E_o\beta + E_m'(1 - \beta)$$

where

$$E_o = \frac{E_m' + 2\beta(E_f - E_m')}{1 + \left[\frac{2\beta(1 - 2\beta)}{E_m' E_f}\right]\left[(E_f - E_m')^2 - (\nu_m E_f - \nu_f E_m')^2\right]}$$

$$\beta = \left[\frac{(1 - V_v)V_f}{\pi}\right]^{\frac{1}{2}}$$

and

$$E'_m = \frac{E_m}{1 - 2\nu_m^2}$$

in which V_v = void volume fraction, and other variables are as previously defined.

The expressions above are as quoted by Allred and Gerstle[14] who point out what they believe to be a misprint in Greszczuk's paper[22]. Good agreement is found with experimental results for glass/epoxide[22] and carbon/epoxide[14] transverse composite.

The equations presented by Halpin and Tsai are widely used within the composites industry for estimating ply stiffness properties. The equation for transverse modulus is in fact a simple interpolation procedure which approximates more complicated self-consistent models. Hill[23] used methods previously developed for describing aggregates of crystals to derive the strain field for a single fibre in an unbounded, homogeneous medium loaded at infinity. A further refinement by Hermans considered a fibre existing within

a cylinder of matrix with the relative radii of fibre and cylinder varied to correspond to varying fibre volume fractions. The Halpin-Tsai equations are an approximation of this solution and are given by[5]:-

$$\frac{E_{22}}{E_m} = \frac{1 + \zeta \eta V_f}{2 - \eta V_f}$$

where

$$\eta = \frac{\left[\frac{E_f}{E_m} - 1\right]}{\left[\frac{E_f}{E_m} + \zeta\right]}$$

and ζ = a fitting constant.

The constant ζ is a parameter whose value depends on fibre geometry, array geometry and loading conditions. Once selected for a given fibre volume fraction the equation should accurately describe the modulus on changing fibre volume fraction, and matrix and fibre modulus. The selection of the appropriate value of ζ represents one of the greatest uncertainties in using the Halpin-Tsai equations, though a value of 2 is often assumed. These equations have been shown to accurately describe the transverse modulus of glass/thermoset plastic over a wide fibre volume fraction range[24], see Figure 3. This Figure also shows the Reuss modulus prediction which is seen to be a gross underestimate. The physical significance of ζ can be highlighted if the extremes of its numerical value are considered. When $\zeta = 0$ the equation reduces to the series connected

Reuss model; a lower bound. When $\zeta = \infty$ the equation becomes the parallel connected Voigt model; and therefore an upper bound. In this respect the approach bears a similarity to an earlier model by Tsai (described by Harris[1]) in which the relative contributions of the Voigt and Reuss stiffness to the transverse modulus is adjusted through an arbitrary constant, i.e.:

$$E_{22} = E_{Reuss} + C(E_{Voigt} - E_{Reuss})$$

A value of $C = 0.2$ is quoted as being appropriate for many high-quality composites.

A recent model proposed by Spencer[25] is appealing because of its relative mathematical simplicity and rigour within its own assumptions. The agreement with the Halpin-Tsai equations is close, and it avoids the use of an arbitrary constant.

The approach uses the idealised square array shown in Figure 4 in which a repeating unit cell is identified and notionally divided into strips. By assuming that under stress the deflection in each strip is identical the load picked up by each strip can be expressed in terms of its effective stiffness which is controlled by the local relative proportion of fibre to matrix. Integrating the forces over the width of the unit cell gives the overall effective stress. This approach also produces a value for the maximum interfibre stress and this important aspect will be reviewed in a later section. Relating the applied deflection or strain, to the resulting overall stress produces an expression for transverse modulus:

$$\alpha = \frac{\gamma - 1}{\gamma} + \frac{1}{K}\left[\frac{2\gamma}{(\gamma^2 - K^2)^{1/2}}\tan^{-1}\left[\frac{\gamma + K}{\gamma - K}\right]^{1/2} - \frac{\pi}{2}\right]$$

where $\alpha = E_{22}/E_m$

$\gamma = P/d$ = fibre pitch/diameter, see Figure 4

and $K = 1 - E_m/E_f$.

Although a square array was used to derive the equation above the result is expressed in terms of a separation parameter (γ) which can be related to fibre volume fraction for packing geometries other than square. This bypasses a problem which such a model would encounter in predicting too high a rate of increase in transverse modulus as the fibre volume fraction approaches 78%; the theoretical maximum packing density for a square array. Figure 5 shows some packing arrays designated triangular, square and hexagonal in order of decreasing fibre separation for a given fibre volume fraction. The separation parameter (γ) for each of these arrays is:

$$\gamma^2 = \frac{1}{1.103V_f}, \text{ triangular}$$

$$\gamma^2 = \frac{1}{1.272V_f}, \text{ square}$$

and $$\gamma^2 = \frac{1}{1.654V_f}, \text{ hexagonal}$$

Experimental evidence of composite cross-sections was quoted to support the (intuitively acceptable) contention that the relative proportions of the triangular array dominate the square and hexagonal arrays at high fibre volume fraction, and conversely that the hexagonal array dominates at low fibre volume fraction. To reflect this notional change in packing geometry an empirical equation relating separation parameter to fibre volume fraction was presented:

$$\gamma^2 = \frac{1}{V_f(1.8 - 0.75V_f)}$$

which approximates to the triangular and hexagonal packing arrays at the extremes of fibre volume fraction.

Agreement with the well established Halpin-Tsai equations was shown to be reasonable.

The model of Adams and Doner[11] represents an advanced, rigorous analysis against which many other workers compare their results for validation. The composite is assumed to consist of a rectangular array of unidirectional fibres perfectly bonded within an infinite elastic matrix. Within these assumptions, and those of linear elasticity, the physical problem is formulated exactly. By treating the problem as plane stress or plane strain as appropriate, differential equations are set up representing the equilibrium displacements and the stress/displacement relations.

A finite difference approach is necessary to solve the equations but by these means not only the stiffness relationships can be obtained, but also the complete interfibre stress state under applied loading and temperature change. Figure 6 shows the predicted normalised transverse stiffness versus the fibre to matrix stiffness ratio for various fibre volume fractions (with ν_f= 0.20 and ν_m = 0.35).

Because a numerical solution is necessary the usefulness from an engineering standpoint is lessened since an explicit equation is unavailable. However, a Fortran listing (of approx. 2800 lines) of the numerical solution technique is contained in reference 26.

By taking the case of a square array, infinitessimal deformations, perfect bonding and elastic linearity, Herman and Pister[27] were able to calculate the elastic, thermal and thermoelastic properties of composite from the fibre and matrix properties. In addition, interfibre strain concentration factors were also calculated. Due to the extreme length and complexity of the analtyical solution required, only numerical results for particular cases were reported. However, a result which has some special significance for the experimental part of the present study is contained in Figure 7. The results show how the ratio of transverse modulus to shear modulus is predicted to rise assymptotically as the resin Poisson's ratio approaches 0.5.

2.1.2 Strain Magnification Theory

Kies[28] in 1962 was the first worker to put forward a quantitative explanation of the drastic reduction in strain to failure on addition of transverse glass fibres to a thermosetting resin. The model presented was of idealised hexagonal and square arrays of high modulus fibres embedded in low modulus resin. Perfect fibre/resin bonding and elastic linearity were assumed. It was argued that since the fibres are much stiffer than the resin most of the applied strain concentrates in the resin between the fibres. The derivation of this strain concentration factor for a square array is reproduced in Appendix 3. The strain concentration factor is a function of fibre and resin moduli and increases with increasing fibre volume fraction. At high volume fractions, when the fibres are virtually touching a strain magnification in the resin equal to the ratio of fibre to matrix modulus is predicted. As has already been mentioned, the appropriate transverse modulus for glass fibre is easy to determine, but for anisotropic fibres such as carbon or aramids this is not so straightforward. Rearranging Kies original equations to express them in terms of fibre volume fractions gives, for a square array:

$$\frac{\epsilon_{max}}{\epsilon_2} = \frac{(\pi/V_f)^{\frac{1}{2}}}{\frac{2E_m}{E_f} - 2 + (\pi/V_f)^{\frac{1}{2}}}$$

and for a hexagonal array:

$$\frac{\epsilon_{max}}{\epsilon_2} = \frac{\left[\frac{2\pi}{\sqrt{3}\ V_f}\right]^{\frac{1}{2}}}{\frac{2E_m}{E_f} - 2 + \left[\frac{2\pi}{\sqrt{3}\ V_f}\right]^{\frac{1}{2}}}$$

where ϵ_{max} = maximum strain in the resin between the fibres

ϵ_2 = applied transverse strain.

Corresponding equations for plane strain are obtained by modifying the effective moduli via the relation:

$$E' = \frac{E}{1 - \nu_m^2}$$

The derivation of Kies strain concentration factor would seem to implicitly assume a Reuss model for transverse modulus which predicts the lowest transverse modulus of any of the models previously reviewed.

Garrett and Bailey[29] carried out a comprehensive investigation into the influence of resin flexibility on transverse failure strain of glass/polyester laminates. They found that Kies theory was able to predict the general trend of the results but not the actual values with any accuracy. Even by using the model for a square array (which predicts the lowest transverse strain to failure) the equation overpredicted the measured transverse failure strain values. Predictions and experimental results were found to agree only if a fibre volume fraction of 58% was assumed, whereas their material was

of 30% volume fraction (see Figure 8). This disparity was explained by fibre bunching in the real composite causing premature cracking at local regions of high fibre volume fraction. The artificial assumption of single modulus values, particularly for the highly non-linear flexibilised resins was pointed out together with the complicating effect of their strong strain rate dependence.

Gagger and Broutman[30] explored the use of flexible resins in a glass mat composite and were able to show that, depending on the degree of matrix constraint, the triaxial stress which results in the resin can reduce the actual strain to failure (particularly for very ductile resins) to values far less than those measured under uniaxial tension. Vasil'ev and Salov[31] also indicate the importance of the Poisson effect in composite transverse performance. They state that to achieve increased transverse deformability while maintaining good axial properties the matrix should have the following characteristics: failure strain not less than 60%; mean Poisson's ratio of 0.35 and an elastic modulus not lower than 3 GPa. Since such a resin is unavailable it was proposed that the function of the matrix be split among two different resin systems. The first high modulus resin was used to coat each fibre and these composite fibres were then aligned in a matrix of high deformablity. In this way 50% volume fraction glass fibre composites were fabricated with transverse failure strains of approximately 4%.

The philosophy of Stevens and Lupton[32,33] is that useful increases in transverse failure strain can be obtained without sacrificing the advantages inherent in using a stiff matrix by using a resin system with a high initial modulus but which is able to cold-draw to high strains before failure. By using a resin system which yielded at 3% strain but which failed at a strain of 38% a composite was fabricated with a transverse failure strain of 2-3%.

There is a considerable body of experimental evidence on the use of flexible resins with glass fibre woven cloth[34], cross-plied laminates[35] and filament wound pipes[36] which demonstrates that the use of resins of very high failure strains produces composites with modest increases in transverse failure strain.

2.1.3 Stress Magnification Theories

The most clear-cut feature of transverse strength is that it is usually less than the strength of the parent resin system[2].

The simplest approach to considering how this strength reduction arises is to imagine no bonding between fibre and resin and to therefore treat the composite as a resin with a series of cylindrical holes[2]. If it is assumed that the stress concentration at the edges of the holes is relieved by plastic flow, the strength will be controlled by the relative cross-sectional area of resin remaining. For a square array this predicts:

$$\frac{\sigma_2}{\sigma_m} = 1 - \left[\frac{4V_f}{\pi}\right]^{\frac{1}{2}}$$

and for a hexagonal array:

$$\frac{\sigma_2}{\sigma_m} = 1 - \left[\frac{2\sqrt{3}V_f}{\pi}\right]^{\frac{1}{2}}$$

where σ_2 = transverse strength

and σ_m = matrix strength.

A non-zero interfacial bond strength can be incorporated by a similar law of mixtures argument of relative areas which modifies the above equations by simply adding a term for interfacial strength[37]. The equation for a square array becomes:

$$\sigma_2 = \sigma_m \left[1 - \left[\frac{4V_f}{\pi}\right]^{\frac{1}{2}}\right] + \sigma_i \left[\frac{4V_f}{\pi}\right]^{\frac{1}{2}}$$

and for a hexagonal array:

$$\sigma_2 = \sigma_m \left[1 - \left[\frac{2\sqrt{3}V_f}{\pi}\right]^{\frac{1}{2}}\right] + \sigma_i \left[\frac{2\sqrt{3}V_f}{\pi}\right]^{\frac{1}{2}}$$

where σ_i = interfacial bond strength.

Although a 'weak-link' argument would question the physical significance of the above approach, Marom and White[38] found that the expression for a hexagonal array fitted their experimental results for (non-surface treated) glass fibre/epoxy composites over a range of fibre volume fractions if an interfacial strength of 5 MPa was assumed, see Figure 9. Experimental data on transverse fracture energies were also presented which were described less well by the above equations. Transverse cracks were observed to extend catastrophically in material with low fibre volume fractions but to grow in a more stable manner with fibre contents greater than approximately 25%.

Several papers have been presented by Chamis[16,39,40] on the use of micromechanics theories for predicting general composite behaviour from constituent properties. An early model[39] neglecting Poisson effects and using an idealised square array describes the maximum stress concentration in the matrix by:

$$\frac{\sigma_m}{\sigma_2} = \frac{1 - V_f[1 - (E_m/E_f)]}{1 - (4V_f/\pi)^{\frac{1}{2}}[1 - (E_m/E_f)]}$$

where σ_m = maximum stress in the matrix.

The derivation of this equation was not described. However, Appendix 4 derives stress concentration factors for both square and hexagonal idealised arrays. The assumptions employed in this

derivation are that the element can be treated as being split into a large number of separate sheets aligned in the loading direction and that the Reuss model of transverse modulus is applicable. The resulting equations are, for a square array:

$$\frac{\sigma_m}{\sigma_2} = \frac{E_f - E_f V_f + E_m V_f}{E_f + (\pi/V_f)^{-\frac{1}{2}}(2E_m - 2E_f)}$$

and for a hexagonal array:

$$\frac{\sigma_m}{\sigma_2} = \frac{E_f - E_f V_f + E_m V_f}{E_f + \left[\frac{2\pi}{\sqrt{3V_f}}\right]^{-\frac{1}{2}}(2E_m - 2E_f)}$$

Since the equation for the square array from Appendix 4 is in fact identical to the Chamis equation it is reasonable to suppose that the same assumptions were employed. The square array stress concentration factor is expressed graphically in Figure 10 for a fibre modulus >> resin modulus. It can be seen that over a wide fibre volume fraction range (30%-60%) the stress concentration factor is approximately 2.

When this, and other, models of stress concentration factor are used for strength prediction an important assumption is made, which is that the transverse composite fails immediately that the maximum predicted stress exceeds the strength of the neat matrix as measured in a uniaxial test.

In a wide ranging experimental study by Bailey and Parvisi[24] the Chamis stress concentration model was used to interpret strain to failure measurements on glass fibre/epoxy and polyester cross-plied laminates fabricated with varying fibre volume fraction. They assumed that fibre bunching ensured that locally the fibre volume fraction would be maintained in the region of 30-60% irrespective of the global fibre volume fraction and therefore that a stress concentration factor of approximately 2 (see Figure 10) applied to the whole range of laminates. By using the Halpin-Tsai equations to predict the increase in modulus with increasing volume fraction a resulting reduction in transverse failure strain was predicted which fits the experimental data for glass/epoxy very well, see Figure 11. The theory does not fit the results for glass/polyester since, it was argued, thermal stresses had caused complete debonding prior to testing. The observation that stress concentration factors may be dominated by areas of fibre bunching correlates with microscopic studies of laminae fracture which confirm that transverse cracks are nucleated in regions of dense packing[2].

A recent, more comprehensive, analysis by Chamis[16] quotes equations by which the microstresses in all three directions at various locations within an idealised square array may be calculated.

In this paper the derivation of the equations is not described, neither are the assumptions outlined. However, the equations are reproduced below with the definition of the coordinate system contained in Figure 12. The predicted microstresses in directions 1, 2 and 3 at locations A and B under an applied transverse stress, σ_2, are:

$$\sigma_{m1} = (\nu_m - \frac{\nu_{12} E_m}{E_{11}}) \sigma_2$$

$$\sigma_{f2} = (\nu_{f12} - \frac{\nu_{12} E_{f11}}{E_{11}}) \nu_2$$

$$\sigma_{m2}^{A} = \left[\frac{E_m}{E_2} \right] \sigma_2$$

$$\sigma_{m2}^{B} = \left[\frac{E_{22}}{E_2^*} \right] \sigma_2$$

$$\sigma_{f2}^{B} = \left[\frac{E_{22}}{E_2^*} \right] \sigma_2$$

$$\sigma_{m3}^{A} = (\nu_m - \nu_{23}) (E_m/E_{22}) \sigma_2$$

$$\sigma_{f3}^{B} = \sigma_{m3}^{B} = - \left[\frac{1 - \sqrt{V_f}}{\sqrt{V_f}} \right] (\nu_m - \nu_{23}) (E_m/E_{22}) \sigma_2$$

In which,

$$E_2^* = E_m(1 - \sqrt{V_f}) + \left[\frac{E_m \sqrt{V_f}}{1 - \sqrt{V_f} (1 - E_m/E_{f22})} \right]$$

$$E_{22} = \frac{E_m}{1 - \sqrt{V_f} (1 - E_m/E_{f22})}$$

and $\nu_{23} = V_f \nu_{f23} + (1 - V_f)(2\nu_m - \nu_{12} E_{22}/E_{11})$.

Materials constants required are:

ν_m = matrix Poisson's ratio

ν_{12} = composite longitudinal Poisson's ratio

E_m = matrix modulus

E_{11} = composite longitudinal modulus

ν_{f12} = fibre longitudinal Poisson's ratio

E_{f11} = fibre longitudinal modulus

E_{f22} = fibre transverse modulus

ν_{f23} = fibre transverse Poisson's ratio.

Some of the above composite materials constants are easily calculated from constituent properties through the law of mixtures i.e.

$$E_{11} = V_f E_{11f} + (1 - V_f) E_m$$

and

$$\nu_{12} = V_f \nu_{f12} + (1 - V_f) \nu_m$$

The more exotic consistent properties are obtainable from reference 16, e.g. for E.glass fibre,

$$\nu_{f12} = \nu_{f21} = 0.22$$

An approach of still further complexity was employed by Greszczuk[41] who considered the stress distribution around idealised distributions of fibres in a matrix containing voids. The most

recent approach calculates the number of 'ineffective fibres' which bound the voids from the difference between measured and expected transverse moduli. This calculated volume fraction of voids is then used in the analysis to predict the transverse strength with, it seems, reasonable accuracy.

The refreshingly straightforward approach by Spencer[25] has already been outlined in a previous section on transverse modulus predictions. In order to produce an expression for modulus the detailed interfibre stress distribution had to be derived. This therefore allows the maximum matrix stress, which exists at the point of minimum separation, to be expressed:

$$\sigma_m = \frac{\sigma_2}{\alpha(1 - K/\gamma)}$$

where $\alpha = E_{22}/E_m$

$K = 1 - E_m/E_f$

and γ = fibre separation parameter.

The transverse modulus, E_{22}, is itself predicted through the Spencer model in terms of K and γ as outlined in Section 2.1.1. The separation parameter γ is related to fibre volume fraction by assuming triangular, square, hexagonal or variable packing geometries, again as described in Section 2.1.1. If the above equation is taken to the limit of maximum fibre volume fraction where $\gamma = 1$ (i.e. the fibres touch) then:

$$\text{limit } \sigma_m = \sigma_2 \frac{E_f}{E_{22}}$$

The Adams and Doner[11,26] analysis as well as predicting transverse modulus (see Section 2.1.1) can generate the complete interfibre stress distribution for a square aarray taking into account Poisson constraint effects, see Figure 13. Unfortunately the finite difference solution employed precludes the quoting of an explicit equation for interfibre stress prediction. However, Figure 14 expresses graphically numerical results for the principal stress concentration factor as a function of fibre/resin modulus ratio for several different fibre volume fractions. The Poisson's ratios used were 0.20 and 0.35 for the fibre and resin respectively. Identical, independent results to these were obtained by the equivalent inclusion method[42].

All of the foregoing theoretical models have employed two quite severe assumptions: namely linear elasticity in both fibre and matrix, and idealised arrays mostly of square or hexagonal form. Three theoretical models which have attempted to relax each of these assumptions have been presented in the literature[43,44,45]. The model of Huang[43] is analytical and would therefore seem that the approach could be adopted by other workers. The large scale transverse deformation of a boron/aluminium composite was accurately predicted by the technique but the model is suggested as only being applicable when plastic strains are large and fibre volume fractions low. A finite element analysis was used by Adams[44] to model

transverse inelastic behaviour. The nature of the solution means that the results are of little applicability to other, different cases but a useful observation which arose was that extensive local yielding and stress redistribution can occur in a composite with little non-linear behaviour being apparent in the composite as a whole. By making the assumption of identical shear modulus of fibre and matrix (which is not too extreme an assumption for anisotropic fibres such as carbon or aramids in epoxy) Sendeckyj and Wu[45] were able to obtain closed form (usable) solutions for interfibre stresses in idealised array transverse composites. A further, more unusual, result of their work was that a non-closed form solution was possible for random arrays of transverse fibres. Numerical results were presented based on an array taken from an actual composite cross section.

The observation that interfibre stresses are highest where fibres most closely approach has led to investigations into the use of thin low modulus fibre coatings. Theoretical results have suggested that stress concentrations can be reduced by the presence of soft fibre- matrix interlayers[46,47] and the beneficial effects of such treatments have been demonstrated in photoelastic and strength tests on model composites[48], and in strength tests on real glass/epoxy composites[49]. A differing approach is advocated by Vasil'ev and Salov[31] who also used coated fibres but with an interlayer of higher stiffness than the flexible matrix in which they were embedded. Hull[2] points out that even a thin interlayer can drastically reduce the effective fibre volume fraction and thereby reduce the longitudinal properties.

2.2 Fracture Mechanics Approaches

This field is reviewed in three parts. In the first: micromechanical fracture mechanics, the material is viewed on the microstructural scale and the initiation and propagation of interfibre microcracks is discussed. Within this section will be presented results on composites with rubber toughened matrices and a discussion of the effects on constraint of crack tip plasticity. The second part: macromechanical fracture mechanics, will be concerned with the influence of global composite toughness on transverse behaviour. The third part: fracture mechanics of constrained plies, will explore attempts to understand the influence of ply thickness on transverse cracking strain in multidirectional laminates.

2.2.1 Micromechanical Fracture Mechanics

Tirosh, Katz, Lifschetz and Tetelman[50] modelled the stress distribution around a single fibre embedded in an elastic matrix and considered the stability of a microcrack situated at, or near, the interface. Several interesting results arose from this study including the prediction that the maximum radial stress occurs not at the interface but at a small distance into the matrix depending on its Poisson's ratio. This implies that a crack may move close to the interface, but not cause debonding. The possible ways in which micro- flaws may extend were considered and case (c) in Figure 15 was seen to be the most damaging. The finite element method was used to analyse the mutual interaction between fibres in idealised arrays. An important, and rather surprising, outcome was that the stress

intensity factor for the most damaging microflaw is not sensitive to crack length. This implies that there is no tendency for flaws to extend unstably and that sub-critical growth of several cracks is possible.

The literature abounds with publications on the use of relatively small additions of elastomers (mostly carboxyl-terminated butadiene acrylonitriles, CTBN) to brittle thermosets (mostly epoxies) as toughening agents. These types of elastomers precipitate out as a second phase during cure to leave dispersions of spherical rubber particles of sizes of the order of μm's in a matrix of the higher modulus constituent. This morphology possesses advantages over the case of a dissolved flexibiliser as it results in relatively small decreases in resin rigidity or glass transition temperature. The mechanism of toughening in these materials has been a contentious subject over the years though recent, in-depth studies by Yee and Pearson[51,52] suggest that energy absorption is due to the rubber particles promoting shear banding in the epoxy matrix with their possible cavitation enhancing the process by relieving the triaxial tension at the crack tip. Whatever the mechanism it is clear that bulk samples of epoxy resin can have their toughness improved by greater than an order of magnitude on addition of a few per cent of CBTN elastomer[53]. It was natural that attempts should be made to exploit these improvements in matrix performance in fibre composite. Scott and Phillips[54] investigated the transverse toughness(G_{IC}) of carbon fibre reinforced epoxies with and without CTBN additions. While the fracture toughness of the epoxy matrix could be dramatically increased by the addition of a small quantity of CTBN (e.g. G_{IC} from ca. 300 to ca. 3000 Jm^{-2} on addition of 9 wt.% CTBN)

only modest increases in G_{IC} were obtained (e.g. G_{IC} from ca. 300 to 500 Jm^{-2}) in 60% fibre volume fraction transverse composite. This disappointingly low relative toughness in the composite was attributed to the fibres limiting the volume at the crack tip within which the matrix could yield and energy could be absorbed. The suppression of resin toughness in composite in both transverse and delamination fracture modes has been widely observed[55,56,57]. Lee[58] took these concepts further by deriving an expression for the plastic zone size by modelling the transverse composite as an 'equivalent adhesive bond'. The theoretical prediction was able to predict the trend of the experimental toughness data on glass/ unmodified epoxy. The important material parameter for controlling transverse toughness was shown to be σ^2_y/E (where σ_y and E are resin yield stress and modulus respectively) rather than resin toughness alone. Surprisingly, for the range of materials investigated, very little correlation was observed between resin toughness and transverse composite toughness.

A urethane (as opposed to a CTBN) elastomer was the epoxy modifier used by Wells and Hancox[59]. The structure of the blends was thought to be a solution up to 30% urethane with a second rubbery phase precipitating out at higher concentrations. Improvements in the transverse strength and strain to failure of 60% volume fraction composites of both glass and carbon fibre were achieved by urethane modification of the epoxy matrix, see Figures 16 and 17.

Improvements in transverse performance were most marked in the carbon fibre composite due, it was argued, to poorer adhesion between the glass and epoxy/urenthane blends. This suggested that greater improvements might be possible in these materials by suitable optimisation of the glass coupling agent.

Many workers have noted that, when using fracture mechanics specimens which induce stable crack growth, the transverse fracture toughness often increases as the crack propagates. Early on, this phenomenon was attributed on a microstructural scale to the presence of fibres criss-crossing the fracture faces leading to the development of a tied zone behind the crack tip[60]. The development of tied zones has alternatively been viewed as a complication in the interpretation of transverse cracking experiments[61,62,63], or as a valuable extra energy absorbing mechanism[64] and useful contributor to transverse crack stability[65]. The origin of criss-crossing fibres has been variously ascribed to fibre misalignment during fabrication[66] and as a natural consequence of the way in which microstructural flaws are activated within the highly stressed region at the crack tip[60]. This study has made original experimental and theoretical contributions to this debate, and a more complete review of the literature on this subject will be made in a later section in which this work will be presented and discussed.

2.2.2 Macromechanical Fracture Mechanics

An original approach which, by ignoring microstructural details, bypasses the problems of calculation of stress/strain concentration factors and non-ideal fibre distributions was made by Christensen and Rinde[67]. They carried out tests on a series of four resin systems of varying flexibility and transverse S-glass fibre composites (of fibre volume fraction 65-69%) fabricated using these resins. While the resins were observed to fail by a process involving high elongation and flow, all the composites failed in a brittle manner. The authors therefore felt justified in analysing the transverse strength results from a fracture mechanics standpoint. The well known Griffith relationship:

$$\sigma = Y \left[\frac{EG}{c} \right]^{\frac{1}{2}}$$

was rewritten in terms of transverse failure strain, ϵ_2 (assuming Hookes law is applicable) to give:

$$\epsilon_2 = Y \left[\frac{G}{cE_{22}} \right]^{\frac{1}{2}}$$

where G = effective fracture toughness

c = critical flaw size

E_{22} = transverse modulus

and Y = geometric constant.

By assuming that the critical flaw size and the effective fracture toughness were constant then:

$$\epsilon_2 = \text{constant} \times E_{22}^{-½}$$

Perhaps surprisingly, the data on transverse failure strain and modulus were found to fit the above proportionality with reasonable accuracy, see Figure 18. Thus, assuming the presence of flaws of a certain size are inevitable, an increased transverse failure strain is achieved by maximising the ratio, G/E_{22}. Unfortunately, no data on composite toughness or flaw sizes were presented; however, while it might be expected that for composites fabricated in an identical manner the flaw sizes might be the same, it seems unlikely that transverse toughness could remain constant for the range of resins studied.

The concept of intrinsic flaws in transverse composite has been used by Morley and Pissinou[68] to understand the formation of transverse cracks in laminates, and by Hahn, Erikson and Tsai[69] to enable the development of a phenomenological model to describe the strength (and the Weibull distribution of strengths) of composites under combined shear and transverse loading.

2.2.3 Fracture Mechanics of Constrained Plies

The literature on the use of fracture mechanics to describe transverse crack suppression contains much elegant theoretical work directed towards gaining a greater understanding of a process of great practical significance. Aveston, Cooper and Kelly[70] carried out important work on the fracture processes of composites with components of differing strains to failure. They reported work by Cooper and Silwood[71] on the multiple cracking of epoxy resin containing embedded steel wires, who stated that under increasing applied strain and increasing wire volume fraction the average matrix crack spacing decreased in a simple way governed by the level of stress transferred by shear from the wires into the portions of resin remaining. However, when the wire volume fraction became great enough or the wires became small enough abnormal behaviour occurred and cracking was suppressed. Aveston, Cooper and Kelly[70] showed that for a crack to form two conditions must be fulfilled:

(1) the stress in the matrix must equal the breaking stress, and

(2) there must be a decrease in the combined energy of the specimen and loading system.

Under conditions of fixed load an energy balance can be set up where a crack will only form provided:

$$2\gamma_m V_m + \gamma_{db} + Us + \Delta Uf \leq \Delta W + \Delta Um$$

where ΔW = work done by applied stress

ΔUm = reduction of strain energy on crack extension

γ_m = matrix fracture surface energy

V_m = volume fraction of matrix

γ_{db} = surface energy of fibre/matrix debonding

Us = friction energy of fibre/matrix sliding

ΔUf = increased strain energy taken up by fibres.

Each of the terms in the inequality above can be expressed as geometrical and material parameters of the system, yielding an equation which specifies the threshold matrix cracking strain

$$\epsilon_{mu} = \left[\frac{12\ \tau\ \gamma_m\ E_f\ V_f^2}{E_c\ E_m^2\ r\ V_m} \right]^{\frac{1}{2}}$$

where ϵ_{mu} = strain below which matrix cracking is suppressed

τ = interface frictional strength

E_f = fibre modulus

E_m = matrix modulus

r = fibre radius.

A direct parallel exists between the premature cracking of a brittle resin reinforced with extensible fibres and the cracking of transverse plies in a cross-ply laminate. The effect of ply dispersion on the transverse cracking strain was studied by Parvizi, Garrett and Bailey[72] in glass/epoxy laminates and by Bailey, Curtis and Parvizi[73] in carbon/epoxy laminates. Since it was found that

the interface between the transverse and longitudinal plies remained intact after transverse cracking, the dissipative friction sliding energy term (Us) in the Aveston-Cooper-Kelly equation was neglected but in a similar way a minimum transverse failure strain (ϵ_2^{min}) was predicted:

$$\epsilon_2^{min} = \left[\frac{b\, E_{11}\, G_{23}\, G_{IC}^{\,2}}{(b + d)\, d^2\, E_c\, E_{22}^{\,3}} \right]^{1/4}$$

where b = thickness of the axial plies

d = thickness of the transverse plies

E_{11} = elastic modulus of the axial ply

G_{23} = shear modulus of the transverse ply

G_{IC} = mode I fracture toughness of transverse ply

E_c = elastic modulus of laminate in axial direction

E_{22} = elastic modulus of the transverse ply.

All of the above terms are either directly measurable or dictated during fabrication. Figure 19 shows the experimentally observed transverse cracking strains together with the theoretical prediction for a range of transverse ply thicknesses. While the prediction underestimates actual values at large ply thicknesses, for thinner plies the agreement is excellent.

Flaggs and Kural[74] carried out experimental measurements of transverse cracking strains in 0°/90°, ± 30°/90° and ± 60°/90° families of carbon/epoxy laminates. These θ°/90° laminates were

treated as cross-ply laminates with the stiffness of the 'axial' plies changing with angle θ. Flaggs and Kural highlighted (as did Bailey, Curtis and Parvizi) the importance of accounting for residual stresses arising from the curing cycle which can be a large fraction of the transverse strength. Using an asymmetric 0°/90° laminate the effective stress free temperature of the material in question was evaluated by measuring the degree of bending of the laminate as a function of temperature. The estimated stress free temperature was then used in a lamination theory analysis to calculate the level of residual stresses acting on the transverse ply so that the influence of mechanical and thermal stresses on transverse cracking strain could be distinguished. Figure 20 shows the relative contributions of applied and residual stresses to the 'in-situ' transverse strengths of the three laminate families considered. Applying the Aveston-Cooper-Kelly theory to the experimental results they found (as did references 72 and 73) reasonable agreement for thin transverse plies but considerable underestimation of the measured cracking strains at large ply thicknesses. The existence of a Weibull effect was suggested as a possible factor. That is, that transverse strength could be viewed as a statistical parameter and related to the volume of material under test such that the thicker the transverse ply, the greater the probability of failure. It was found that the Weibull strength theory provided an excellent fit with results but only if the Weibull shape parameter (a measure of the distribution of strengths) was varied between the laminate families under consideration.

Wang and Crossman[75], as part of a wider study on transverse cracking and delamination, developed a sophisticated finite element model based on linear elastic fracture mechanics to predict the onset of transverse cracking in laminates as a function of material and geometrical variables. The model was correlated with experimental evidence on a $(\pm 25°/90°_n)_s$ carbon/epoxy laminate family by Crossman, Warren, Wang and Law[76]. The decrease in strain for onset of transverse cracking in the 90° plies with increase in their relative thickness (n) was predicted by the model with great accuracy.

The Aveston-Cooper-Kelly type constrained cracking analysis considers the energy change between an initial, crack free state and a final state in which a transverse crack exists. An approach which takes a closer look at the mechanism of transverse crack formation is suggested by Ogin and Smith[77]. By considering the stress intensity factor which exists at the tip of a crack which spans the thickness of the transverse ply, but has not yet propagated across the width, it is possible to express the conditions for stablity of this intrinsic transverse crack in terms of the ply stiffnesses and thicknesses. The equation which results:

$$\epsilon_2 = \left[\frac{G_c}{E_{22} 2d} \right]^{\frac{1}{2}}$$

where ϵ_2 = strain for onset of transverse cracking

G_c = transverse fracture toughness

E_{22} = transverse ply modulus

2d = transverse ply thickness

is much simpler than the equation presented by Parvizi, Garrett and Bailey[72], and yet for the same cross-plied carbon/epoxy material, makes predictions which are very similar. The above equation similarly underestimates the cracking strain for thick transverse plies and the explanation put forward for this was that for thicker plies the critical defect size was smaller than the ply thickness and so the model of an incipient crack which spanned the ply thickness was invalid. Instead, when the applied strain reaches a value sufficient to propagate the incipient crack it propagates completely across both the thickness and width. Taking values of large ply failure strain, transverse modulus and toughness from reference 72 the critical defect size was calculated to be approximately 0.6 mm, which agreed quite well with the thickness of transverse ply at which the theoretical prediction began to disagree with experiment, see Figure 19.

Morley and Pissinou[68] also considered the growth of incipient transverse cracks in laminates but treated the energetics of their propagation in a more sophisticated manner. A model was adapted for the case of transverse cracking which was originally developed to describe the energetics of growth of a crack across which some stress could be carried by bridging fibres. The model relied on values of intrinsic transverse flaw sizes which were calculated, through the Griffith equation, from literature values of toughness, modulus and failure strain. This gave a range of intrinsic crack lengths from 0.30 to 0.83 mm. The expression for strain energy released by the growing crack required numerical integration but the solution yielded

predictions of cracking strain as a function of ply thickness which agreed very closely with the experimental results in references 73, 74 and 76 over the whole range of ply thicknesses.

3. RATIONALE OF THE EXPERIMENTAL PROGRAMME

A clear dichotomy of thought on the origins of transverse cracking behaviour is apparent in the literature. On the one hand, micromechanics models of widely varying levels of sophistication consider stress and strain distribution between fibres and predict transverse fracture when the matrix strength or failure strain are exceeded at any point. Whether the failure process is one of yielding or brittle fracture is not stated explicitly and little account is generally taken by these theories of matrix non-linearity, debonding or gradual damage development. On the other hand, fracture mechanics models, again of a range of complexity, consider the presence of intrinsic flaws as inevitable and treat the energetics of their propagation as cracks, either at the interfibre level or from a global viewpoint which assumes the material to be macroscopically homogeneous.

A validation of the range of theories put forward requires a knowledge of the full mechanical properties of the material including the modulus, strength, strain to failure and toughness. None of the papers reviewed has measured the necessary range of properties on a single material.

The intention of this experimental study has been to use urethane rubber modified epoxy resins to produce both neat matrix material and corresponding transverse composites, which display a systematic gradation in mechanical properties, to allow a validation of the available theories.

The fibre type selected for manufacture of transverse composite was E-glass. The anisotropic nature of carbon or aramid fibres would have introduced the complication of identification of the appropriate transverse fibre modulus for use in the micromechanics models, whereas the isotropic nature of glass fibre allows the easily obtained longitudinal modulus to be taken for this value. Using glass fibre, transparent composite can be fabricated. This has two advantages. Firstly, the quality of the composite material can be instantly assessed since if significant debonding or voidage is present the material becomes translucent. Secondly, when carrying out crack propagation experiments the location of the crack can be easily visually determined. This is surprisingly difficult with carbon fibre composites which can require the use of reflective, brittle coatings for precise crack location.

It was considered desirable that the alignment of fibre be closely controlled since this may well have an influence on the transverse crack propagation behaviour. This requirement dictated that the composite manufacturing route should be filament winding in which continuous fibre is impregnated with liquid resin and drawn onto a rotating mandrel or former in a highly controlled manner. By pressing the composite to a calculated thickness the fibre volume fraction could be controlled to a reasonable tolerance (65% - 76%). Material manufacture will be described in more detail in a later section. It was felt that the fibre volume fraction should be maintained within narrow limits so that the systematic variation of only one material parameter; resin flexibility, could be sensibly explored.

The particular choice of resin formulation allowed the manufacture of epoxy/urethane neat resin, and composite materials which ranged from 100% rigid epoxy to 100% urethane rubber. The actual blend ratios eventually chosen for the experimental programme were:

100% epoxy / 0% urethane
90% epoxy / 10% urethane
80% epoxy / 20% urethane
60% epoxy / 40% urethane
40% epoxy / 60% urethane
0% epoxy /100% urethane

In order to make meaningful measurements of materials mechanical properties the correct choice of test specimen is vital. Since it was not self-evident which test specimen geometries were the best for measuring the strength and toughness values required, an initial experimental test specimen selection programme was undertaken which used transverse composite and neat resin specimens manufactured using a more conventional, rigid epoxy resin system.

4. MATERIALS PRODUCTION AND PHYSICO-CHEMICAL CHARACTERISATION

This Chapter will describe the selection of the resin system, and the materials manufacturing route which dictated it. Also presented will be the results of attempts to characterise the structural, physical and chemical nature of the materials by microsection, density, dynamic mechanical analysis and infra-red spectroscopy measurements.

4.1 Resin Selection and Materials Manufacture

The perceived requirement for accurate fibre alignment, outlined in the previous section, suggested the use of filament winding for unidirectional composite fabrication. The process is shown schematically in Figure 21. Two plate samples were produced from each wind after pressing between platens and curing the matrix. A few hoop-wound tubular specimens were manufactured to assess their potential as rather more unusual strength specimens in the initial programme of test specimen development. Careful control of the winding process allowed the manufacture of composite plates which were truly unidirectional, within the precision of the winding machine. This was achieved by building-up the thickness of composite required while traversing the winding carriage in one direction only and 'tying-off' and 'tying-on' again after each traverse. A much simpler method of production was to build-up the material thickness by traversing in both directions. This produced material with successive layers which crossed each other at 1°.

These two types of material are labelled '0°' and '± ½°' respectively. The fibre used for the initial and main experimental programmes was Silenka 1200 tex E-glass with an epoxy/polyester compatible size.

The first composite and resin samples for an initial test specimen development programme were manufactured using a conventional, rigid epoxy resin system (MY750/HY917/DY070), obtained from Ciba-Geigy. The details of composite production and resin formulation and cure are given in Appendix 5.

Wet filament winding requires that the impregnating resin should have a viscosity less than approximately 200 Poise and a pot-life greater than approximately two hours. The conventional resin described above fulfils these requirements, but the identification of a suitable epoxy/urethane system required considerable investigation.

Solidification of epoxy resins can be accomplished by cross-linking using polyfunctional amines or anhydrides[78]. With amines, cross-linking occurs by reaction of an active hydrogen in the amine molecule with the oxygen atom in the epoxy group:

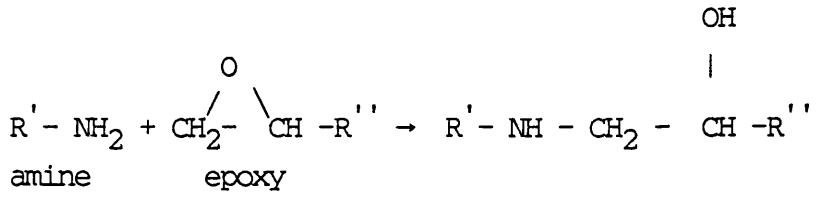

The secondary amine so formed can then react with another epoxy group:

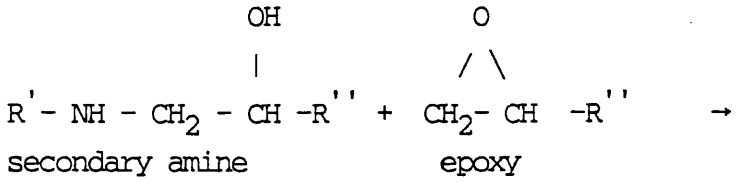

secondary amine — epoxy

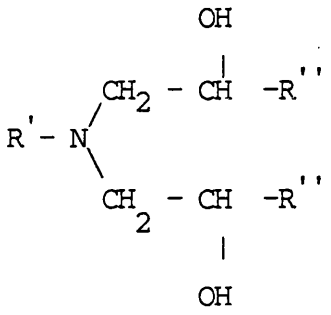

Commercial amine curing agents are usually based on molecules containing more than one amine group to produce an extensive network structure.

Urethane rubbers contain the isocyanate group (- N = C = O) which is highly reactive with molecules containing active hydrogen[79]. It reacts with amines to form the urea linkage:

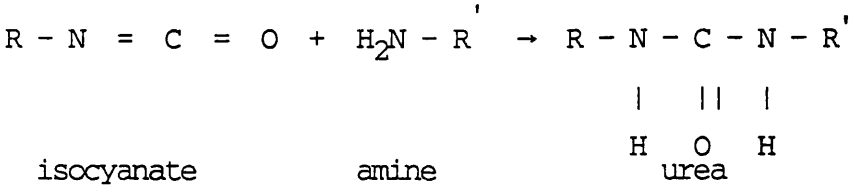

isocyanate — amine — urea

or with polyols to form the urethane linkage:

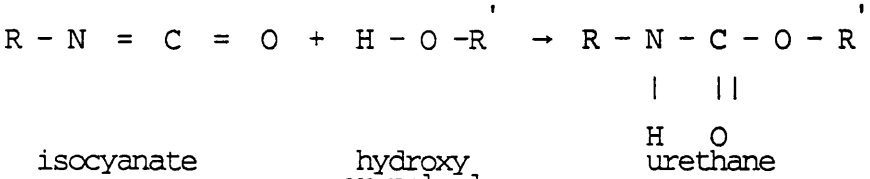

isocyanate — hydroxy or polyol — urethane

These urea and urethane groups can further react with available isocyanates to form chain branches:

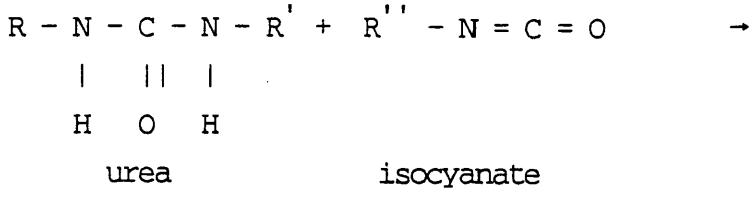

urea isocyanate

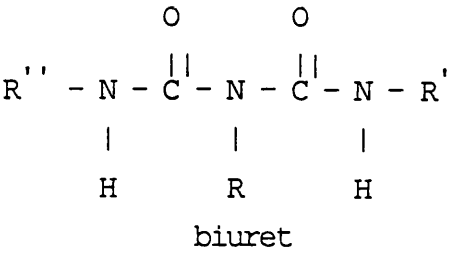

biuret

and

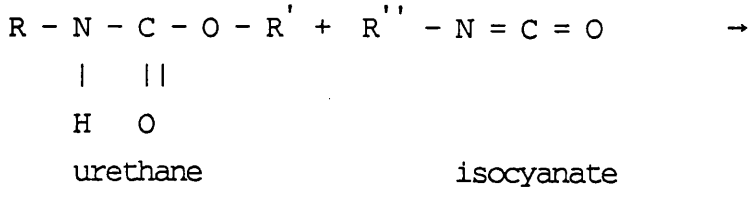

urethane isocyanate

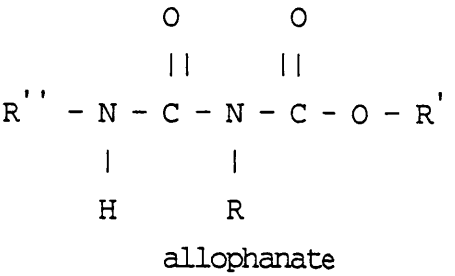

allophanate

Since the epoxy group also reacts readily with amines a polyfunctional amine initially appeared to be a convenient single curing agent for the epoxy/urethane blends. Initial trials with Adiprene L100 urethane from DuPont showed the system to be too reactive, even with aromatic diamines such as diamino diphenyl

sulphone to provide sufficient pot-life for winding. The range of 'Monothane' urethanes from Compounding Ingredients Limited are one component systems containing the curing agent (in the present case a polyol) 'ready formulated' but with the isocyanate groups blocked by an undisclosed proprietary chemical. At room temperature the blocking agent prevents reaction of the isocyanate groups but on heating above 70°C the blocking agent begins to become unfixed and cross-linking commences. Such a system allowed the epoxy/amine/urethane/polyol mixtures, in all proportions, to be wet filament wound 'at leisure' below 70°C and then to be heated above this temperature to solidify the resin. The epoxy resin selected was the commercial system; MY778/HY932 from Ciba-Geigy. Discussions with Compounding Ingredients Limited were held to ensure compatibility of the components in the epoxy/amine/'Monothane' mixtures employed. Full details of these materials and their manufacture are contained in Appendix 6. The cure schedule was chosen to allow sufficient time for the epoxy and amine to cure at a temperature below which the isocyanate became unblocked. It has previously been found that the most transparent composite plates are obtained by pressing when the resin is on the point of gelling[80]. This was an added complication since the gel time was found to vary with urethane concentration. Final cure was carried out at 135°C (which is the Manufacturer's recommendation for neat 'Monothane') at which temperature the isocyanate became completely unblocked and, assuming sufficient molecular mobility, the polyol already present in the one-part 'Monothane' system was free to complete the urethane

cure. Due primarily to problems associated with identification of gel time, sixteen attempts were made to manufacture pairs of composite and resin plates. Of these, six at the urethane proportions 0%, 10%, 20%, 40%, 60% and 100% were successfully manufactured for use in the main experimental programme. A single mix of resin was divided for use in composite manufacture and for casting the neat resin plates. The use of the same mixture for simultaneous production of composite and neat resin material was considered necessary for direct comparisons as Scott, Wells and Phillips [81] have shown that minute changes in the proportion of curing agent dramatically alters fracture toughness and crack propagation mode in epoxy resins. The initial test specimen development programme (described later) showed that there was no difference in crack propagation behaviour between the 0° and ± ½° filament wound plates and therefore the plates manufactured for the main experimental programme were all of the ± ½° type.

4.2 Density and Fibre Volume Fraction Determination

The Archimedes immersion technique (in which the weight in air and the weight in water are measured) was used in determining the densities of the six neat epoxy/urethane blends and the densities of the corresponding selected composites. Figure 22 shows the densities of resin blends measured in this way, together with the expected variation in density from the law of mixtures (which takes into account the fact that the percentage of urethane is a weight

fraction). It is interesting that the blends display a significantly higher density than would be expected if they were simple mixtures. The only explanation offered here is the obvious one; that packing of the molecular chains is better with blends of the two polymers, though why this should be the case is not understood.

After evaluating the densities of the composites the acid digestion technique (in which the resin is dissolved, leaving the fibre component) was used to determine the weight fraction of fibres. Using the literature density value of E-glass fibre of 2.56 g/cm^3 and the previously measured resin densities, the fibre and void volume fractions were calculated. The void volume fractions were zero (plus and minus a fraction of a percentage point) confirming what was seen visually. The measured fibre volume fractions of the selected plates were:

Resin-type used in composite plate (% urethane)	Fibre volume fraction (%)
0%	74%
10%	66%
20%	74%
40%	65%
60%	76%
100%	69%

The average fibre volume fraction is 70.7% ± 5.5%.

4.3 Composite Microsections

Optical micrographs were taken of sections of the composites cut across the fibres and polished down to 1μm diamond paste. These confirmed that all the composites were of good quality and high fibre volume fraction. See Figures 23 to 28.

4.4 Dynamic Mechanical Analysis

Dynamic mechanical analysis (DMA) is a technique in which a coupon of material is subjected to forced vibrations and the resonant frequency of vibration and power input required to maintain a constant vibration amplitude are measured as the specimen is subjected to a temperature change. Figures 29 to 34 are DMA traces for the epoxy/urethane neat resin blends produced using a DuPont 982 DMA head with a 1090 computer controller. The frequency trace is related to sample modulus, which in all the blends shows a monotonic decrease with increase in temperature. The rate of decrease is not constant however, there being certain temperatures at which the frequency fall-off is more rapid. These are transition temperatures at which further modes of molecular motion within the polymer network are freed. These transitions are more clearly seen in the damping traces which show a peak in energy absorption at the transition temperature. The higher temperature transition is the glass transition temperature, Tg. Below Tg the polymer behaves as a rigid, glassy material but above Tg becomes a more compliant, rubbery material. The Tg for the range of blends is plotted in Figure 35

versus the urethane proportion. It can be seen that Tg (as defined by the damping peak) falls continuously from a temperature of 121°C for the unblended epoxy resin to -22°C for the unblended urethane elastomer. For the 40% and 60% urethane content blends, the Tg is around room temperature and for this reason these materials are leathery and 'lossy' with a marked temperature and rate dependence of their mechanical properties. For the 0%, 10% and 20% urethane content blends a lower temperature damping peak is apparent at approximately -45°C which is largely unaffected by urethane content. For urethane contents higher than 40%, if this damping peak exists, it is masked by the approaching Tg peak. This secondary, lower temperature, so called γ, transition has been well documented in amine cured epoxy resins and has been postulated to be due to mobility of the segment $-CH_2 - CH(OH) - CH_2 - O -$ in the epoxy resin chain in a 'crankshaft' motion[82]. The strong dependence of Tg on urethane content would be expected if the epoxy and urethane polymer chains are intimately mixed since, in general, Tg corresponds to coordinated motion of polymer chains about the chain axis over distances of 50 to 100 atoms in length[83]. The lower temperature γ transition meanwhile involves motion of a smaller number of successive carbon atoms (usually 4 to 8[83]). This possibly explains the urethane independence of the γ transition temperature as there may be little interaction of epoxy and urethane chains over these short distances.

There is no evidence of a transition peak at the urethane Tg (-22°C) in the epoxy/urethane blends, which would be expected if a discrete rubber phase were present[83].

4.5 Infra-Red Spectroscopy

It was felt that infra-red spectroscopy of the cured resin blends might provide some insight into the chemistry of the curing reactions and identify if any cross-reaction of the urethane and epoxy components might be occurring[84]. Specimens were prepared by pressing pellets of KBr powder containing approximately 1½% by weight of the pulverised resin blends. A Pye Unicam Infra-Red Spectrometer was used which is capable of operating in both transmission or absorption modes. Scanning the pellets through wavenumbers 4000 cm^{-1} to 600 cm^{-1} produced the absorption traces given in Figures 36 to 41. Interpretation of such traces is problematic since a particular absorption peak often cannot be unambiguously attributed to a particular chemical group. Those peaks which have been identified and which correspond to significant chemical groups are marked. The epoxy peak is indicated as is the carbonyl peak which is a particular characteristic of urethane elastomers. The epoxy and carbonyl peaks show the systematic change in relative peak heights expected from a change in epoxy/urethane concentration. A principal aim of the infra-red spectroscopy investigation was to identify whether there were cross-reactions between the epoxy/amine and the urethane/polyol components. Figure 42 shows two infra-red spectra, one of which is from a 40% urethane/epoxy co-cured blend (marked 'blend') while the other trace (marked 'mix') is from a mixture of 100% epoxy resin and 100% urethane elastomer pulverised separately and added to the KBr pellet in the proportions 40:60. The difference in height of the background absorption and overall peak height can be attributed to small differences in thickness of

the two pellets and/or quantity of polymer added. However, differences in relative peak height between mix and blend may indicate differences in proportion of certain chemical groups and therefore evidence of chemical interaction of the epoxy/amine and urethane/polyol components. Significant differences are marked (i) to (iv). However, the only one of these peaks to have been identified is (i), which is associated with the epoxy group. This would seem to show a higher level of residual epoxy groups remaining in the blend, due perhaps to the urethane component hindering the mobility of epoxy and amine molecules and thereby suppressing their reaction.

4.6 Summary

A urethane elastomer system has been identified as a suitable component of epoxy/urethane blends for fabrication of unidirectional composite by filament winding. Dynamic mechanical analysis shows that the Tg of the blends decreases continuously as the urethane content is increased. A low temperature relaxation peak associated with the epoxy resin is apparent, but no relaxation peak at the elastomer Tg is apparent in any of the epoxy/urethane blends. This evidence and the observation that the epoxy/urethane blends are all transparent suggests that no discrete urethane rich phase is precipitated. The results of the infra-red spectroscopy are difficult to interpret and inconclusive. Cross reaction between the epoxy/amine and the urethane/polyol components may, or may not, have occurred. Density measurements of the epoxy/urethane neat resin

blends display an interesting positive deviation from the law of mixtures. Microsections and acid digestion measurements show that the composites are of good quality and high fibre volume fraction (average 71%).

5. TEST SPECIMEN DEVELOPMENT

As outlined in Chapter 3, because of the range of materials properties to be measured, and because of the particular problems associated with testing fibre composite materials[85], an initial programme of test specimen development was considered necessary. The material used was the conventional, rigid epoxy based composite described in Appendix 5 in plate form (wound at 0° and ±½°) and in hoop wound tube form. For completeness, the properties of the neat rigid epoxy resin were also evaluated.

5.1 Strength Test Specimen Development

Several different specimen geometries were explored in order to identify one which could provide a valid transverse tensile strength. These included straight-sided coupons, dogbones, 3 and 4 point bend of coupons and 4 point bend and uniaxial tension of hoop wound tubes. The tubular configurations were explored because they avoided the problems of damage introduction which seem to be inevitable when machining transverse specimens. The machined edges of the straight-sided coupons were polished to two different grades of abrasive paper to explore the consequences of machining damage on strength. An Instron 1195 screw driven testing machine was used with wedge action jaws or a flexural testing fixture, as appropriate.

5.1.1 Straight-Sided Coupons

Small coupons of approximately 35mm x 10mm x 1.6mm were machined using a 1/32 inch slitting saw on a milling machine. Although the plate was clamped between sheets of plywood to minimise machining damage, some tearing of the specimen edges did occur which, in some specimens, was removed by polishing on coarse (240 grade) or fine (600 grade) wet wheels using a special jig to maintain edge squareness. Subsequent to these early tests a water lubricated high-speed diamond wheel cutter was acquired which minimises edge damage, and this has been used to prepare the epoxy/urethane blend composites described in the main experimental programme. The practice of edge polishing has continued however, and the polishing jig shown in Figure 43 has continued to be used. The jig has lips machined on the inside surface at 10mm and 11mm from the polishing face at either side. Roughly cut specimens of 12mm width are butted against first the 11mm lip and then the 10mm lip and clamped in place and the exposed composite polished away. This removes 1mm from either edge leaving a rectangular cross-section specimen of uniform width.

Aluminium end tabs 1.5mm thick and machined to a ½ inch radius taper were bonded to the specimens to provide a smooth stress introduction. Even so, of the 16 specimens tested, only 7 broke at locations remote from the end tabs. A summary of the results is contained in Appendix 7(i). Strain gauge measurements on two of the ± ½° composite specimens indicated an average modulus (up to 0.3% strain) of 14.38 GPa.

5.1.2 Dogbones

Dogbone shaped specimens of gauge length 60mm by 2.03mm thickness and tapered to a width of 9.9mm were machined from 0° and ± ½° material using a Wallace-Rapra routing machine. The edges were rough, but due to the difficulty of polishing the edges of such a geometry, the specimens were tested as-machined. The results are contained in Appendix 7(ii). Of the 5 specimens tested, only 2 broke remote from the shoulder at the extremities of the specimen.

The dogbone specimen was found to be ideal for testing conventional neat resin. Specimens were made at gauge length 60mm by 4.1mm thickness and width tapered to 7.5mm using a 1¼ inch radius end milling tool. These specimens provided high strengths with fracture initiation within the gauge length associated with yielding and necking. Appendix 7(iii) summarises these neat resin strength results. From tests on two resin dogbone specimens with strain gauges bonded to each face the average modulus (up to 1.1% strain) was 3.09 GPa. Interestingly, these two strain gauged specimens failed at low strain with no evidence of yielding. Microscopic examination of the fracture surfaces revealed that crack initiation had occurred in the brittle strain gauge adhesive (Eastman 910; a cyanoacrylate, 'instant' adhesive) which propagated through the specimen thickness. It was therefore decided that in the main experimental programme strain gauges would not be used.

5.1.3 Three Point Flexure of Coupons

Coupons of average dimensions 50mm length, 8mm width and 1.9mm thickness were cut from 0° and ± ½° composite plates and tested in the as-machined condition in 3 point bending with a 38.3mm span. The results are summarised in Appendix 7(iv).

5.1.4 Four Point Flexure of Coupons

Coupons of both the 0° and ± ½° material were machined to average dimensions 50mm length, 8mm width and 1.9mm thickness. They were tested in the as-machined condition with a minor span of 19.1mm and major span of 38.3mm. The results are summarised in Appendix 7(v).

5.1.5 Tensile Testing of Hoop Wound Tubes

The testing of a tubular specimen is attractive since it avoids the possibility of machining damage within the gauge length giving rise to premature failure. A self-aligning fixture as described by Allred, Street and Martinez[86] was fabricated (with several modifications) to allow testing of hoop wound tubes of dimensions: outside diameter = 38.2mm and inside diameter = 34.3mm. Problems of failure of specimens close to, or within the end grips drove the specimen end fixture design from square ended steel to tapered steel, aluminium, resin and short fibre filled resin. Figure 44 shows the

tube testing rig with a specimen fitted with a tapered aluminium bonded end fixture. The wedge shaped tube end fixture is enclosed within a matched split collet into which is screwed the ball-and-socket self aligning loading point. In addition to the major problems of end grip failure, analysis of the strain distribution around the circumference of a loaded tube (measured by six equally spaced strain gauges) indicated that the stress introduction was highly non-uniform. See Figure 45. The strength results are summarised in Appendix 7(vi).

5.1.6 Four Point Flexure of Hoop Wound Tubes

An original specimen, which avoids both the problems of edge machining damage and uncontrolled stress introduction, is the tube flexure geometry. Four point flexure of a tube causes a line of maximum tensile stress (σ_{max}) given by:

$$\sigma_{max} = \frac{32 \; do \; M}{\pi \; (do^4 - di^4)}$$

where do = tube outside diameter

di = tube inside diameter

and M = bending moment

to exist along the axis of the tube on the outer surface, remote from the loading points. The results from tubes of do = 38.2mm, di = 34.3mm and length of 300mm tested with a minor span of 150mm and major span of 250mm are summarised in Appendix 7(vii).

5.2 Strength Test Specimen Selection

For a given test specimen geometry little difference was found between the strengths of 0° and ± ½° material or between the strengths of composite specimens which broke close to, or remote from, the end grips. Grouping all the data together for each specimen geometry the average strengths can be summarised:

	Strength (MPa)	Standard Deviation (MPa)
Composite		
Straight sided tensile coupon	64.3	6.2
Dogbone (routed)	38.9	3.0
Three point coupon flexure	72.2	14.0
Four point coupon flexure	72.9	8.7
Tensile hoop wound tube	36.5	3.0
Four point tube flexure	62.6	4.3
Neat Resin		
Dogbone (milled)	82.8	0.2

The low measured strengths from the composite dogbones and the tensile hoop wound tubes indicate that these specimens suffer from excessive machining damage and stress concentration effects (respectively) and are not therefore ideal specimens. Though the results of the remaining specimens are comparable, the straight-sided coupon with polished edges was the specimen selected for the main experimental programme since it is relatively easy to manufacture, it is suitable for testing highly flexible material, the strain can be easily measured (so that the whole stress/strain response to failure can be defined) and the same plate can be used for both strength and toughness specimens.

Initial trials with strain gauges indicated that the adhesive used to attach them caused premature failure of rigid material and it would be expected that the strain gauges themselves would cause local stiffening (and therefore strain underestimation) in the more flexible materials. In the main experimental programme, therefore, clip-on extensometers were used for the rigid materials while a specially acquired Wallace non-contact optical extensometer was used for strain measurement of the flexible materials.

5.3 Toughness Test Specimen Development

A variety of fracture mechanics specimens are available to measure the mode I critical strain energy release rate (G_{IC}) or critical stress intensity factor (K_{IC}) toughness parameters[87].

A more detailed discussion of fracture mechanics testing is contained in Chapter 6. In this initial study three fracture mechanics specimens were explored to measure the toughness of conventional resin composite and, for completeness, the toughness of neat rigid resin. In two of these specimens crack propagation was stable (the double cantilever beam and double torsion geometries) and provided several G_{IC} toughness values per specimen, in the third specimen (the single edge notch type) crack propagation was unstable and only one value of K_{IC} was obtained per specimen.

5.3.1 Double Cantilever Beam

The Double Cantilever Beam (DCB) specimen described by Mostovoy, Crossley and Ripling[88] used side grooves to ensure central crack propagation. Fortunately in this study the unidirectional nature of the reinforcement provided crack guidance and side grooves were unnecessary (See Figure 46). It is easily shown that the energy required to create unit area of Mode I crack extension, which is the definition of G_{IC}, can be calculated for any specimen geometry using the expression[89]:

$$G_{IC} = \frac{P^2}{2b} \frac{dc}{da}$$

where P = load at which crack propagation begins

b = specimen thickness

c = compliance of specimen at crack length a.

The rate of change of compliance with crack length (dc/da) can be made constant by using a tapered specimen, see Figure 47, though for machining convenience, rectangular specimens were tested here. The results, previously presented by Phillips and Wells [65] and contained in Figure 48, show that the initial fracture energy is 170 J/m^2 but that as the crack grows the toughness increases, and at a rate which depends on the specimen geometry. No significant difference was observed between the 0° or ± ½° material. The increase in fracture energy with crack growth is due to the development of a tied zone of fracture face bridging fibres and, as outlined in the literature review, has been observed by other workers. This phenomenon will be discussed in considerably more detail in Chapter 7.

5.3.2 Double Torsion

The Double Torsion (DT) configuration (see Figure 49) which has been fully described elsewhere [90] is widely used since with easily machined rectangular coupons a constant dc/da is observed. A simple compliance calibration allows G_{IC} to be calculated through the equation in Section 5.3.1. G_{IC} versus increase in crack length observed for ±½° conventional resin composite is shown in Figure 50.

The average initial G_{IC} value of 190 J/m² is comparable with the initial G_{IC} values from the DCB tests and again there is an increase of G_{IC} with increasing crack length. Specimen dimensions were 30mm width by 80mm length by 1.9mm thickness.

5.3.3 Single Edge Notch

The Single Edge Notch (SEN) specimen (see Figure 51) provides a single value of K_{IC} per specimen, calculated from the expression[91]:

$$K_{IC} = Y \frac{P}{BW} a^{\frac{1}{2}}$$

where P = fracture load

B = specimen thickness

W = specimen width

a = crack length

and Y is the isotropic finite width correction factor which according to Brown and Srawley[91] is represented to within 0.4% (for all values of a/W up to 0.6) by the series:

$$Y = 1.99 - 0.41\ (a/W) + 18.70\ (a/W)^2 -$$

$$38.48\ (a/W)^3 + 53.85\ (a/W)^4$$

Strictly, since unidirectional glass/epoxy is elastically anisotropic, an appropriate anisotropic finite width correction factor should have been used. Smith and Mullinix[92] calculated the anisotropic finite width correction factors for centre-cracked, transverse carbon fibre reinforced epoxy specimens and compared them with the isotropic values. The correction factors for the isotropic and anisotropic cases were found to agree to within 2% for a wide range of crack lengths and since carbon/epoxy is considerably more anisotropic than glass/epoxy the isotropic correction factor has been taken as an accurate value for this material.

The equation defining K_{IC} presented at the beginning of this section can be rearranged to give:

$$\log (\sigma Y) = \log (K_{IC}) - \tfrac{1}{2} \log (a)$$

where σ is the fracture stress.

Figure 52 presents two sets of fracture toughness data for two sets of SEN conventional resin composite specimens of dimensions 90mm long by 22mm wide by 1.9mm thick with a range of crack lengths. One set, marked 'notched', were notched prior to testing with a jewellers saw and the notch tip carefully sharpened with a razor blade.

The second set, marked 'cracked' were cracked prior to testing by tapping the specimen edge with a razor blade to propagate a crack to the desired length. In the former case a very small tied zone was created while in the latter case a tied zone existed along the whole length of the crack. Crack lengths were accurately measured using a travelling telescope prior to testing. Figure 52 plots log (σY) against log (a). For fracture mechanics to be applicable the slope of the data should be - 0.5. The linear regression gradient of the notched specimens is - 0.44, sufficiently close to - 0.5 to lend confidence in the applicability of fracture mechanics for this specimen and material. For the 'cracked' specimens the gradient is - 0.27, the higher than expected stresses at larger crack lengths being due to the existence of an increasing area of tied zone. Figure 53 plots the same data but as K_{IC} versus 'crack' and 'notch' length. The average 'notched' K_{IC} is seen to be 1.27 MPa$(m)^{\frac{1}{2}}$ while the best line fit by linear regression through the 'cracked' data is seen to give an intercept at zero crack length of 1.22 MPa$(m)^{\frac{1}{2}}$. It might be expected that as the crack approaches zero length the contribution to toughness from the tied zone vanishes and the 'cracked' and 'notched' data should coincide. The evidence tends to support this argument.

The SEN specimen was found to be convenient for testing the neat conventional resin. Figure 54 shows log (σY) versus log (a) for this material. The linear regression line was - 0.60 and the average K_{IC} was 0.46 MPa$(m)^{\frac{1}{2}}$.

5.4 Toughness Test Specimen Selection

That little significant difference in initial G_{IC}, or in particular dG_{IC}/da, was observed between the 0° and ± ½° wound composite plates provided justification for fabricating the epoxy /urethane matrix composites for the main experimental programme using the more straightforward ± ½° filament winding method.

The fracture mechanics specimens explored here have evaluated the critical strain energy release rate (G_{IC}) and the critical stress intensity factor (K_{IC}) for conventional resin composite. These are both descriptions of material toughness and are related through the elastic constants of the material. For isotropic material in plane stress [89].

$$G_I = \frac{K^2_I}{E}$$

where E = Youngs modulus.

For orthotropic materials such as unidirectional composite a more complicated relationship applies [92]:

$$G_I = K_I \left[\frac{S_{11}S_{22}}{2}\right]^{½} \left[\left[\frac{S_{22}}{S_{11}}\right]^{½} + \left[\frac{2S_{12} + S_{66}}{2S_{11}}\right]\right]^{-½}$$

Where,

$$\frac{1}{S_{11}} = E_{11} \quad \text{, modulus in fibre direction}$$

$$\frac{1}{S_{12}} = \frac{-E_{11}}{\nu_{12}} \quad \text{, modulus in fibre direction divided by the major Poisson's ratio}$$

$$\frac{1}{S_{22}} = E_{22} \quad \text{, transverse modulus}$$

$$\frac{1}{S_{66}} = G_{12} \quad \text{, shear modulus}$$

Using the measured value of E_{22} of 14.4 GPa and inferred values of E_{11} = 45 GPa, G_{12} = 7.2 GPa and ν_{12} = 0.3, an effective modulus, E* can be calculated, i.e.

$$E^* = \frac{K_I^2}{G_I} = 16.8 \text{ GPa}$$

The effective modulus, E* is seen to be slightly higher than the transverse modulus, E_{22}.

Using this relationship the averaged results of K_{IC} from the SEN specimen and initial G_{IC} from the DCB and DT specimens can be compared:

Material	Specimen	Measured Parameter	Effective Modulus (GPa)	Inferred Parameter
composite	DCB	$G_{IC} = 170\ Jm^{-2}$	16.8	$K_{IC} = 1.69\ MPa\ m^{½}$
composite	DT	$G_{IC} = 190\ Jm^{-2}$	16.8	$K_{IC} = 1.79\ MPa\ m^{½}$
composite	SEN	$K_{IC} = 1.27\ MPa\ m^{½}$	16.8	$G_{IC} = 96.0\ Jm^{-2}$
neat resin	SEN	$K_{IC} = 0.46\ MPa\ m^{½}$	3.09	$G_{IC} = 68.5\ Jm^{-2}$

The composite SEN specimen is seen to give a K_{IC} value some 27% lower than the average inferred value from the DCB and DT specimens. In spite of this, and the fact that it provides no information on crack growth behaviour, the SEN specimen was selected for the main experimental programme since it alone of the three specimens explored is suitable for testing the materials over the whole flexibility range.

6. MAIN EXPERIMENTAL PROGRAMME

This Chapter describes the experimental techniques and the results obtained, using the test specimens selected in the initial experimental programme. Measurements have been made of the stress-strain and fracture toughness properties of the varying flexibility resins and composites (described in Chapter 4) which are required to allow a validation of the range of theories of transverse behaviour outlined in the literature search.

6.1 Tensile Tests

The uniaxial tensile stress-strain response to failure has been measured for the epoxy/urethane neat resins and corresponding transverse composites. The practical details and experimental results are described.

6.1.1 Experimental Method

Transverse coupons of approximate width 12mm were cut from the filament wound plates using a wet diamond wheel cutter. Though edge machining damage was minimal all specimens were abraded with 600 grade paper down to a nominal width of 10mm using the polishing rig described in Chapter 5 and shown in Figure 43. It was felt to be necessary that in order to ensure smooth stress introduction over the whole strain range up to failure, the materials chosen for the coupon end tabs should match as closely as possible the stress-strain response of the specimen materials themselves. This dictated the

use of tapered end tabs machined from the same composite plate bonded to the ends of the specimen with an adhesive of similar flexibility. A schematic of the straight sided coupon specimen is shown in Figure 55.

Dogbone shaped specimens of neat resin (with 0% to 60% urethane content) were machined to shape using a milling tool of 50mm diameter. The direction of cut was along the axis of the specimen so as to minimise the 'notching' effect of machining striations. A schematic of the specimen is shown in Figure 56. The difficulty of machining pure elastomer dictated that the 100% urethane specimens be prepared using a technique similar to pastry cutting in which a sharpened steel tool of the correct profile is pressed through a sheet of the material. The resulting specimens were narrower than the other dogbones. See Figure 57.

Mechanical testing was performed on a Instron 1195 screw driven machine. Specimens were gripped between wedge-action jaws and special care was taken to ensure correct mounting. A purpose-built magnetic alignment fixture was attached to the jaw faces while the specimen was gripped centrally. The fixture was then carefully removed prior to testing.

Strains were measured in most of the specimens by conventional clip-on extensometers directly calibrated using a micrometer, with the signal processed through the Instron console and used as the chart drive to provide load versus strain chart output. No evidence

of preferential failure at the point of contact of the extensometer knife edges was observed. For the 100% urethane neat resin and transverse composite specimens the high failure strains and relative susceptibility to damage by extensometer knife edges dictated the use of a non-contact extensometer for strain measurement. The Wallace non-contact extensometer is able to optically track the displacement of two marks of known initial separation painted on the specimen surface. The relative displacement of the two optical followers is processed through the Instron console, and knowing the initial separation of the surface markings, provides a chart output of load versus strain in an identical manner to the clip-on extensometers. To allow the optical followers to properly 'lock-on' to the surface marks it was found to be necessary to silk-screen print the white arrow-head marks onto a specimen surface previously blackened using a felt-tip pen. Improved results were obtained by arranging for the specimen surface to be at an angle to the optical extensometer to reduce confusing back-reflections.

For all specimens, apart from the 100% urethane neat resin dogbones, the Instron cross-head speed was 1mm/min. A cross-head speed of 10mm/min was chosen for the pure elastomer to reach the failure strain within a reasonable period of time. This gave a strain-rate of approximately 15%/min for the pure elastomer and approximately 1.5%/min for all the other specimens. For one material type only, the 60% urethane neat resin, the strain-rate dependence of mechanical properties was explored by varying the cross-head speed between 1mm/min and 500mm/min.

Initial Poisson's ratios were measured on the neat resin specimens using a clip-on axial extensometer and a spring loaded transverse extensometer. The simultaneous input from three transducers (one load and two strains) necessitated the use of a microcomputer based multi-channel data acquisition system which, given calibration factors and specimen dimensions, stored, processed and plotted stress-strain curves directly.

6.1.2 Results

The stress-strain responses to failure of the transverse composites are summarised in Figures 58 to 63. These stress-strain curves are representative of the results of six individual specimens of each material type. The key parameters such as initial modulus, maximum stress, failure stress and failure strain were averaged and the curves presented are the 'best fit curves' which conform to these calculated key parameters. The composites with resins of 0% to 60% urethane content displayed increasing non-linearity, but a monotonic stress-strain response with failure in an apparently brittle manner. The composite with a 100% urethane matrix however, displayed a distinct peak in the stress-strain curve which was preceeded by the appearance of distinct whitened bands on the specimen associated with debonding and matrix cavitation.

The stress-strain curves of the neat resins are displayed in Figures 64 to 70. As with the composite data these are the average best fit curves from a minimum of six specimens. The curves from

the 0% to 20% urethane resins all display a peak stress, beyond which localised necking down of the specimen cross-sections is observed. The neat (0% urethane) epoxy resin is one which would normally be considered a brittle, low failure strain system. By taking extreme care with specimen surface condition, in this study, failure strains of over 8% have been measured compared with the Manufacturers quoted value of 2-3%. The 40% urethane system displays the unusual stress-strain response of high initial stiffness with a changeover to a highly yielding state at approximately 5% strain. The 60% urethane resin displays an almost linear stress-strain response. This is not linear elasticity, however, but a continuous yielding behaviour from a low strain. Unloading the material would not result in a return along the loading curve but rather a large permanent set at zero load. For this material only, the effects of strain rate have been explored. Figure 69 shows the stress-strain response over a two orders of magnitude change in strain rate. Higher strain rates are seen to considerably increase the failure stress with a virtually constant failure strain. The behaviour of the 100% urethane is typical of many pure elastomers in displaying a marked increase in stiffness at strains close to failure. For these specimens, in common with the other results presented here, it is not the true stress or strain which is quoted but the stress calculated using the current load divided by the original cross-sectional area. The difference between true stress and nominal stress is most marked for the 100% urethane since, assuming a Poisson's ratio of 0.5, the reduction in cross-sectional area at the failure strain (765%) is a factor of approximately 15, and the true failure stress for this

material is greater, by this amount, than the quoted value. The non-linear behaviour of the 100% urethane, in contrast to the other neat resins, is predominantly elastic and recoverable.

The key mechanical parameters measured on the neat resin blends and corresponding transverse composites are summarised in Table 2.

The significance of these values and the relations between them will be explored in detail in the Discussion, but several points can be highlighted here. Firstly, the extreme range of the data is readily apparent. In particular, the initial moduli values cover almost six orders of magnetude. The trend in neat resin is one of rapid fall in initial modulus with increasing urethane contents beyond 20%. This trend is generally reflected in the transverse composites (allowing for Vf) though the values are, naturally, higher. The neat resin initial Poisson's ratios show an increase from 0.23 to 0.39 from pure epoxy to 60% urethane. A value of approximately 0.3 is typical for a rigid epoxy resin while a value of 0.5 would be expected for an elastomer. An accurate measurement of the Poisson's ratio of pure elastomer proved extremely difficult and so a value of 0.5 has been assumed. The maximum stresses for neat resins show a consistent decrease with increasing urethane content while the variation with transverse composites is less easy to understand. Increasing urethane content produces a dramatic increase in failure strain in the neat resins. The same trend occurs in the transverse composites though the strain values are much lower. Indeed, the failure strain of 0.11% for the pure epoxy

matrix composite is lower than most values quoted in the literature, though the 74% fibre volume fraction is higher than most glass fibre composites investigated in the literature.

6.2 Fracture Toughness Tests

Fracture mechanics is a formalism by which the resistance of a material to crack growth may be quantified. If correctly carried out, a fracture mechanics test provides a measurement of fracture toughness which is a fundamental material parameter, independent of test specimen geometry, which is of great interest in materials science and of great value from the very practical standpoint of prediction of the load carrying capacity of engineering structures containing flaws of known dimensions. Fracture mechanics is a vast subject to which several excellent introductions have been written[87, 89, 91, 93]. Aspects of the subject will be discussed here only where they relate to testing of materials under consideration in this study.

Cracks may extend in three different ways, as shown in Figure 71. Mode I is the form of cracking being studied here, though resin cracking in unidirectional composite can occur under combined transverse and in-plane shear loading (ie Mode I and II) as discussed in the Introduction. Mixed mode cracking is therefore of significant practical importance [62, 94].

The development of linear elastic fracture mechanics began with Griffith[95] who postulated that a pre-existing flaw in a solid would grow only if the total energy of the system would be decreased by it doing so. As a crack grows the compliance of the solid increases and so reductions in energy can arise from work done by the external forces acting on the body and reduction in stored elastic energy. These reductions are balanced by the increase in energy associated with the work done against cohesive forces acting at the crack tip. Considering the case of a crack of length 2a in an infinite plate Griffith was able to show that, for both constant load and constant displacement, the condition for stability of the crack was:

$$\sigma \leq \left[\frac{2E\gamma_s}{\pi a}\right]^{\frac{1}{2}}$$

where σ = stress in the plate remote from the crack

E = elastic modulus of the solid

γ_s = surface energy associated with crack tip cohesive forces.

Other workers subsequently realised that the energy associated with creation of fracture surface is (for all but perfectly brittle solids) orders of magnetude greater than true surface energy since considerable energy absorption occurs by plastic deformation in the highly stressed zone at the crack tip. Provided that the volume of material undergoing plastic deformation is small, so that the total strain energy in the specimen is not significantly different from the perfectly brittle case, then the plastic deformation term can be simply added to the surface energy term. Usually the Griffith relation is expressed as below, in which the term G_c, the critical

energy release rate, is the energy required to form unit area of crack extension.

$$\sigma \leq \left[\frac{EG_c}{\pi a} \right]^{\frac{1}{2}}$$

It is important to emphasise that this approach can still be considered linear elastic fracture mechanics provided the material behaves in a non-linear manner only in a small region close to the crack tip, while the rest of the solid behaves in a linear elastic manner.

By consideration of the changes in potential energy and energy expended by external loads on crack extension it is possible to show that for any solid under load or displacement control:

$$G_c = \frac{P^2}{2} \frac{dC}{dA}$$

where: P = load at crack extension

C = compliance of solid (ie displacement per unit load)

A = crack area.

This equation is the basis of most methods of evaluating G_c in which a compliance calibration is carried out for the particular specimen being used. This provides dC/dA as a function of crack length which is used in conjunction with the corresponding cracking load to calculate G_c. The compliance calibration is simplified for some

specimen geometries such as the tapered double cantilever beam (Figure 47) and double torsion specimens (Figure 49) in which dC/dA is constant. The use of this technique for measurement of G_c in transverse composites has already been described in Chapter 5.

An alternative fracture toughness parameter to G_c is the critical stress intensity factor K_c defined by:

$$K_c = \sigma_c \ (\pi a)^{1/2}$$

where σ_c = stress remote from the crack at crack extension

a = semi-crack length in an infinite plate.

K_c is a single parameter which, by incorporating the remote stress state and crack geometry, characterises the critical stress distribution at the crack tip at the instant of crack growth. Specimen geometries most often used to evaluate K_c are centre notched plates, double edge notched plates, and single edge notched plates in tension and bending (see Figures 72 to 75). In finite sized specimens the proximity of the edges perturbs the flow of stress around the crack tip leading to an increased stress concentration over the infinite size case. This requires that a geometry dependent term be introduced into the definition of K_c given above, ie:

$$K_c = Y' \ \sigma_c \ (\pi \ a)^{1/2}$$

or $$K_c = Y \ \sigma_c \ (a)^{1/2}$$

For the specimen geometries mentioned above (and others) the isotropic finite width correction factors have been calculated and Y values are available expressed as polynomials in a/w where w is the specimen width [91]. For anisotropic materials, such as unidirectional composites, the degree of redistribution of stresses due to proximity of specimen edges is not the same as in isotropic materials and so anisotropic finite width correction factors are required. The calculation of such correction factors is extremely complicated but an analytical solution for the centre notched case has been obtained by Bowie and Freese [96] and numerical solutions have been made for centre notched, double edge notched and single edge notched geometries by Konish [97] and Mandell, McGarry, Wang and Im [98]. In Chapter 5 the use of the isotropic finite width correction factor was justified for conventional rigid resin transverse composite by reference to numerical results for the centre cracked geometry which showed that the isotropic and anisotropic correction factors were very similar for this type of material. For the more flexible composites being tested in the main experimental programme, however, the degree of axial to transverse anisotropy is orders of magnitude greater and so the use of the isotropic finite width correction factors cannot strictly be justified. An analytical solution which provides an explicit equation (from which values of anisotropic finite width correction factor could be obtained from measured values of material moduli) is not available for the single edge notched geometry. A solution for the single

edge notched geometry which is available[98] uses a finite element analysis for the particular case of carbon fibre/epoxy which is of limited applicability for materials of different elastic moduli (See Figure 76). The finite element analysis is used to predict the change in compliance of the anisotropic specimen with increasing crack length so that, in effect, a (theoretical) compliance calibration procedure, as described above for measurement of G_C, is carried out. The K_C value is then related to G_C through an expression previously presented in Chapter 5. The compliance calibration could, of course, be performed experimentally, and this is the approach advocated by Harel, Marom, Fischer and Roman [99] for single edge notched 3-point bend composite specimens.

To obtain valid fracture toughness data certain requirements relating to crack length, crack growth direction and specimen size must be met. Test results which satisfy these criteria, as specified by the BSI[100] or ASTM[91] for example, can be quoted as Mode I plane strain fracture toughness values, K_{IC}. Until it is shown that the test satisfies these criteria the fracture toughness is referred to as K_Q, the candidate fracture toughness. The published standards were developed almost exclusively with metals in mind, and since there are no standards available for fibre composites toughness testing it has become common practice to quote only K_Q fracture toughness for these materials[92].

The stress acting in the direction of loading ahead of a sharp crack in an isotropic solid is given by:

$$\sigma = \frac{K_I}{(2\pi r)^{\frac{1}{2}}}$$

where K_I = stress intensity factor

r = distance ahead of the crack tip.

This would predict an infinite stress at the crack tip (where r = 0). If the material is elastic/plastic with a yield stress of σ_y then plastic flow occurs where σ_y is exceeded. The extent of this plastic region (r_p') might be expected to be given by:

$$r_p' = \frac{K_I^2}{2\pi \sigma_y^2}$$

but redistribution of stress out of the yielded region causes a larger plastic zone size (r_p) given approximately by[87]:

$$r_p = \frac{K_I^2}{\pi \sigma_y^2}$$

To avoid general yielding, which would invalidate the assumptions of linear elastic fracture mechanics, it is necessary that this plastic zone size be small in comparison to the specimen dimensions. The effective yield stress under triaxially loaded conditions can be considerably higher than under uniaxial conditions, and Poisson contractions which are constrained in the centre of thick walled specimens give rise to triaxially stressed, plane strain conditions. At the specimen surface the stress state can only be biaxial, or plane stress. This means that crack tip yielding is suppressed in the centre of a specimen relative to regions close to the surface. Since plasticity is the major energy absorbing process in most materials, higher fracture toughnesses are usually observed with specimens containing higher proportions of plane stress to plane strain regions. Plane strain fracture toughness values therefore are conservative. The necessity of avoiding general yielding and of ensuring plane strain conditions imposes certain minimum dimensions on the crack length and specimen thickness. Experience with metals suggests that the crack length and thickness should both be greater than $2.5 \times (K_{IC}/\sigma_y)^2$ for a valid K_{IC}[90]. The maximum usuable crack length is limited by the finite width correction factors which become inaccurate beyond a crack length to width ratio of 0.6.

In cases where significant plasticity occurs other approaches than Linear Elastic Fracture Mechanics must be used[89]. One such approach uses the concept of Crack Tip Opening Displacement (CTOD).

The proposal is that once a critical value of plastic strain at the crack tip is exceeded fracture will occur. The CTOD (δ) is practically impossible to measure directly but can be inferred from the relationship:

$$\delta = \frac{G_{IC}}{\sigma_y}$$

in which the yield stress (σ_y) acting over the displacement at the crack tip gives rise to the energy absorped per unit area of crack growth (G_{IC}).

The presence of a large plastic zone disrupts the elastic stress field making it impossible to calculate the critical rate of release of strain energy, G_{IC}. In such cases the use of a quantity called the J-integral has been proposed[87]. In a similar way to G_{IC} the J_{IC} is defined as the rate of change of potential energy with extension of the crack, and for linear elastic material J and G are equivalent. Where G and J differ is in the case of non-linear material. Figure 77 shows graphically how J values may be determined. The shaded area represents the energy supplied to the extended crack in a non-linear elastic material. These concepts imply that on unloading the material returns along the loading curve. For yielding material this is not so. However, for such materials the J method has been shown to be a useful approach.

6.2.1 Experimental Method

The previous section has outlined many of the techniques and highlighted some of the pitfalls involved in fracture mechanics testing. The materials addressed in the main experimental programme represent some of the most difficult that can be tested using fracture mechanics; the neat resins ranging from brittle, linear elastic to high strain non-linear materials, and the transverse composites displaying extreme stiffness anisotropy. The policy adopted for these tests has been a pragmatic one, in which the simple Single Edge Notch specimen shown in Figure 78 has been used for both neat resins and transverse composites with a range of crack lengths, and the validity criteria described above have been applied to the results. For the tests on transverse composites, in view of the complexity of the anisotropic finite width correction factors (and the fact that disagreement between solutions still exists[92]) coupled with the considerable experimental complication of carrying out compliance calibrations, it was decided to use the <u>isotropic</u> finite width correction factor and closely monitor the results for any obvious trends in the variation of fracture toughness with crack length, indicative of invalidity of the correction factor. In line with common practice for fracture tests on composites[92] the candidate fracture toughness K_Q will be quoted.

The notches in the SEN specimens (shown schematically in Figure 78) were introduced into the neat resin specimens using a razor blade tapped onto the edge which propagated a crack the length of which was varied from approximately 1mm to 6mm. Notching the transverse composites in a similar way would have created cracks with extensive tied zones (as described in Chapter 5). Instead, these materials were notched from lengths 1-6mm with a jewellers saw and subsequently sharpened using a light tap on a razor blade. Crack lengths were measured for each specimen using a travelling microscope with vernier stage.

All the specimens were gripped in well-aligned wedge action jaws and tested at 1mm/min cross head speed in an Instron 1195 mechanical testing machine. In all specimens the cracks propagated in an unstable manner at a well-defined maximum load which was read from the load/displacement chart output. As previously explained the maximum load (P) and measured specimen dimensions were used to calculate K_Q through the equation:

$$K_Q = \frac{Y\ P\ a^{1/2}}{BW}$$

where a = crack length

B = specimen thickness

W = specimen width

and Y is the isotropic finite width correction factor, given by Brown and Srawley[91] as:

$$Y = 1.99 - 0.41\,(a/w) + 18.70\,(a/w)^2 - 38.48(a/w)^3 + 53.85\,(a/w)^4$$

6.2.2 Results

Measured K_Q values are plotted against a/w for the transverse composites in Figures 79-84 and for the neat resins in Figures 85-90.

The most striking feature of the data for the composites is the high degree of scatter. This may well be due to variability in the notch sharpening procedure. Too heavy a tap on the razor blade would result in growth of a crack with an associated tied zone, giving an artificially high fracture toughness; as would too light a tap, which would result in a blunt notch tip. No trends in variation of K_Q with crack length are apparent except for the results for 100% urethane matrix composite which show a clear increase in K_Q with increasing crack length. If it is the use of the <u>isotropic</u> finite width correction factor which is responsible for the inconsistancy of K_Q value then the effect would be expected to be most marked for the more flexible matrix composites. For example the ratio of longitudinal to transverse modulus is approximately 2.5 for the pure epoxy matrix composite, but approximately 2700 for the pure urethane matrix composite.

The K_Q versus a/w results for the neat resins are a little less scattered with K_Q values apparently independent of a/w for 0%, 10% and 20% urethane content resins. A clear trend of increasing K_Q with a/w is however apparent for the 40%, 60% and 100% urethane content resins. The inapplicability of the isotropic finite width correction factor cannot be the reason for the geometry dependence of K_Q in this case since the neat resins are isotropic. Instead, the explanation is probably the lower yield stress of the more flexible materials giving rise to gross yielding invalidating the assumptions implicit in the use of linear elastic fracture mechanics. Although the K_Q values for these flexible resins and composites are probably invalid, an average K_Q value has nevertheless been calculated and in represented by a horizontal dotted line on the graphs of K_Q versus crack length. Although the pure urethane rubber does not yield, its stress/strain response (Figure 70) is highly non-linear and so would be more suited to a J test approach as outlined in the beginning of this Chapter. The early work of Rivlin and Thomas[101] on tearing of rubbers predated development of the J-integral but in a similar way attempted to quantify the level of potential energy in a non-linear material by a series of direct measurements of stored energy as a function of load, crack length and extension ratio.

The criterion for valid K_{IC} measurement outlined earlier:

$$X = 2.5 \left[\frac{K_Q}{\sigma_y} \right]^2$$

where X is the allowed minimum specimen thickness, crack length and ligament length, has been calculated for the neat resin and transverse composite materials. The identification of yield stress for the 0%, 10% and 20% urethane neat resins is straightforward since these materials showed a distinct maximum in the stress/strain response. For the 40%, 60% and 100% urethane materials the maximum stress has been taken as the σ_y value and the resulting X values will therefore represent lower bounds. The application of these concepts of plane strain toughness validity to composites has little justification, but the same calculations have nonetheless been carried out for these materials. The σ_y values used are the measured σ_{max} values quoted in Table 2. The measured K_Q values and standard deviations are summarised in Table 3 along with the calculated validity dimension, x. For completeness, the plastic zone sizes (r_p) calculated using:

$$r_p = \frac{K_Q^2}{\pi \sigma_y^2} ,$$

(described earlier), the corresponding G_Q values calculated using

$$G_Q = \frac{K_Q^2}{E^*}$$

where E* is the appropriate elastic modulus (described earlier), and the crack tip opening displacements (∂) calculated using:

$$\partial = \frac{G_Q}{\sigma_Y}$$

(described earlier) are also quoted in Table 3.

A judgement of the validity, or geometry independence, of each K_Q value given in Table 3 has been made, in part, by comparison of the calculated x values with specimen dimensions, but primarily by direct inspection of the K_Q versus a/w graphs.

7. DISCUSSION

In this Chapter an appraisal is made of the micromechanics and fracture mechanics theories put forward in the Literature Review in the light of the results generated by the main experimental programme. Before this however, as promised in Chapter 5, a more detailed discussion will be presented of the unusual transverse crack propagation phenomena observed in the test specimen development programme.

7.1 Transverse Crack Propagation

In the test specimen development programme transverse crack propagation in the conventional resin unidirectional glass fibre composite was studied. Figure 48, previously presented in Chapter 4, shows the measured change in fracture toughness with crack length for this material in Double Cantilever Beam specimens of varying height. The increase in toughness with crack growth is a result of the presence of fracture face bridging fibres behind the crack tip leading to the formation of a tied zone. Figure 91 shows a transverse DCB specimen with an extensive tied zone. Several other workers have previously explored this phenomenon. Engelberg and Marom [66] noted an increase of the total energy to failure in transverse GRP with increasing fibre misalignment and Marom and White [38] reported improved crack stability with an increase in fibre volume fraction. Sidey and Bradshaw [102] showed that an increase in mode II fracture toughness with crack growth

occurred in unidirectional CFRP. In particular, Wu[60, 103] has made detailed experimental studies of crack growth under both shear and normal loading in which the increase of K_{IC} and K_{IIC} with crack growth caused by a tied zone closing pressure were measured. The suggestion was made that crack propagation could occur by nucleation of flaws at a characteristic distance from the crack tip and at locations not necessarily within the plane of the crack. Similar ideas were expressed by Bradley and Jordan [55], from which Figure 92 is taken, which shows schematically how out-of-plane crack nucleation leads inevitably to bridging fibres. Circumstantial evidence to support these concepts arises from this study in which the effect of the tied zone was identical for 0° and ±½° aligned unidirectional composites.

The increase in fracture toughness with crack growth clearly has implications for crack stability which might be of considerable practical significance. Phillips and Wells[65] used the Griffith equation for crack initiation to show that cracks could be stable (ie would only grow under an increasing load) if the increase in toughness (G) with crack length (a) was sufficiently high. The condition which defined the transition from stability to instability was shown to be:

$$\frac{dG}{da} \geq \frac{G}{a}$$

That is, cracks initially less than the defined size propagate catastrophically at a stress controlled by the initial fracture energy. This paper is reproduced in full as Appendix 8. In a

later, more general approach, summarised in Appendix 9, Atkins and Mai[93] considered the influence of specimen geometry and loading conditions on crack stability. The derivations show that where dG/da is zero, which is the case for most brittle materials, stability is controlled purely by the geometry and whether the specimen is under load or displacement control. For example, the DCB geometry is shown to be stable under displacement control but unstable under load control, whereas the SEN geometry is unstable under both load and displacement control. Where dG/da is positive, stability also depends on the crack length. The stability conditions for a Griffith crack as derived by Atkins and Mai and Phillips and Wells are identical, with Atkins and Mai's approach showing that the same condition holds under both load and displacement control for this particular geometry.

In order to better understand the energy absorbing mechanisms occurring within the tied zone, and to predict the conditions under which tied zones might form, the behaviour of an individual fracture face bridging stringer has been modelled. A stringer is defined here as a fibre or bundle of fibres which cross the fracture face behind the crack tip. Appendix 10 presents an analysis of the equilibrium conditions of a stringer, which considers the balance between elastic energy stored in the stringer stretched across the fracture face and the fracture energy required to tear a stringer away from the crack face. An assumption made in the analysis is that the stringers are virtually straight, that is the elastic energy content is small within the flexing region where they emerge from the crack face. Further assumptions are that the fracture surface energy of a running stringer is only that associated with the

projected area under the stringer and, most importantly, that as a stringer runs it does not have to tear out from progressively greater depths from the crack face. This last assumption implies either that the fibres are manufactured perfectly parallel or that the flaw nucleation process operates at a distance above and below the fracture plane which is greater than the divergence of the fibres. Within these assumptions the following expression is derived for the equilibrium angle to the fracture surface (α) adopted by the stringer.

$$\frac{G_s b}{EA} = \frac{\sin^2\alpha}{\cos^4\alpha} - \frac{\sin^2\alpha}{\cos^3\alpha} - \frac{1}{2\cos^2\alpha} + \frac{1}{\cos\alpha} - \frac{1}{2}$$

where G_s = fracture surface energy of stringer tearing.

b = width of stringer.

A = cross sectional area of stringer.

E = elastic modulus of stringer.

The expression, though cumbersome, shows that the equilibrium stringer angle directly depends on only a few geometric and material parameters and is independent of crack opening. Figure 93 is a graphical representation of the above expression. For the E-glass composite used in the test specimen development programme a longitudinal modulus of 50 GPa might be expected. The fracture energy of stringer tearing might be given approximately by the initial fracture energy of 170 J/m^2 measured in the DCB crack propagation experiments. By assuming that the stringers are individual fibres (which have diameters of 15μm, b = 15μm and A is

approximately = b^2) an approximate value of $G_s b/EA$ for GRP might therefore be 2.27×10^{-4}, which from the graph predicts an equilibrium stringer angle of 9°. Appendix 11 contains experimental measurements of stringer angles taken from micrographs of the tied zone, of which Figure 94 is typical. The measured stringer angles are in the range 8° to 15° (average 11.3°) with no apparent dependence of angle on crack opening. The agreement between predicted and measured stringer angles (9° and 11.3°) is good, and the observed lack of dependence on crack opening is as predicted.

Early in the analysis in Appendix 10 the strain within the stringer (ε) was shown to depend only on the stringer angle (α) through the expression:

$$\varepsilon = \frac{1}{\cos\alpha} - 1$$

Values of ε corresponding to α are shown in Figure 93. For the equilibrium stringer angle of approximately 9° the predicted strain is 1.25% which is approximately half the failure strain of GRP. An initial assumption of the analysis was that the stringers were straight. In reality however, the stringers bend as they emerge from the fracture face and at these points the additional flexural strain will cause the predicted value to be an underestimate. The magnitudes of predicted stringer strain have important implications for the formation of the tied zone. If a material has a $G_s b/EA$ value which results in an equilibrium stringer angle sufficiently large that the stringer strain exceeds the fibre failure strain the prediction is that an extensive tied zone could not form in that material. Immediately a stringer formed it would break. This

might give an increased initial toughness due to a contribution to energy absorption by fibre breakage, but the toughness would not increase with crack growth. This might be the case with low strain to failure fibre composites such as high modulus carbon fibre reinforced plastics or with composites of very high toughness such as those with thermoplastic matrices. Circumstantial evidence supporting this is provided by Slepetz and Carlson[64] who report less fibre bridging in compact tension specimens of carbon fibre than glass fibre composites. Lang, Heym, Tesch and Stutz[104] in interlaminar fracture tests using DCB's also report less fibre bridging with carbon than glass unidirectional composites which they attribute to a reduced capability of carbon fibres to sustain a minimum radius of curvature at the point of emergence.

Several workers report an initial increase in toughness with interlaminar and transverse crack growth which 'levels off' at sufficiently large crack lengths[64, 102, 105]. The eventual decrease in dG/da at sufficiently large crack lengths is discussed by Phillips and Wells,[65, Appendix 8] as being due to growth of the tied zone to a maximum size, characteristic of the degree of fibre misalignment. However, in this study using DCB specimens with dimensions up to the exceptional length of 200mm the tied zone was found to extend over the whole fracture surface area with a corresponding continually increasing toughness with crack length . This difference might be attributable to the high degree of fibre alignment achieved in the composite used in this study. Theoretical support for a continually increasing toughness with crack growth comes from the analysis of individual stringers previously presented

in Appendix 10. The equilibrium stringer angle (and therefore stringer strain) relates only to material constants and dimensions of the stringers themselves and does not depend on the degree of crack opening. This has important implications for the magnitude of the closing pressure exerted by the tied zone. Since the stringer strain depends only on the stringer angle, the force exerted by each stringer depends only on the stringer angle, modulus and cross-sectional area, each of which are independent of crack opening. Therefore, provided the number of stringers per unit area is constant, the closing pressure should be constant. The magnitude of the closing pressure depends crucially on the number of stringers per unit area in the tied zone. This is a difficult value to determine independently since it will be controlled either by the degree of fibre misalignment or by the distribution of flaws activated at the growing crack tip.

As the crack grows, the fracture faces open behind the crack tip and do irreversible work against the tied zone closing pressure. This is the origin of energy absorption in the tied zone. The geometry dependence of rate of change of toughness with crack length arises from the differing rate of crack face opening with different height specimens. Appendix 12 is an analysis of the energy absorption within the tied zone as a function of DCB specimen geometry, material stiffness, crack length and closing pressure. The analysis first of all uses a conventional strength of materials approach[106] to predict the shape of each arm of a straight-sided DCB by treating it as an encastered beam deflecting under an opening end load and a distributed closing load. The energy expended within

the tied zone is then obtained by integrating the closing force times opening distance between the arms of the DCB. The rate of change of this energy with increase in crack area gives the effective tied zone contribution to fracture toughness. This is expressed in terms of applied load which is substituted by the total fracture toughness and the rate of change of compliance with crack length. The resulting equation is:

$$G_{Total} = G_I + G_T = G_I + \tfrac{1}{2}\,[6A + (36A^2 + 48G_IA)^{1/2}]$$

$$\text{in which} \quad A = \frac{F^2a^4}{Eh^3}$$

where G_T = tied zone contribution to fracture toughness.

G_I = initial fracture toughness.

E = longitudinal elastic modulus.

F = closing pressure.

h = height of DCB arm.

a = crack length.

The short Basic program given in Appendix 13 uses the above equation to calculate G_{Total} as a function of crack length given the height of the straight-sided DCB, the elastic modulus, the closing pressure and the initial fracture toughness. Numerical results are given in Figure 95 using the above equation which are compared with experimental results taken from Figure 48. The G_I value of 170 J/m^2 has been taken from the experimental results. A value of 50 GPa has been taken for the elastic modulus. The only uncertain parameter on the right hand side of the above equation is the closing pressure, F.

Earlier measurements of the load required to separate fully cracked transverse specimens suggested a closing pressure of 0.58 MPa[9]. However, taking a value of 1.5 MPa for this value gives a set of predictions very similar to the experimental results. While the absolute values of theoretical predictions and experimental results may not agree precisely, the form of the predicted variation of toughness with crack length and specimen geometry shows excellent qualitative agreement with the results. Precise numerical agreement might not be expected since the experimental results are from DCB's which were initially notched to a depth of approximately 30mm whereas the theoretical model assumes the tied zone extends to the edge of the specimen. Numerical results predict that dG/da increases with decreasing E and h and with increasing a, F and (interestingly) G_I. The dependence of G_T on G_I arises because a higher G_I requires a higher beam deflection for crack propagation and therefore a higher contribution from the tied zone.

The approach outlined here is general. It has been used here to predict G versus a for the special case of a straight-sided DCB with constant closing pressure. It can be used for any geometry provided the crack opening profile can be predicted. The prediction of the tied zone contribution to transverse toughness, in 0°/90° cross-ply laminates for example, will require a knowledge of the transverse 90° crack opening profile which will be controlled by the adjacent 0° axial plies to which it is bonded. It can, in principle, be used in cases where the crack closing pressure is not constant, provided that the variation in closing pressure with distance from the crack tip can be predicted. It may therefore be

of value in understanding sub-critical crack growth in a wide variety of different materials.

It could be argued that this approach violates one of the assumptions of linear elastic fracture mechanics, which is that energy absorping processes should be localised at the crack tip. The approach is self consistent, however, in that it considers the energy absorbed in propagation, not of a well defined crack, but of a planer region of damage. Certainly, the tied zone toughness contribution, G_T, cannot be considered to be a fundamental material constant since it is geometry dependent. It is, however, a parameter which could be of considerable practical importance since it may control whether or not incipient flaws in a real structure are stable or unstable.

7.2 Transverse Moduli

Chapter 6 described the measurement of neat resin and transverse composite stress/strain response. The results of initial moduli, summarised in Table 2, show the extraordinary range of the data, which cover five orders of magnetude. The literature review, Chapter 2, presented ten theoretical models which attempt to predict transverse composite modulus from fibre volume fraction and component moduli. Of these, eight are accompanied by explicit equations which can be applied independently. Five of these models require a knowledge of matrix Poisson's ratio, which has been measured for the neat resins in this study (apart from the 100% urethane resin for which a Poisson's ratio of 0.5 has been assumed). The results, summarised in Table 2, show considerable scatter but a definite trend of increasing Poisson's ratio with urethane content is discernable.

In order to more clearly establish the trends of predicted transverse modulus as a function of resin modulus, a monotonic variation in Poisson's ratio is preferable. For this reason the measured Poisson's ratios, shown graphically in Figure 96, have been fitted against a linear relationship which has been used to identify the appropriate Poisson's ratio for the theoretical models.

The eight models explored here include the Reuss model[1] and those varients of it which incorporate Poisson effects; the Ekvall [15], Allred [14] and longitudinal Poisson constraint models[2]. More sophisticated approaches investigated are those by Hashin[13, 20] and Greszczuk [14, 22] which include a Poisson contribution, and those by Spencer [25] and Halpin and Tsai [5], which do not. All of these models have been discussed in more detail in Section 2.1.1. The measured neat resin and transverse composite moduli are plotted in Figure 97 against the urethane content in the resin system. Also shown in this Figure are the predictions of transverse modulus based on the theoretical models mentioned above, which use the corresponding measured resin modulus and assume, for clarity, a constant fibre volume fraction of 70%. A fibre modulus of 76 GPa has been taken from the literature[107] and (where required) a fibre Poisson's ratio of 0.2 has been assumed[11]. Resin Poisson's ratios (where required) have been taken from the linear relationship in Figure 96 as explained above. The values of bulk and shear modulus required by the Hashin model were calculated using the conventional relationships for isotopic materials[5] from the elastic modulus and Poisson's ratio. The transverse modulus predictions were calculated using the Basic program given in Appendix 14.

From the results, the broad generalisation can be made that those theories based on the Reuss model considerably underestimate the actual transverse modulus for the three most rigid resin composites, while the more sophisticated theories (Hashin, Greszczuk, Spencer and Halpin - Tsai) predict the transverse moduli for these three materials very well. In fact, if the variations in fibre volume fraction from 70% are taken into account the agreement for these three materials is even better. See Table 4. It is, of course, for these more conventional rigid materials that the models were derived and against which they have previously been validated. All the theories (with one exception) increasingly underpredict the measured transverse moduli for the three more flexible resin composites. For the 60% and 100% urethane matrix composites the error is greater than an order of magnetude. The one exception to this trend is the Allred model which predicts a transverse modulus tending to infinity with the 100% urethane composite. This arises because of the assumption in this model that the effective modulus of the resin approaches infinity as the resin Poisson's ratio approaches 0.5, which is the value assumed for 100% urethane. Figure 98 plots the predicted transverse modulus for 100% urethane composite as a function of Poisson's ratio. It is clear that only by incorporating a large Poisson constraint contribution to effective resin modulus can these theories have any prospect of predicting the observed transverse composite modulus of the most flexible materials.

In attempting to understand the elastic behaviour of material under constraint it is useful to consider the three-dimensional case of Hooke's law[108]. Appendix 15 uses the general case of Hooke's law to predict the effective modulus of a matrix under a, the case of total constraint in one direction (ie fibres prevent any strain in fibre direction) and b, the case of total biaxial constraint (ie fibres prevent any strain both in the fibre direction and in the direction normal to the plane containing the fibres and the applied load). The resulting effective moduli are given by:

$$E' = \frac{E}{1 - \nu^2} \quad , \text{ case a.}$$

and

$$E'' = \frac{E}{1 - \frac{2\nu^2}{1-\nu}} \quad , \text{ case b.}$$

It can be seen that the case 'a' effective modulus is, in fact, that used in the longitudinal Poisson constraint model. Though the strain in the fibre direction in a transversely loaded unidirectional composite may not be zero it will certainly be very small and it is entirely reasonable that an, at least partially, constrained effective modulus, should be used in this context. Case 'b' represents the effective modulus where the strain is zero in the two directions normal to the applied load (ie total Poisson constraint). This form of constraint could only be possible at the junction between two closely approaching fibres. It is seen that case 'b' predicts an infinite effective modulus when the Poisson's ratio is 0.5. In reality of course the effective modulus could not exceed the modulus of the constraining component, in this case E-glass with a

modulus of 76 GPa. If the constraint of the matrix at junctions of adjacent fibres approximated to case 'b' and if the Poisson's ratio were 0.5, as it might be for pure rubber, we can begin to see a mechanism by which an unexpectedly high transverse modulus could arise. In a high fibre volume fraction composite the fibres might approach close enough for case 'b' constraint to operate. A glass/rubber transverse composite might then behave as a network of high modulus fibres bridged by a matrix whose modulus approached that of the fibres themselves. It would require only a small contribution from such a mechanism to account for the unexpectedly high observed 100% urethane transverse composite modulus.

The theoretical predictions grossly underestimate the transverse modulus not only for the 100% urethane composite but also for the 60% urethane composite. The above argument could only be invoked in this case if the initial Poisson's ratio approached 0.5 and not 0.4 as measured for 60% urethane neat resin. An alternative explanation might be linked to the effect of strain rate. That high strain concentration factors operate in the matrix between fibres has already been discussed in Chapter 2. For a given overall strain rate therefore the strain rate in the matrix between fibres will be considerably higher. In the limit, as fibres touch, the Kies strain magnification factor gives the maximum strain concentration factor equal to the ratio of fibre and resin modulus. The highest strain concentration factor then would be obtained using the low strain rate resin modulus (7.11 MPa) giving a value of approximately 1.1×10^4. Figure 69 presented stress/strain results for neat 60% urethane resin

in which a one hundred fold increase in strain rate produced an approximately two fold increase in modulus. It is debatable whether an increase in strain rate of even a factor of 10^4 could lead to a high enough matrix modulus to account for the observed unexpectedly high transverse modulus. A further explanation again calls on the effects of strain concentration between fibres. Adams[44], from results of a Finite Element study, suggested that matrix microplasticity could occur at stress levels well below those at which overall non-linearity in a transverse composite were observed. Identification of the yield point in such a viscoelastic material as the 60% urethane resin is probably meaningless. However, Vasil'ev and Salov[31], and others, have shown that as resins begin to yield the effective Poisson's ratio tends toward 0.5. It is possible, therefore, that very early on, microyielding between fibres might occur with an associated increase in Poisson's ratio and concomitant increase in effective matrix modulus. This is, however, pure conjecture. Questions such as these can probably be resolved only by recourse to a sophisticated, fully 3-dimensional Finite Element analysis which is also able to model the non-linear behaviour of the matrix.

7.3 Strain Magnification Theory

The Kies strain magnification approach[28], discussed in Section 2.1.2, was the first quantitative description of transverse cracking. Predictions of Kies strain magnification model are presented together with measured failure strains for transverse composite and neat resin in Figure 99. The error bars represent one standard deviation.

Immediately apparent is a general correspondence of the resin and composite results showing similarly increasing failure strain with increasing urethane content, though the composite does not show the initial drop in failure strain strain displayed by the neat resin. The extreme non-linearity of most of these materials (see Figures 58 - 70) should not be overlooked. The equations for Kies strain magnification factors ($\epsilon_{ult\ resin}/\epsilon_{ult\ composite}$) require values for fibre and resin moduli. Garrett and Bailey[29] also applied the Kies model to the interpretation of their results and appear to have used the secant modulus as an appropriate value for the resin. This is the approach adopted here in which the resin secant modulus is calculated by dividing the ultimate stress by the ultimate strain given in Table 2. A fibre modulus of 76 GPa has been assumed[107]. The prediction of transverse failure strain for the hexagonal and square arrays given in Figure 99 was calculated using the measured composite fibre volume fractions. The Basic program used to calculate these predictions is given in Appendix 16. In nearly all cases the predictions considerably exceed the measured values. An exception is the square array prediction for the 60% urethane case. It is seen that the fibre volume fraction has a strong influence on the predicted strain magnification factor. Where the volume fraction approaches close packing (79% for a square array and 91% for a hexagonal array) the predicted strain magnification factor rises very rapidly. The Kies theory predicts a strain magnification equal to the ratio of fibre to resin modulus at the limit of close packing and this case is also shown in Figure 99. While this prediction is close to the measured value for 0% urethane composite the values for the flexible materials are clearly absurd. The trend is downwards since with increasing urethane content the resin modulus decreases faster than the failure strain increases.

The Kies theory predicts an increased strain magnification in the resin with increasing difference between fibre and resin modulus. If the initial resin modulus (as given in Table 2) had been used in the prediction instead of the secant modulus the agreement with experiment would have been worse.

Clearly, none of the various forms of the Kies prediction fits the experimental data over the whole range of flexibility. Exploring some of the assumptions in the theory may highlight the reasons for this. The theory included a modification to the effective modulus through plane-strain Poisson constraint, ie $E' = E/1 - \nu^2$. The effect of this modification is small (even for $\nu = 0.5$) but would tend to increase the effective resin modulus, reducing the fibre to resin modulus mismatch which in turn would reduce the predicted strain magnification factor pushing the predictions further away from the observed values. A possibly stronger effect arising from Poisson constraint, has been highlighted by Gagger and Broutman[30] who pointed out that the triaxial stress state which can be generated even under uniaxial tension in areas of biaxial Poisson constraint can reduce the effective failure strain, particularly of the more flexible resins, to low values. In the context of this discussion it is appropriate to mention an observation made during testing of the 100% urethane matrix composite. At approximately 7% strain, bands of whitened areas were observed to form which were associated with debonding and cavitation. Beyond this strain level the stress began to level off and then to decrease, see Figure 63. Failure finally occurred at a strain of 17.3% by which point the

cavitated regions had developed long fibrils of rubber as shown in Figure 100. Clearly these fibrils are not subject to Poisson constraint and can extend individually to strain values close to those measured in neat rubber. It is probably this mechanism (which has an analogy with craze formation at the crack tip in a thermoplastic) which allows the transverse composite to extend to the very large observed failure strain.

The Kies theory would seem to implicitly assume a Reuss model for transverse modulus. The previous section has already shown that this model substantially underestimates transverse modulus, which would suggest that the transverse failure strain might therefore be overestimated.

The Kies theory bypasses any consideration of premature failure of the fibre/matrix interface which might well be the weak link in the transverse system.

Finally, the model assumes regular packing in either hexagonal or square arrays. Garrett and Bailey[29], recognised this as a drawback and suggested that a fibre volume fraction higher than the measured average value should be used in the model to allow for areas of fibre clumping which are inevitable in a real composite. By adjusting the assumed fibre volume fraction the Kies model can predict failure strains anywhere between that for the hexagonal array or for close packing, which covers from one to four orders of magnitude for these materials. The degree of clumping necessary to fit the predictions to the results would need to be progressively decreased with increasing urethane content, which could not be justified from the composite microsections (Figures 23 to 28). Using

the resin secant modulus and assuming a hexagonal array the predictions can be made to agree with observations if the chosen fibre volume fractions are varied only slightly from 90.5% to 87%. This is due to the high sensitivity of the predicted failure strain to the fibre volume fraction as close packing is approached. It is difficult to see how such predictions could have more physical significance beyond that of simple 'curve fitting'.

7.4 Stress Magnification Theories

Measured maximum stresses for neat resin and corresponding transverse composites (as in Table 2) have been plotted against urethane content in Figure 101. The error bars are standard deviations. As outlined in Chapter 6, the 0%, 10% and 20% urethane neat resins showed a pronounced peak in the stress/strain curve while the 40%, 60% and 100% resins failed at the maximum stress after varying degrees of non-linearity. The 0%, 10% and 20% urethane composites displayed little non-linearity though the stress/strain curves were still monotonic. The 100% urethane composite showed considerable non-linearity with a well defined peak in the stress/strain response. These distinct failure modes should be borne in mind when interpreting the maximum stress data in Figure 101. To articulate what is obvious from the Figure it can be seen that for 'rigid' resins (0%, 10% and 20% urethane) the composite has a lower strength than the resin; for 'flexible' resins (40% and 60% urethane) the composite is stronger than the resin while for the rubber (100% urethane) the neat resin again becomes stronger than the composite. A further observation is the extreme range of the data, which cover almost two orders of magnitude.

Also contained in Figure 101 are predictions of transverse strength from those models discussed in Chapter 2 which provided useable equations. The Basic program in Appendix 17 makes numerical predictions using these equations. Materials parameters required as input to the models were measured values of fibre volume fraction, initial resin moduli and maximum resin stresses, as summarised in Table 2. In contrast to the strain magnification approach which used the secant modulus at failure, it was considered more appropriate in this case to use the initial resin modulus since, for most of the resins, the ratio of maximum stress to the corresponding strain was closer to the initial modulus than the secant modulus at failure. The fibre modulus has been taken as 76 GPa[107] and, where required, a fibre Poissons ratio of 0.2 has been assumed[11]. The resin Poisson's ratios, where required, have been taken from the straight line relationship in Figure 96.

The theoretical models highlighted in the literature survey and which have been applied here include the relative cross-sectional area model[2], the stress magnification models derived along lines suggested by Chamis[39], the model put forward by Spencer[25] and the recent three-dimensional approach by Chamis[16]. Comparisons of predicted transverse strengths from each of the theoretical models with experimental results will be discussed individually.

Predictions of transverse strength from the relative cross-sectional area theory are shown in Figure 101 for square and hexagonal arrays. It can be seen that in all cases the predictions considerably underestimate actual results. The particular model used here assumes that the interface has zero strength. Therefore predicting zero strength at close packing. A further assumption is that stress concentrations at the edges of debonded fibres are relieved by plastic flow. Applying a stress concentration factor would of course reduce the predictions and push them further away from the experimental results. Marom and White[38] suggested adding a contribution to transverse strength from a non-zero interfacial strength multiplied by the relative fibre cross-sectional area. No independent measurement of interfacial strength has been made in this study however, and in any case the use of such a simple approach cannot strictly be justified through arguments of a 'weakest-link' controlled strength. As has already been mentioned in the previous section the failure process in the 100% urethane transverse composite was one of debonding, cavitation and fibrillation. It might have been expected therefore that the relative cross-sectional area theory (with zero interfacial strength) should describe quite well the behaviour of this material since a certain area fraction of matrix across the cross-section of the composite would be drawn out as fibrils which would then exhibit strengths close to the measured values for neat resin. The fact that the predictions underestimate the observed transverse strength suggests either that a greater fraction of the rubber is drawn out than would be expected from the relative resin volume fraction, or that the strength of individual

fibrils is greater than that observed in larger scale tests on rubber specimens. If the measured macroscopic rubber strength is appropriate it would appear that at the critical section approximately 50% of the cross-sectional area is drawn into fibrils. This relative cross-sectional area theory clearly has no prospect of predicting the higher composite than resin strengths observed for the 40% and 60% material.

The simple Chamis type predictions for a square array show a considerable underestimate for all but the two most rigid matrix composites, for which the agreement is quite good. The corresponding hexagonal array predictions are, naturally, higher and overestimate the strengths of the two most rigid matrix composites. The agreement with the 40% and 100% urethane composites is good while, again, the prediction greatly underestimates the strength of the intermediate flexibility composites. The agreement with the observed 100% urethane composite is thought to be fortuitous since the failure process for this material would not be expected to be described by a stress concentration type model. Arguments of fibre clumping would tend to increase stress concentration factors and reduce predicted transverse strengths. There must be regions in any real composite irrespective of the overall fibre volume fraction, where the fibres are close packed. If the transverse strength were controlled by the strength of these densely packed regions then it might be expected that transverse strength should be predictable from the stress concentration factor at the limit of close packing. The line in Figure 101 marked 'Chamis (hexagonal array - close packed)'

is the strength prediction at the fibre volume fraction limit of 90.56%. It is seen that the agreement with the results for 0% and 10% urethane composite is good but the prediction progressively underestimates the measurements for the more flexible composites. Clearly, the stress concentration theories discussed so far cannot predict the circumstance of higher transverse strength than resin strength, as observed for the 40% and 60% urethane materials.

The particular version of the Spencer model[25] used for the predictions in Figure 101 is the variable array mode model which assumes a changing average array with fibre volume fraction. At the high fibre volume fractions of the materials in this study the array mode tends toward hexagonal and is seen to give predictions very close to those of the Chamis hexagonal array. The previous discussion therefore applies equally to this model.

A recent, more sophisticated set of equations by Chamis[16] provide values of the three-dimensional stress state for a square array exposed to stress, temperature change and moisture absorption. By choosing the most critical interfibre location, and by predicting transverse cracking when the stress in any direction exceeds the measured resin strength, the failure prediction in Figure 101 marked 'Chamis 3D-max stress' was derived. It can be seen that the predicted interfibre stress concentration factor is small and the prediction can only fit the results where the resin strength and composite transverse strength are similar. Resin brittle fracture might be predictable from a consideration of the maximum interfibre stresses but resin yield is controlled by the full three-dimensional stress state. By comparing the stress state at the most critical

interfibre location with the measured uniaxial maximum resin stress (σ_{max}) through the Von Mises relationship[109]:

$$(\sigma_1 - \sigma_2)^2 + (\sigma_2 - \sigma_3)^2 + (\sigma_3 - \sigma_1)^2 = 2\sigma_{max}^2$$

the failure prediction marked 'Chamis 3D-Von Mises' in Figure 101 was made. It is seen that this prediction is raised above the corresponding '3D max stress' prediction but remains slightly lower than the neat resin failure stress. This model then is again unable to respond to the observation of higher transverse than neat resin strength for the intermediate flexibility materials. It is not known what form of constraint is assumed in the Chamis derivation of the Poisson generated lateral stresses. However, if a very high degree of matrix Poisson constraint is assumed it is possible to envisage how the composite yield stress could exceed the neat resin yield stress. In Appendix 15 expressions predicting the secondary stresses generated by two forms of Poisson constraint were derived. Taking the extreme case of total Poisson constraint (case B) it was shown that:

$$\sigma_z = \sigma_x = \left[\frac{\nu}{1-\nu}\right]\sigma_y$$

It can be seen that as $\nu \rightarrow 0.5$ the stresses in all three directions became equal. Through the Von Mises relationship such a hydrostatic stress state cannot cause yield. By taking extreme examples of degree of constraint and Poisson's ratio, it is therefore possible to see how very high in-situ matrix yield stresses can arise and how a greater transverse than resin strength might be possible.

The magnitude of the hydrostatic, relative to deviatoric, component of stress in the interfibre regions will depend crucially on the effective Poisson's ratio and location within the fibre array. By fibrillating, the resin in the 100% urethane composite would bypass such a mechanism and the matrix behaviour would then be that observed in the neat resin under uniaxial loading.

The 3D Chamis model allows the prediction of stresses generated by differential thermal contraction of fibre and matrix during cool down after cure. Taking thermal expansion coefficients for glass fibre and epoxy resin from reference 16, matrix stresses of 10-15 MPa are predicted for the most rigid composites in this study. Thermoelastic data for the more flexible resins are unavailable, precluding predictions, but the thermal stresses would be expected to be lower for these composites.

Stresses at the fibre matrix interface are expected to be of the same order as the interfibre matrix stresses[16]. No measurements have been made of interface strength of the materials in this study. However, it is probable that the interfacial strength is lower than the matrix strength and that debonding is a precursor to transverse failure. Fractographic evidence for this contention comes from the scanning electron micrographs, Figures 102 to 107, which show, for the most rigid materials, very smooth fibres remaining on the transverse fracture surfaces with little resin remaining bonded. It is apparent that more resin remains on the fibre as the proportion of urethane is increased, suggesting an improvement in the fibre/matrix bond.

The variation in fibre volume fraction between composites, though modest, is a major complication in the interpretation of transverse strength results since the materials in this study approach close packing which results in predicted stress concentration factors which are very sensitive to fibre volume fraction.

7.5 Fracture Mechanics

The candidate critical stress intensity factors (K_Q) measured for the whole range of neat resins and transverse composites are plotted in Figure 108. The error bars are a single standard deviation. It is seen that, within the large experimental error, there is little difference between the resin and composite K_Q fracture toughnesses and that the toughness remains virtually constant up to 40% urethane content. The 60% and 100% urethane data show a marked reduction in apparent K_Q toughness with the composite values considerably higher than the neat resin values. The corresponding candidate critical rate of release of strain energy fracture toughness G_Q, (calculated from K_Q using the Paris, Sih and Irwin[92] relationship described in Chapter 6) has also been plotted, see Figure 109.

It is an interesting point that K_Q and G_Q both characterise fracture toughness but the great change in elastic modulus with increasing urethane content means that while the K_Q values <u>decrease</u> over an order of magnitude, the calculated G_Q values <u>increase</u> over almost two orders of magnitude.

It is important that the question of validity of the measured fracture toughness not be overlooked. As described in Chapter 6, calculation of K_{IC} fracture toughness validity factors and examination of the measured fracture toughness for crack length dependence indicated that the measured fracture toughnesses were only valid for the 0%, 10% and 20% urethane neat resins and the 0%, 10%, 20%, 40% and 60% urethane composites.

The Literature Survey, Chapter 2, referred to several previous observations of suppression of resin toughness in transverse composites. The G_Q data, Figure 109, from the materials in this study would confirm this observation. Values of crack tip opening displacement, ∂, calculated from:

$$\partial = \frac{G_Q}{\sigma_{max\ resin}}$$

using the composite and resin G_Q measurements and the resin strength are summarised in Table 3 and have been plotted against urethane content in Figure 110. It is seen that the crack tip opening displacement of the neat resins (excluding those data of doubtful validity) range from 2μm to 10μm. The corresponding values for transverse composite are much smaller, as would be expected from a consideration of the reduced volume at the crack tip within which energy absorption by yielding could occur. The crack tip opening displacements in neat resin and transverse composite increase rapidly with increasing urethane content since G_Q increases and $\sigma_{max\ resin}$ decreases with greater material flexibility. The crack tip opening

displacements of the transverse composites (excluding the 100% urethane case) are all below 15μm, which is approximately the fibre diameter. The composite microsections, Figures 23 - 28, show that the average interfibre spacing is considerably smaller than this dimension.

The theory by Christensen and Rhinde[67] outlined in Chapter 2 suggested (by using the Griffith equation) that the transverse failure strain (ϵ_2) might be related to transverse modulus (E_{22}) via:

$$\epsilon_2 = \text{constant.} \quad (E_{22})^{-\frac{1}{2}}$$

It can be seen from Figure 111 that the above relationship does not hold for these materials. In the absence of direct measurements Christensen and Rhinde assumed that the fracture toughness and inherent defect size remained constant. Fracture toughness has been measured in this study however and Figure 112 plots the measured transverse strength against measured transverse toughness (K_Q). The 100% urethane composite has been excluded on grounds of doubtful validity but the data on the conventional resin composite used in the test specimen development programme has been included. If the inherent defect size were constant a straight line relationship would be expected. Also shown in Figure 112 are predictions of the inherent defect sizes relating toughness to strength. These are calculated through the equation:

$$K_Q = 1.13\ \sigma_2\ (a)^{\frac{1}{2}}$$

in which a is the radius of an embedded penny shaped crack [110]. To simplify the discussion, questions of what shape inherent defects

in a real composite might be or whether the measured K_Q value is dependent on crack growth direction, have not been raised. It is seen that for all the composites explored, the diameter of the inherent defects lies between 0.6mm and 2.6mm. These dimensions are large. It would be expected that transverse strength specimens containing such defects would be easily detected and discarded. Attempts to trace the origin of fracture by following crack growth surface markings, in the way described by Purslow [111], proved extremely difficult due to the 'brush-like' nature of the fracture surface. Identification of the origin of fracture in the neat resin strength specimens was, however, possible by optical microscopy. Figure 113 is a typical optical micrograph of the crack initiation location at a dust particle on a 0% urethane neat resin fracture surface. Comparisons of critical defect sizes (predicted from the fracture toughness and strength measurements) with observed inherent defects may be less meaningful for the neat resins as they failed by extensive yielding prior to fracture. However, for a resin to yield the inherent flaws must be too small to be activated at the yield stress. This suggests that the inherent defects, if they are penny shaped cracks, must have diameters less than 97 μm, 115μm and 360μm in the 0%, 10% and 20% urethane resins respectively.

Given that inherent defects of the large sizes calculated for the transverse composite could not be inadvertently introduced during filament winding or remain undetected after machining of the specimens, a possible explanation is that they were nucleated during loading. This could occur by subcritical growth of fibre/matrix

debonds, or defects of the order of the fibre dimensions, with their gradual coalescence forming cracks which only become unstable when they reach the calculated critical defect size.

8. CONCLUSIONS AND SUGGESTIONS FOR FURTHER WORK

As an introduction to the importance of transverse cracking in composites technology, classical lamination theory has been used to predict the sequential damage process in cross-plied laminates. By inputting the properties of a notional, flexibilised lamina the possibilities for postponement of damage initiation are demonstrated.

The literature on transverse stiffness, strength and toughness has been comprehensively reviewed, with special emphasis on papers which present quantative theoretical models. A dichotomy of thought has been highlighted on whether it is the matrix strength and failure strain or the toughness which control transverse failure. No work presented in the literature has measured the full range of properties necessary to resolve this apparent conflict.

A resin system, based on epoxy/urethane mixtures, has been identified which allows high quality unidirectional glass fibre composites to be filament wound which display a systematic variation in transverse flexibility.

A preliminary experimental programme, using a conventional rigid resin glass fibre composite, allowed the selection of those test specimens which could be used to measure the full transverse stress/strain and fracture toughness properties necessary for a rational assessment of the available theoretical models. The main experimental programme has then characterised these properties for the flexibilised composites.

The preliminary experimental programme showed that when transverse cracks extend they do so with an increasing fracture toughness with crack length due to the creation of a tied zone of fracture face bridging fibres or stringers. The rate of increase of toughness with crack extension is shown to be dependent on the geometry of the fracture test specimen.

The conditions under which an increasing toughness can pin cracks are shown to be defined by a simple stability criterion.

By considering a balance between elastic strain energy and fracture energy of individual stringers within the tied zone a mathematical model has been developed which defines the equilibrium stringer state. The equilibrium stringer angle is shown to depend only on a few independently measureable geometric and material parameters and is independent of crack opening. Theoretical predictions of stringer angle agree with direct observations. The model shows that the strain in the stringer depends only on the stringer angle. Stringer strains are high, and are predicted to exceed the fibre failure strain with only modest increases in matrix fracture toughness. There is great scope here for further work to explore tied zone development with changes in fibre type, fibre misalignment and matrix toughness. It would be interesting to see if, as the model predicts, tied zone development would be greatly hampered for materials, such as thermoplastic matrix composites, which display very high toughness.

An important consequence of a predicted constant stringer angle is that, provided the number of stringers per unit area remains constant, the closing pressure exerted by the tied zone on the fracture faces remains independent of crack opening. This allows a relatively straightforward model of a Double Cantilever Beam with a tied crack to be developed. Each arm of the DCB is treated as an encastered beam deflecting under an opening end point load and a closing constant distributed load. The irreversible work expended in opening the arms of the DCB against the closing pressure is then integrated over the whole tied zone, and the rate of change of this energy with crack growth provides an expression for the tied zone contribution to fracture toughness in terms of a few material and geometric constants of the specimen. The only parameter in the expression which is not independently measurable is the number of stringers per unit area, which controls the magnetude of the closing pressure.

By assuming a constant value of 1.5 MPa for the closing pressure, this model accurately predicts the observed increase of toughness with crack extension, as well as the geometry dependence of the toughness increase.

This theoretical approach is quite general and should be applicable to a wide range of fracture toughness test geometries. It is possible that the approach may be of value in describing sub-critical crack growth in materials other than transverse composites. Further investigations could explore, both theoretically and experimentally, what contribution the tied zone makes to the toughness of constrained transverse cracks in cross-plied laminates.

It would also be interesting to see if this tied zone model could be successfully extended to mode II and mixed mode transverse crack propagation.

Comparison of results from the main experimental programme with theories of transverse modulus from the literature shows that those models based on a Reuss, series connected modulus are almost always underestimates. More sophisticated models predict very well the transverse modulus of the rigid composites but grossly underpredict transverse modulus of the flexible materials. It is demonstrated that the high transverse modulus of the more flexible composite can be understood only if a high degree of matrix Poisson constraint is assumed to be in operation.

The Kies strain magnification theories considerably overestimate the observed transverse failure strains if the measured fibre volume fractions are used in the model. If arguments of fibre clumping are invoked the predictions can fit the results by using variable fibre volume fractions approaching close packing. However, it is thought that such exercises have little significance beyond that of simple curve fitting.

The neat resin and transverse composite strengths display a complex relationship. For intermediate flexibility materials the composites are stronger than the neat resin, while for the very rigid and the very flexible materials the reverse is true. None of the stress magnfication theories from the literature seem able to model this complete behaviour. However, it is possible to indicate which models provide the best agreement with experimental results within

particular regimes of material flexibility. For the three most rigid materials the various forms of the simple Chamis model and the Spencer model display reasonable correlation with experiment. The Chamis hexagonal array model at the limit of close packing in fact provides quite good correlation with the results for the two most rigid materials. The observation of higher resin than composite strength for the intermediate materials may be attributable to suppression of resin yielding in the composite through a high degree of matrix Poisson constraint giving rise to an interfibre stress state with a large hydrostatic component. The failure process of 100% urethane rubber composite is exceptional, involving as it does cavitation and fibrillation of the matrix with eventual failure at a relatively very high strain. It would be expected that the strength of this composite would be better described by a model reflecting the relative area of matrix able to support load by fibrillating, rather than a stress concentration type model.

In general, there is a disappointing lack of agreement between the theoretical failure predictions and the experimental results. However, the transverse properties cover such a large range that it might not be expected that a single model could describe this whole behaviour. The following practical points are suggested if future work along similar lines were contemplated. Production of material with less variation in properties would allow a more detailed examination of trends in material behaviour without the complication of changes in failure mode. Production of composites with tighter control of fibre volume fraction would simplify data interpretation especially for materials such as those in this study in which the fibres approach close packing and predicted stress and strain

concentration factors change rapidly.

There are several possibly important aspects of transverse behaviour which have received little attention in this study. The influence of residual microstresses arising from fibre/resin thermal mismatch have only been touched upon. A relatively simple model has indicated that these stresses may be significant and should be included in any micromechanical failure prediction. It has been assumed throughout that the curing process of the resin in a composite, and therefore its mechanical performance, is identical to that of bulk resin. Interfacial failure has been largely ignored because of the lack of information of fibre/matrix bond strength and the considerable experimental difficulty in obtaining it. Gradual damage development such as progressive fibre/matrix debonding, matrix non-linearity, and progressive interfibre matrix yielding are impossible to analyse using the simple models previously outlined. Further work is currently in hand to apply a true three-dimensional Finite Element analysis with non-linear capability to the solution of strain distributions in transverse composites. Theoretical strains predicted by this method will be compared with experimentally measured strain distributions in model transverse composites determined by laser Moiré interferometry[112]. This is a novel technique which makes use of submicron cross gratings which are bonded to the surface of the specimen. By superimposing over this a virtual grating (caused by the interference of two laser beams) strains in the specimen produce interference fringes which correspond to deformations as small as 0.4μm. The deformation map shown in

Figure 114, which is currently being analysed, was obtained in this way for a model transverse composite of 3mm diameter glass rods embedded in epoxy resin.

Fracture mechanics tests on the range of neat resins and transverse composites provided K_Q values from which G_Q values have been calculated. The validity of the results for the more flexible materials is in doubt. Further work which attempts to characterise fracture toughness of materials such as these should consider the use of non-linear fracture mechanics techniques such as the J-integral. Comparisons of predicted crack tip opening displacements with interfibre spacing point to crack tip yield zone constraint as a possible explanation of the lower G_Q fracture toughness in the composite than in the corresponding resin. Future attempts to improve transverse performance by increasing resin toughness might be advised to neglect rubber toughening additions to the matrix which require a large volume at the crack tip for shear yielding to operate, in favour of a process such as whisker toughening which could be expected to contribute to energy absorbtion even in the constrained volume at the tip of a transverse crack.

Critical defect sizes for the transverse composites are calculated to be of the order of mm's in diameter. No inherent defects of this size were observed in the composite strength specimens. The calculated maximum possible critical defects in the neat resins, are by contrast, typically an order of magnetude

smaller. As the same mixture of resin was used to manufacture both resin plates and transverse composites, a contention that the composite critical defects are extraneous particles introduced into the composite with the resin would have little basis. A more likely explanation is that defects of the large sizes calculated are formed by gradual coalescence of debonds or other sub-critical flaws.

It is possible that stress concentration models and fracture mechanics concepts are not mutually exclusive but are both valid descriptions of different stages of the same transverse fracture process. Stress concentration theories may describe how debonds or other sub-critical flaws may initiate in the highly stressed regions between fibres, while macroscopic fracture mechanics may describe how congregations of sub-critical defects form a single critical crack which propagates to failure.

ACKNOWLEDGEMENTS

The work described in this thesis was undertaken as part of the underlying research programme of the UKAEA at the Harwell Laboratory. I am indebted to the Authority, and to Dr D H Bowen, Leader of the Polymers and Composites Group, for the provision of research facilities and for allowing a proportion of my time to be spent in carrying out this work.

I would like to extend my sincere thanks to Dr D C Phillips, my Supervisor at Harwell, who initially suggested the topic of transverse cracking and with whom useful (and entertaining) discussions were held. I also wish to thank Mr M G Phillips, my Supervisor at Bath University, for his encouragement during the period of this research. I would like to express my gratitude to my colleagues, Mr R J Lee and Dr R Davidson, for many stimulating discussions, to Dr R Davidson for assistance in generating the laser Moire photograph, and to Dr S Burnay for help in interpreting the infra-red spectra. I would like to thank the members of the Polymers and Composites Group for general practical assistance, but in particular to Mr G Rhodes who managed to filament wind good quality composite plates when supplied with intractable resin blends.

The quality of the figures in this thesis owes much to the skill of the Photographic Group and the Tracing Office.

Special thanks are due to Veronica and Val for their strenuous efforts in typing this thesis to meet the deadline. I wish to express my sincere thanks to my wife for her patience and understanding during the hectic time of preparation of this thesis.

REFERENCES

1. B Harris, Engineering Composite Materials, The Institute of Metals, 1986.

2. D Hull, An Introduction to Composite Materials, Cambridge Solid State Science Series, Cambridge University Press, 1981.

3. A Kelly and N H MacMillan, Strong Solids, 3rd Edition, Clarendon Press, Oxford, 1986.

4. J E Ashton, J C Halpin and P H Petit, Primer on Composite Materials : Analysis, Technomic, Stamford, Conn, USA, 1969.

5. R M Jones, Mechanics of Composite Materials, Scripta, Washington, USA, 1975.

6. M N Nahas, Survey of Failure and Post-Failure Theories of Laminated Fibre-Reinforced Composites, Journal of Composites Technology and Research, v8, n4, Winter 1986, p 138.

7. J H Greenwood, German Work On GRP Design, Composites, July 1977, p 175.

8. B R Collins and P L Crane, A Graphical Representation of the Failure Surface of a Composite, J Comp. Mats, v5, July 1971, p 408.

9. G M Wells, A Preliminary Investigation Into Transverse Fracture of Unidirectional Fibre Composities, AERE R-11494, Report Submitted for Transfer from MSc to PhD Study, Jan 1985.

10. C C Chamis and G Sendeckyj, Critique on Theories Predicting Thermoelastic Properties on Fibrous Composities, J Comp. Mats, v2, 1968, p332.

11. D F Adams and D R Doner, Transverse Normal Loading of a Unidirectional Composite, J Comp. Mats., v1, (1967), p152.

12. P E Chen and J M Lin, Transverse Properties of Fibrous Composites, Materials Research and Standards, Aug 1969, p29.

13. Z Hashin and B Rosen, The Elastic Moduli of Fibre Reinforced Materials, J Appl. Mech, v31, 1964, P223.

14. R E Allred and P F Gerstle, The Effect of Resin Properties on the Transverse Mechanical Behaviour of High-Performance Composities, 30th Ann Tech Conf, 1975, Reinforced Plastics Composites Inst., Soc. Plastics Industry, Section 9-B.

15. J Ekvall, Structural Behaviour of Monofilament Composities, AIAA/ASME 7th Structures, Structural Dynamics and Materials Conference, Palm Springs, California, 1965, p250.

16. C C Chamis, Simplified Composite Micromechanics for Predicting Microstresses, 41st Ann Tech Conf., 1986, Reinforced Plastics Composities Inst., Soc. Plastics Industry, Session 25-B.

17. R Smith, Ultrasonic Elastic Constants of Carbon Fibres and their Composities, J Appl. Phys, v43, 1972, p2555.

18. L B Greszczuk, Applications and Design of Fibrous Composites, A Short Course at Trinity College Cambrige, 10-15 Aug 1980.

19. Z Hashin, Analysis of properties of Fibre Composities with Anisotropic Constituents, J Appl. Mech., v46, 1979, p543.

20. H T Hahn, Simplified Formulas for Elastic Moduli of Unidirectional Continuous Fibre Composities, Composites Technology Review, 2, 3, p5, 1980.

21. I M Kowalski, Determining the Transverse Modulus of Carbon Fibres, 31st Int. SAMPE Symposium, April 7-10, 1986, P303.

22. L B Greszczuk, Theoretical and Experimental Studies on Properties and Behaviour of Filamentary Composities, 21st Ann. Tech, Conf., 1966, Reinforced Plastics Composities Inst., Soc. Plastics Industry, Section 8A.

23. R Hill, Theory of Mechanical Properties of Fibre-Strengthened Materials : III. Self Consistent Model, J Mech, Phys. Solids, v13, 1965, P189.

24. J E Bailey and A Parvizi, On Fibre Debonding Effects and the Mechanism of Transverse - Ply Failure in Cross-Ply Laminates of Glass Fibre/Thermoset Composites, J Mats, Sci., v16, (1981), P649.

25. A Spencer, The Transverse Moduli of Fibre Composite Material, Comp. Sci, and Tech. v27, 1986, p93.

26. S W Tsai, D F Adams and D R Doner, Effect of Constituent Material Properties on the Strength of Fibre-Reinforced Composite Materials, AFML-TR-66-190, 1966.

27. L R Herrmann and K S Pister, Composite Properties of Filament - Resin Systems, Presented at the Winter Annual Meeting, Philadelphia, Nov 17-22, 1963 of ASME.

28. J A Kies, Maximum Strains in the Resin of Fibreglass Composities, NRL Report 5752, March 1962.

29. K W Garrett and J E Bailey, The Effect of Resin Failure Strain on the Tensile Properties of Glass Fibre-Reinforced Polyester Laminates, J Mats. Sci., v12, 1977, p2189.

30. S K Gaggar and L J Broutman, Effect of Matrix Ductility and Interface Treatment on Mechanical Properties of Glass Fibre Mat Composities, Polym. Eng. and Sci., v16, n8, 1976, p537.

31. V V Vasil'ev and V A Salov, Development and Study of a Two-Matrix Glass Fibre Composite with Enhanced Transverse Deformation, Mekhanika Kompozitnykh Materialov, 4, p662, 1984.

32. G T Stevens and A W Lupton, Transverse Cracking in Orthotropic Glass Fibre/Epoxy Composities, Australian Atomic Energy Commission Report E 382, Oct 1976.

33. G T Stevens and A W Lupton, Transverse Cracking in Cross-Plied Composities, J Mats. Sci. Letters, v11, 1986, p568.

34. M H B van der Beek and G Hamm, The Influence of the Ultimate Strain of a Polyester Resin on Mechanical Properties of Laminates, 5th Int. Reinforced Plastics Conf., 1966, paper 12.

35. R E Lavengood and O Ishai, The Mechanical Performance of Cross-Plied Composites, Polym. Eng. and Sci. May 1971, v11, n3, p226.

36. D Hull and M J Legg, Effect of Resin Flexibility on the Failure Properties of Fibre Composities, 2nd Int. Conf. on Deformation Yield and Fracture of Polymers, April 1979.

37. G A Cooper and A Kelly, Role of Interface in the Fracture of Fibre Composite Materials, ASTM STP 452, 1968, P90.

38. G Marom and E F T White, Improvements in the Transverse Properties of Composites. Part 1 : Fracture Surface Energy and Mechanism of Transverse Fracture in Glass Fibre Composites, J Mats. Sci., v7, 1972, P1299.

39. C C Chamis, Micromechanics Strength Theories, Chapter 3 of Fracture and Fatigue, L J Broutman and R H Krock Ed, Adademic Press, New York, 1984.

40. C C Chamis, Simplified Composite Micromechanics Equations for Strength, Fracture Toughness and Environmental Effects, SAMPE Quarterly, July 1984, p41.

41. L B Greszczuk, Consideration of Failure Modes in the Design of Composite Structures, AGARD Conf. Proc. No 163, March 1975.

42. Xing Ji, Peng-Fei He and De-Chun Lin, The Stress Analysis of the Matrix in Fibre Reinforced Composities, Proc. Int. Symp. on Composite Materials and Structures, June 10-13, 1986, Beijing, China.

43. Wu-Cheng Huang, Elastoplastic Transverse Properties of a Unidirectional Fibre Reinforced Composite, J Comp. Mats., v7, 1973, p482.

44. D F Adams, Inelastic Analysis of a Unidirectional Composite Subjected to Transverse Normal Loading, J Comp. Mats., v4, 1980, p310.

45. G P Sendeckyj and Ing-Wu Yu, Some Exact Results in Transverse Deformation of Fibre Reinforced Composities, J Comp. Mats., v5, 1971, P533.

46. L J Broutman and B D Agarwal, A Theoretical Study of the Effect of an Interfacial Layer on the Properties of Composities, Polym. Eng. and Sci., v14, n8, 1974, p581.

47. R G C Arridge, The Effect of Interlayers on the Transverse Stresses in Fibre Composities, Polym. Eng. and Sci., v15, n10, 1975, p757.

48. G Marom and R G C Arridge, Stress Concentrations and Transverse Modes of Failure in Composities with a Soft Fibre-Matrix Interlayer, Mats. Sci. and Eng., v23, 1976, P23.

49. L D Tryson and J L Kardos, The Use of Ductile Interlayers in Glass Fibre Reinforced Epoxies, 36th Ann. Tech. Conf., 1981, Reinforced Plastics Composites Inst., Soc. Plastics Industry, Session 2-E.

50. J Tirosh, E Katz, G Lifschuetz and A S Tetelman, The Role of Fibrous Reinforcements Well Bonded or Partially Debonded on the Transverse Strength of Composite Materials, Engineering Fracture Mechanics, v12, 1979, p267.

51. A F Yee and R A Pearson, Toughening Mechanisms in Elastomer-Modified Epoxies. Part 1, Mechanical Studies, J Mats. Sci., v21, 1986, p2462.

52. R A Pearson and A F Yee, Toughening Mechanisms in Elastomer Modified Epoxies. Part 2, Microscopy Studies, J Mats. Sci., v21, 1986, p2475.

53. A R Siebert, E H Rowe, C K Riew and J M Lipiec, Toughness vs Flexibility in Epoxy Resins (Part A), 28th Ann. Tech. Conf., 1981, Reinforced Plastics Composities Inst., Soc. Plastics Industry, Section 1-A.

54. J M Scott and D C Phillips, Carbon Fibre Composities with Rubber Toughened Matrices, J Mats. Sci., v10, 1985, p551.

55. W L Bradley and W M Jordon, The Relationship Between Resin Ductility and Composite Delamination Fracture Toughness, Proc. Int. Symp. on Composite Materials and Structures, June 10-13, 1986, Beijing, China.

56. P E Keary, L B Ilcewicz, C Shaar and J Trostle, Mode I Interlaminar Fracture Toughness of Composites Using Slender Double Cantilever Beam Specimens. J Comp. Mats., v19, 1985, p154.

57. D L Hunston, Composite Interlaminar Fracture : Effect of Matrix Fracture Energy, Comp. Tech. Review, v6, n4, 1984, p176.

58. S M Lee, Correlation Between Resin Materials Variables and Transverse Cracking in Composites, J Mats. Sci., v19, 1984, p2279.

59. H Wells and N L Hancox, The Use of Urethane Rubber/Epoxide Resin Blends as Matrix Materials for Glass and Carbon Fibre Composites, Polym. Eng. and Sci., v18, 1978, n2, p87.

60. E M Wu, Some Unique Crack Propagation Phenomena in Unidirectional Composites and their Mathematical Characterisation, Proc. 1969 Civil Engineering Materials Conf., Part 2, Southampton.

61. S M Lee, Double Torsion Fracture Toughness Test for Evaluating Transverse Cracking in Composities, J Mats. Sci., Letters, v1, 1982, p511.

62. W S Johnson and P D Mangalgiri, Investigation of Fibre Bridging in Double Cantilever Beam Specimens, J Comp. Tech. and Research, v9, n1, 1987, p10.

63. S M Lee, A Comparison of Fracture Toughness of Matrix Controlled Failure Modes : Delamination and Transverse Cracking, J Comp. Mats., v20, 1986, p185.

64. J M Slepetz and L Carlson, Fracture of Composite Compact Tension Specimens, ASTM STP 593, 1975, p143.

65. D C Phillips and G M Wells, The Stability of Transverse Cracks in Fibre Composities, J Mats. Sci., Letters, v1, 1982, p321.

66. I Engelberg and G Marom, Some Observations on Transverse Fracture Energies of Unidirectional Composites, Fibre Sci. and Tech., v9, 1976, p63.

67. R M Christensen and J A Rinde, Transverse Tensile Characteristics of Fibre Composites with Flexible Resins: Theory and Test Results, Polym. Eng. and Sci., v19, 1979, n7, p506.

68. J G Morley and G Pissinou, Transverse Ply Cracking Strains in (0°/90°) and (±θ°/90°) laminates, J Mats. Sci., v21, 1986, p4206.

69. H T Hahn, J B Erikson and S W Tsai, Characterisation of Matrix/ Interface Controlled Strength of Unidirectional Composites, AFML-TR-78-85, 1978.

70. J Aveston, G A Cooper and A Kelly, The Properties of Fibre Composites, in National Physical Laboratory Conference Proceedings, 1971, p15, London. IPC.

71. G A Cooper and J M Silwood, Multiple Fracture in a Steel Reinforced Epoxy Resin Composite, J Mats. Sci., v7, 1972, p325.

72. A Parvizi, K W Garrett and J E Bailey, Constrained Cracking in Glass Fibre-Reinforced Epoxy Cross Ply Laminates, J Mats. Sci., v13, 1978, p195.

73. J E Bailey, P T Curtis and A Parvizi, On the Transverse Cracking and Longitudinal Splitting Behaviour of Glass and Carbon Fibre Reinforced Epoxy Cross Ply Laminates and the Effect of Poisson and Thermally Generated Strain, Proc. R. Soc. London. A. 366, p599, 1979.

74. D L Flaggs and M H Kural, Experimental Determination of the In-Situ Transverse Lamina Strength in Graphite/Epoxy Laminates, J Comp. Mats., v16, 1982, p103.

75. A S D Wang and F W Crossman, Initiation and Growth of Transverse Cracks and Edge Delamination in Compositie Laminates, Part 1. An Energy Method, J Comp. Mats. Supplement, v14, 1980, p71.

76. F W Crossman, W J Warren, A S D Wang and G E Law, Initiation and Growth of Transverse Cracks and Edge Delamination in Composite Laminates, Part 2. Experimental Correlation, J Comp. Mats. Supplement, v14, 1980, p88.

77. S L Ogin and P A Smith, Fast Fracture and Fatigue Growth of Transverse Ply Cracks in Composite Laminates, Scripta Metallurgica, v19, 1985, p779.

78. H Lee and K Neville, Handbook of Epoxy Resins, McGraw-Hill, 1967.

79. Bayer, Polyurethanes, Manufactures Guide, 1979.

80. E Brown, The Effect of a Two-Stage Curing Schedule on the Fibre Loading and Transparency of Unidirectionally Wound Glass Fibre/Epoxy Resin Plates, AERE-R 8161, Oct 1975.

81. J M Scott, G M Wells and D C Phillips, Low Temperature Crack Propagation in an Epoxide Resin, J Mats, Sci., v15, 1980, p1436.

82. R G C Arridge and J H Speake, Mechanical Relaxation Studies of the Cure of Epoxy Resins : 1, Measurement of Cure. Polymer, v13, 1972, p443.

83. R F Boyer, Dependence of Mechanical Properties on Molecular Motion in Polymers, Polym. Eng. and Sci., v8, n3, 1968, p161.

84. J H van der Maas, Basic Infra-Red Spectroscopy, Heyden and Son, 1972.

85. J M Whitney, I M Daniel and R B Pipes, Experimental Mechanics of Fibre Reinforced Composite Materials, Soc., Experimental Stress Analysis, 1982, USA.

86. R E Ellred, H K Street and R J Martinez, Improvement of Transverse Composite Strengths : Test Specimen and Materials Development, National SAMPE Symposium and Exhibition, v24, 1979, p31.

87. K J Pascoe, General Fracture Mechanics, Chap. 7 in Failure of Plastics, W Brostow and R Corneliussen Ed's, Hanser Publishers, 1986.

88. S Mostovoy, P B Crossley and E J Ripling, Use of Crack-Line-Loaded Specimens for Measuring Plane-Strain Fracture Toughness, J. of Materials, v2, 1967, p661.

89. J F Knott, Fundamentals of Fracture Mechanics, Butterworths, London, 1973.

90. D C Phillips, J M Scott and M Jones, Crack Propagation in an Amine Cured Resin, AERE-G 828, 1977.

91. W F Brown and J E Srawley, Plane Strain Crack Toughness Testing of High Strength Metallic Materials, ASTM STP 410, 1966.

92. D G Smith and B R Mullinix, Fracture Mechanics Design Handbook for Composite Materials, US Army Missile Research and Development Command, Tech. Report T - 78-6, Sept. 1977.

93. A G Atkins and Y-W Mai, Elastic and Plastic Fracture, Ellis Horwood Ltd, 1985.

94. R J Sanford and F R Stonesifer, Fracture Toughness Measurements in Unidirectional Glass-Reinforced-Plastics, J Comp. Mats. v5, 1971, p241.

95. A A Griffith, The Phenomena of Rupture and Flow in Solids, Phil. Trans. Roy. Soc., A221, p163, 1921.

96. O L Bowie and C E Freese, Central Crack on Plane Orthotropic Rectangular Sheet, Int. J. of Fracture Mechanics, v8, n1, 1972, p49.

97. H J Konish, Mode I Stress Intensity Factors for Symmetrically - Cracked Orthotropic Strips, ASTM STP 593, 1975, P99.

98. J F Mandell, F J McGarry, S S Wang and J. Im, Stress Intensity Factors for Anisotropic Fracture Test Specimens of Several Geometries, J Comp. Mats, v8, 1974, p106.

99. H Harel, G Marom, S Fischer and I Roman, Effect of Reinforcement Geometry on Stress Intensity Factor Calibrations in Composites, Composites, April 1980, p69.

100. B S 5447, Methods of Test for Plane Strain Fracture Toughness (K_{IC}) of Metallic Materials, British Standards Institution, London 1977.

101. R S Rivlin and A G Thomas, Rupture of Rubber. I. Characteristic Energy for Tearing, J Polym. Sci., v10, n3, 1952, p291.

102. G R Sidey and F J Bradshaw, Some investigations on Carbon-Fibre - Reinforced Plastics Under Impact Loading, and Measurements of Fracture Energies, Int. Conf. on Carbon Fibres, Their Composites and Applications, Plastics Institute, London, 1971.

103. E M Wu, Strength and Fracture of Composites, Chap. 5 of Composite Materials, Ed. L J Broutman and R H Krock, v5, Academic Press, 1974.

104. R W Lang, M Heym, H Tesch and H Stutz, Influence of Constituent Properties on Interlaminar Crack Growth in Composites, p261, High Tech - The Way into the Nineties, Ed K. Brunsch, H-D Golden and C-M Herkert, Elsevier, 1986.

105. D Guedra, D Lang, J Rouchon, C Marais and P Sigety, Fracture Toughness in Mode I: A Comparison Exercise of Various Test Methods, Int. Conf. on Composite Materials VI, 20-24 July 1987, Imperial College, London.

106. S Timoshenko, Elements of Strength of Materials, Van Nostrand Reinhold, 1935.

107. J A Quinn, Design Data Fibreglass Composites, Fibreglass Ltd.

108. S G Lekhnitskii, Theory of Elasticity of an Anisotropic Elastic Body, Holden-Day 1963.

109. I M Ward, Review : The Yield Behaviour of Polymers, J Mats. Sci., v6, 1971, p1397.

110. A de S Jayatilaka, Fracture of Engineering Brittle Materials, Applied Science Publishers Ltd., London, 1979.

111. D Purslow, Matrix Fractography of Fibre-Reinforced Epoxy Composites, Composites, v17, n4, 1986, p289.

112. D Post, Moiré Interferometry at VPI and SU, Experimental Mechanics, v23, n2, 1983, p203.

TABLES

Table I

Approximate Property Data For 60% Fibre Volume Fraction Unidirectional Composites And Some Metals

Units	Property	Glass		Boron	Kevlar		Carbon		Jute	Aluminium/ Copper Type Alloys	Carbon Steels	Titanium Alloy	Beryllium
		E	R		49	29	High Modulus	High Strength					
GPa	E_{11}	45-55	53	200	76	51	180-300	110-150	45	72	215	110	310
GPa	E_{22}	15-25		22	5.5	5.1	8	9-10		72	215	110	310
	ν_{12}	0.3		0.3	0.34			0.3					
GPa	G_{12}	5-9		7	2			5					
MPa	σ_1	700-1200	1800	1400	1400	1400	1000-1500	150-5400	420	300-500	400-3000	900	550
MPa	σ_2	20-50		90	30		50	50-70		300-500	400-3000	900	550
MPa	τ_{12}	50-80		140	60			70					
MPa	σ_{1c}	350-700		2800	280			1200					
MPa	σ_{2c}	170-220		280	140								
%	ϵ_1	1.8-2.2	3.4	0.7	1.8	2.7	0.4-0.8	1.1-1.8	1.0	8-15	10-25	15	1.5
%	ϵ_2	0.4-0.5	0.4-0.5	0.45	0.6		0.6	0.5-0.7		8-15	10-25	15	1.5
Specific gravity	ρ	2.03	2.04	2.05	1.36	1.36	1.61-1.67	1.52-1.58	1.20	2.7	7.87	4.5	1.8
GPa/SG	$E_{11/\rho}$	22-27	26	98	56	38	110-185	70-95	35	27	27	24	170
MPa/SG	$\sigma_{1/\rho}$	345-590	880	680	1030	1030	600-910	900-3500	350	110-180	50-380	200	300

TABLE 2

Summary of Measured Properties Properties of Neat Epoxy/Urethane Resin Blends And Corresponding Transverse Composites.

Neat Resins

% Urethane	E (GPa)	σ_{max} (MPa)	ϵ_{ult} (%)	σ_{ult} (MPa)	ν	Tg (°C)
0%	3.13 ± 0.16	79.9 ± 0.7	9.84 ± 1.18	72.8 ± 3.3	0.23 ± 0.06	121
10%	3.24 ± 0.13	76.0 ± 1.1	8.25 ± 1.41	65.9 ± 2.7	0.34 ± 0.03	105
20%	2.58 ± 0.07	62.0 ± 0.9	11.15 ± 2.52	50.3 ± 1.5	0.27 ± 0.06	92
40%	0.33 ± 0.05	16.6 ± 1.4	37.7 ± 6.23	ult = max	0.32 ± 0.04	38
60%	7.11 MPa ± 0.54	3.20 ± 0.26	43.6 ± 2.1	ult = max	0.39 ± 0.06	5
100%	81.3 KPa ± 0.91	1.92 ± 0.61	765.0 ± 32.0	ult = max	0.50 *	-22

* Assumed Value

Transverse Composites

% Urethane	E_{22} (GPa)	σ_{max} (MPa)	ϵ_{ult} (%)	σ_{ult} (MPa)	Vf (%)
0%	21.6 ± 3.3	22.9 ± 6.7	0.11 ± 0.03	ult = max	74
10%	15.9 ± 2.7	19.5 ± 3.9	0.12 ± 0.01	ult = max	66
20%	18.7 ± 3.0	30.2 ± 4.6	0.17 ± 0.03	ult = max	74
40%	4.0 ± 0.5	21.9 ± 3.7	0.76 ± 0.17	ult = max	65
60%	3.3 ± 0.4	13.4 ± 0.4	0.96 ± 0.11	ult = max	76
100%	0.0188 ± 0.0098	0.90 ± 0.04	17.3 ± 3.14	0.81 ± 0.06	69

Where E and E_{22} = initial moduli
σ_{max} = highest nominal stress
σ_{ult} = nominal stress at failure
ϵ_{ult} = strain at failure
T_g = resin glass transistion temperature
Vf = fibre volume fraction
ν = initial Poissons ratio

TABLE 3

Summary of Fracture Toughness Data for Neat Resins and Corresponding Composites

Neat Resin

Urethane Proportion	K_Q (MPa $\sqrt{m}$)	x (mm)	r_p (μm)	G_Q (J/m^2)	∂ (μm)	Judgement of Validity
0%	0.63 ± 0.05	0.16	19.8	127	1.59	√
10%	0.65 ± 0.05	0.18	23.3	130	1.71	√
20%	0.94 ± 0.34	0.58	73.2	342	5.52	√
40%	0.97 ± 0.18	8.01	1020.0	2851	171.75	x
60%	0.090 ± 0.035	1.96	250.0	1139	355.94	x
100%	0.028 ± 0.011	0.53	67.7	9643	5.02 mm	x

Composite

Urethane Proportion	K_Q (MPa $\sqrt{m}$)	x* (mm)	r_p* (μm)	G_Q (J/m^2)	∂* (μm)	Judgement of Validity
0%	0.935 ± 0.419	0.34	43.3	35.1	0.44	√
10%	0.747 ± 0.120	0.24	30.6	30.0	0.39	√
20%	0.694 ± 0.090	0.31	39.5	22.1	0.36	√
40%	0.778 ± 0.071	5.49	699.0	121.1	7.29	√
60%	0.401 ± 0.026	39.26	4998.7	37.4	11.69	√
100%	0.111 ± 0.048	8.36	1064.4	468.5	244.01	x

* Calculated using yield stress of corresponding neat resin.

TABLE 4

Predictions of Composite Transverse Moduli

From Various Theories Using The Measured Resin Moduli,

Measured Fibre Volume Fractions And Inferred Poisson's Ratio's

Resin Type	Measured Resin Modulus	Measured Composite Volume Fraction	Inferred Resin Poisson's Ratio
0%	3.13 GPa	74%	0.26
10%	3.24 GPa	66%	0.28
20%	2.58 GPa	74%	0.30
40%	0.33 GPa	65%	0.35
60%	7.11 MPa	76%	0.40
100%	81.3 KPa	69%	0.50

Fibre modulus = 76 GPa, Fibre Poisson's ratio = 0.20.

Resin Type	Measured	Predicted Composite Modulus (Same units as measured)							
		Reuss	Long' Poiss'	Ekvall	Allred	Hashin	Greszczuk	Halpin - Tsai	Spencer
0%	21.6 GPa	10.8	11.5	13.0	9.7	20.5	25.7	21.0	17.9
10%	15.9 GPa	8.8	9.5	11.1	8.5	16.4	16.3	16.8	14.6
20%	18.7 GPa	9.0	9.9	11.8	9.5	17.4	24.4	18.3	15.6
40%	4.0 GPa	0.9	1.1	1.4	1.3	1.9	2.6	2.1	1.8
60%	3.3 GPa	0.03	0.04	0.05	0.06	0.07	0.38	0.07	0.07
100%	18.8 MPa	0.26	0.35	0.70	∞	0.59	1.71	0.62	0.55

APPENDICES

1. A summary of classical lamination theory.

2. Predictions of the sequential damage process of 0°/90° laminates using classical lamination theory.

3. Derivation of the Kies strain magnification factor. (From Kies, ref 28).

4. Derivation of Chamis type stress concentration factors.

5. Details of conventional rigid resin and composite fabrication methods for material used in initial test specimen development trials.

6. Details of the range of epoxy/urethane blends used to manufacture neat resin plates and ±½° unidirectional plates used in the main experimental programme.

7. (i) Transverse tensile strength results from the straight-sided coupons of conventional resin composites.

   (ii) Transverse tensile strength results from dogbone shaped specimens of 0° and ±½° conventional resin composites.

   (iii) Tensile strength results from conventional neat resin dogbones.

(iv) Transverse strength results from 3 point flexure of 0° and ±½° conventional resin composites.

(v) Transverse strength results from 4 point flexure of 0° and ±½° conventional resin composites.

(vi) Transverse tensile strength results from axially loaded hoop wound tubes.

(vii) Transverse strength results from 4 point flexure of hoop wound tubes.

8. The paper : The Stability of Transverse Cracks in Fibre Composites by D C Phillips and G M Wells.

9. Derivation of geometric crack stability conditions. (From Atkins and Mai, ref 93).

10. Calculation of the equilibrium conditions of an individual stringer within the tied zone.

11. Summary of measured stringer angles.

12. Calculation of the energy absorbtion within the tied zone as a function of crack extension and straight-sided double cantilever beam geometry.

13. Basic program which calculates G_I plus G_T as a function of crack length given double cantilever beam specimen geometry and elastic modulus.

14. Basic program which calculates predicted transverse modulus from several theoretical models.

15. Derivation of effective modulus of material under different constraint modes.

16. Basic program which predicts transverse failure strain using Kies strain magnification theory.

17. Basic program which predicts transverse strength from various stress magnification theories.

APPENDIX 1

A Summary of Classical Lamination Theory

Major assumptions implicit within Classical Lamination theory are[4,5]:

(a) Accurate input data for unidirectional composite are available from measurements (or predictions) which are representative of the lamina in the laminate.

(b) No out-of-plane stresses, such as through-thickness or interlaminar shear stresses, exist in the laminate.

(c) The elastic constants are invariant with strain (i.e. linear elasticity). Some scope exists for modelling non-linear elasticity for each lamina in shear. This has been demonstrated to be necessary for accurately predicting the behaviour of angle ply laminates at high strain.

(d) The elastic constants are invariant with temperature. Clearly the matrix dominated moduli (such as the shear and transverse stiffnesses) will be strongly temperature dependent, but it is currently necessary to make the assumption that they are constant in order to predict the magnitudes of thermally generated stresses.

(e) No viscoelastic relaxation. This assumption is linked to assumptions (c) and (d), but emphasises that time dependent deformation or stress decay is neglected.

(f) Thermal expansion coefficients are constant. Many data are available which show that the thermal expansion coefficients are temperature dependent. Therefore when attempting to predict thermal residual stresses it is necessary to choose an average or representative expansion coefficient over the temperature range of concern rather than use a room temperature derived value.

(g) Thin ply constraint effects are neglected. It is well known that by dispersing low strain to failure phases within higher strain to failure phases the failure strain of the former can be increased. For example, the transverse cracking strain in 0°/90° laminates can be increased if thin transverse 90° plies are dispersed among thin axial 0° plies. This is a phenomenon which is only adequately explicable through models which consider the energetics of the fracture process and is therefore not amenable to a simple stress analysis approach such as Classical Lamination Theory. This effect is explained in greater detail in Chapter 2.

(h) No stress concentrations in undamaged plies result from cracking in adjacent damaged plies.

(i) Modulus in appropriate directions in cracked plies falls to zero. This is a conservative estimation since stress transfer by shear is possible into segments of cracked plies. For example as transverse cracking develops in a 0°/90° laminate the effective transverse modulus of the transverse plies, does not fall instantly to zero, but decreases as the crack density increases. Some workers refer to this effect as 'overexertion' [7].

The general form of classical lamination theory is capable of calculating out-of-plane stiffnesses and deformations, such as bending and twisting in thin laminates. However, the following summary, in matrix notation, sets out stage by stage the analysis as it applies only to in-plane properties and effects.

1. The Lamina

The basic building block of the laminate analysis is the lamina, or unidirectional ply for which the complete elastic, thermal expansion and strength data must be accurately known for each lamina type. Data required are:

E_{11} = Longitudinal modulus

E_{22} = Transverse modulus

ν_{12} = Major Poisson's ratio (ν_{21} = minor Poisson's ratio)

G_{12} = Shear modulus

α_1 = Longitudinal thermal expansion coefficient

α_2 = Transverse thermal expansion coefficient

$\sigma_{1T\ ult}$ = Longitudinal tensile strength

$\sigma_{1C\ ult}$ = Longitudinal compressive strength

$\sigma_{2T\ ult}$ = Transverse tensile strength

$\sigma_{2C\ ult}$ = Transverse compressive strength

$\tau_{12\ ult}$ = Shear strength.

Hookes Law in two dimensions for a specially orthotropic lamina can be written:

$$\begin{bmatrix} \sigma_1 \\ \sigma_2 \\ \tau_{12} \end{bmatrix} = \begin{bmatrix} Q_{11} & Q_{12} & 0 \\ Q_{12} & Q_{22} & 0 \\ 0 & 0 & Q_{66} \end{bmatrix} \begin{bmatrix} \epsilon_1 \\ \epsilon_2 \\ \gamma_{12} \end{bmatrix}$$

↑ Longitudinal, transverse and shear stresses.

↑ Longitudinal, tranverse and shear strains.

where $Q_{11} = \dfrac{E_{11}}{1 - \nu_{12}\,\nu_{21}}$

$Q_{12} = \dfrac{\nu_{12}E_{22}}{1 - \nu_{12}\,\nu_{21}}$

$Q_{22} = \dfrac{E_{22}}{1 - \nu_{12}\,\nu_{21}}$

$Q_{66} = G_{12}$.

2. Transform Lamina Stiffnesses

The stiffness matrix of each lamina (the K^{th} lamina) is transformed to the direction (θ_K) in which it will lay in the laminate.

$$\begin{bmatrix} Q_{11} & Q_{12} & 0 \\ Q_{12} & Q_{22} & 0 \\ 0 & 0 & Q_{66} \end{bmatrix}_K \xrightarrow{\theta_K} \begin{bmatrix} \bar{Q}_{11} & \bar{Q}_{12} & \bar{Q}_{16} \\ \bar{Q}_{12} & \bar{Q}_{22} & \bar{Q}_{26} \\ \bar{Q}_{16} & \bar{Q}_{26} & \bar{Q}_{66} \end{bmatrix}_K \equiv \left[\bar{Q}_{ij}\right]_K$$

where:

$$\bar{Q}_{11} = Q_{11}\cos^4\theta_K + 2(Q_{12} + 2Q_{66})\sin^2\theta_K\cos^2\theta_K + Q_{22}\sin^4\theta_K$$

$$\bar{Q}_{12} = (Q_{11} + Q_{22} - 4Q_{66})\sin^2\theta_K\cos^2\theta_K + Q_{12}(\sin^4\theta_K + \cos^4\theta_K)$$

$$\bar{Q}_{22} = Q_{11}\sin^4\theta_K + 2(Q_{12} + 2Q_{66})\sin^2\theta_K\cos^2\theta_K + Q_{22}\cos^2\theta_K$$

$$\bar{Q}_{16} = (Q_{11} - Q_{12} - 2Q_{66})\sin\theta_K\cos^3\theta_K + (Q_{12} - Q_{22} + 2Q_{66})\sin^3\theta_K\cos\theta_K$$

$$\bar{Q}_{26} = (Q_{11} - Q_{12} - 2Q_{66})\sin^3\theta_K\cos\theta_K + (Q_{12} - Q_{22} + 2Q_{66})\sin\theta_K\cos^3\theta_K$$

$$\bar{Q}_{66} = (Q_{11} + Q_{22} - 2Q_{12} - 2Q_{66})\sin^2\theta_K\cos^2\theta_K + Q_{66}(\sin^4\theta_K + \cos^4\theta_K)$$

3. Sum Transformed Lamina Stiffnesses

The stiffness matrices for each ply relevant to the laminate direction are averaged, taking into account the relative thicknesses of each lamina (t_K/t_{total}).

$$\left[\bar{Q}_{ij}\right]_{laminate} = \sum_{K=1}^{K=N} \left[\bar{Q}_{ij}\right]_K \cdot \frac{t_k}{t_{total}}$$

where N = total number of laminae.

$$\begin{bmatrix} \sigma_x \\ \sigma_y \\ \tau_{xy} \end{bmatrix} = \left[Q_{ij}\right]_{\text{laminate}} \begin{bmatrix} \epsilon_x \\ \epsilon_y \\ \gamma_{xy} \end{bmatrix}$$

↑ Laminate stress system.

↑ Laminate strain system.

In general the subscripts x and y refers to the laminate coordinate system while the subscripts 1 and 2 refer to the lamina coordinate system.

4. Transform Lamina Expansion Coefficients

The expansion coefficients for each lamina are transformed into the direction in which they lay in the laminate.

$$\begin{bmatrix} \alpha_x \\ \alpha_y \\ \alpha_{xy} \end{bmatrix}_K = \left[T\right]_K \begin{bmatrix} \alpha_1 \\ \alpha_2 \\ 0 \end{bmatrix}$$

where $$\left[T\right]_K = \begin{bmatrix} \cos^2\theta_K & \sin^2\theta_K & -\tfrac{1}{2}\sin 2\theta_K \\ \sin^2\theta_K & \cos^2\theta_K & \tfrac{1}{2}\sin 2\theta_K \\ \sin 2\theta_K & -\sin 2\theta_K & \cos 2\theta_K \end{bmatrix}$$

5. Calculate Constrained Thermal Stresses

The whole laminate is notionally constrained while a notional temperature change is imposed and the thermal stresses which result in each lamina are summed.

$$\begin{bmatrix} \sigma_x \\ \sigma_y \\ \tau_{xy} \end{bmatrix}_{\substack{\text{constrained} \\ \text{thermal} \\ \text{laminate}}} = \sum_{K=1}^{K=N} \left[\bar{Q}_{ij}\right]_K \begin{bmatrix} \alpha_x \\ \alpha_y \\ \alpha_{xy} \end{bmatrix}_K . \Delta T . \frac{t_k}{t_{total}}$$

where ΔT = temperature change.

6. Calculate Expansion of Laminate

The effective thermal strains of the laminate due to the temperature change are calculated using the notional laminate constrained thermal stresses and the overall laminate stiffness matrix.

$$\begin{bmatrix} \epsilon_x \\ \epsilon_y \\ \gamma_{xy} \end{bmatrix}_{\substack{\text{thermal} \\ \text{laminate}}} = \left[\bar{Q}_{ij}\right]^{-1}_{\text{laminate}} \begin{bmatrix} \sigma_x \\ \sigma_y \\ \tau_{xy} \end{bmatrix}_{\substack{\text{constrained} \\ \text{thermal} \\ \text{laminate}}}$$

↑ Effectively the laminate expansion coefficient x ΔT.

↑ The inverse of the stiffness matrix.

7. Calculate Stresses Arising from Differential Expansions

The thermal strain matrix calculated previously exists in all laminae within the laminate, but it is the difference between the imposed laminate thermal strain and the thermal strain that the individual laminae would take up if unconstrained that results in a real mechanical thermal stress.

$$\begin{bmatrix} \sigma_x \\ \sigma_y \\ \tau_{xy} \end{bmatrix}_K^{thermal} = \left[\bar{Q}_{ij}\right]_K \begin{bmatrix} \epsilon_x - \alpha_x.\Delta T \\ \epsilon_y - \alpha_y.\Delta T \\ \gamma_{xy} \quad \alpha_x.\Delta T \end{bmatrix}_K$$

8. Transform Individual Lamina Stresses

The lamina thermal stresses are transformed from the global laminate direction to the local material direction.

$$\begin{bmatrix} \sigma_1 \\ \sigma_2 \\ \tau_{12} \end{bmatrix}_K^{thermal} = [T]_K^{\sigma} \begin{bmatrix} \sigma_x \\ \sigma_y \\ \tau_{xy} \end{bmatrix}_K$$

$$\text{where } [T]_K^{\sigma} = \begin{bmatrix} \cos^2\theta_K & \sin^2 2\theta_K & \sin 2\theta_K \\ \sin^2\theta_K & \cos^2 2\theta_K & -\sin\ 2\theta_K \\ -\tfrac{1}{2}\sin 2\theta_K & \tfrac{1}{2}\sin 2\theta_K & \cos 2\theta_K \end{bmatrix}$$

9. Apply External Mechanical Stress

The overall laminate strain system resulting from an applied mechanical stress is calculated using the laminate stiffness matrix.

$$\begin{bmatrix} \epsilon_x \\ \epsilon_y \\ \gamma_{xy} \end{bmatrix}_{laminate}^{mechanical} = \left[\bar{Q}_{ij}\right]_{laminate}^{-1} \begin{bmatrix} \sigma_x \\ \sigma_y \\ \tau_{xy} \end{bmatrix}_{laminate}^{mechanical}$$

10. Calculate Lamina Stresses

The overall laminate strain system, which exists equally in all the laminae, is used to calculate the individual laminae stresses via each lamina stiffness matrix.

$$\begin{bmatrix} \sigma_x \\ \sigma_y \\ \tau_{xy} \end{bmatrix}_{K}^{mechanical} = \left[\bar{Q}_{ij}\right]_{K} \begin{bmatrix} \epsilon_x \\ \epsilon_y \\ \gamma_{xy} \end{bmatrix}_{laminate}^{mechanical}$$

11. Transform Lamina Stresses to Material Direction

The mechanical stresses for each lamina are transformed into the lamina material directions.

$$\begin{bmatrix} \sigma_1 \\ \sigma_2 \\ \tau_{12} \end{bmatrix}_{K}^{mechanical} = \left[T\right]_{K}^{\sigma} \begin{bmatrix} \sigma_x \\ \sigma_y \\ \tau_{xy} \end{bmatrix}_{K}^{mechanical}$$

12. Sum the Lamina Mechanical and Thermal Stresses

The stresses which can give rise to damage are the sum of the residual thermal and mechanical stresses for each lamina.

$$\begin{bmatrix} \sigma_1 \\ \sigma_2 \\ \tau_{12} \end{bmatrix}_K = \begin{bmatrix} \sigma_1 \\ \sigma_2 \\ \tau_{12} \end{bmatrix}_K^{\text{thermal}} + \begin{bmatrix} \sigma_1 \\ \sigma_2 \\ \tau_{12} \end{bmatrix}_K^{\text{mechanical}}$$

13. Apply Failure Criterion

The decision as to whether or not a particular lamina will fail under the predicted stress system is made by applying a failure criterion which compares the applied stress system with a function which incorporates the strengths of the lamina. Over twenty failure criteria for unidirectional composites are available in the literature. However, two examples are:

Maximum stress criterion:

$\sigma_1 > \sigma_{1T\ ult}$ - longitudinal tensile failure

$\sigma_1 < \sigma_{1C\ ult}$ - longitudinal compressive failure

$\sigma_2 > \sigma_{2T\ ult}$ - transverse tensile failure

$\sigma_2 < \sigma_{2C\ ult}$ - transverse compressive failure

$\tau_{12} > \tau_{12\ ult}$ - shear failure.

or the

Tsai-Hill criterion (ignoring difference between tensile and compressive strengths):

$$\frac{\sigma_1^2}{\sigma_{1\ ult}^2} - \frac{\sigma_1\sigma_2}{\sigma_{1\ ult}^2} + \frac{\sigma_2^2}{\sigma_{2\ ult}^2} + \frac{\tau_{12}^2}{\tau_{12\ ult}^2} > 1$$

14. Increment Applied Stress to Failure

If none of the laminae has exceeded the failure criterion the applied laminate stress is incrementally increased and stages 9 to 13 repeated.

15. Sequential Damage Process

Once any of the laminae has exceeded the failure criterion the mode of failure for that ply may be assessed. For non-interactive failure criteria such as maximum stress this is straightforward, but for the interactive failure criteria such as Tsai-Hill no indication of failure mode is immediately apparent.

If it is necessary to predict laminate performance after first ply failure a decision is taken as to the amount by which the elastic modulus of the failed ply might be reduced. A conservative estimate is to reduce it to zero. Whether it is the matrix controlled moduli alone which are reduced is a decision which can only be taken if an assessment of the lamina failure mode is possible.

The whole calculation is then repeated from stage 3 by using the modified lamina elastic properties for those plies which have been predicted to have failed. The process is continued until the strain in the laminate is predicted to have become infinite.

An example in which this sequential damage process is demonstrated for 0°/90° cross-ply glass reinforced epoxide laminates is given in Appendix 2.

APPENDIX 2

Predictions of the Sequential Damage Process for 0°/90° Laminates using Classical Lamination Theory

A computer program, written in Basic, and based on the analysis outlined in Appendix 1 has been used to predict the stress levels and modes of damage development under uniaxial tension in two types of 0°/90° symmetrical glass fibre based composite laminates. One composite, designated material A, has mechanical properties typical of a 60% fibre volume fraction E-glass/epoxide unidirectional lamina. Material B is a notional flexibilised material in which all properties apart from the matrix controlled moduli and matrix controlled strain to failure are the same as material A. In material B the transverse moduli has been halved which, with the same transverse strength, gives a doubling of the transverse strain to failure.

The relevant lamina data used as input to the laminate analysis program are:

	Material A	Material B
Longitudinal modulus (GPa)	45	45
Transverse modulus (GPa)	18	9
Shear modulus (GPa)	9	5
Major Poisson's ratio	0.3	0.3
Longitudinal tensile strength (MPa)	1200	1200
Transverse tensile strength (MPa)	40	40
Shear strength (MPa)	80	80
Longitudinal expansion coefficient ($\times 10^{-6}\ ^{\circ}C^{-1}$)	6.3	6.3
Transverse expansion coefficient ($\times 10^{-6}\ ^{\circ}C^{-1}$)	20.5	20.5

Running the laminate analysis program for 0°/90° symmetrical laminates of materials A and B with equal thicknesses of 0° and 90° laminae leads to a predicted stress/strain response, under uniaxial tension, as shown in Figure 1.

For each stress/strain curve there are three failure stress levels. The first failure process is transverse cracking in the 90° laminae. The program then reduces the transverse modulus of these laminae to zero, and because the program assumes load control, a sudden increase in the strain of the laminate occurs. The next failure process predicted is longitudinal splitting in the 0° laminae the stress for which arises because the Poisson contraction which would occur in a free 0° lamina is prevented by the 90° laminae in the laminate. At the lamina level this longitudinal splitting is

identical to transverse cracking except that the stresses which cause it are Poisson generated rather than directly applied. The next, and final, fracture process is longitudinal fibre failure of the 0° laminae.

Tabulated below are the stress and strain levels at which the damage processes described above take place. Included here, but for clarity not drawn on Figure 1, are the failure stress levels for a 0°/90° laminate of material A with the inclusion of thermal stresses. These are predicted to be 15.6 MPa in tension transverse in each lamina, balanced by 15.6 MPa in compression longitudinally in each ply, which arise from a notional reduction in temperature of 100°C after cure.

	Transverse Cracking Stress and Strain	Longitudinal Splitting Stress and Strain	Longitudinal Fibre Fracture Stress and Strain
Material A, 0°/90° laminate	72 MPa, 0.23%	231 MPa, 1.00%	601 MPa, 2.57%
Material A, 0°/90° laminate with thermal stress	44 MPa, 0.14%	125 MPa, 0.54%	603 MPa, 2.57%
Material B, 0°/90° laminate	122 MPa, 0.45%	406 MPa, 1.78%	601 MPa, 2.62%

It is seen in Figure 1 that the material B laminate has a lower modulus than the material A laminate. This is a natural consequence of the reduced contribution that the material B transverse properties make to overall laminate stiffness. For completeness, the 0°/90° laminate initial elastic properties are:

	Material A	Material B
Youngs modulus (in both x and y directions)	31.7 GPa	27.2 GPa
Shear modulus	9.0 GPa	5.0 GPa
Poissons ratio	0.17	0.10
Expansion coefficient (in both x and y directions)	10.8×10^{-6} °C^{-1}	9.1×10^{-6} °C

APPENDIX 3

Derivation of Strain Concentration Factor for an Idealised Square Fibre Array under Simple Tensile Extension using Kies Nomenclature (From Kies, ref 28)

$$\bar{\epsilon}_x = \frac{\partial}{2R + \Delta} = \frac{\partial g + \partial r}{2R + \Delta} \qquad (1)$$

where $\bar{\epsilon}_x$ = overall transverse strain

$\partial g, \partial r$ = deflection in glass and resin respectively

Δ = distance between fibres

R = fibre radius

∂ = overall deflection

∂ is proportional to the relative fraction of phases present and inversely proportional to modulus of phases.

$\therefore$ along a line between the centres of two close fibres $\frac{\partial g}{\partial r} = \frac{2R}{\Delta} \cdot \frac{Er}{Eg}$ (2)

(1) + (2)

$$\bar{\epsilon}_x = \frac{\partial r\left[\frac{2R}{\Delta} \cdot \frac{Er}{Eg}\right] + \partial r}{2R + \Delta}$$

$$\epsilon_r = \frac{\partial r}{\Delta} = \frac{\epsilon_x [2R + \Delta]}{\Delta\left[\frac{2R}{\Delta} \cdot \frac{Er}{Eg} + 1\right]}$$

$\therefore$ strain magnification factor $= \frac{\epsilon_r}{\epsilon_x} = \frac{2R + \Delta}{\Delta\left[\frac{2R}{\Delta} \cdot \frac{Er}{Eg} + 1\right]}$

APPENDIX 4

Derivation of Stress Concentration Factors

Consider the two fibre element below as being split into separate sheets all extended by the same displacement:

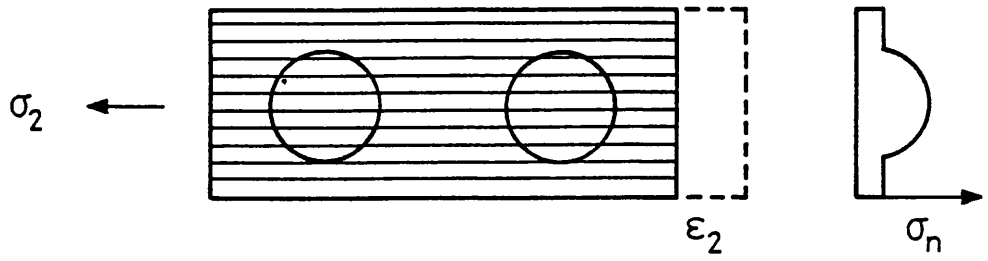

Effective modulus of each sheet (n) will be different since they contain variable proportions of high modulus fibre. Therefore there will be a distribution of stresses (σ_n) whose average is equal to the applied stress (σ_2).

The modulus of each sheet (En) is given by the Reuss modulus:

$$En = \frac{Ef \cdot Em}{Ef(1-Vf) + Em\ Vf} \qquad (1)$$

and the stress within each sheet (σ_n) is given by:

$$\sigma_n = En \cdot \epsilon_2 = En \cdot \frac{\sigma_2}{E_2} \qquad (2)$$

where ϵ_2 is the applied strain (same in each sheet).

The maximum stress (σ_m) is given by the σ_n value along the centre line of the two fibres (i.e. $\sigma_m = \sigma_n$ along centre line)

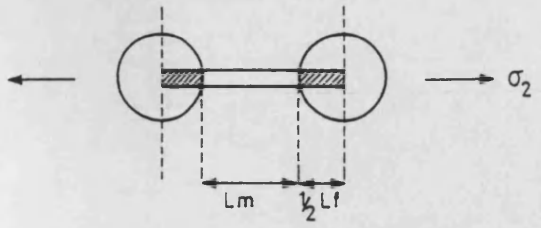

For which equation (1) operates:

$$En = \frac{Ef \cdot Em}{Ef(1-Lf) + Em\ Lf}$$

For the square array:

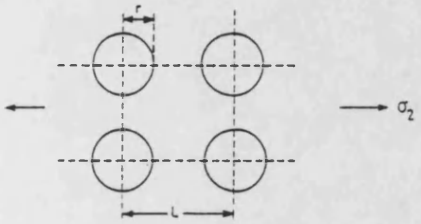

$$Lf = \frac{2r}{L}$$

$$Vf = \frac{\pi r^2}{L^2}$$

$$\therefore L = \left[\frac{\pi r^2}{Vf}\right]^{\frac{1}{2}}$$

$$\therefore Lf = \frac{2}{(\pi/Vf)^{\frac{1}{2}}} \qquad (4)$$

(4) + (3) gives:

$$En = \frac{Ef\ Em}{Ef\left[1-\frac{2}{(\pi/Vf)^{\frac{1}{2}}}\right] + Em\left[\frac{2}{(\pi/Vf)^{\frac{1}{2}}}\right]} \qquad (5)$$

(5) + (2) gives:

$$\sigma_n = \left[\frac{Ef\ Em}{Ef\left[1-\frac{2}{(\pi/Vf)^{\frac{1}{2}}}\right] + Em\ \frac{2}{(\pi/Vf)^{\frac{1}{2}}}}\right] \cdot \frac{\sigma_2}{E_2} \qquad (6)$$

Assuming the Reuss modulus applies to whole element: i.e.

$$E_2 = \frac{Ef\ Em}{Ef(1-Vf) + Em\ Vf} \qquad (7)$$

(6) + (7) eventually gives:

$$\frac{\sigma_n}{\sigma_2} = \frac{Ef - EfVf + EmVf}{Ef + \left[\frac{\pi}{V}\right]^{-\frac{1}{2}} (2Em - 2Ef)} \qquad \underline{Ans}$$

For the hexagonal array:

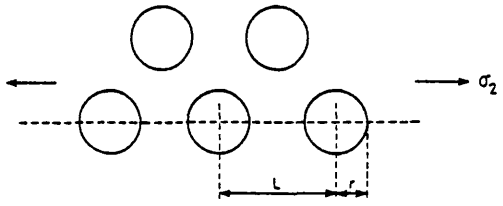

$$Lf = \frac{2r}{L}$$

$$Vf = \frac{\frac{1}{2}\pi r^2}{\frac{\sqrt{3}\,L^2}{4}}$$

$$\therefore L = \left[\frac{2\pi r^2}{\sqrt{3}\,Vf}\right]^{\frac{1}{2}}$$

$$\therefore Lf = 2\left[\frac{2\pi}{\sqrt{3}\,Vf}\right]^{-\frac{1}{2}} \quad (8)$$

(8) + (3) gives:

$$En = \frac{Ef\ Em}{Ef[1-2(^{2\pi}/_{\sqrt{3}\,Vf})^{-\frac{1}{2}}] + Em[2(^{2\pi}/_{\sqrt{3}\,Vf})]^{-\frac{1}{2}}} \qquad (9)$$

(9) + (2) gives:

$$\sigma_n = \frac{Ef\ Em}{Ef[1-2(^{2\pi}/_{\sqrt{3}\,Vf})^{-\frac{1}{2}}] + Em\ (2(^{2\pi}/_{\sqrt{3}\,Vf})]^{-\frac{1}{2}}} \cdot \frac{\sigma_2}{E_2} \qquad (10)$$

(10) + (7) eventually gives:

$$\frac{\sigma_n}{\sigma_2} = \frac{Ef - EfVf + EmVf}{Ef + \left[\frac{2\pi}{\sqrt{3}\,Vf}\right]^{-\frac{1}{2}} (2Em - 2Ef)} \qquad \underline{Ans}$$

APPENDIX 5

Details of the Conventional Rigid Resin and Composite Fabrication Method for Material Used in Initial Test Specimen Development Trials

Resin:	100 parts by weight	MY750 epoxy resin
	87 "	HY917 curing agent
	0.5 "	DY070 accelerator

MY750 is a diglycidyl ether of bisphenol A with an epoxide content of 5.0 - 5.3 equiv/kg and a viscosity at 25°C of 80 - 200 Poise, available from Ciba-Geigy. HY917 is methyl tetrahydrophthalic anhydride and DY 070 is 2 methyl imidiazol both from Ciba-Geigy.

This resin formulation was used to manufacture neat resin plates and composite plates cured by 4 hours at 100°C and 4 hours at 160°C.

Two types of composite plates were manufactured, both void free and with fibre volume fractions of 61% and 69%. The lower volume fraction plates were of the ±½° type while the higher volume fraction plates were of the 0° type.

APPENDIX 6

Details of the Range of Epoxy/Urethane Blends used to Manufacture Neat Resin Plates and ±½° Unidirectional Composite Plates used in the Main Experimental Programme

Epoxy Resin: 100 parts by weight MY778 epoxy resin
32 " HY932 curing agent

MY778 is a diglycidyl ether of bisphenol A containing a reactive diluent with an epoxide content of 5.0 - 5.3 equiv/kg and a viscosity at 25°C of 10 - 14 poise. HY932 is a liquid form of diamino diphenyl methane. Both resin and hardener are available from Ciba-Geigy.

Urethane Rubber

Ready formulated A10 grade 'Monothane' urethane elastomer containing a polyol curing agent.

Blends

In order to eliminate the problems of batch to batch variability single drums of MY778 and A10 'Monothane' were secured and used for all the epoxy/urethane blends.

The same resin mixture and cure schedule was used to manufacture the neat resin plates and composite plates.

Component Proportions (by weight)		
MY778/HY932	A10	
100	0	3 hours @ 70°C + 6 hours @ 135°C
90	10	10 hours @ 70°C + 6 hours @ 135°C
80	20	10 hours @ 70°C + 6 hours @ 135°C
60	40	10 hours @ 70°C + 6 hours @ 135°C
40	60	10 hours @ 70°C + 6 hours @ 135°C
0	100	5 hours @ 70°C + 6 hours @ 135°C

APPENDIX 7

Summary of Strength Test Results for Conventional Rigid Resin (MY750/HY917/DY070) Composite and Neat Resin Specimens

7(i) Transverse tensile strength results from straight-sided ±½° composite coupons.

as-machined edges:

Specimen	Strength (MPa)	Failure Within Gauge-Length
1	58.7	N
2	77.8	N
3	60.6	Y
4	70.5	N
5	57.8	Y
6	71.6	Y
	$\bar{\sigma}$ = 66.2 MPa	S.D. = 8.25 MPa

240 grade (coarse) polished edges:

Specimen	Strength (MPa)	Failure Within Gauge-Length
1	58.0	Y
2	61.7	Y
3	61.9	N
4	64.5	N
5	53.4	N
6	61.3	N
	$\bar{\sigma}$ = 60.1 MPa	S.D. = 3.90 MPa

600 grade (fine) polished edges:

Specimen	Strength (MPa)	Failure Within Gauge-Length
1	66.1	N
2	65.2	Y
3	64.4	N
4	72.8	Y
5	66.5	N
	$\bar{\sigma}$ = 67.0 MPa	S.D. = 3.34 MPa

NB. No significant effect of edge polishing is apparent and so the summary in Section 5.2 contains the average of all the coupon results irrespective of edge condition.

From tests on two straight-sided ±½° transverse composite specimens with strain gauges on each face the average modulus up to 0.3% strain was 14.38 GPa.

7(ii) Transverse tensile strength results from dogbone shaped specimens of 0° and ±½° composite.

±½° material:

Specimen	Strength (MPa)	Failure Within Gauge-Length
1	41.8	Y
2	38.3	N
3	40.3	Y
	$\bar{\sigma}$ = 40.1 MPa	S.D. = 1.76 MPa

0° material:

Specimen	Strength (MPa)	Failure Within Gauge-Length
1	40.2	N
2	34.0	N
	$\bar{\sigma}$ = 37.1 MPa	S.D. = 4.38 MPa

7(iii) Tensile strength results on conventional neat resin dogbones.

all surface polished with 600 grade (fine) paper:

Specimen	Strength (MPa)	Failure Within Gauge-Length
1	69.7	N
2	82.5	Y
3	82.6	Y
4	82.9	Y
5	65.6	N
6	82.7	Y
7	83.1	Y
8	82.8	Y
	———	
	*$\bar{\sigma}$ = 82.8 MPa	S.D. = 0.22 MPa

* In contrast to the calculation of average strengths made previously only those specimens which broke within the gauge-length have been included in the average. This is because only those specimens which failed within the gauge length displayed yielding with a distinct maximum in the load-displacement curve. The average value therefore represents the yield stress.

From two resin dogbone specimens with strain gauges on each face the average modulus up to 1.1% strain was 3.09 GPa.

7(iv) Transverse strength results from three point flexure of 0° and ±½° conventional resin composite.

±½° material:

Specimen	Strength (MPa)	Failure Within Gauge Length
1	91.9	Y
2	66.8	Y
3	72.4	Y
4	93.0	Y
5	70.3	Y
6	86.2	Y
7	54.7	Y
8	59.8	Y
	$\bar{\sigma}$ = 74.4 MPa	S.D. = 14.50 MPa

0° material:

Specimen	Strength (MPa)	Failure Within Gauge Length
1	61.3	Y
2	80.6	Y
3	85.2	Y
4	89.3	Y
5	51.1	Y
6	64.4	Y
7	82.6	Y
8	61.7	Y
9	56.8	Y
	$\bar{\sigma}$ = 70.3 MPa	S.D. = 14.06 MPa

7(v) Transverse strength results from four point flexure of ±½° and 0° conventional resin composite.

±½° material:

Specimen	Strength (MPa)	Failure Within Gauge-Length
1	64.9	Y
2	84.6	Y
3	56.9	Y
4	80.6	Y
5	74.6	Y
6	64.6	Y
7	59.0	Y
8	70.6	Y
	$\bar{\sigma}$ = 69.5 MPa	S.D. = 9.95 MPa

0° material:

Specimen	Strength (MPa)	Failure Within Gauge-Length
1	83.5	Y
2	72.1	Y
3	65.6	Y
4	70.0	Y
5	77.6	Y
6	86.2	Y
7	78.2	Y
8	74.7	Y
9	75.9	Y
	$\bar{\sigma}$ = 76.0 MPa	S.D. = 6.41 MPa

7(vi) Transverse tensile strength results from axially loaded hoop wound tubes.

Specimen	Strength (MPa)	Failure Within Gauge-Length
square ended steel end fixtures	39.0	N
tapered steel end fixtures	35.0	N
tapered resin end fixtures	33.0	N
chopped glass filled tapered resin end fixtures	39.0	N
	$\bar{\sigma}$ = 36.5 MPa	S.D. = 3.00 MPa

7(vii) Transverse strength results from four point flexure of hoop wound tubes.

Specimen	Strength (MPa)	Failure Within Gauge-Length
1	65.5	Y
2	57.7	Y
3	64.6	Y
	$\bar{\sigma}$ = 62.6 MPa	S.D. = 4.26 MPa

APPENDIX 8

JOURNAL OF MATERIALS SCIENCE LETTERS 1 (1982) 321–324

The stability of transverse cracks in fibre composites

D. C. PHILLIPS, G. M. WELLS
Materials Development Division, AERE, Harwell, Oxfordshire, UK

In the design of structures to be manufactured from high-performance fibre composites, great care is taken to ensure that sufficient reinforcement is provided in highly stressed directions to bear the loads. Despite this, failure can, and frequently does, occur through splitting of the composite on planes parallel to the fibres due to interlaminar or intralaminar crack growth. The resistance of a composite to this mode of failure is an important factor in determining the suitability of a particular combination of fibre and matrix for any specific application.

Earlier work has shown that the resistance to crack growth parallel to fibres in a unidirectional composite can increase as the crack grows through the development of a tied zone at the crack tip [1–4]. Fig. 1 shows some typical results obtained for a composite consisting of 60 vol% of aligned carbon fibres in an epoxide resin matrix [2]. These data were obtained through a double cantilever beam (DCB) experiment in which a sharp crack was first introduced by cutting a notch in the beam and then sharpening it with a scalpel. Initially the crack faces were not bridged by fibres but as the crack grew, there developed behind the crack tip a region in which fibres bridged the crack faces and contributed to the toughness. This is shown for a glass–fibre composite in Fig. 2. In general, initial fracture energies G_0 are found to be low, and comparable with that of the resin matrix, but the development of a tied zone increases the toughness through processes such as fibre debonding and pull-out. It would be anticipated that eventually the tied zone would develop to a size characteristic of the degree of misalignment, at which point the toughness would not increase further, as shown in Fig. 3. The rate of increase of toughness with crack length, dG/da, and the final toughness, G_u, are expected to depend on the degree of misalignment, as shown in Fig. 3.

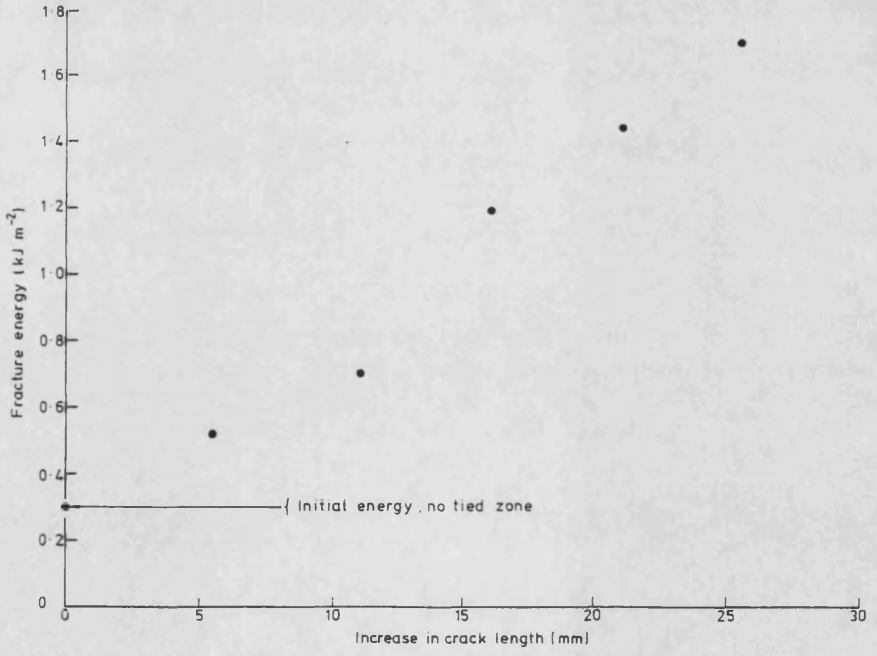

Figure 1 Variation of toughness with crack length for a carbon fibre composite.

0261–8028/82/080321–04$02.98/0

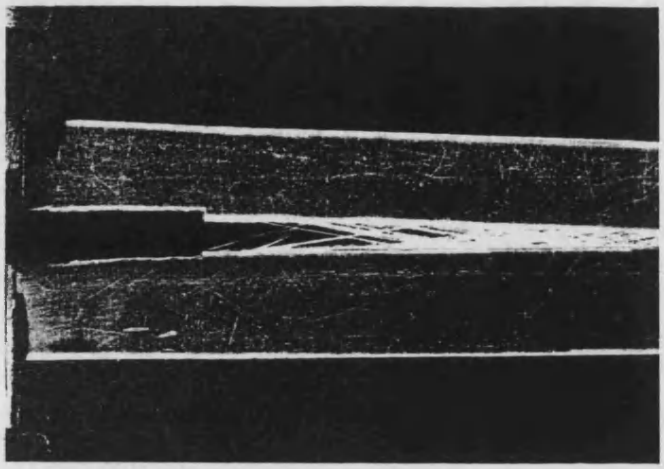

Figure 2 Photograph of fibres bridging the crack faces behind the crack tip in a glass-fibre composite.

Recently there has been an increasing interest in the measurement of fracture energies for interlaminar and intralaminar cracks and in methods of enhancing toughness for these modes of failure through the use of tougher matrices. It is the purpose of this letter to draw attention to the variation of G with a and the implication of this for such energy measurements. It is important that G_0, dG/da and G_u be measured, as average energy values obtained by measuring large increments of crack growth can provide a mistaken optimism about the stability of cracks in a composite.

This can be demonstrated by considering a sharp crack of length $2a$ at the centre of a plate. The stress, σ, necessary for this to grow is

$$\sigma = A\left(\frac{EG}{a}\right)^{1/2} \quad (1)$$

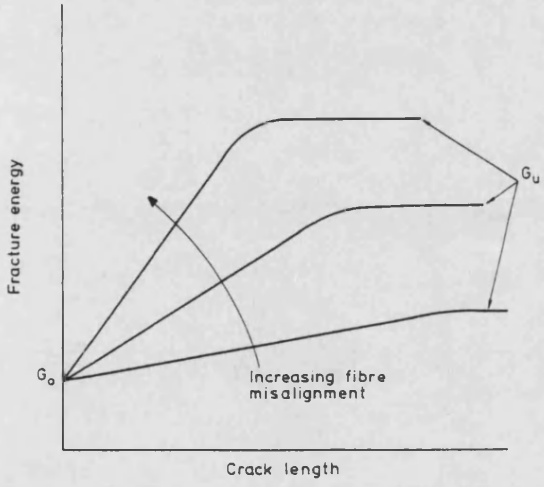

Figure 3 Hypothetical variation of toughness with fibre misorientation.

where A is a geometrical factor, E an elastic constant and G the critical rate of release of strain energy or fracture surface energy. Differentiating Equation 1 gives

$$\frac{d\sigma}{da} = A\bar{E}^{1/2}\left[\frac{1}{2(aG)^{1/2}}\frac{dG}{da} - \frac{1}{2}\left(\frac{G}{a^3}\right)^{1/2}\right] . \quad (2)$$

If $d\sigma/da$ is negative the crack is unstable and will grow spontaneously under decreasing load. If $d\sigma/da$ is positive the crack will not grow unstably but will require increasing stress. For most materials dG/da is zero and cracks are inherently unstable. For a composite however, in which the fracture energy increases with the development of a tied zone, $d\sigma/da$ can be positive, the crack will be stable, and the ultimate load will be determined by the final toughness. From Equation 2 the condition for the transition from stability to instability is

$$\frac{dG}{da} \leqslant \frac{G}{a} . \quad (3)$$

Cracks which are initially less than the size defined by Equation 3 are unstable and will propagate catastrophically at a stress determined by the initial fracture energy G_0. Cracks which are initially larger than the critical size are stable and will only grow as the load increases. Where G is a linear function of a, the crack will grow stably until the tied zone grows to its maximum extent, at which point dG/da becomes zero and the crack becomes unstable at a stress determined by G_u and the sum of the initial crack size and the tied zone length.

This is best understood by considering a numerical example. Consider a crack of initial length a_0

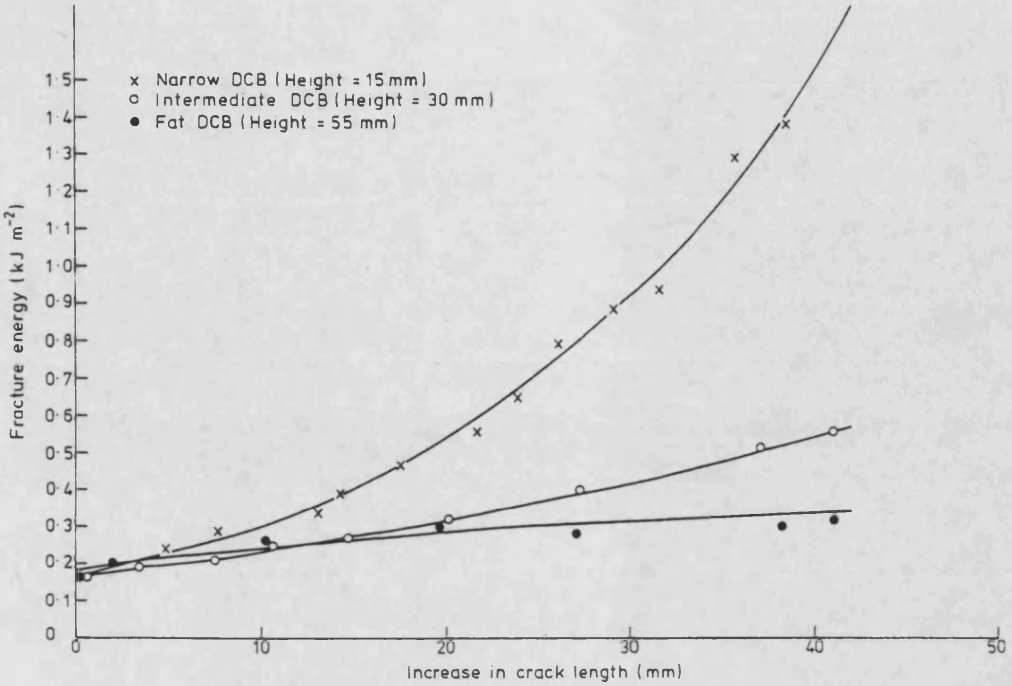

Figure 4 Variation of toughness with crack length for three different glass-fibre composite, double cantilever beams of different heights.

and energy G_0 which begins to grow when the stress reaches $\sigma_0 = AE^{1/2}(G_0/a_0)^{1/2}$. When the crack has grown an increment Δa to a_1, the stress required for further growth is

$$\sigma_1 = AE^{1/2}\left(\frac{G_0 + \Delta a\, dG/da}{a_1}\right)^{1/2}.$$

For the carbon fibre composite, whose data are shown in Fig. 1, $dG/da = 5.2 \times 10^4\ J\,m^{-3}$ and $G_0 = 300\ J\,m^{-2}$. The crack size in which the transition from stability to instability occurs is therefore approximately 6 mm and Table I shows relative values of σ_0 and σ_1 for initial crack sizes smaller and larger than the stability transition size.

In this particular CFRP composite cracks less than 6 mm in size will propagate unstably at a stress determined by the low fracture energy G_0. Since the critical (Griffith) flaw size for transverse fracture is approximately 80 μm

TABLE I

a_0 (mm)	a_0 (mm)	a_1 (mm)	σ_0*	σ_0*
< 6	1	2	547	420
> 6	10	20	173	202

*In SI units × $AE^{1/2}$.

it is clear that for this composite the increase of toughness due to the development of a tied zone is of less relevance than the initial toughness, and that improvements in matrix toughness could increase the transverse strength. In this case therefore an average fracture energy measured over some large crack extension is not relevant to estimating the resistance of the material to small flaws. This is not necessarily true for all composites since where $dG/da > G_0/a_0$ ultimate unstable crack growth will be preceded by stable growth and the ultimate stength will be determined by G_u and the size reached by the crack during its stable growth. In that case increases in matrix toughness which affect only G_0 will have little effect on transverse strength.

The variation of G with increasing crack length depends on both the degree of misalignment of fibres and on the rate of separation of the faces of the crack as the crack tip advances through the matrix. The amount of separation which can occur at some distance behind the crack tip depends on the way the specimen is stressed and its compliance. For example, Fig. 4 shows data obtained from three different DCB experiments on glass–fibre composites. As the specimen height increases the variation of G with a decreases as

the crack-face separation becomes smaller. Strictly the dG/da data used in the above carbon-fibre composite calculation are not the most appropriate, as Equation 1 is more applicable to a plate rather than a DCB, but the stiffness of carbon-fibre composites and the relatively small tied zones of the carbon-fibre DCB experiment suggest that the data are adequate for demonstrating the principle.

These ideas can be extended to interply cracking in laminates and woven materials. Here between the plies there may be resin-rich regions of intrinsically low toughness interspersed between regions where fibres protude into the interlaminar space to intersect the crack plane. A crack growing in a resin-rich area may or may not become unstable, depending on the length that it can grow in the resin-rich zone, and then the value of dG/da in the fibre-filled zone. This can only be determined by detailed experimental examination of specific materials and, in general, fracture energy measurements made over large increments of crack growth do not, by themselves, provide sufficient information.

References

1. G. R. SIDEY and F. J. BRADSHAW, in "International Conference on Carbon Fibres, their Composites and Applications" (Plastics Institute, London, 1971).
2. J. M. SCOTT and D. C. PHILLIPS, *J. Mater. Sci.* 10 (1975) 551.
3. G. MAROM and E. F. T. WHITE, *ibid* 7 (1972) 1299.
4. I. ENGELBERG and G. MAROM, *Fibre Sci. Technol.* 9 (1976) 63.

Received 8 March
and accepted 22 March 1982

APPENDIX 9

Derivation of Geometric Crack Stability Factors

(From A G Atkins and T W Mai, Ref 93)

For a linear elastic system:

$$G = \frac{P^2}{2} \cdot \frac{dC}{dA}$$

where G = fracture toughness

P = crack propagation load

C = compliance = u/P, where u = displacement

A = crack area

$$\therefore \quad P = 2G/\frac{dC}{dA}$$

Recognising that G may change during crack propagation, the variation of G with load P may be obtained by differention:

$$\frac{2}{P}\left[\frac{dP}{dA}\right] = \frac{1}{G}\left[\frac{dG}{dA}\right] - \frac{d^2C}{dA^2} \Big/ \frac{dC}{dA}$$

For stability in a soft testing machine (i.e. load controlled), dx/x > 0 so:

$$\frac{1}{G} \cdot \frac{dG}{dA} \geq \frac{d^2C}{dA^2} \Big/ \frac{dC}{dA} \qquad (1)$$

For stability in a stiff testing machine (i.e. displacement controlled), du/u > 0 and by using:

$$u^2 = 2G \Big/ \frac{d(1/C)}{dA}$$

It can be shown that:

$$\frac{1}{G} \cdot \frac{dG}{dA} \geq \frac{d^2(1/C)}{dA^2} \Big/ \frac{d(1/C)}{dA} \qquad (2)$$

Equations (1) and (2) define the stability conditions under load and displacement control respectively. It is seen that the left hand side of these equations define materials properties while the right hand side define geometric characteristics of the system. The equations may be rewritten as:

$$\frac{1}{G} \cdot \frac{dG}{dA} \geq \frac{nx}{A} \text{ or } \frac{nu}{A}$$

where the right hand side represents the geometric stability factor, and nx and nu are numbers characteristic of the system.

The first and second differentials of C or $^1/C$ are usually easily determined for the more common specimen geometries using strength of materials techniques. Clearly for the geometry to be stable over all crack lengths, with a material which displays zero dG/dA, the nx or nu values must be negative. Values of nx and nu are given below for a selection of different geometries.

Specimen	Displacement Control		Load Control	
	nu	Usual Observation	nx	Usual Observation
Straight-Sided DCB (point loaded)	-4	stable	2	unstable
Straight-Sided DCB (distributed load)	-6	stable	4	unstable
Griffith Crack	1	unstable	1	unstable

It is seen that the stability criterion derived by Phillips and Wells for a Griffith crack agrees with the Atkins and Mai derivation and is the same for displacement or load control.

APPENDIX 10

Calculation of the Equilibrium Condition for Stringers within the Tied Zone

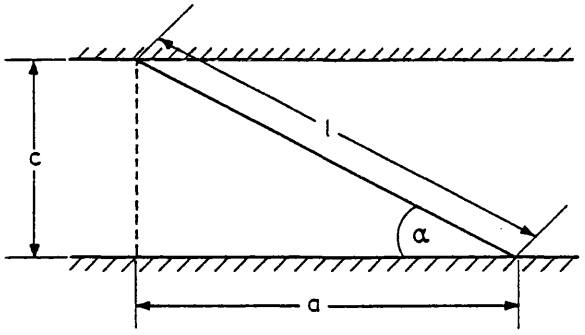

for a single stringer bridging the crack faces:

original length = a

current length = ℓ

$\therefore$ extension = $\ell - A$

$$\text{strain } (\epsilon) = \frac{\ell - a}{a} = \frac{\dfrac{C}{\sin\alpha} - \dfrac{C}{\tan\alpha}}{\dfrac{C}{\tan\alpha}}$$

$$= \frac{1}{\cos\alpha} - 1 \qquad (1)$$

$$\text{Since} \quad E = \frac{\alpha}{\epsilon}, \; \sigma = E\left[\frac{1}{\cos\alpha} - 1\right] \qquad (2)$$

Note:

1. The strain in the stringer depends only on the stringer angle.

2. The strain (and therefore strain energy) is reduced by a decreased stringer angle. However this increases the fracture surface area between the stringer and crack face. There is therefore a balance between elastic and surface energies.

For a single stringer:

$$\frac{U_e}{A\ell} = \tfrac{1}{2}\sigma\epsilon \qquad (3)$$

where U_e = elastic energy in stringer

A = stringer cross sectional area

ℓ = stringer length

Substituting (1) and (2) into (3)

$$\frac{U_e}{A\ell} = \tfrac{1}{2}E\left[\frac{1}{\cos\alpha} - 1\right]\left[\frac{1}{\cos\alpha} - 1\right]$$

and since $\ell = \dfrac{C}{\sin\alpha}$

$$U_e = \tfrac{1}{2}A\frac{C}{\sin\alpha} \cdot E\left[\frac{1}{\cos\alpha} - 1\right]\left[\frac{1}{\cos\alpha} - 1\right] \qquad (4)$$

If U_s = surface energy created by single stringer

$$U_s = G_s ab = G_s b\frac{C}{\tan\alpha} \simeq \frac{Gbc}{\sin\alpha} \quad \text{for small angles} \qquad (5)$$

where G_s = fracture surface energy of resin or fibre/resin interface

b = stringer width

Total energy associated with stringer $(U) = U_e + U_s$

$\therefore$ from (4) and (5)

$$U = \tfrac{1}{2}A\frac{C}{\sin\alpha}E\left[\frac{1}{\cos\alpha} - 1\right]\left[\frac{1}{\cos\alpha} - 1\right] + \frac{G_s bc}{\sin\alpha}$$

At equilibrium $\frac{dU}{d\alpha} = 0$

$$\frac{dU}{d\alpha} = \frac{1}{\sin\alpha}\left(CEA\sec^2\alpha\tan\alpha - CEA\sec\alpha\tan\alpha\right)$$

$$-\left[\frac{CEA}{2\cos^2\alpha} - \frac{CEA}{\cos\alpha} + \frac{CEA}{2} + G_s bC\right] \cdot \operatorname{cosec}\alpha\cot\alpha$$

$$= 0.$$

$$\therefore \quad 0 = \frac{CEA\tan\alpha}{\cos^2\alpha\sin\alpha} - \frac{CEA\tan\alpha}{\cos\alpha\sin\alpha} - \frac{CEA}{2\cos^2\alpha\tan\alpha\sin\alpha}$$

$$+ \frac{CEA}{\cos\alpha\tan\alpha\sin\alpha} - \frac{CEA}{2\tan\alpha\sin\alpha} - \frac{G_s bC}{\tan\alpha\sin\alpha}$$

Note: C goes out. $\therefore$ stringer angle independent of crack opening.

$$0 = \frac{EA}{\cos^3\alpha} - \frac{EA}{\cos^2\alpha} - \frac{EA}{2\cos\alpha\sin^2\alpha} + \frac{EA}{\sin^2\alpha}$$

$$- \frac{EA\cos\alpha}{2\sin^2\alpha} - \frac{G_s b\cos\alpha}{\sin^2\alpha}$$

$$\frac{G_s b}{EA} = \frac{\sin^2\alpha}{\cos^4\alpha} - \frac{\sin^2\alpha}{\cos^3\alpha} - \frac{1}{2\cos^2\alpha} + \frac{1}{\cos\alpha} - \tfrac{1}{2}$$

APPENDIX 11

Stringer Angle Measurements

Photograph	Crack Opening (mm)	Stringer Approx. Apparent Width (μm)	Stringer Angle
1	0.88	27	14°
		15	8°
2	0.76	15	8°
		27	10°
3	0.57	68	12°
		73	12°
4	0.39	24	13°
		49	12°
		68	11°
5	0.36	73	11°
		15	12°
6	0.18	39	13°
7	0.11	29	15°
		15	9°
		15	9°

Stringer widths of 15μm refer to individual fibres.

APPENDIX 12

Calculation of Change of Fracture Toughness with Crack Growth Due to Effect of Tied Zone

Each arm of a straight sided Double Cantilever Beam can be considered as an encastered beam opened by end loading and closed by a distributed loading due to the tied zone.

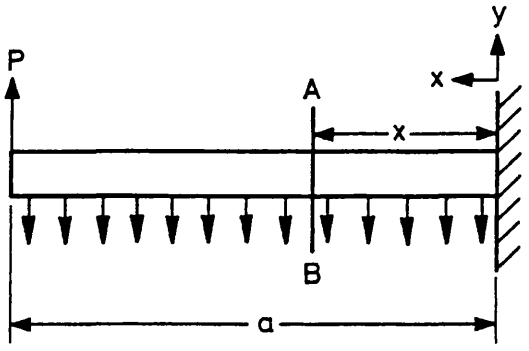

Bending moment at Section AB = M

$$M = P(a-x) - q(a-x) \cdot \tfrac{1}{2}(a-x)$$

where q = distributed load/unit length.

$$\therefore \quad M = P(a-x) - \frac{q}{2}(a^2 + x^2 - 2xa)$$

Now $$EI \cdot \frac{d^2y}{dx^2} = -M \qquad \text{(ref 106)}$$

$$= \frac{qa^2}{2} + \frac{qx^2}{2} - qxa - Pa + Px$$

where y = beam deflection (+ ve downwards)

E = elastic modulus

and I = moment of inertia

1st Integration

$$EI\frac{dy}{dx} = \frac{qa^2x}{2} + \frac{qx^3}{6} - \frac{qx^2a}{2} - Pax + \frac{Px^2}{2} + A$$

Boundary Condition:

$$\frac{dy}{dx} = 0 \quad \text{at} \quad x = 0$$

$$\therefore \quad A = 0$$

2nd Integration

$$EI \,.\, y = \frac{qa^2x^2}{4} + \frac{qx^4}{24} - \frac{qax^3}{6} - \frac{Pax^2}{2} + \frac{Px^3}{6} + B$$

Boundary Condition:

$$y = 0 \quad \text{at} \quad x = 0$$

$$\therefore \quad B = 0$$

Considering deflection of the arm of the DCB from the mid-plane, y as + ve upwards.

$$\therefore \quad EIy = \frac{qax^3}{6} + \frac{Pax^2}{2} - \frac{Px^3}{6} - \frac{qa^2x^2}{4} - \frac{qx^4}{24}$$

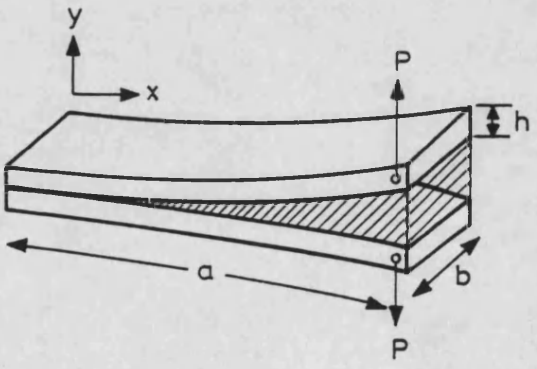

Force per unit area, $F = q/b$

$$\therefore \quad y = \frac{12}{Ebh^3}\left[\frac{Fbax^3}{6} + \frac{Pax^2}{2} - \frac{Px^3}{6} - \frac{Fba^2x^2}{4} - \frac{Fbx^4}{24}\right] \quad (1)$$

$$\text{as} \quad I = \frac{bh^3}{12} \qquad \text{(ref 106)}$$

The energy, E', expended in creating the half zone above the mid-plane is given by:

$$E' = Fb \int_{x=o}^{x=a} y \, . \, dx$$

$$= Fb \int_{x=o}^{x=a} \frac{12}{Ebh^3}\left[\frac{Fbax^3}{6} + \frac{Pax^2}{2} - \frac{Px^3}{6} - \frac{Fba^2x^2}{4} - \frac{Fbx^4}{24}\right] dx$$

$$= \frac{12F}{Eh^3}\left[\frac{Fba^5}{24} + \frac{Pa^4}{6} - \frac{Pa^4}{24} - \frac{Fba^5}{12} - \frac{Fba^5}{120}\right]$$

$$= \frac{12F}{Eh^3}\left[\frac{Pa^4}{8} - \frac{Fba^5}{20}\right]$$

Total energy, E, in tied zone = 2E'

$$\therefore \quad E = \frac{24F}{Eh^3}\left[\frac{Pa^4}{8} - \frac{Fba^5}{20}\right]$$

Now, fracture toughness associated with tied zone, G_T is the change in energy with crack growth.

$$\text{i.e.} \qquad G_T = \frac{dE}{dA} = \frac{1}{B} \cdot \frac{dE}{da} = \frac{12F}{Ebh^3}\left[Pa^3 - \frac{Fba^4}{2}\right] \qquad (2)$$

$$\text{Now} \qquad G_{total} = \frac{P^2}{2b} \cdot \frac{dc}{da} = G_I + G_T \qquad \text{(ref 89)}$$

Where G_I = initial fracture toughness, and $c = \frac{d}{p}$

where d = deflection

Now, $d = 2\,y_{max}$, which from eq. (1) gives:

$$c = \frac{24}{PEbh^3}\left[\frac{Pa^3}{3} - \frac{Fba^4}{8}\right] \quad \text{since y is max at } x = a$$

$$\therefore \qquad \frac{dc}{da} = \frac{24}{PEBh^3}\left[Pa^2 - \frac{Fba^3}{2}\right]$$

$$\therefore \qquad G_I + G_T = \frac{P^2}{2b} \cdot \frac{24}{PEbh^3}\left[Pa^2 - \frac{Fba^3}{2}\right] \qquad (3)$$

Now, from (2)

$$G_T = \frac{12F}{Ebh^3}\left[Pa^3 - \frac{Fba^4}{2}\right]$$

$$\therefore \quad P = \frac{G_T Ebh^3}{12Fa^3} + \frac{Fba}{2} \qquad (4)$$

Substituting (4) → (3)

$$G_I + G_T = \frac{12a^2}{Eb^2h^3}\left[\frac{G_T Ebh^3}{12Fa^3} + \frac{Fba}{2}\right]^2$$

$$- \frac{6Fa^3}{Ebh^3}\left[\frac{G_T Ebh^3}{12Fa^3} + \frac{Fba}{2}\right]$$

$$= \frac{12a^2}{Eb^2h^3}\left[\frac{G_T^2E^2b^2h^6}{144F^2a^6} + \frac{FbaG_T Ebh^3}{12Fa^3} + \frac{F^2b^2a^2}{4}\right]$$

$$- \frac{G_T}{2} - \frac{3F^2a^4}{Eh^3}$$

$$\therefore \quad G_I + G_T = \frac{G_T^2Eh^3}{12F^2a^4} + G_T + \frac{3F^2a^4}{Eh^3} - \frac{G_T}{2} - \frac{3F^2a^4}{Eh^3}$$

$$= \frac{G_T^2\, Eh^3}{12F^2a^4} + \frac{G_T}{2}$$

$$\therefore \quad 0 = \frac{G_T^2\, Eh^3}{12F^2a^4} - \frac{G_T}{2} - G_I$$

$$\therefore \quad 0 = G_T^2 - \left[\frac{6F^2a^4}{Eh^3}\right] \cdot G_T - \frac{12G_IF^2a^4}{Eh^3}$$

Using $x = \dfrac{-b \pm (b^2 - 4ac)^{\frac{1}{2}}}{2a}$ gives:

$$G_T = \frac{\dfrac{6F^2a^4}{Eh^3} \pm \left[\left[\dfrac{6F^2a^4}{Eh^3}\right]^2 + \dfrac{48G_IF^2a^4}{Eh^3}\right]^{\frac{1}{2}}}{2}$$

The short program in Basic given in Appendix 13, based on the above equation, shows that, when using realistic values of the parameters, G_T increases with a only if the + ve solution to the quadratic is taken.

$$G_{TOTAL} = G_I + G_T$$

$$\therefore \quad G_{TOTAL} = G_I + \tfrac{1}{2}\left[\frac{6F^2a^4}{Eh^3} + \left[\left[\frac{6F^2a^4}{Eh^3}\right]^2 + \frac{48G_IF^2a^4}{Eh^3}\right]^{\frac{1}{2}}\right]$$

In Figure 95 experimental results of G_{TOTAL} versus a for three different beam heights, h, are compared with predictions using the above equation for which E = 50 GPa and F = 1.5 MPa have been assumed.

APPENDIX 13

Basic Program Which Uses the Equation Derived in Appendix 12 to Predict the Change in Toughness with Crack Growth for a Straight-Sided DCB

```
 100 PRINT"□"
 110 PRINT"THIS PROGRAM CALCULATES"
 120 PRINT"THE PREDICTED TOUGHNESS INCREASE"
 130 PRINT"WITH CRACK GROWTH FOR DCB'S"
 140 PRINT:PRINT"INPUT SOME MATERIALS DATA"
 150 PRINT"MODULUS (GPA)"
 160 INPUT E :E=E*1E9
 170 PRINT"BEAM HALF HEIGHT (MM)"
 180 INPUT H :H=H*1E-3
 190 PRINT"TIED ZONE CLOSING PRESSURE (MPA)"
 200 INPUT F
 201 F=F*1E6
 210 PRINT"INITIAL TOUGHNESS (J/M↑2)"
 220 INPUT GI
 230 PRINT"LOOK AT CRACK LENGTHS ,FROM TO (MM)"
 240 INPUT A1,A2
 250 A1=A1*1E-3:A2=A2*1E-3
 260 PRINT"IN STEPS OF (MM)"
 270 INPUTSA
 280 SA=SA*1E-3
 290 PRINT:PRINT"ROUTE ONE"
 291 PRINT"A (MM)      GI+GT (J/M↑2)"
 300 REM
 310 REM
 320 FOR A=A1TOA2 STEP SA
 330 XX=(F↑2*A↑4)/(E*H↑3)
 340 GT=(6*XX+((6*XX)↑2+48*GI*XX)↑0.5)/2
 370 PRINT(A*1E3),(GT+GI)
 380 NEXT
 390 PRINT:PRINT"PRESS SPACE BAR"
 391 GET G$: IF G$="" THEN 391
 400 PRINT:PRINT"ROUTE TWO"
 401 PRINT"A (MM)      GI+GT (J/M↑2)"
 430 FOR A=A1TOA2 STEP SA
 440 XX=(F↑2*A↑4)/(E*H↑3)
 450 GT=(6*XX-((6*XX)↑2+48*GI*XX)↑0.5)/2
 480 PRINT(A*1E3),(GT+GI)
 490 NEXT
 500 PRINT:PRINT"PRESS SPACE BAR"
 510 G$=""
 520 GET G$: IF G$="" THEN 520
 530 G$=""
 540 PRINT"CHANGE RANGE OF A OR RESTART (1 OR 2)"
 550 INPUTG
 560 IF G=1 THEN230
 570 GOTO 100
READY.
```

APPENDIX 14

Basic Program Which Calculates Predicted Transverse Modulus from Several Theoretical Models Given Component Materials Data

```
100 PRINT"□"
110 PRINT"TRANSVERSE MODULUS PREDICTION"
120 PRINT"REUSS,EKVALL,LONG POISS,ALLRED,HASHIN"
121 PRINT"GRESZCZUK,HALPIN-TSAI AND SPENCER"
130 PRINT:PRINT"INPUT SOME DATA"
140 PRINT"FIBRE VOLUME FRACTION (%)"
150 INPUT VF
160 VF=VF/100
170 PRINT"MATRIX MODULUS (PA)"
180 INPUT EM
190 PRINT"MATRIX POISSONS RATIO"
200 INPUT PM
210 PRINT"ASSUMES FIBRE MODULUS=76 (GPA)
220 PRINT"FIBRE POISSONS RATIO=0.2"
230 EF=76E9
240 PF=0.2
250 KF=EF/(3*(1-2*PF))
260 PRINT"FIBRE BULK MODULUS= ";KF
270 GF=EF/(2*(1+PF))
280 PRINT"FIBRE SHEAR MODULUS= ";GF
290 VM=(1-VF)
300 E1=VF*EF+VM*EM
310 P1=PF*VF+PM*VM
320 PRINT"COMPOSITE MODULUS= ";E1
330 PRINT"COMPOSITE POISSONS RATIO= ";P1
340 GM=EM/(2*(1+PM))
350 KM=EM/(3*(1-2*PM))
360 PRINT"MATRIX BULK MODULUS= ";KM
370 PRINT"MATRIX SHEAR MODULUS= ";GM
375 PRINT
376 PRINT
380 REM
390 REM*****REUSS********
400 E2=(EF*EM)/(VF*EM+VM*EF)
410 PRINT"REUSS MODULUS= ";E2
420 PRINT
430 REM
440 REM*****LONG' POISS' CONSTRAINT
450 ED=EM/(1-PM↑2)
460 E2=(EF*ED)/(VF*ED+VM*EF)
470 PRINT"LONG' POISS' CON' MOD= ";E2
480 REM
490 REM*****EKVALL*********
500 PRINT
510 ED=EM/(1-2*PM↑2)
520 E2=(EF*ED)/(VF*ED+VM*EF*(1-PM↑2))
530 PRINT"EKVALL MODULUS= ";E2
540 PRINT
550 REM*****ALLRED*********
560 ED=EM/(2*(1+PM)*(1-2*PM))
570 E2=(EF*ED)/(VF*ED+VM*EF*(1-PM↑2))
575 PRINT"ALLRED MODULUS= ";E2
580 PRINT
590 REM
600 REM******HASHIN********
610 NG=(3-4*PM+GM/GF)/(4*(1-PM))
620 NK=(1+GM/KF)/(2*(1-PM))
```

```
 630 GT=(VF/GF+NG*VM/GM)/(VF+NG*VM)
 640 GT=1/GT
 650 KT=(VF/KF+NK*VM/KM)/(VF+NK*VM)
 660 KT=1/KT
 670 M=(1+4*KT*P1)/E1
 680 E2=(4*KT*GT)/(KT+M*GT)
 690 PRINT"HASHIN MODULUS= ";E2
 700 PRINT
 710 REM
 720 REM******GRESZCZUK*******
 730 BB=(VF/3.1416)↑0.5
 740 ED=EM/(1-2*PM↑2)
 750 XX=(2*BB*(1-2*BB))/(ED*EF)
 760 YY=(EF-ED)↑2-(PM*EF-PF*ED)↑2
 770 E0=(ED+2*BB*(EF-ED))/(1+XX*YY)
 780 E2=E0*BB+ED*(1-BB)
 790 PRINT"GRESZCZUK MODULUS= ";E2
 800 PRINT
 810 REM*********HALPIN-TSAI*******
 820 EE=2:REM EPSILON VALUE
 830 XX=EM*(EF+EE*EM+EE*(EF-EM)*VF)
 840 YY=EF+EE*EM-VF*(EF-EM)
 850 E2=XX/YY
 860 PRINT"HALPIN-TSAI MODULUS= ";E2
 870 PRINT
 880 REM*********SPENCER***********
 890 REM WITH VARIABLE PACKING ARRAY
 900 GG=((1.8-0.75*VF)*VF)↑(-0.5)
 910 K=1-EM/EF
 920 TT=ATN(((GG+K)/(GG-K))↑0.5)
 930 IT=2*GG/((GG↑2-K↑2)↑0.5)
 940 JT=(GG-1)/GG
 950 AL=JT+1/K*(IT*TT-3.1416/2)
 960 E2=AL*EM
 970 PRINT"SPENCER MODULUS= ";E2
 980 PRINT
1000 PRINT"PRESS SPACE BAR"
1010 GET G$:IF G$="" THEN 1010
1020 GOTO100
READY.
```

APPENDIX 15

Derivation Of The Effective Moduli Of A Matrix In A Composite Under Differing Degrees Of Constraint By The Fibres

Hookes law for a 3-dimensional Cartesian coordinate system[108]:

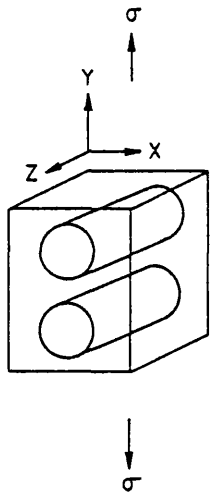

$$\epsilon_y = \frac{1}{E}\left[\sigma_y - \nu\,(\sigma_x + \sigma_z)\right] \qquad (1)$$

$$\epsilon_y = \frac{1}{E}\left[\sigma_x - \nu\,(\sigma_y + \sigma_z)\right] \qquad (2)$$

$$\epsilon_z = \frac{1}{E}\left[\sigma_z - \nu\,(\sigma_x + \sigma_y)\right] \qquad (3)$$

CASE A

Boundary conditions $\sigma_x = 0$ (4)

$\epsilon_z = 0$ (5)

i.e. Fibres total constrain the matrix in the z direction.

Subs (4) → (1)

$$\epsilon_y = \frac{1}{E}\left[\sigma_y - \nu\sigma_z\right] \qquad (6)$$

Subs (5) → (3)

$$\frac{1}{E}\left[\sigma_z - \nu\sigma_y\right] = 0$$

$$\therefore \quad \sigma_z = \nu\sigma_y \tag{7}$$

Subs (7) → (6)

$$\frac{\sigma_y}{\epsilon_y} = E' = \frac{E}{1-\nu^2}$$

This is the effective modulus used in the longitudinal Poisson's constraint model.

CASE B

Boundary conditions $\epsilon_x = 0$ (8)

$\epsilon_z = 0$ (9)

i.e. Fibres (lying in the z direction) totally constrain the matrix in the z direction and also in the x direction. This might be possible at the junction of two closely approaching fibres.

Subs (8) → (2)

$$\frac{1}{E}\left[\sigma_x - \nu\,(\sigma_y + \sigma_z)\right] = 0$$

$$\therefore \quad \sigma_x = \nu\,(\sigma_y + \sigma_z) \tag{10}$$

Subs (9) → (3)

$$\frac{1}{E}\left[\sigma_z - \nu\,(\sigma_x + \sigma_y)\right] = 0$$

$$\therefore \quad \sigma_z = \nu \ (\sigma_x + \sigma_y) \qquad (11)$$

$$\therefore \quad \sigma_y = \frac{\sigma_z - \nu\sigma_x}{\nu} \qquad (12)$$

Subs (12) → (10)

$$\sigma_x = \nu \left[\frac{\sigma_z - \nu\sigma_x}{\nu} + \sigma_z \right]$$

$$\therefore \quad \sigma_x + \nu\,\sigma_x = \sigma_z + \nu\sigma_z$$

$$\therefore \quad \sigma_x = \sigma_z \qquad (13)$$

Subs (13) → (11)

$$\sigma_x = \nu \ (\sigma_y + \sigma_x)$$

$$\sigma_x = \left[\frac{\nu}{1 - \nu} \right] \sigma_y \qquad (14)$$

Subs (13) and (14) → (1)

$$\epsilon_y = \frac{1}{E} \left[\sigma_y - \nu \left[\sigma_y \left[\frac{\nu}{1 - \nu} \right] + \left[\frac{\nu}{1 - \nu} \right] \sigma_y \right] \right]$$

$$\therefore \ \epsilon_y E = \sigma_y - \sigma_y \ \frac{2\nu^2}{1 - \nu} = \sigma_y \left[1 - \frac{2\nu^2}{1 - \nu} \right]$$

$$\therefore \quad \frac{\sigma_y}{\epsilon_y} = E'' = \frac{E}{1 - \frac{2\nu^2}{1 - \nu}}$$

This implies that as $\nu \rightarrow 0.5$ the effective modulus $\rightarrow \infty$. In reality, the effective modulus could only tend toward the fibre modulus.

APPENDIX 16

Basic Program Which Calculates Predicted Transverse Failure Strain Using Kies Strain Magnification Theory

```
 100 PRINT"□"
 110 PRINT"KIES STRAIN MAGNIFICATION"
 130 PRINT:PRINT"INPUT SOME DATA"
 140 PRINT"FIBRE VOLUME FRACTION (%)"
 150 INPUT VF
 160 VF=VF/100
 170 PRINT"MATRIX MODULUS (PA)"
 180 INPUT EM
 210 PRINT"ASSUMES FIBRE MODULUS=76 (GPA)
 230 EF=76E9
 240 PRINT"MATRIX FAILURE STRAIN (%)"
 250 INPUT FS
 260 PRINT
 270 PRINT"SQUARE ARRAY"
 280 XX=(π/VF)↑0.5
 290 YY= 2*EM/EF-2+(π/VF)↑0.5
 300 SM=XX/YY
 310 PRINT"STRAIN MAG' FACTOR= ";SM
 325 E2=FS/SM
 330 PRINT"PREDICTS FAILURE STRAIN= ";E2;" %"
 340 PRINT
 350 PRINT"HEXAGONAL ARRAY"
 355 R3=3↑0.5
 360 XX=(2*π/(R3*VF))↑0.5
 370 YY=2*EM/EF-2+(2*π/(R3*VF))↑0.5
 380 SM=XX/YY
 390 PRINT"STRAIN MAG' FACTOR= ";SM
 410 E2=FS/SM
 420 PRINT"PREDICTS FAILURE STRAIN= ";E2;" %"
 430 PRINT
 440 PRINT"PRESS SPACE BAR"
 450 GETG$:IF G$="" THEN450
 460 GOTO100
READY.
```

APPENDIX 17

Basic Program Which Calculates Predicted Transverse Strength from Various Stress Magnification Theories

```
100 PRINT"□"
110 PRINT"STRESS CONC' THEORIES"
120 PRINT"FOR TRANSVERSE STRENGTH PREDICTION"
130 PRINT"--------------------------------"
140 PRINT:PRINT"INPUT SOME DATA"
150 PRINT
160 PRINT"FIBRE VOLUME FRACTION (%)"
170 INPUT VF
180 VF=VF/100
190 PRINT"MATRIX MODULUS (PA)"
200 INPUT EM
210 PRINT"MATRIX POISSONS RATIO"
220 INPUT PM
230 PRINT"MATRIX STRENGTH"
240 INPUT SS
250 PRINT
260 PRINT"ASSUMES FIBRE MODULUS=76 (GPA)
270 PRINT"FIBRE POISSONS RATIO=0.2"
280 EF=76E9
290 PF=0.2
300 VM=(1-VF)
310 E1=VF*EF+VM*EM
320 P1=PF*VF+PM*VM
330 RV=VF↑0.5
340 ES=EM*(1-RV)+(EM*RV)/(1-RV*(1-EM/EF))
350 E2=EM/(1-RV*(1-EM/EF))
360 P2=VF*PF+VM*(2*PM-P1*E2/E1)
370 PRINT
380 PRINT"================================"
390 PRINT"CHAMIS 3D STRESS CONC' THEORY"
400 SX=SS/10:REM***** SEED STRESS******
410 SX=SX*1.01
420 S1=(PM-P1*EM/E1)*SX
430 S2=(E2/ES)*SX
440 S3=-1*(1-RV)/RV*(PM-P2)*(EM/E2)*SX
450 IFS1>SS OR S1<(-1*SS)THEN500
460 IFS2>SS OR S2<(-1*SS)THEN500
470 IFS3>SS OR S3<(-1*SS)THEN500
480 GOTO410
490 PRINT
500 PRINT"MAX STRESS EXCEEDED AT ";SX
510 SX=SS/10:REM***** SEED STRESS******
520 SX=SX*1.01
530 S1=(PM-P1*EM/E1)*SX
540 S2=(E2/ES)*SX
550 S3=-1*(1-RV)/RV*(PM-P2)*(EM/E2)*SX
560 BB=(S1-S2)↑2+(S2-S3)↑2+(S3-S1)↑2
570 IFBB>2*SS↑2THEN590
580 GOTO520
590 PRINT"VON MISES EXCEEDED AT ";SX
600 PRINT
610 PRINT"PRESS SPACE BAR"
620 GETG$:IFG$=""THEN620
630 PRINT
640 REM
650 PRINT"================================"
660 REM****SPENCER*******
```

```
 670 REM****VARIABLE PACKING MODE***
 680 GG=((1.8-0.75*VF)*VF)↑-0.5
 690 K=1-EM/EF
 700 TT=ATN(((GG+K)/(GG-K))↑0.5)
 710 IT=2*GG/((GG↑2-K↑2)↑0.5)
 720 JT=(GG-1)/GG
 730 AL=JT+1/K*(IT*TT-π/2)
 740 SC=1/(AL*(1-K/GG))
 750 PRINT:PRINT"SPENCER PREDICTED STRENGTH"
 760 PRINT"VAR' PACK' MODE: ";SS/SC
 770 PRINT
 780 PRINT"PRESS SPACE BAR"
 790 GETG$:IFG$=""THEN790
 800 REM
 810 PRINT"=============================="
 820 REM****SIMPLE CHAMIS*****
 830 XX=EF-EF*VF+EM*VF
 840 YY=EF+(π/VF)↑-0.5*(2*EM-2*EF)
 850 ZZ=XX/YY
 860 S2=SS/ZZ
 870 Q=((2*π)/((3↑0.5)*VF))↑-0.5
 880 YY=EF+Q*(2*EM-2*EF)
 890 ZZ=XX/YY
 900 S3=SS/ZZ
 910 PRINT:PRINT"SIMPLE CHAMIS STRENGTH PREDICTIONS:"
 920 PRINT"SQUARE ARRAY: ";S2
 930 PRINT"HEXAGONAL ARRAY: ";S3
 940 PRINT
 950 PRINT"PRESS SPACE BAR"
 960 GETG$:IFG$=""THEN960
 970 REM
 980 PRINT"=============================="
 990 REM***RELATIVE X-SECT AREA THEORIES
1000 S2=(1-(4*VF/π)↑0.5)*SS
1010 S3=(1-(2*(3↑0.5)*VF/π)↑0.5)*SS
1020 PRINT:PRINT"RELATIVE CROSS-SECTIONAL AREA"
1030 PRINT"STRENGTH PREDICTIONS"
1040 PRINT"SQUARE ARRAY: ";S2
1050 PRINT"HEXAGONAL ARRAY: ";S3
1060 PRINT
1070 PRINT"PRESS SPACE BAR"
1080 GETG$:IFG$=""THEN1080
1090 GOTO100
READY.
```

FIGURES

1. Predicted stress/strain response of two 0°/90° GRP laminates with different lamina transverse properties.

2. Model of idealised fibre array in voidy matrix used by Greszczuk. (From Greszczuk, ref 18).

3. Comparison of Halpin-Tsai and Reuss predictions of transverse modulus with experimental data. (From Bailey and Parvizi, ref 24).

4. Model used by Spencer to derive transverse modulus and stress distribution. (From Spencer, Ref 25).

5. Fibre separation parameters (γ) related to various packing geometries. (From Spencer, ref 25).

6. Predicted relation between composite transverse stiffness and fibre to resin modulus ratio for various fibre volume fractions. (From Adams and Doner, ref 11).

7. The relation of various elastic properties to resin Poisson's ratio. (From Herrmann and Pister, ref 27).

8. Comparison of measured transverse ply cracking strain as a function of resin failure strain. (From Garrett and Bailey, ref 29).

9. Comparison of measured transverse flexural strength as a function of fibre volume fraction with the theoretical expression (for a hexagonal array) assuming an (untreated) interfacial strength of 5 MPa. (From Marom and White, ref 38).

10. Predicted square array stress concentration factor as a function of fibre volume fraction for $E_f >> E_m$. (From Chamis, ref 39).

11. Comparison of theoretical prediction with experimental results on transverse failure strain as a function of fibre volume fraction. (From Bailey and Parvizi, ref 24).

12. Diagram of the coordinate system used by the Chamis equations for predicting three-dimensional microstresses. (From Chamis, ref 16).

13. Distribution of maximum principle stress in matrix for a square array of circular filaments. V_f = 55%, E_f/E_m = 120, ν_f = 0.20 and ν_m = 0.35. (From Chamis, ref 39).

14. Normalised maximum principle stress in matrix as a function of fibre/resin stiffness ratio for several different fibre volume functions in a square array. ν_f = 0.20, ν_m = 0.35. (From Adams and Doner, ref 11).

15. Various possible cases of crack extension from micro-flaws. The case which has maximum K_I under a given load initiates failure. (From Tirosh, Katz, Lifschuetz and Tetelman, ref 50).

16. Transverse tensile properties of glass fibre in modified epoxy versus percentage urethane rubber in matrix. (From Wells and Hancox, ref 59).

17. Transverse tensile properties of carbon fibre in modified epoxy versus percentage urethane rubber in matrix. (From Wells and Hancox, ref 59).

18. Correlation of transverse failure strain and modulus for flexibilised glass reinforced plastic. (From Christensen and Rinde, ref 67).

19. Comparison of transverse cracking strains experimentally measured and predicted theoretically. The dotted line represents the limiting values for large ply thicknesses. (From Parvizi, Garrett and Bailey, ref 72).

20. Contributions to the in-situ transverse strength from applied and residual stresses for the $(0_2°/90_n°)_s$, $(\pm 30°/90_n°)_s$ and $\pm(60°/90_n°)_s$ CFRP laminates with varying transverse ply thicknesses. (From Flaggs and Kural, ref 74).

21. Schematic of the wet filament winding process for producing unidirectional composite plates.

22. Variation of the density of epoxy/urethane blends as a function of urethane weight fraction.

23 - Microsections of glass epoxy/urethane composites.

28.

48. Variation of G_{IC} fracture toughness with crack length for double cantilever beams of different heights of conventional rigid resin composite.

49. Schematic of the double torsion toughness test specimen.

50. Variation of G_{IC} fracture toughness with crack length for double torsion specimens of conventional rigid resin composite.

51. Schematic of the single edge notched toughness test specimen.

52. Single edge notched results for conventional rigid resin composite with notches and cracks. Data plotted as log (σY) versus log (a).

53. Single edge notched results for conventional rigid resin composite with notches and cracks. Data plotted as K_{IC} versus crack or notch length (a).

54. Single edge notched results for conventional neat rigid resin with varying crack lengths. Data plotted as log (σY) versus log (a).

55. Schematic of the transverse composite straight sided coupons.

56. Schematic of the dogbone specimen used for 0 - 60% urethane neat resins.

57. Schematic of the dogbone specimen used for 100% urethane neat resin.

58 - Stress-strain curves of transverse composites.
63.

64 - Stress-strain curves of neat resins.
70

71. The three modes of crack extension. (From Pascoe, ref 87).

72. Schematic of centre notched plate specimen in tension.

73. Schematic of double edge notched plate specimen in tension.

74. Schematic of single edge notched plate specimen in tension.

75. Schematic of single edge notched specimen in 3-point bending.

76. Anisotropic finite width correction factors for various orientations of carbon fibre/epoxy single edge notched specimens. (From Mandell, McGarry, Wang and Im, ref 98).

77. Graphical description of the determination of J integrals. (From Knott, ref 89).

78. Single edge notched specimen used for fracture mechanics tests on neat resin and transverse composite materials.

79 - Candidate fracture toughness values (K_Q) for transverse
84. composites plotted against the ratio of crack length to specimen width.

85 - Candidate fracture toughness values (K_Q) for neat resins plotted
90. against the ratio of crack length to specimen width.

91. Photograph of narrow double cantilever beam showing the tied zone of fracture face bridging stringers.

92. Schematic of transverse crack propagation by nucleation of flaws ahead of a crack tip. (From Johnson and Mangalgiri, ref 62).

93. Graph of the expression predicting equilbrium stringer angles and stringer strains.

94. Micrograph of the tied zone on a transverse double cantilever beam specimen.

95. Comparison of experimental results and theoretical predictions of the change of fracture toughness with crack length.

96 Experimental results for Poisson's ratio versus urethane content in resin. The straight line identifies the Poisson's ratio value used in the models for transverse modulus prediction.

97. Graph of the measured values of neat resin and transverse composite moduli against urethane content, together with transverse composite modulus predictions using various theoretical models.

98. Graph of predicted transverse 100% urethane resin composite moduli from several theoretical models versus Poisson's ratio.

99. Measured resin and transverse composite failure strains plotted against urethane content with predictions from Kies strain magnification theory.

100. Microsection of a cavitated region in 100% urethane transverse composite showing highly strained fibrils of pure rubber.

101. Measured resin and transverse composite strengths plotted against urethane content, with predictions from stress magnification theories.

102 -Scanning electron micrographs of transverse fracture surfaces.
107.

108. Candidate critical stress intensity factors (K_Q) for neat resin and transverse composites plotted against urethane content of the resin.

109. Candidate critical rate of release of strain energies (G_Q) for neat resin and transverse composites plotted against urethane content of the resin.

110. Crack tip opening displacements for neat resin and transverse composites plotted against proportion of urethane.

111. Measured transverse failure strain plotted against root reciprocal of measured transverse modulus.

112. Measured transverse strengths plotted against measured transverse toughness with various inherent defect sizes indicated.

113. Optical micrograph of crack initiation location on the fracture surface of a 0% urethane neat resin strength specimen.

114. Deformation map of a model transverse composite obtained by laser Moiré interferometry.

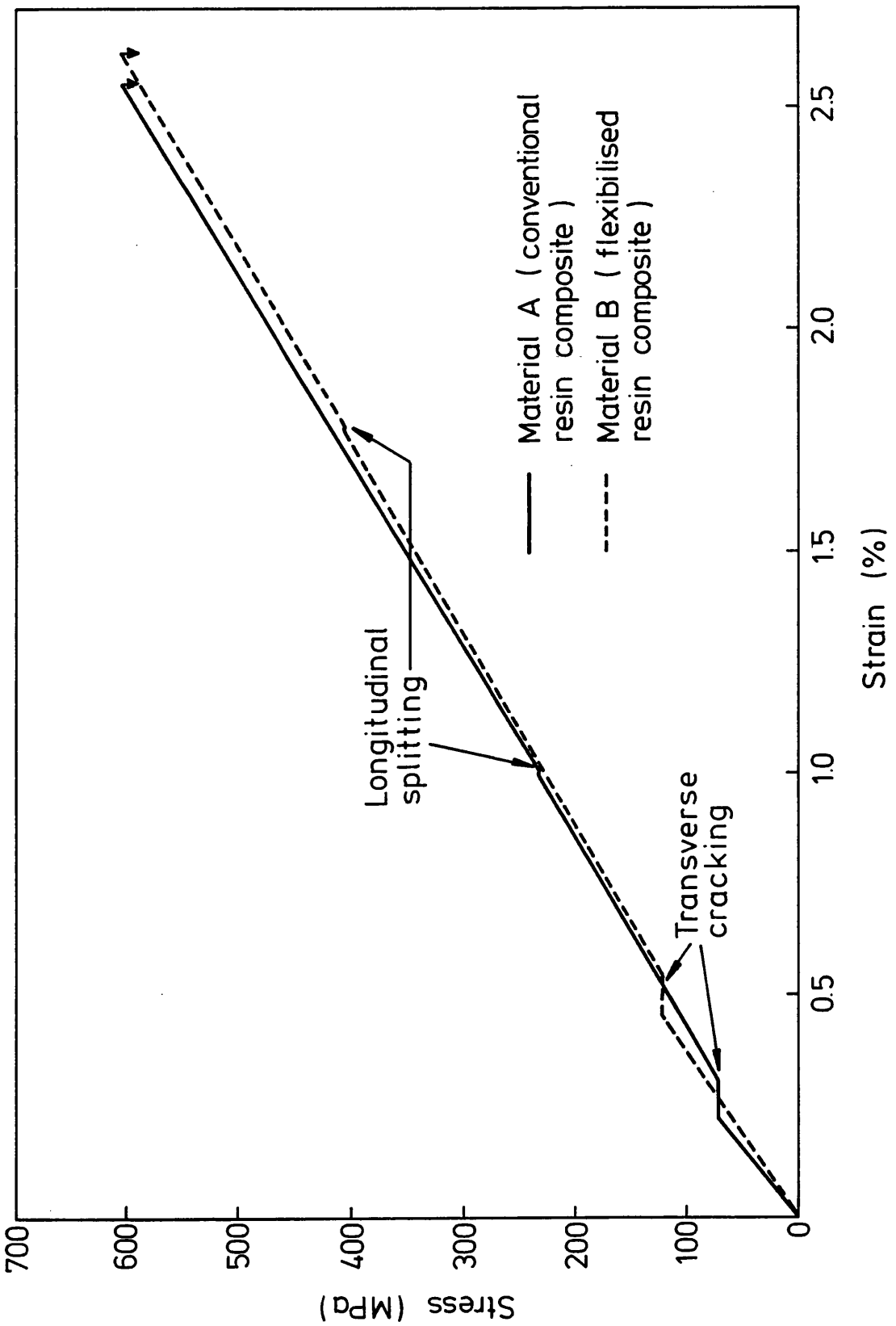

FIG. 1. Predicted stress/strain response of two 0°/90° GRP laminates with different lamina transverse properties.

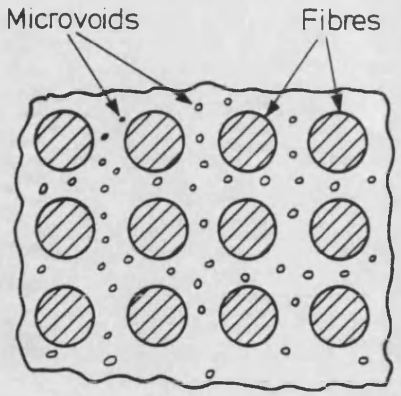

FIG. 2. Model of idealised fibre array in voidy matrix used by Greszczuk. (From Greszczuk, ref 18).

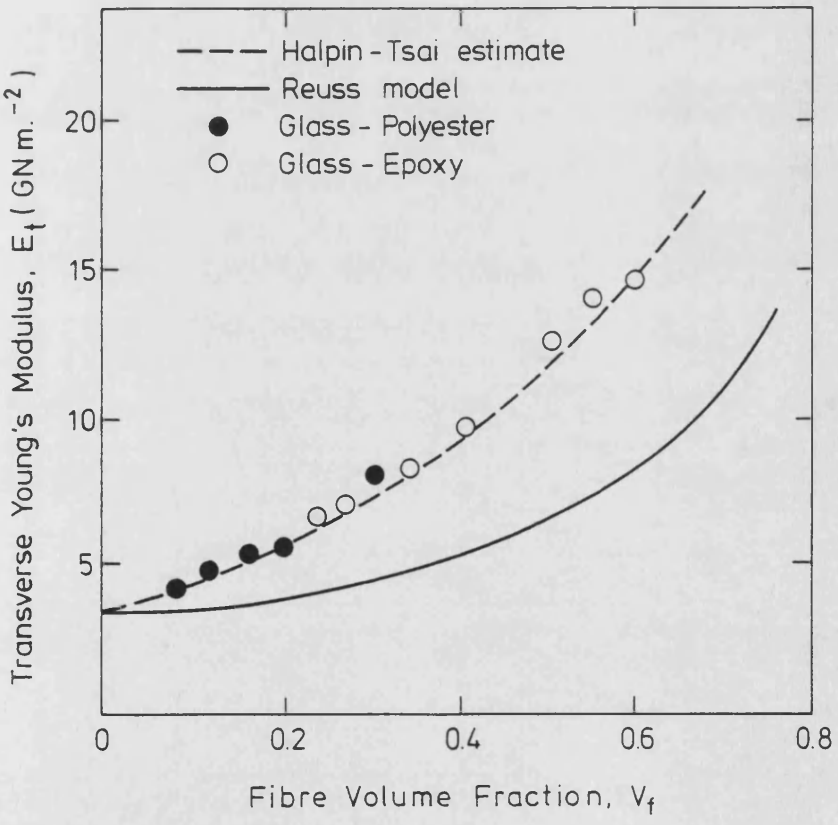

FIG. 3. Comparison of Halpin-Tsai and Reuss predictions of transverse modulus with experimental data. (From Bailey and Parvizi, ref 24).

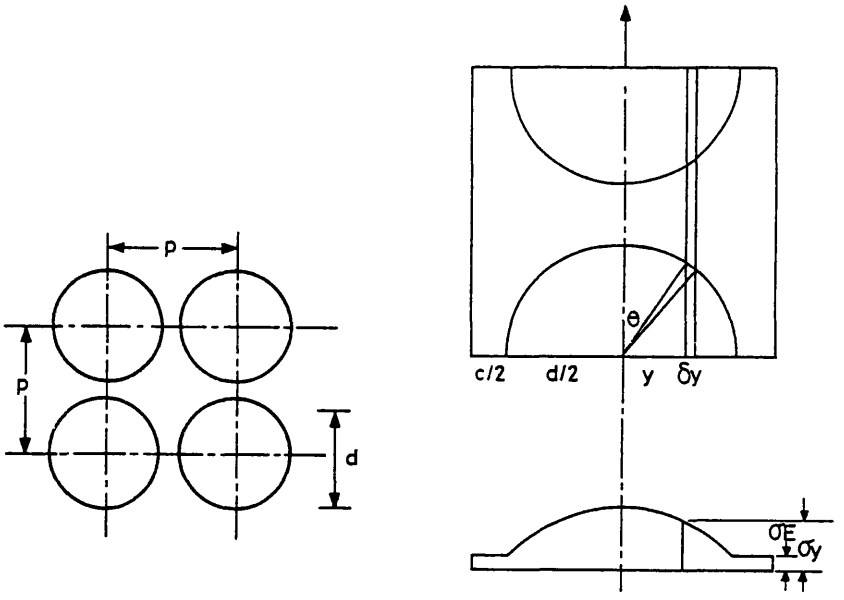

FIG. 4. Model used by Spencer to derive transverse modulus and stress distribution. (From Spencer, Ref 25).

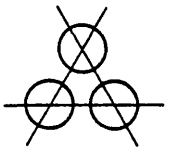

Triangular packing $V_f = \frac{1}{\gamma^2}\frac{\pi}{2\sqrt{3}} = \frac{1}{(1.050\gamma)^2}$

$\gamma^2 = \frac{1}{1.103V_f}$

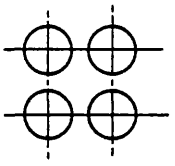

Square packing $V_f = \frac{1}{\gamma^2}\frac{\pi}{4} = \frac{1}{(1.128\gamma)^2}$

$\gamma^2 = \frac{1}{1.272V_f}$

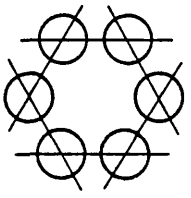

Hexagonal packing $V_f = \frac{1}{\gamma^2}\frac{\pi}{3\sqrt{3}} = \frac{1}{(1.286\gamma)^2}$

$\gamma^2 = \frac{1}{1.654V_f}$

FIG. 5. Fibre separation parameters (γ) related to various packing geometries. (From Spencer, ref 25).

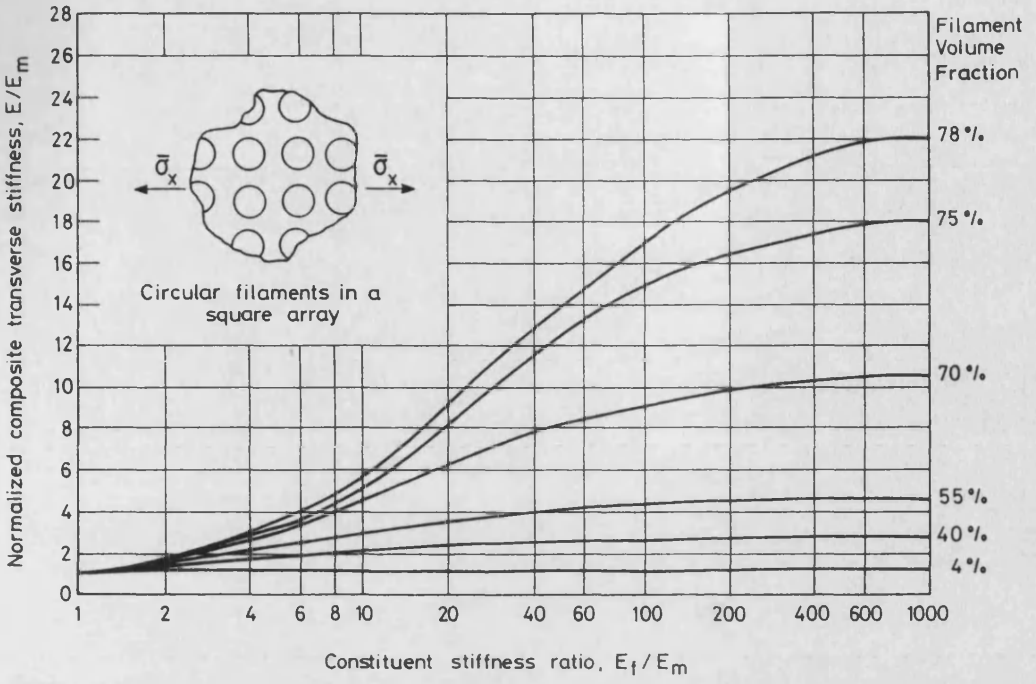

FIG. 6. Predicted relation between composite transverse stiffness and fibre to resin modulus ratio for various fibre volume fractions. (From Adams and Doner, ref 11).

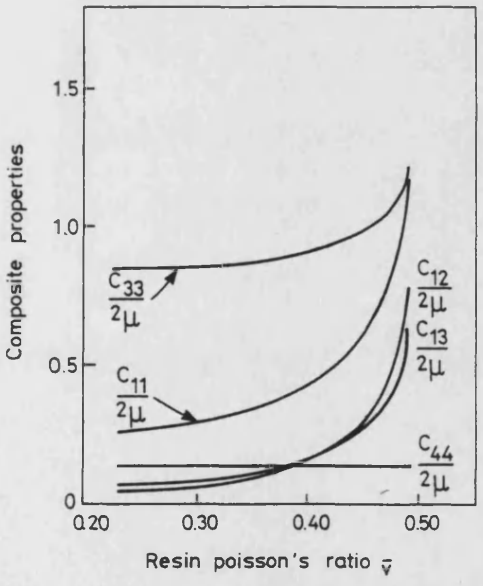

$$\begin{bmatrix}\sigma_1\\ \sigma_2\\ \sigma_3\\ \sigma_{12}\\ \sigma_{13}\\ \sigma_{23}\end{bmatrix} = \begin{bmatrix} C_{11} & C_{12} & C_{13} & & & \\ C_{12} & C_{11} & C_{13} & & & \\ C_{13} & C_{13} & C_{33} & & & \\ & & & C_{44} & & \\ & & & & C_{55} & \\ & & & & & C_{55} \end{bmatrix} \begin{bmatrix}\varepsilon_1\\ \varepsilon_2\\ \varepsilon_3\\ \varepsilon_{12}\\ \varepsilon_{13}\\ \varepsilon_{23}\end{bmatrix}$$

in which the coordinate system is :

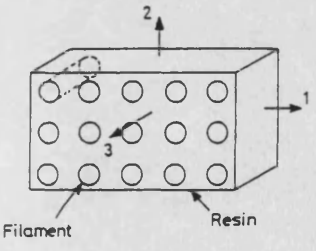

Where μ = fibre shear modulus, and the elastic constants are defined as :

FIG. 7. The relation of various elastic properties to resin Poisson's ratio. (From Herrmann and Pister, ref 27).

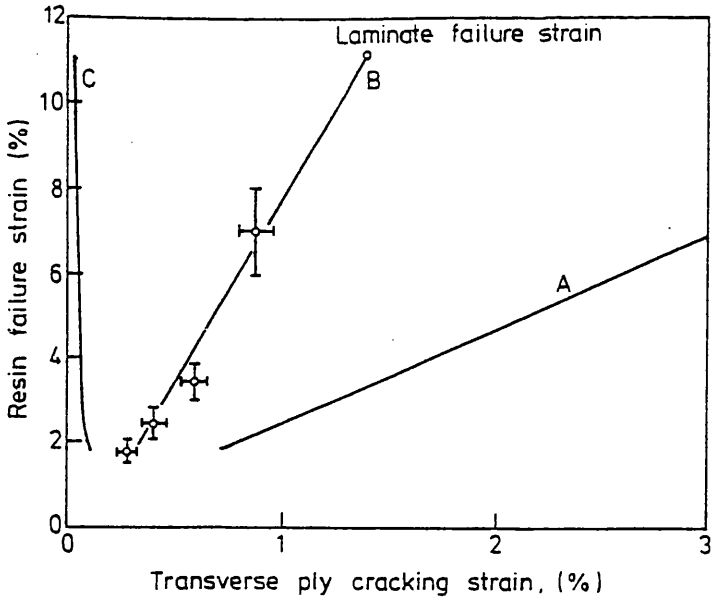

FIG. 8. Comparison of measured transverse ply cracking strain as a function of resin failure strain. Curves A and B are theoretical predictions for regular cubic arrays of fibres for V_f = 30% and 58% respectively. Curve C is for touching fibres. (From Garrett and Bailey, ref 29).

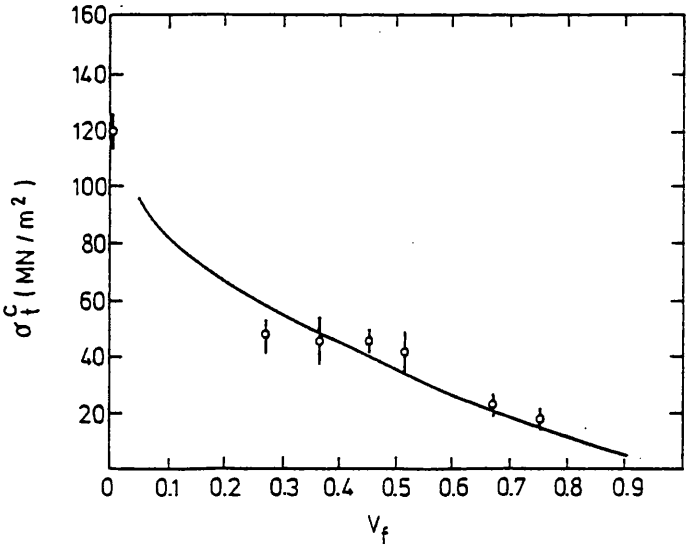

FIG. 9. Comparison of measured transverse flexural strength as a function of fibre volume fraction with the theoretical expression (for a hexagonal array) assuming an (untreated) interfacial strength of 5 MPa. (From Marom and White, ref. 38).

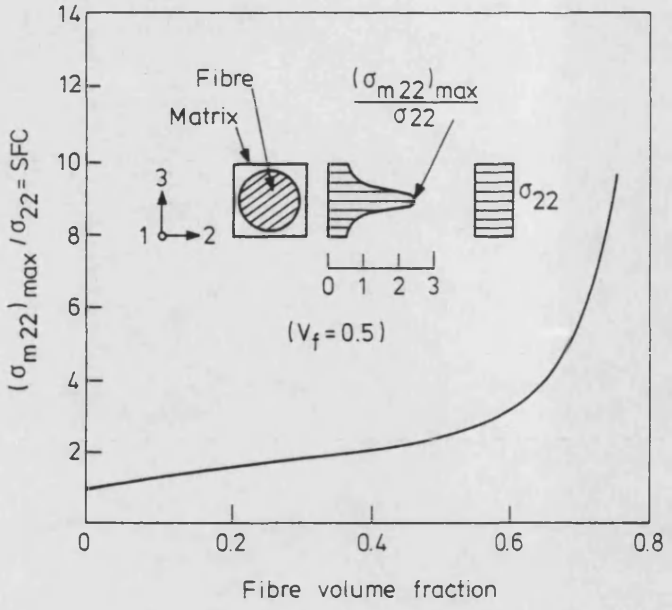

FIG. 10. Predicted square array stress concentration factor as a function of fibre volume fraction for $E_f >> E_m$. (From Chamis, ref 39).

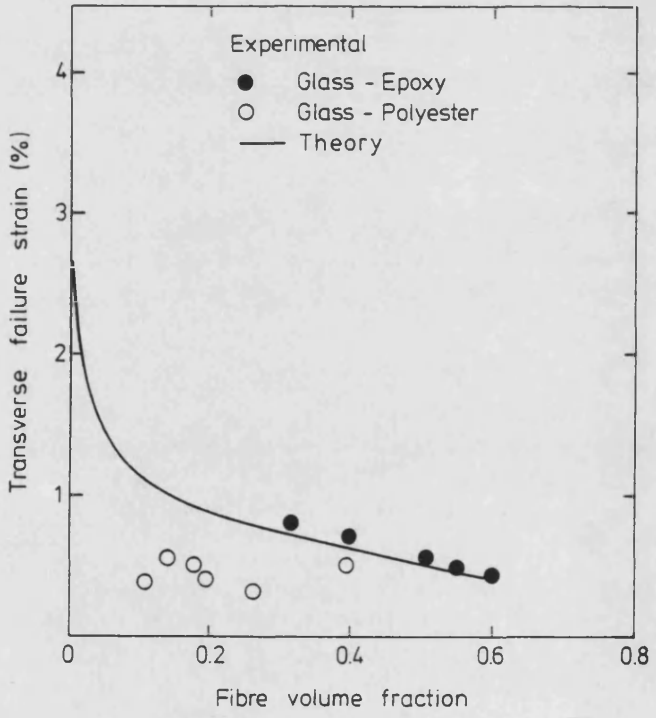

FIG. 11. Comparison of theoretical prediction with experimental results on transverse failure strain as a function of fibre volume fraction. (From Bailey and Parvizi, ref 24).

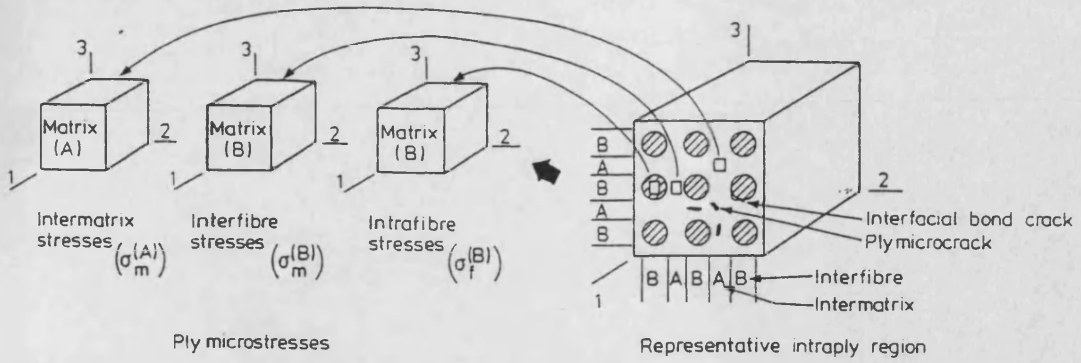

FIG. 12. Diagram of the coordinate system used by the Chamis equations for predicting three-dimensional microstresses. (From Chamis, ref 16).

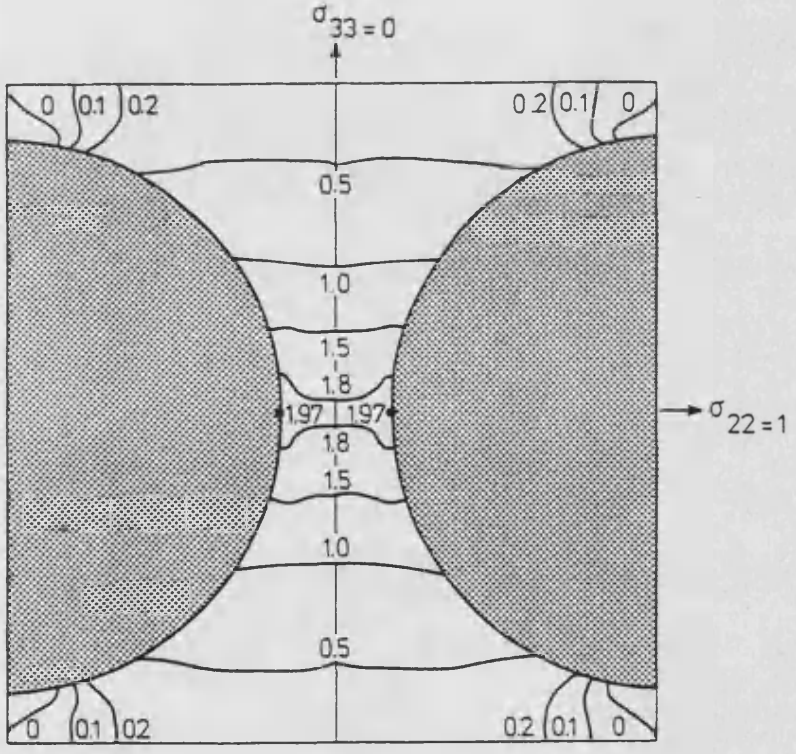

FIG. 13. Distribution of maximum principal stress in matrix for a square array of circular filaments. V_f = 55%, E_f/E_m = 120, ν_f = 0.2 and ν_m = 0.35. (From Chamis, ref 39).

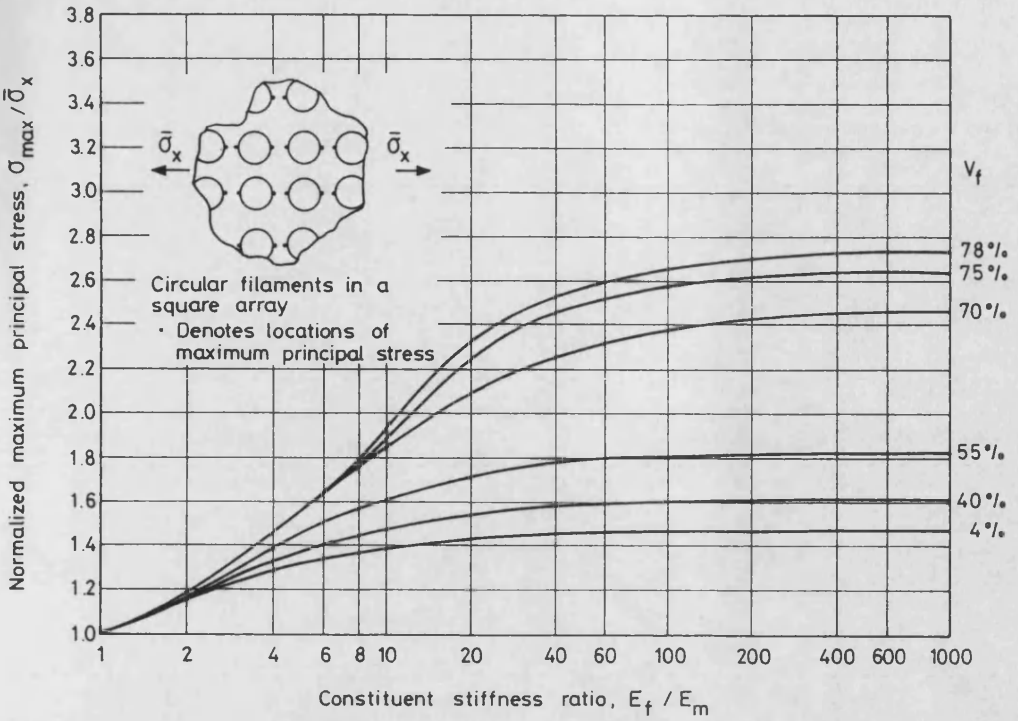

FIG. 14. Normalised maximum principle stress in matrix as a function of fibre/resin stiffness ratio for several different fibre volume functions in a square array. $\nu_f = 0.20$, $\nu_m = 0.35$. (From Adams and Doner, ref 11).

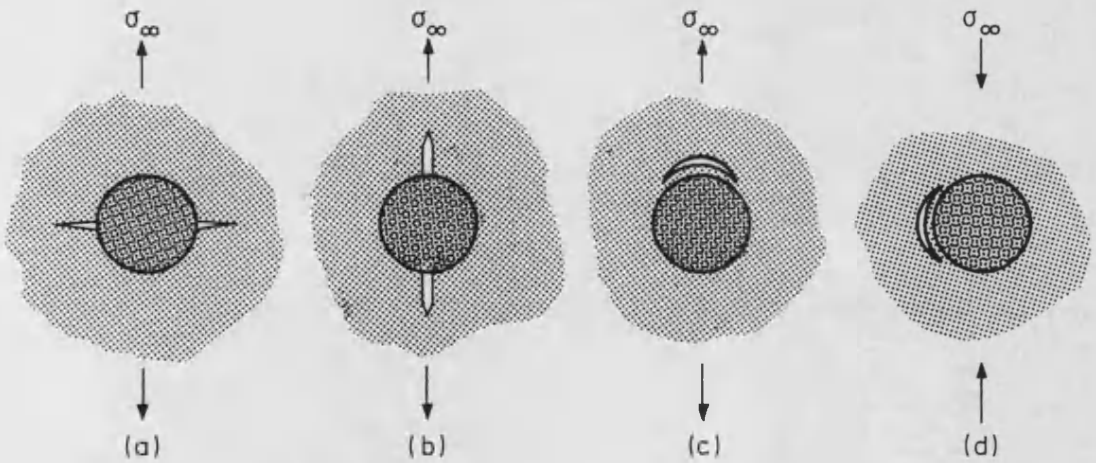

FIG. 15. Various possible cases of crack extension from micro-flaws. The case which has maximum K_I under a given load initiates failure. (From Tirosh, Katz, Lifschuetz and Tetelman, ref 50).

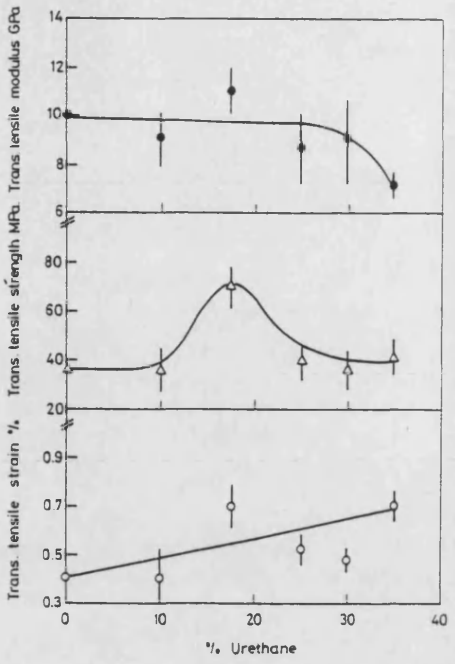

FIG. 16. Transverse tensile properties of glass fibre in modified epoxy versus percentage urethane rubber in matrix. (From Wells and Hancox, ref 59).

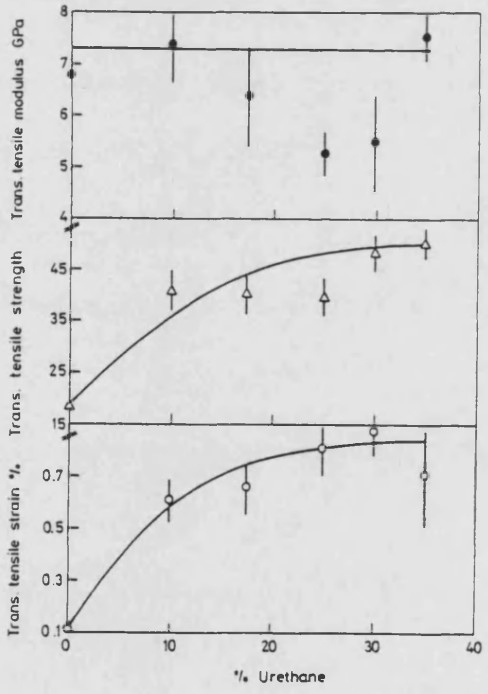

FIG. 17. Transverse tensile properties of carbon fibre in modified epoxy versus percentage urethane rubber in matrix. (From Wells and Hancox, ref 59).

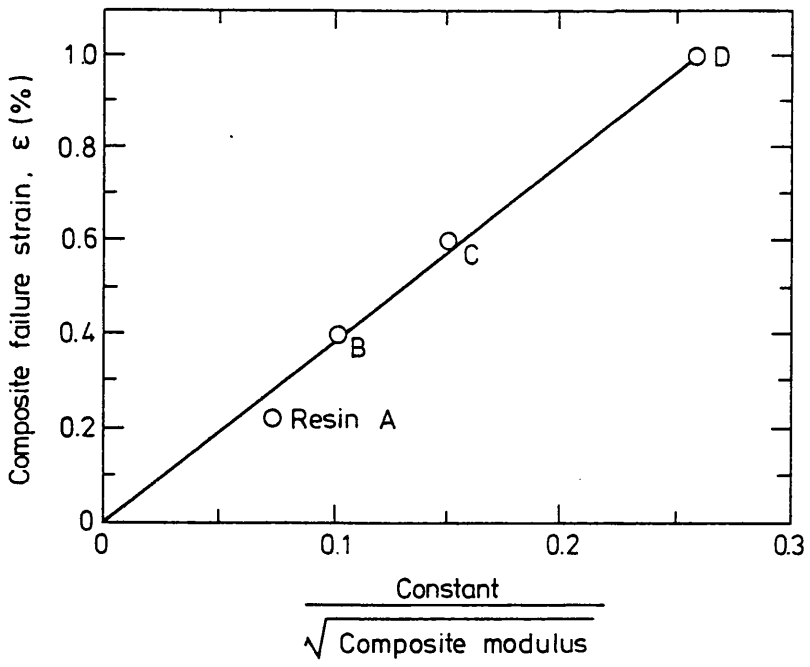

FIG. 18. Correlation of transverse failure strain and modulus for flexibilised glass reinforced plastic. (From Christensen and Rinde, ref 67).

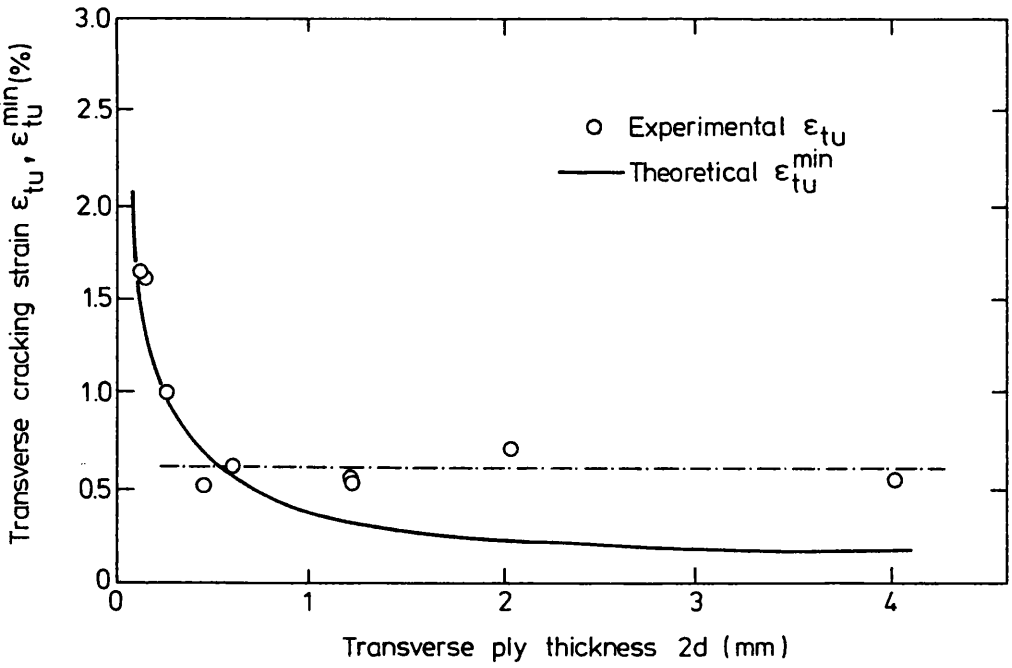

FIG. 19. Comparison of transverse cracking strains experimentally measured and predicted theoretically. The dotted line represents the limiting values for large ply thicknesses. (From Parvizi, Garrett and Bailey, ref 72).

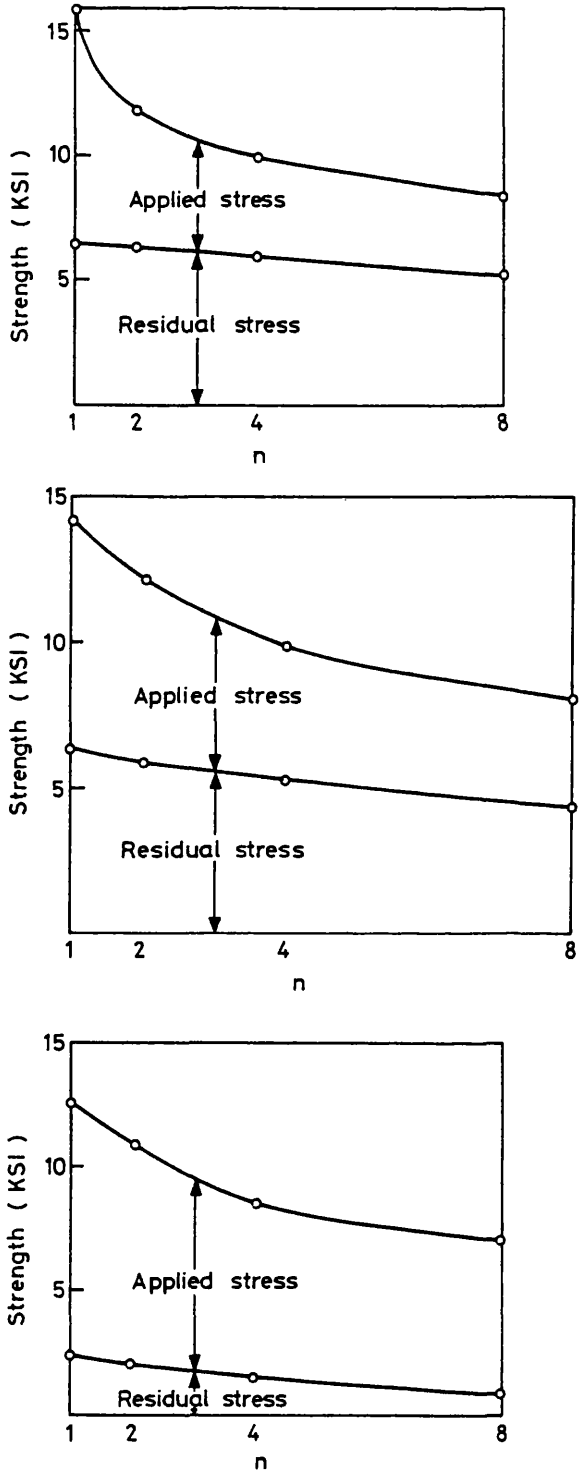

FIG. 20. Contributions to the in-situ transverse strength from applied and residual stresses for the $(0_2°/90_n°)_s$, $(\pm 30°/90_n°)_s$ and $\pm(60°/90_n°)_s$ CFRP laminates with varying transverse ply thicknesses. (From Flaggs and Kural, ref 74).

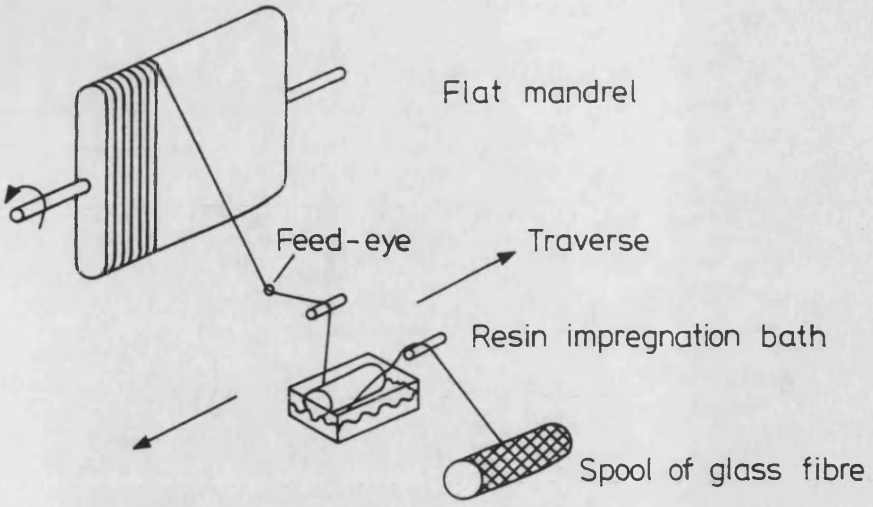

FIG. 21. Schematic of the wet filament winding process for producing unidirectional composite plates.

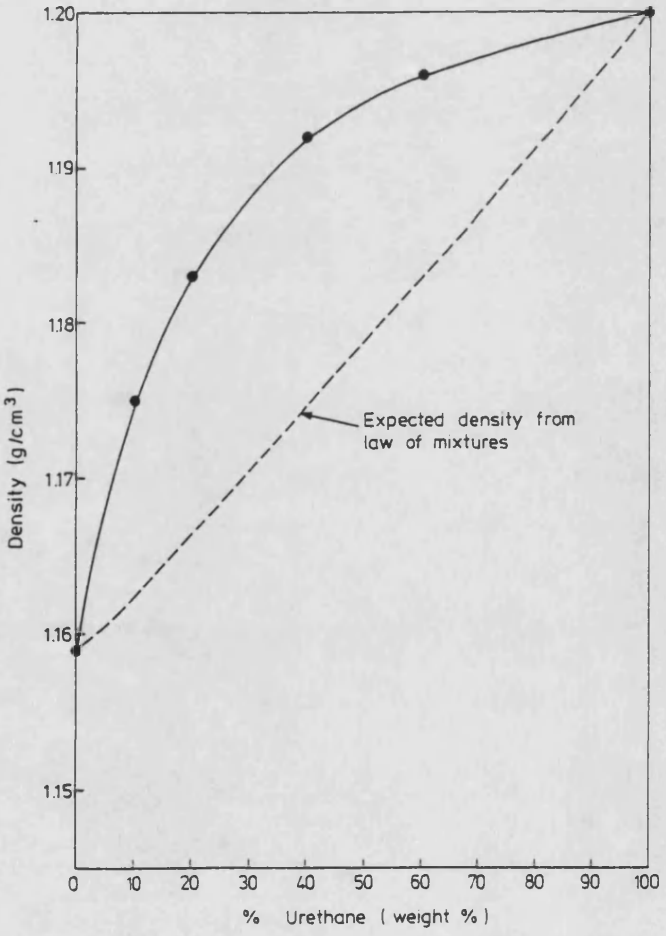

FIG. 22. Variation of the density of epoxy/urethane blends as a function of urethane weight fraction.

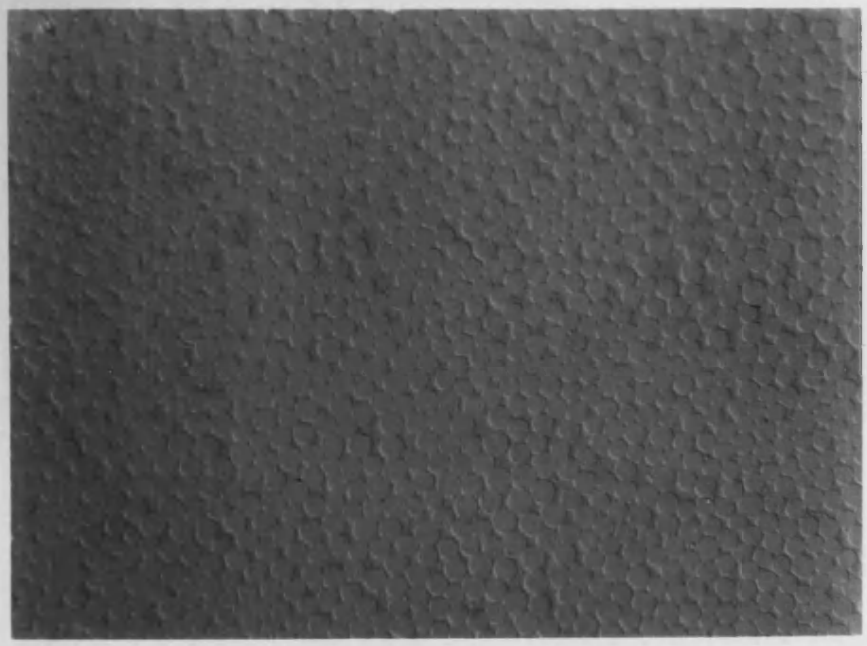

FIG. 23. Microsection of 0% urethane matrix composite. Mag'200x.

FIG. 24. Microsection of 10% urethane matrix composite. Mag'200x.

HARWELL LABORATORY
PHOTOGRAPHIC GROUP

HR 38768

NOT FOR PUBLICATION

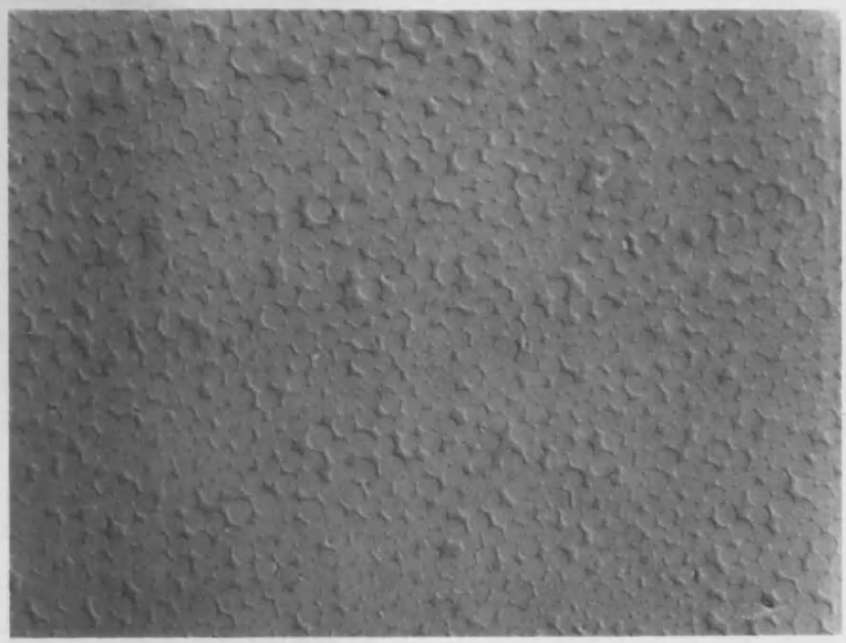

FIG. 25. Microsection of 20% urethane matrix composite. Mag'200x.

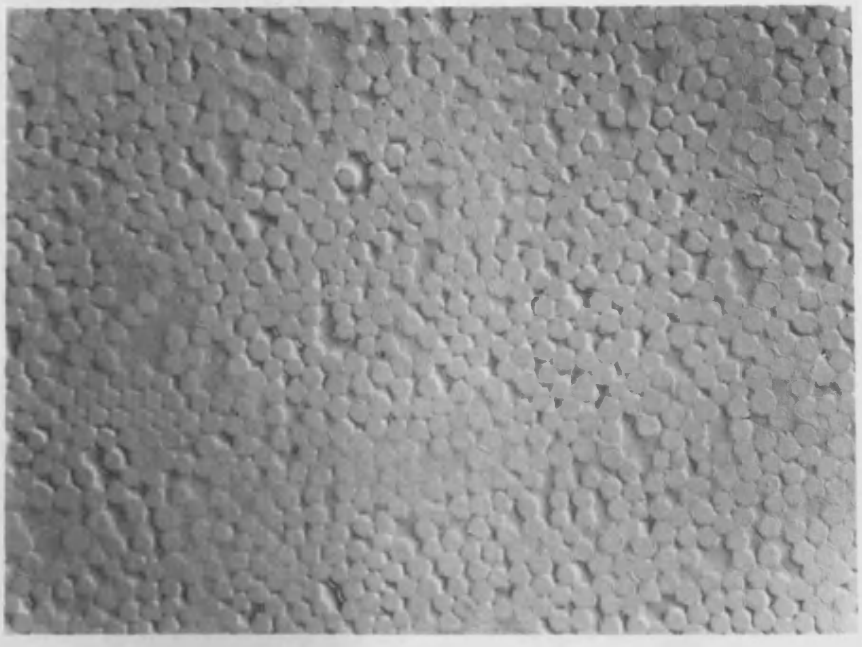

FIG. 26. Microsection of 40% urethane matrix composite. Mag'200x.

HARWELL LABORATORY
PHOTOGRAPHIC GROUP

HR 38769

NOT FOR PUBLICATION

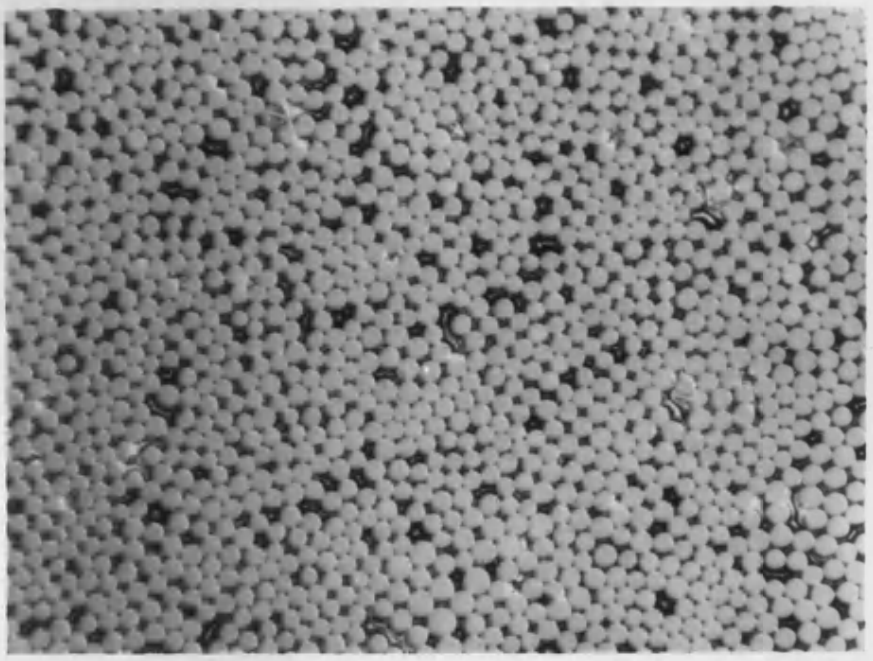

FIG. 27. Microsection of 60% urethane matrix composite. Mag'200x.

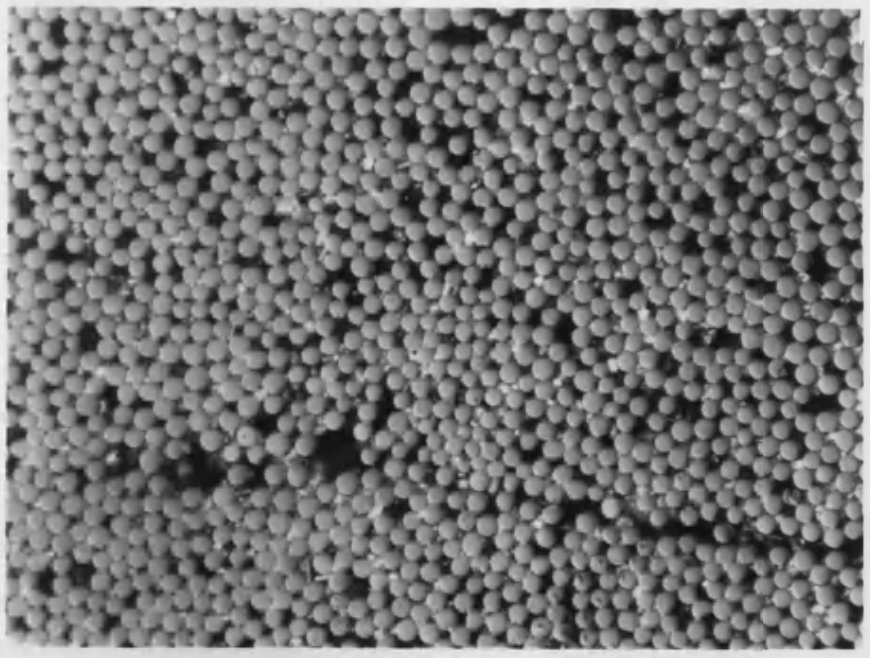

FIG. 28. Microsection of 100% urethane matrix composite. Mag'200x.

HARWELL LABORATORY
PHOTOGRAPHIC GROUP

HR 38776

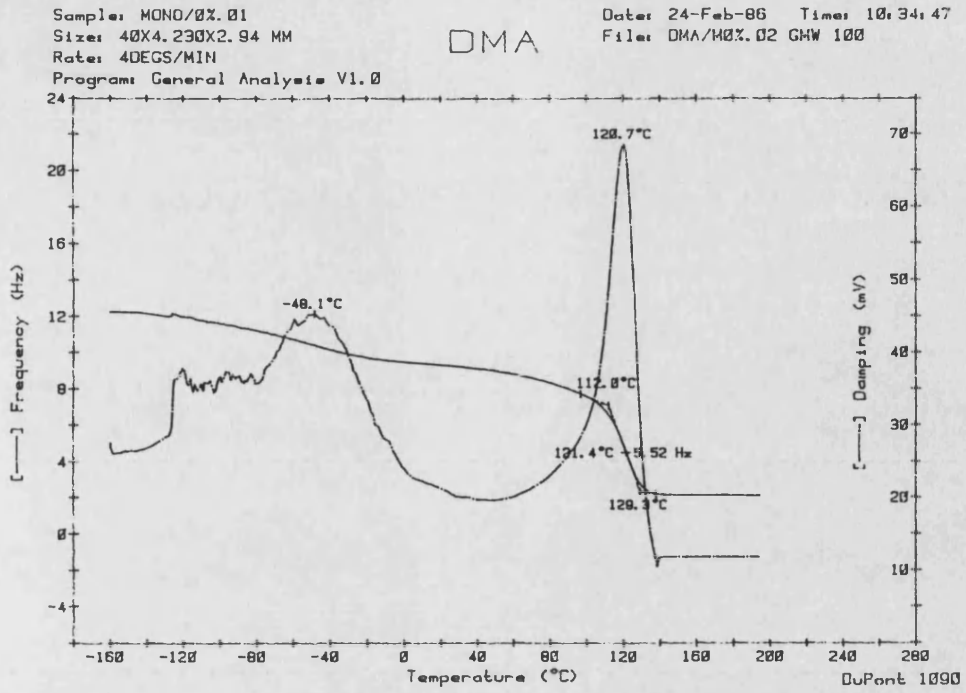

FIG. 29. DMA trace for 0% urethane neat resin.

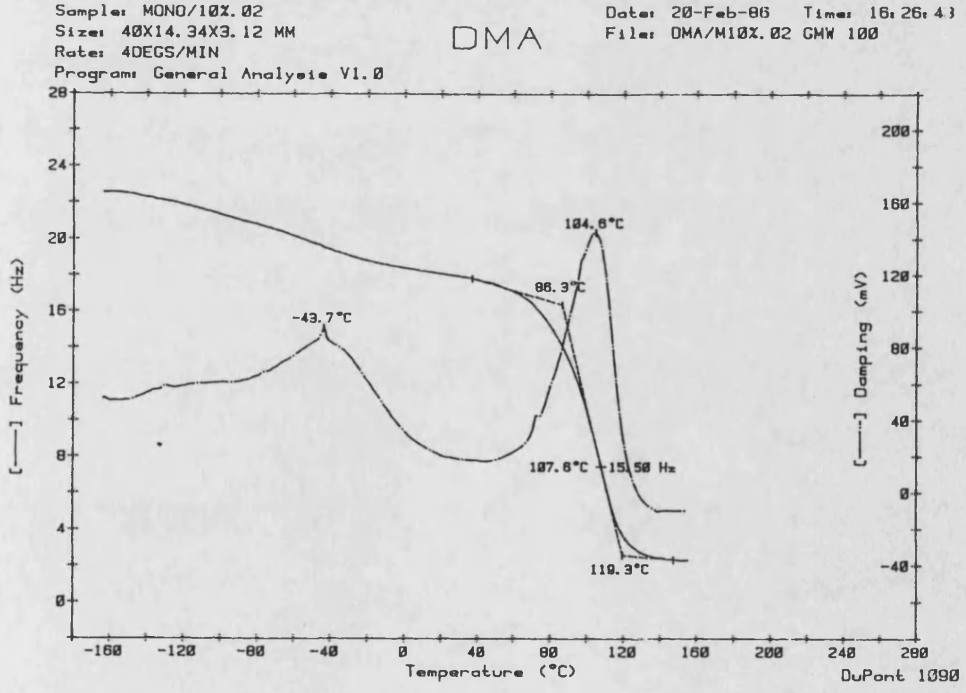

FIG. 30. DMA trace for 10% urethane neat resin.

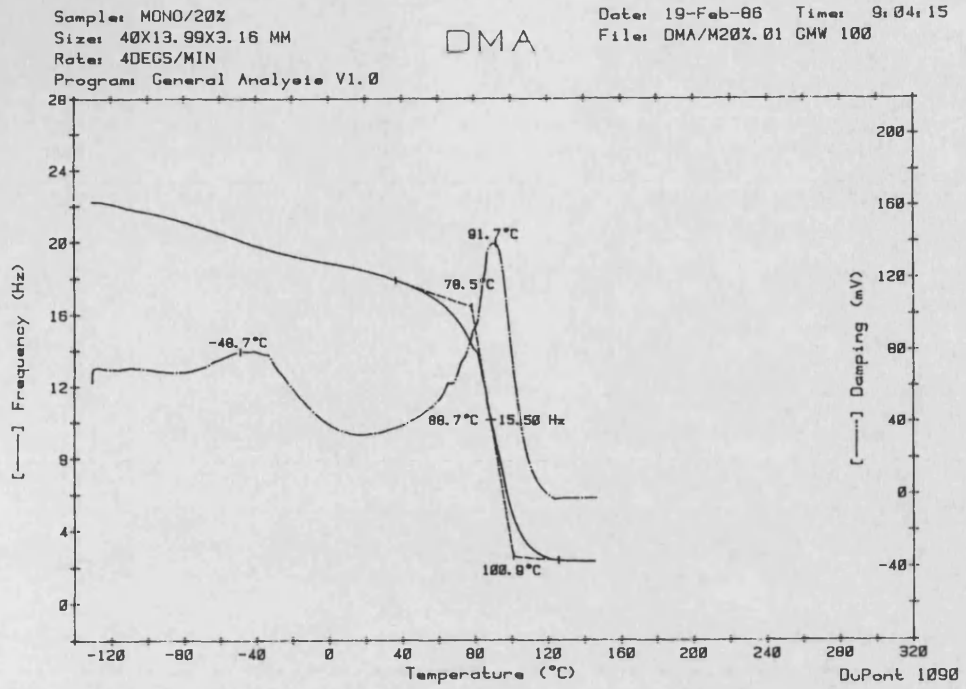

FIG. 31. DMA trace for 20% urethane neat resin.

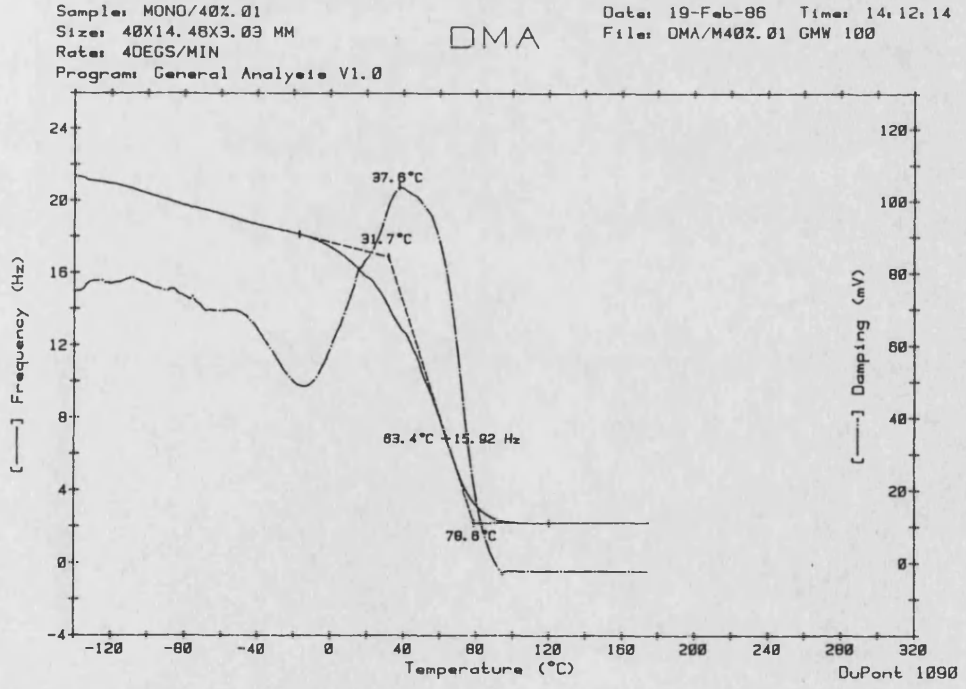

FIG. 32. DMA trace for 40% urethane neat resin.

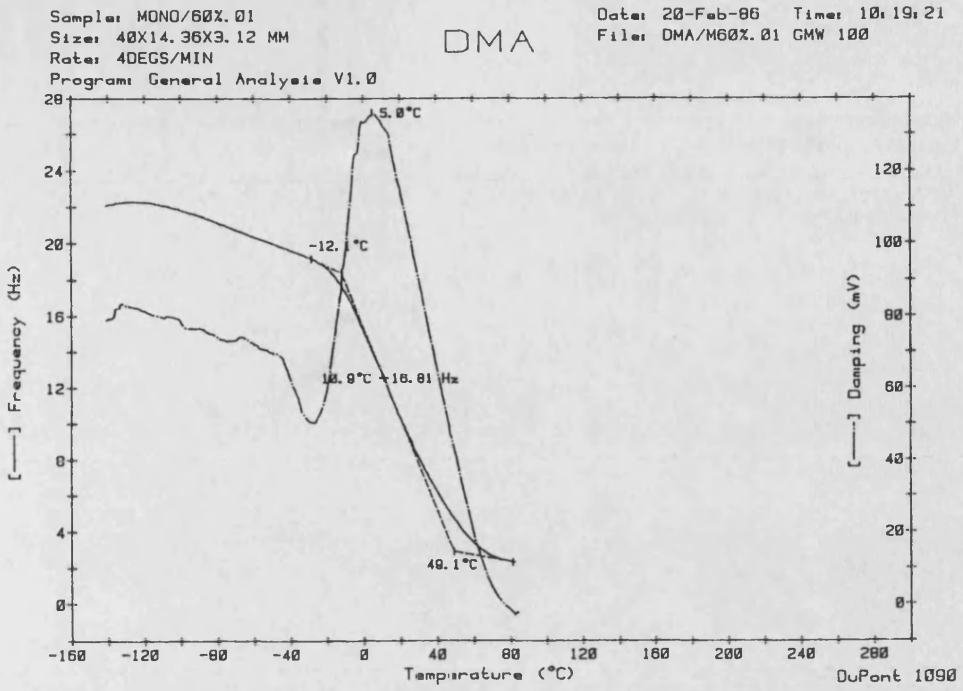

FIG. 33. DMA trace for 60% urethane neat resin.

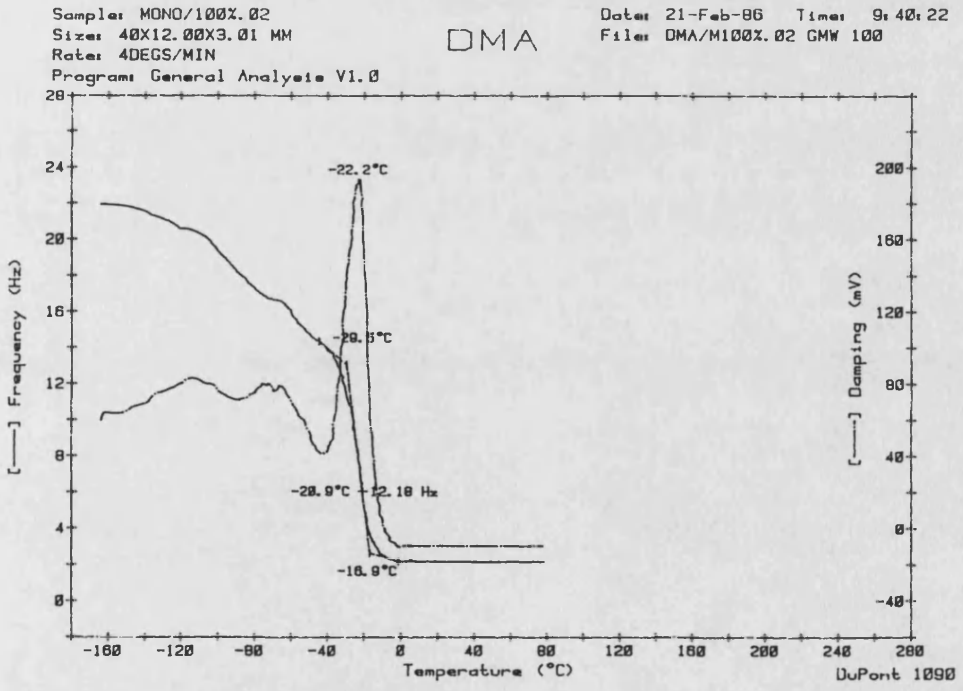

FIG. 34. DMA trace for 100% urethane neat resin.

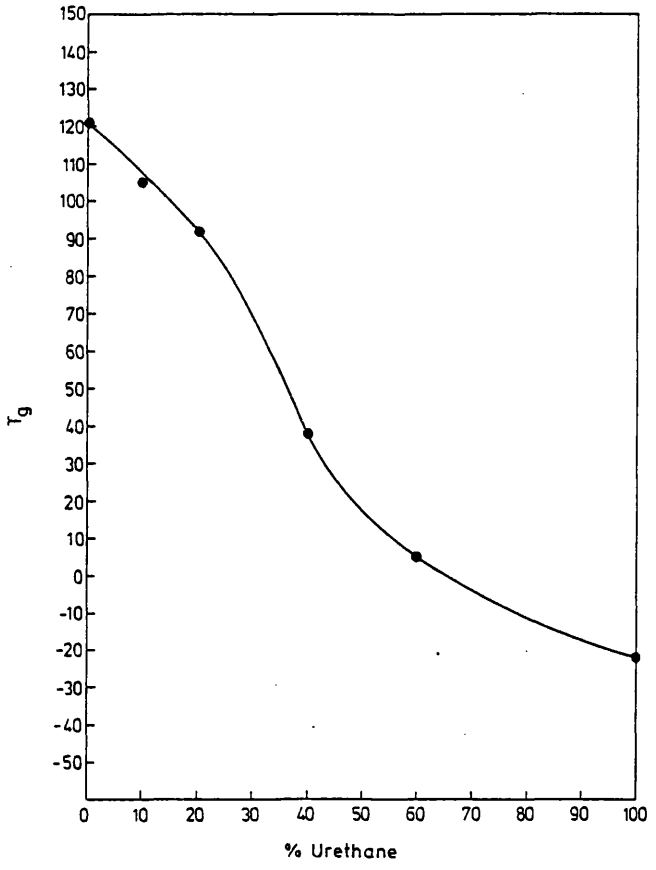

FIG. 35. Glass transition temperature versus urethane concentration for epoxy/urethane resin blends, measured using DMA.

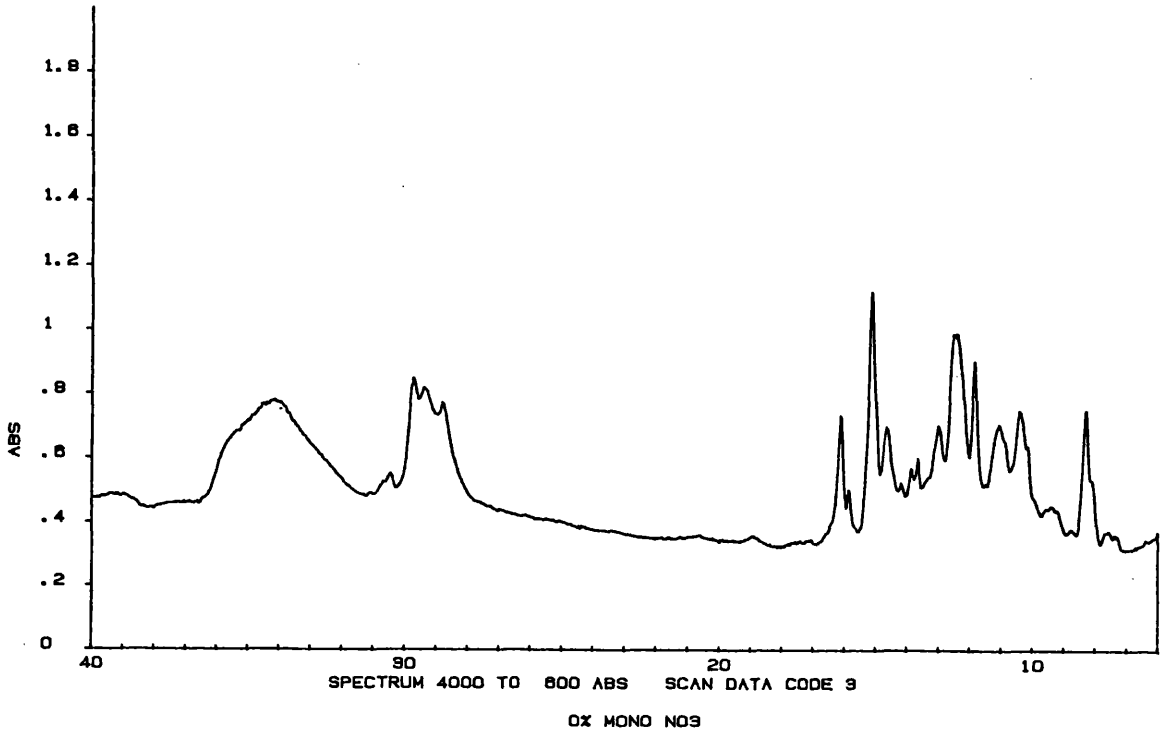

FIG. 36. Infra-red spectrum of 0% urethane neat resin.

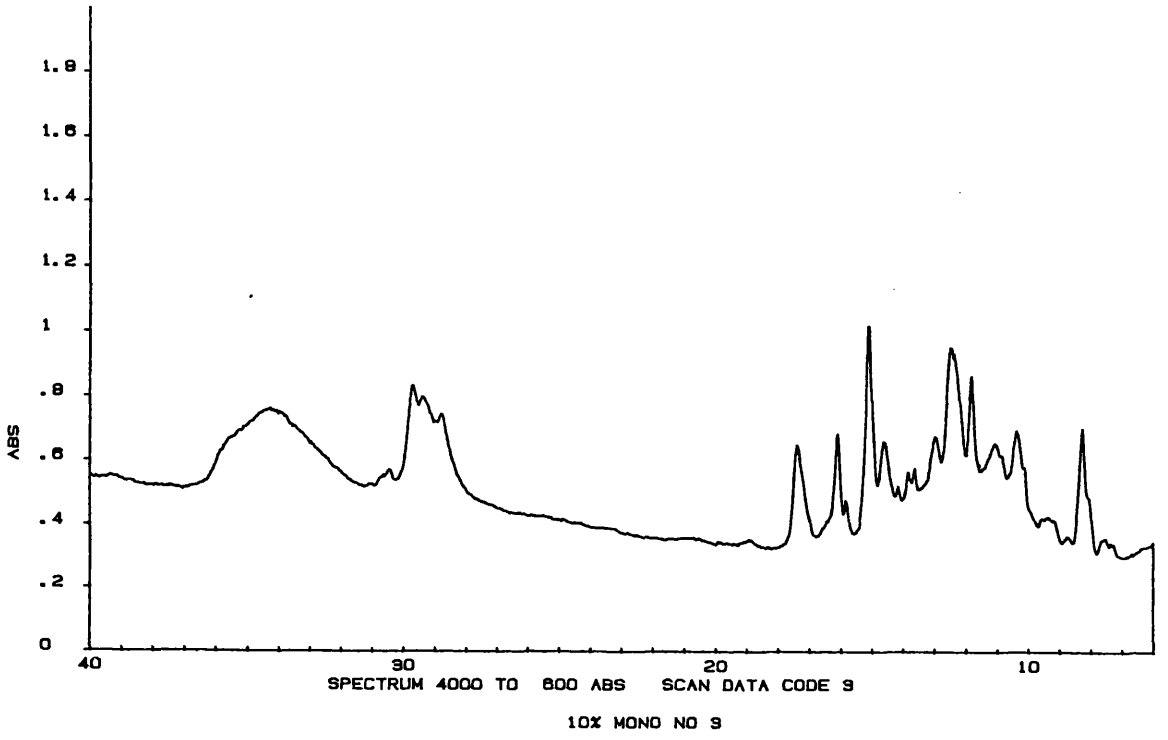

FIG. 37. Infra-red spectrum of 10% urethane neat resin.

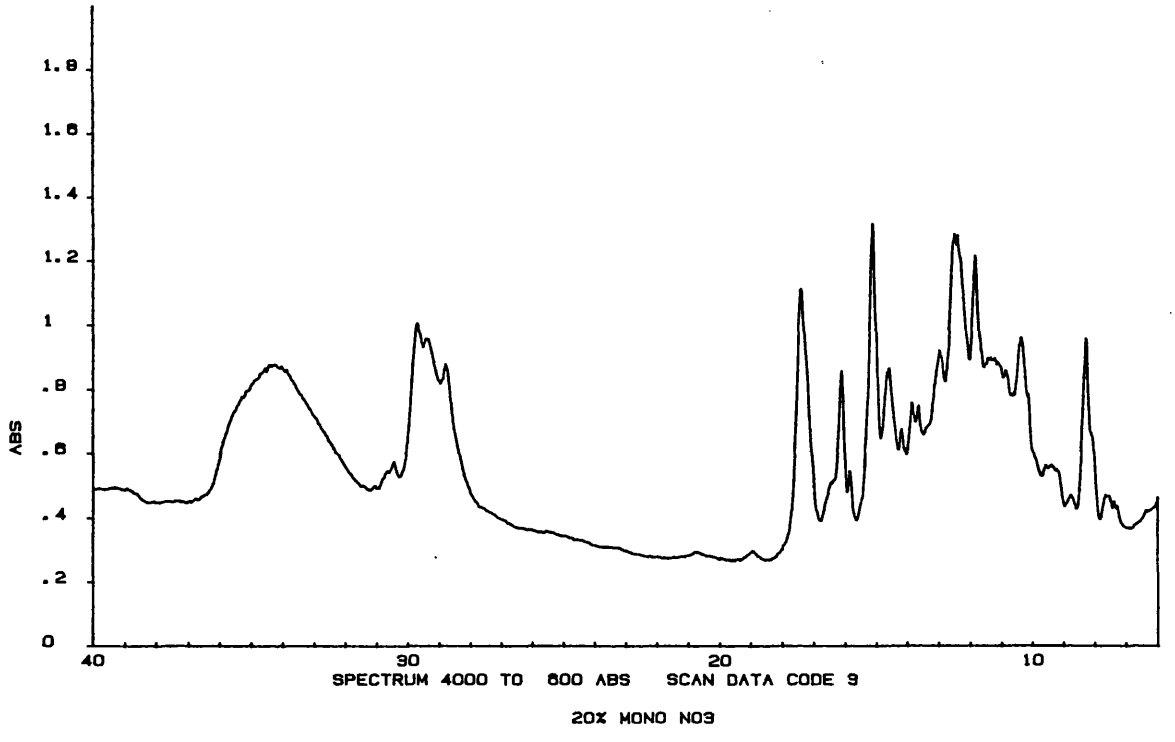

FIG. 38. Infra-red spectrum of 20% urethane neat resin.

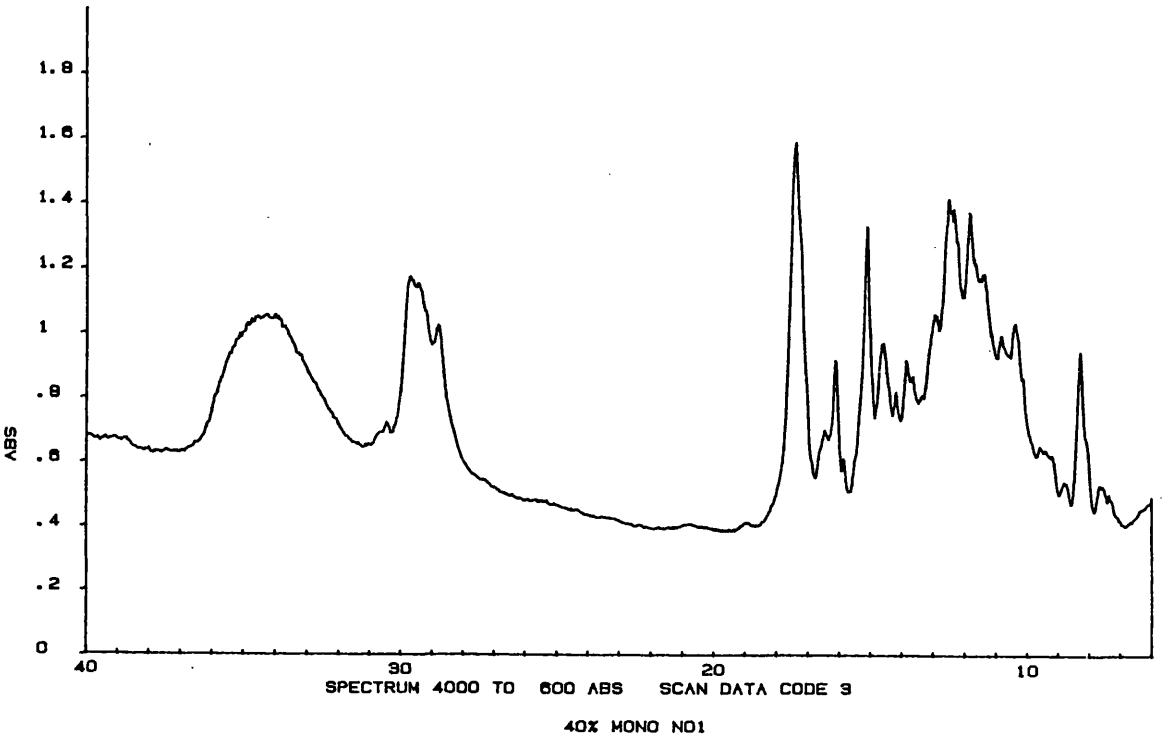

FIG. 39. Infra-red spectrum of 40% urethane neat resin.

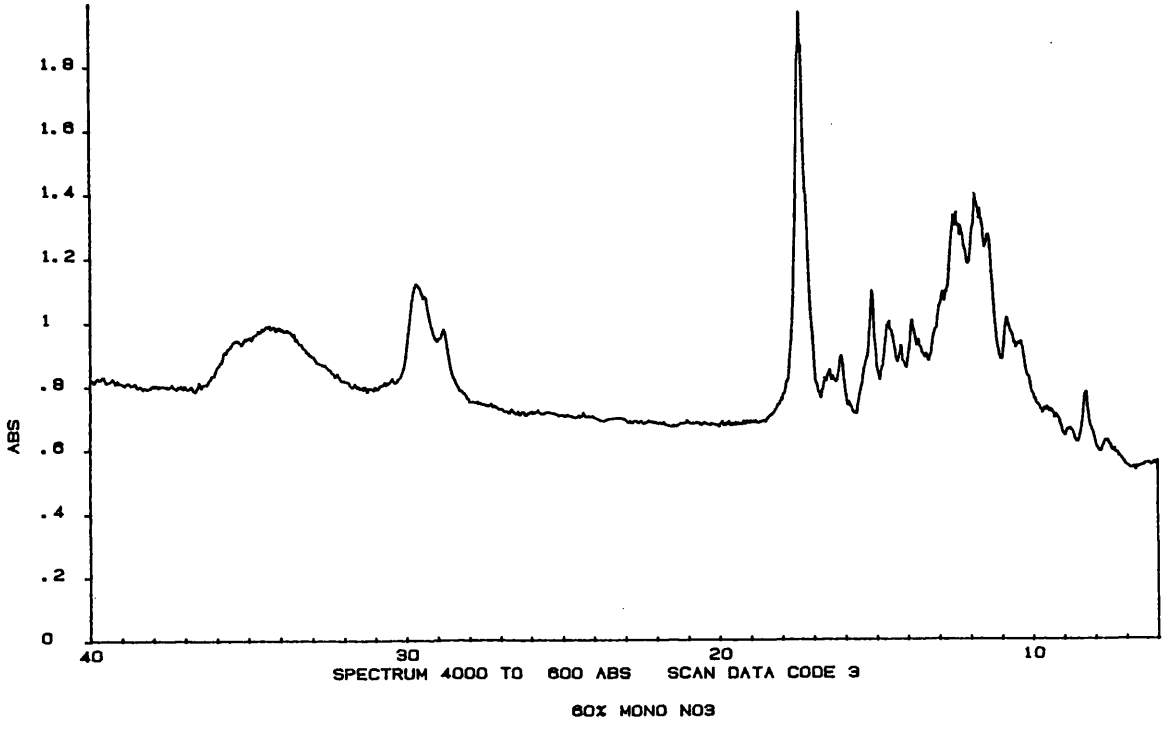

FIG. 40. Infra-red spectrum of 60% urethane neat resin.

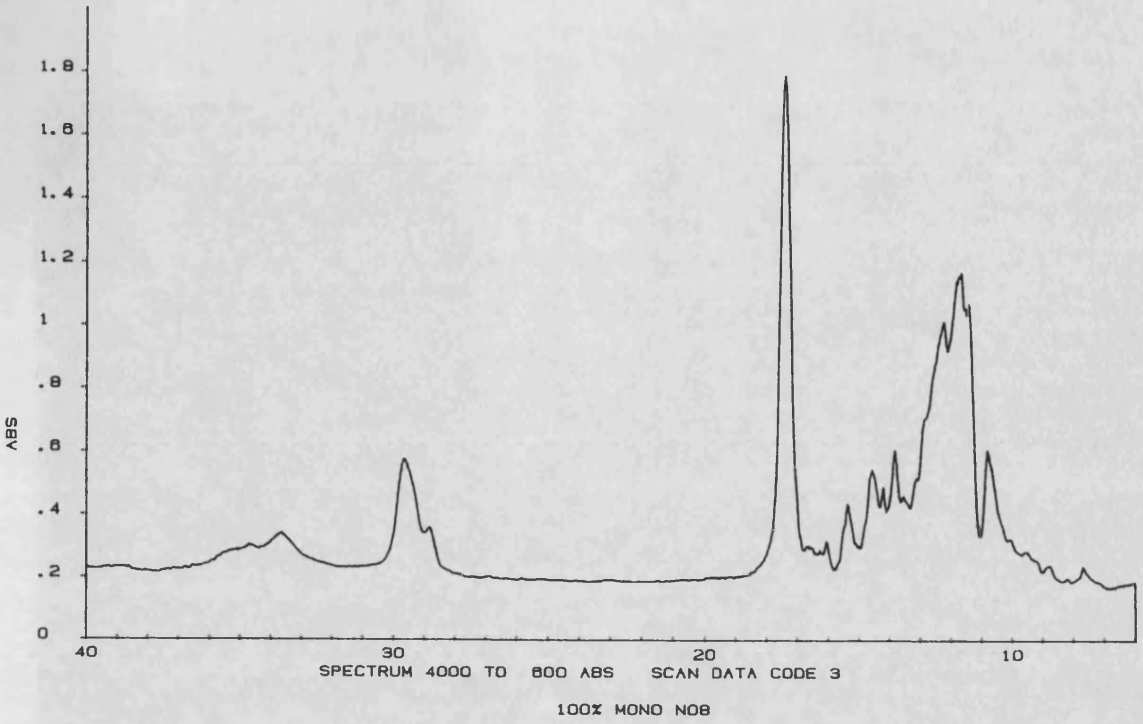

FIG. 41. Infra-red spectrum of 100% urethane neat resin.

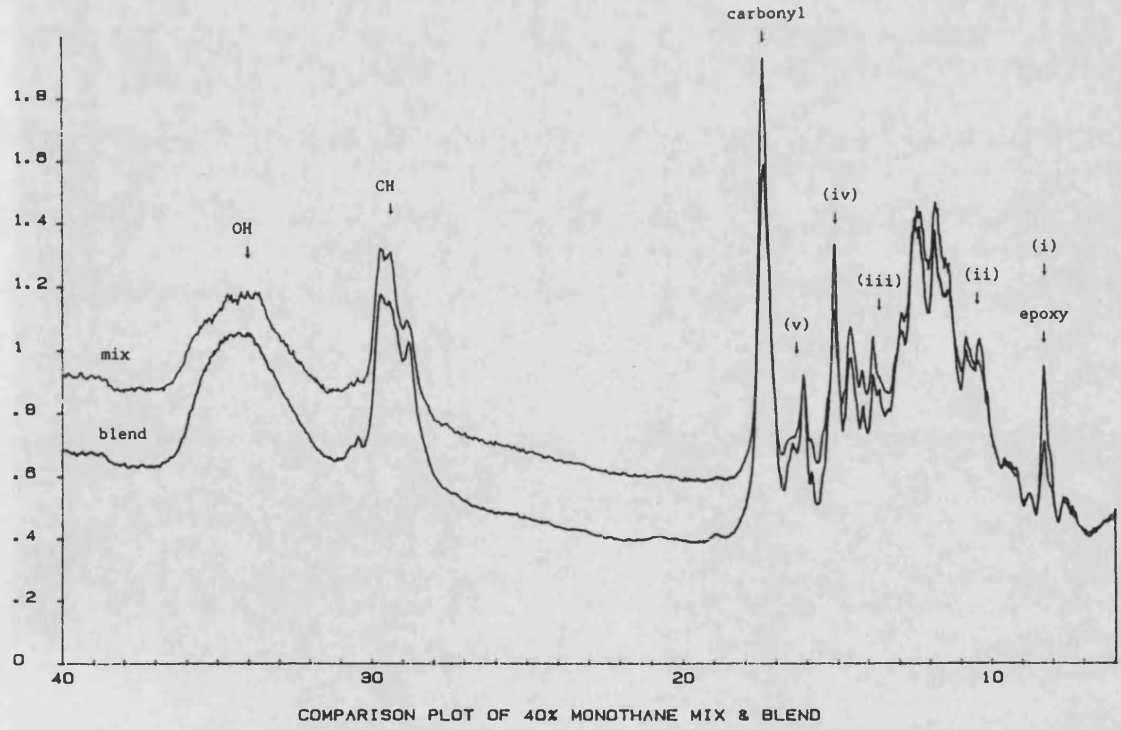

FIG. 42. Comparison of the infra-red spectra of a mixture and blend of 40% urethane/60% epoxy resins.

FIG. 43. Photograph of polishing jig used to prepare coupon specimens.

HARWELL LABORATORY
PHOTOGRAPHIC GROUP

HRC 35830

NOT FOR PUBLICATION

FIG. 44. Photograph of self-aligning tube testing rig with tapered aluminium end fixture.

HARWELL LABORATORY
PHOTOGRAPHIC GROUP

HRC 35829

NOT FOR PUBLICATION

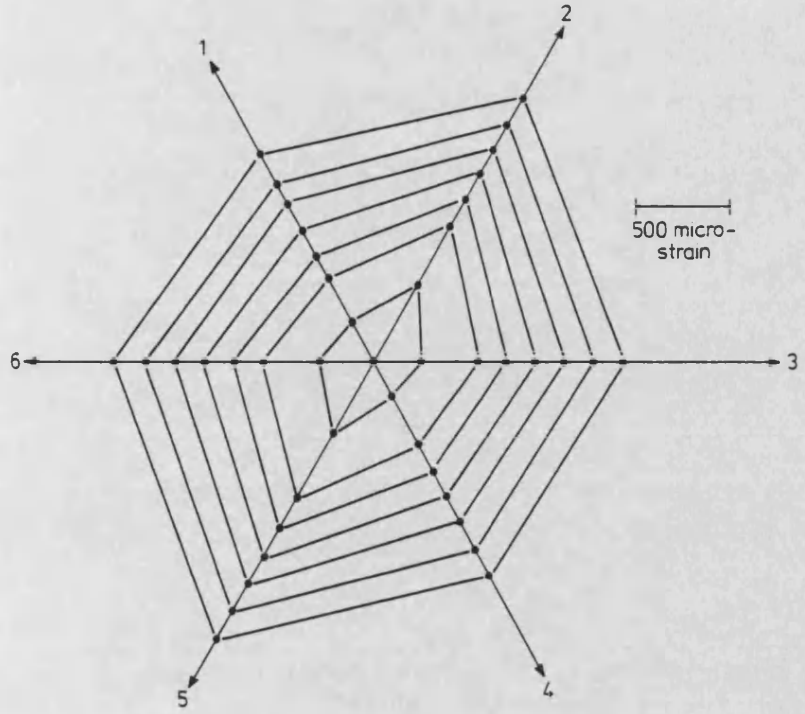

FIG. 45. Strain distribution around the circumference of an axially loaded hoop wound tube.

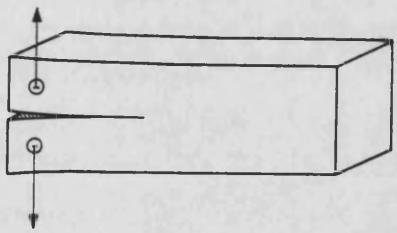

FIG. 46. Schematic of a straight-sided double cantilever beam toughness test specimen.

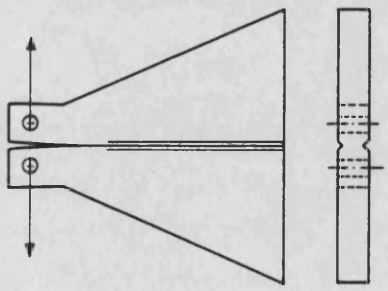

FIG. 47. Schematic of a tapered double cantilever beam toughness test specimen with side grooves for crack guidance.

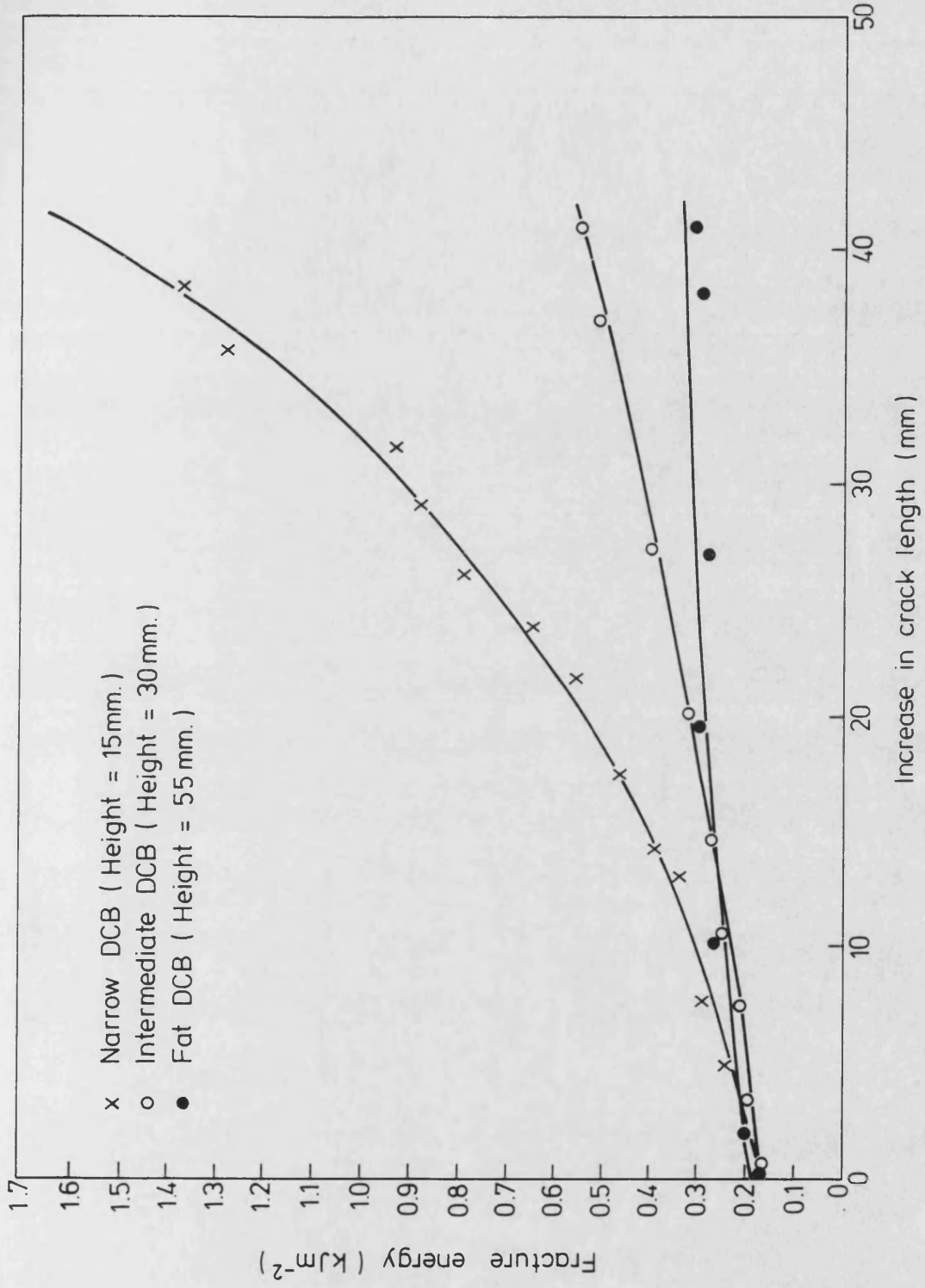

FIG. 48. Variation of G_{IC} fracture toughness with crack length for double cantilever beams of different heights of conventional rigid resin composite.

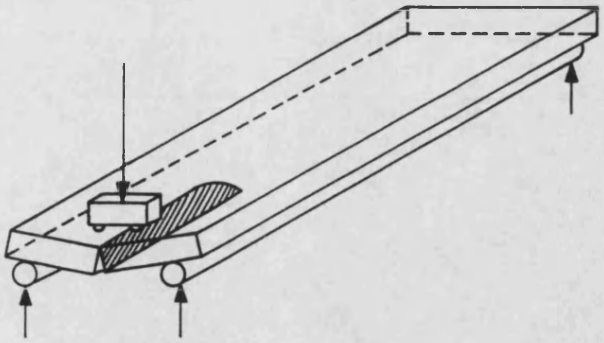

FIG. 49. Schematic of the double torsion toughness test specimen.

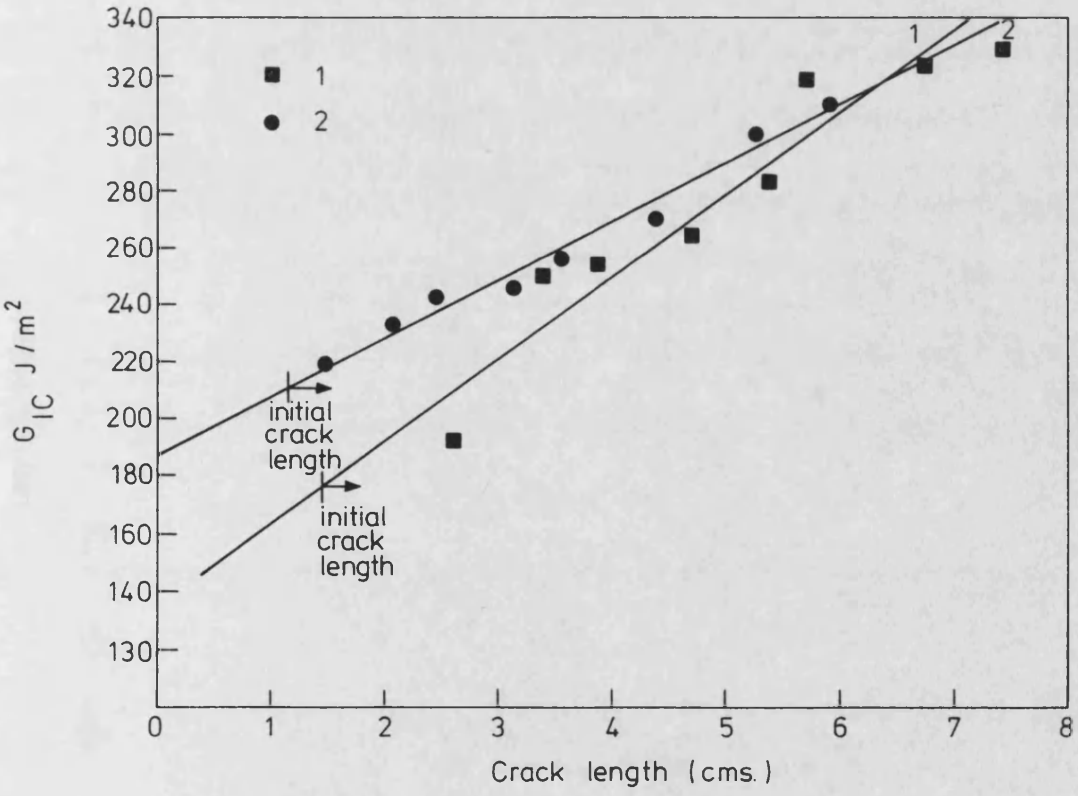

FIG. 50. Variation of G_{IC} fracture toughness with crack length for double torsion specimens of conventional rigid resin composite.

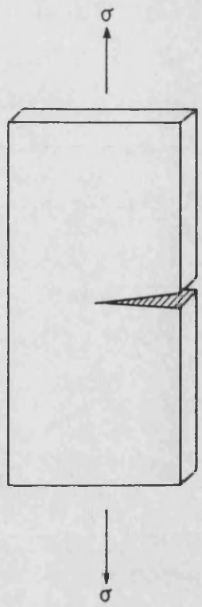

FIG. 51. Schematic of the single edge notched toughness test specimen.

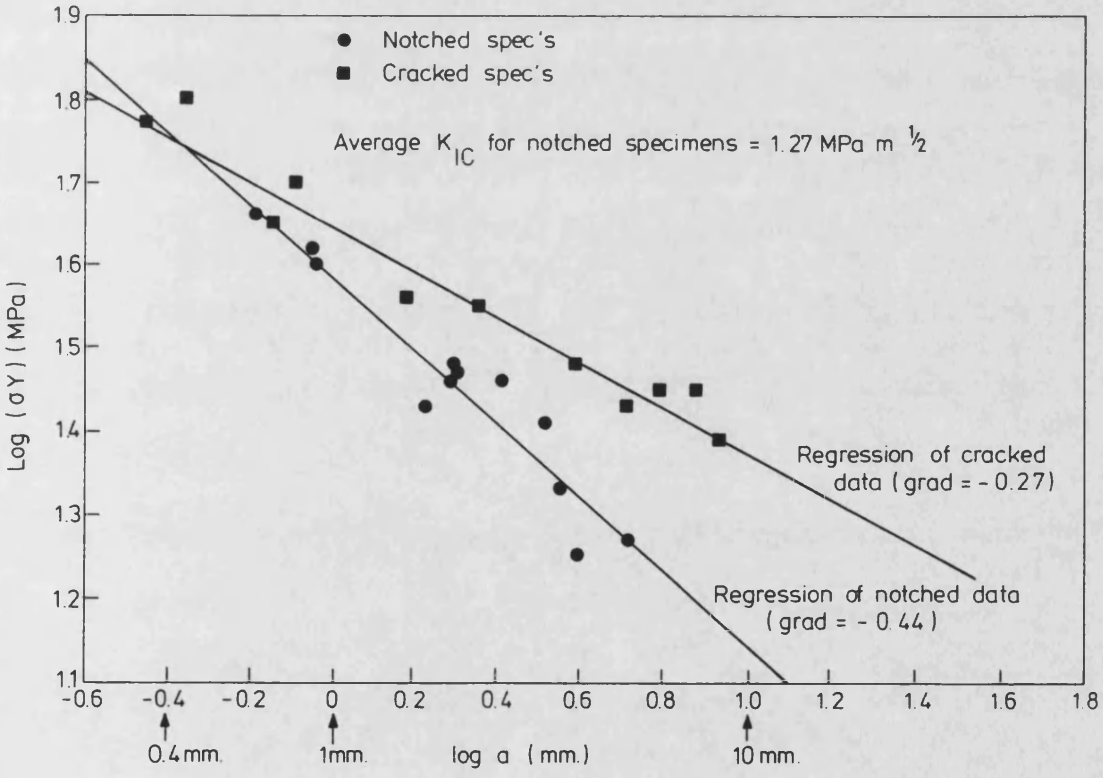

FIG. 52. Single edge notched results for conventional rigid resin composite with notches and cracks. Data plotted as log (σY) versus log (a).

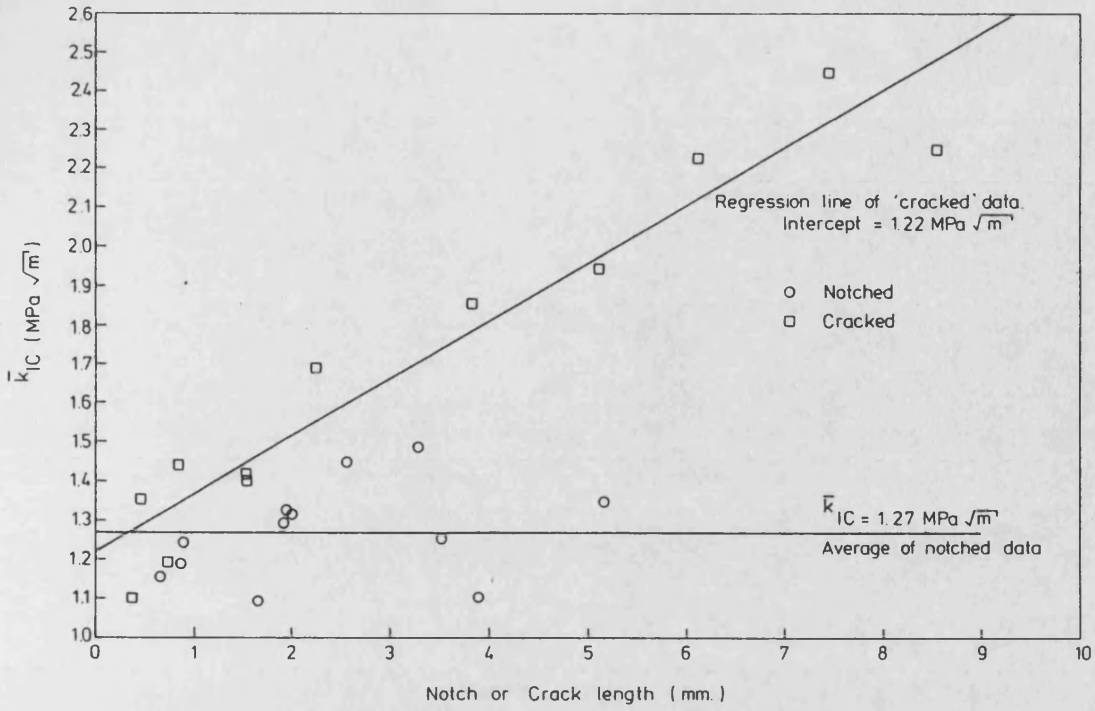

FIG. 53. Single edge notched results for conventional rigid resin composite with notches and cracks. Data plotted as K_{IC} versus crack or notch length (a).

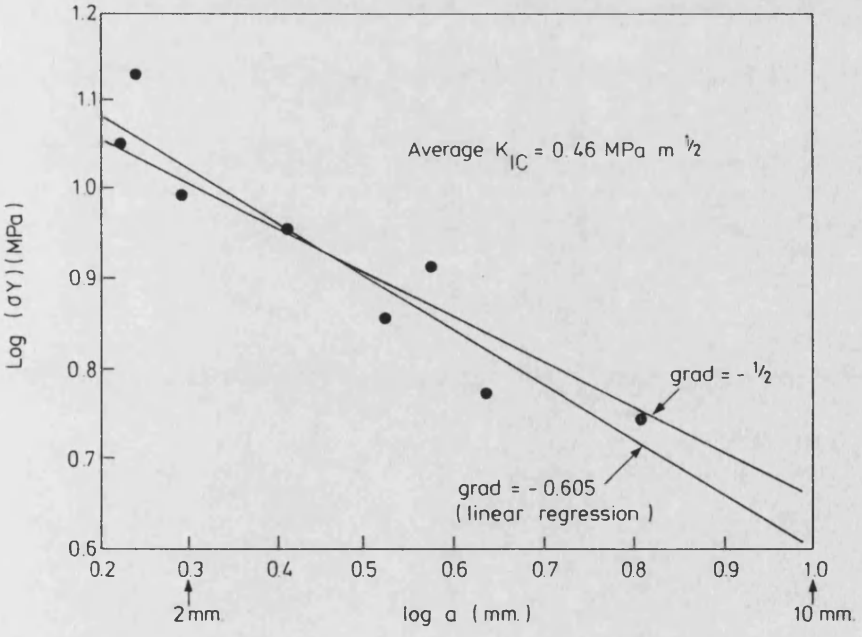

FIG. 54. Single edge notched results for conventional neat rigid resin with varying crack lengths. Data plotted as log (σY) versus log (a).

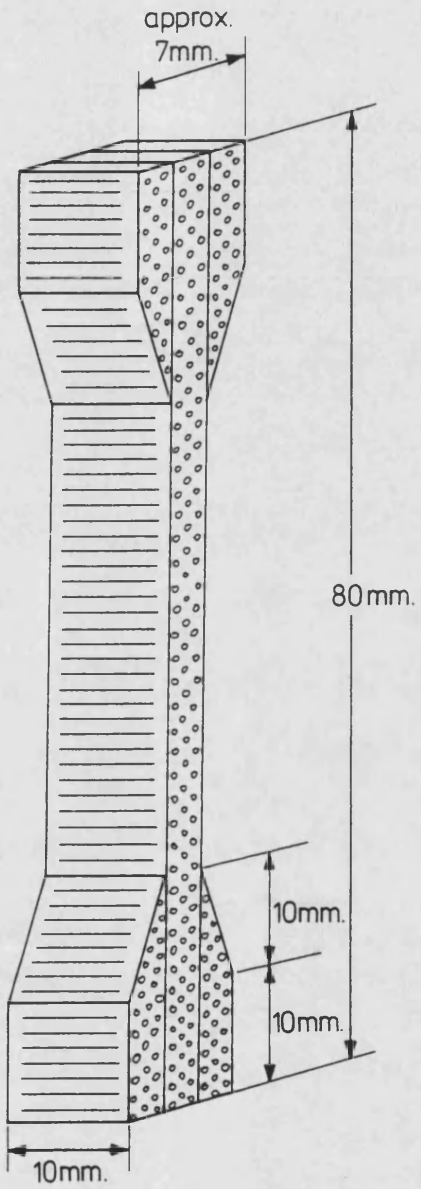

FIG. 55. Schematic of the transverse composite straight sided coupons.

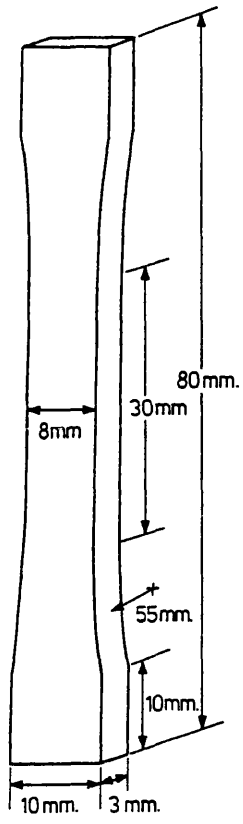

FIG. 56. Schematic of the dogbone specimen used for 0 - 60% urethane neat resins.

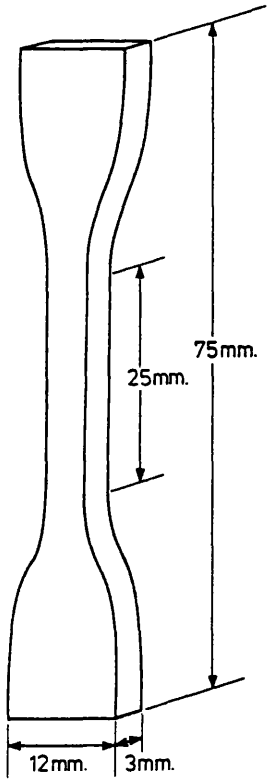

FIG. 57. Schematic of the dogbone specimen used for 100% urethane neat resin.

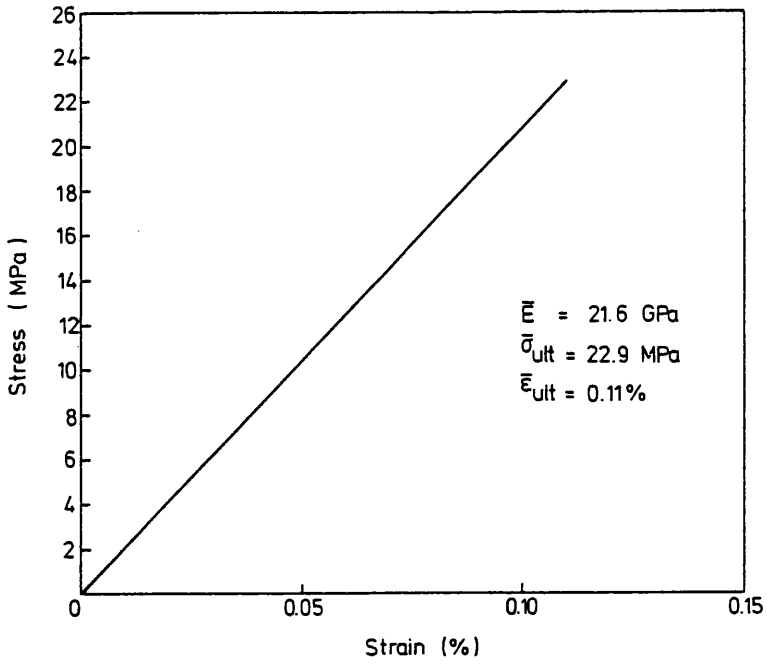

FIG. 58. Stress/strain response of 0% urethane transverse composite.

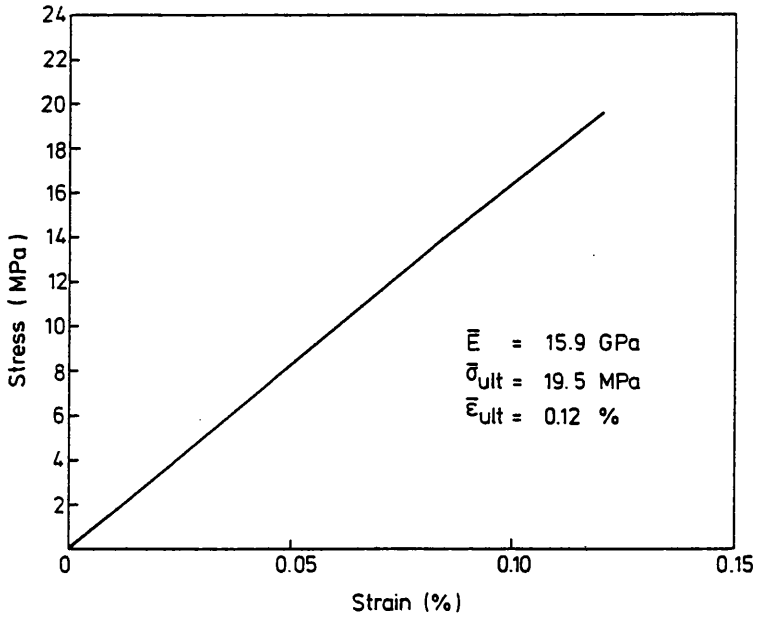

FIG. 59. Stress/strain response of 10% urethane transverse composite.

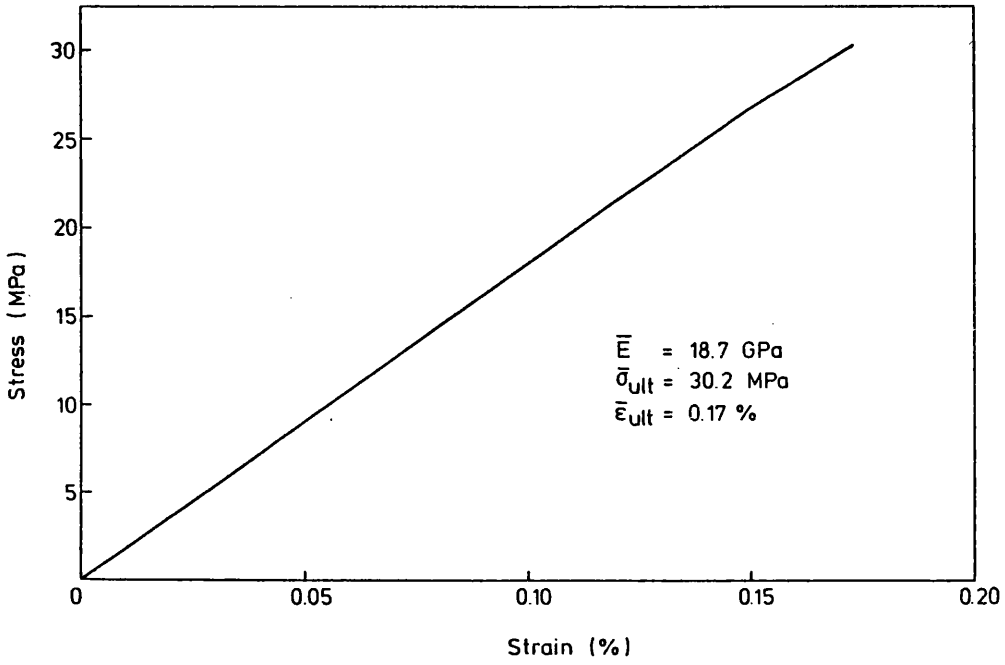

FIG. 60. Stress/strain response of 20% urethane transverse composite.

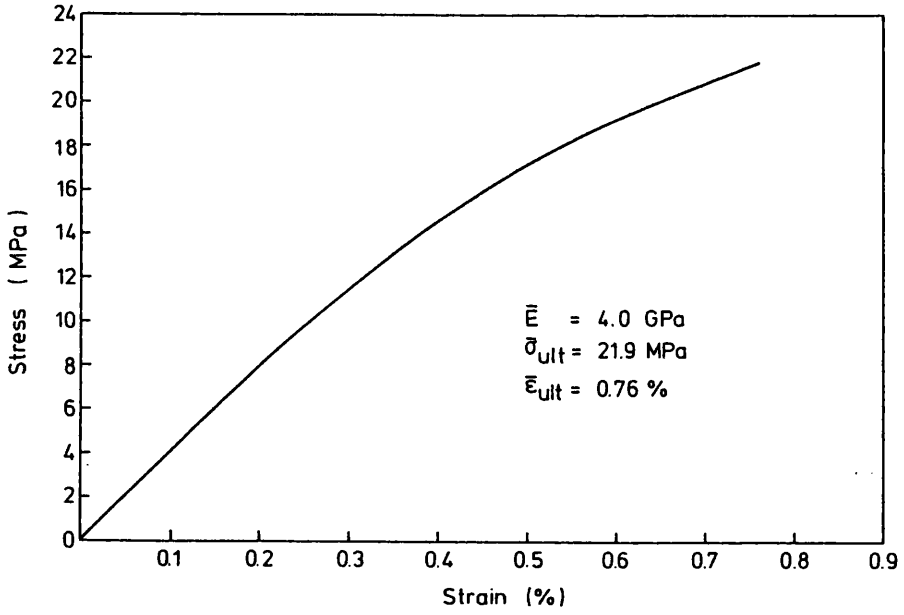

FIG. 61. Stress/strain response of 40% urethane transverse composite.

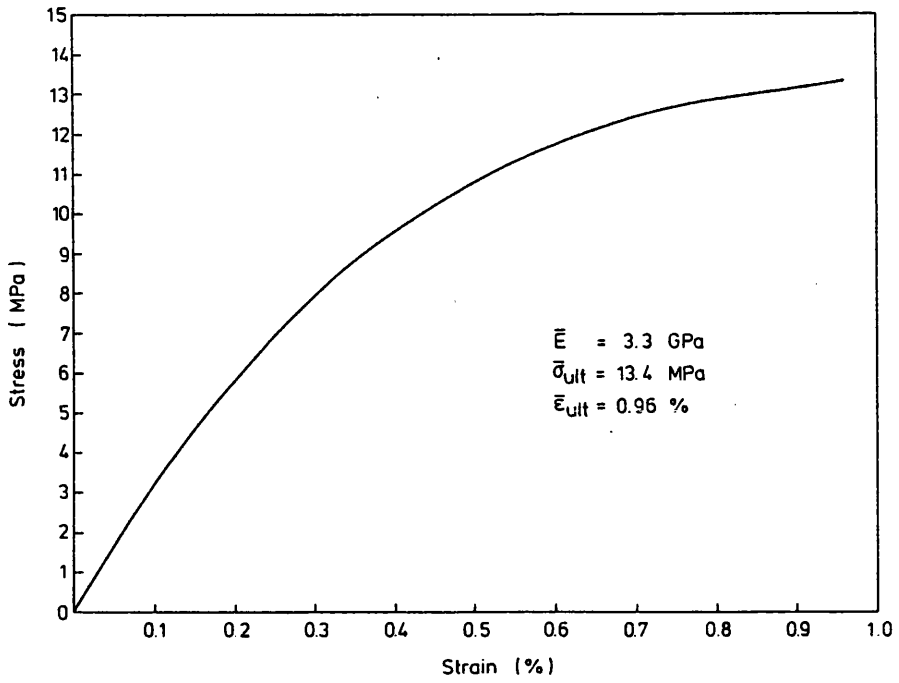

FIG. 62. Stress/strain response of 60% urethane transverse composite.

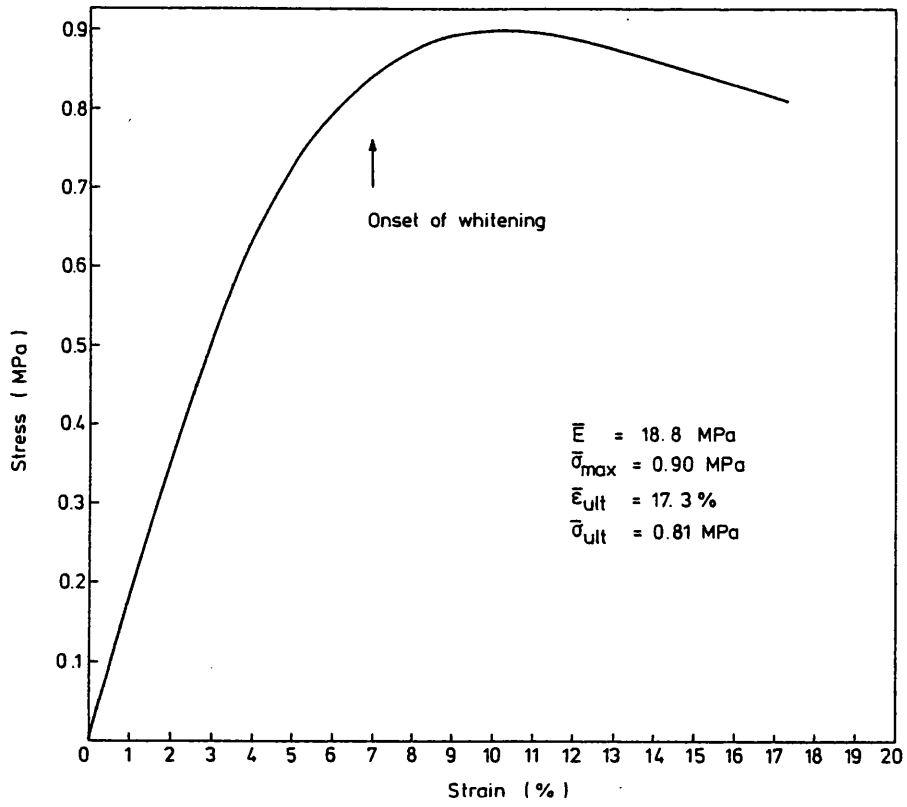

FIG. 63. Stress/strain response of 100% urethane transverse composite.

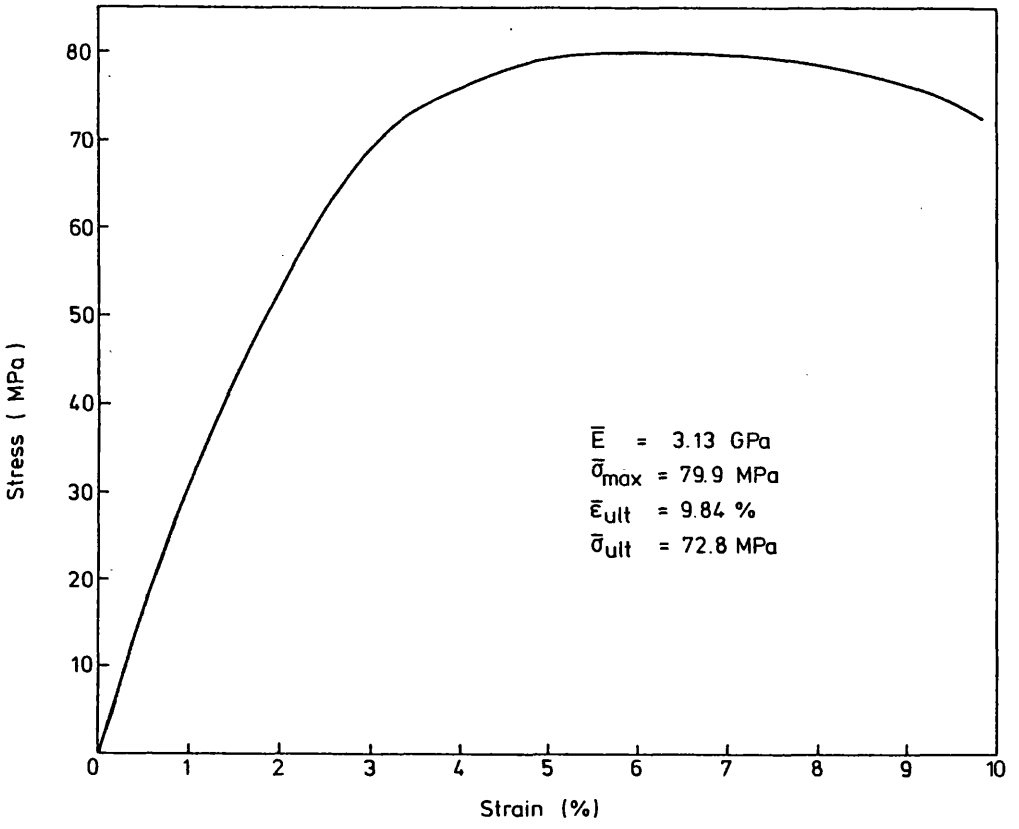

FIG. 64. Stress/strain response of 0% urethane neat resin.

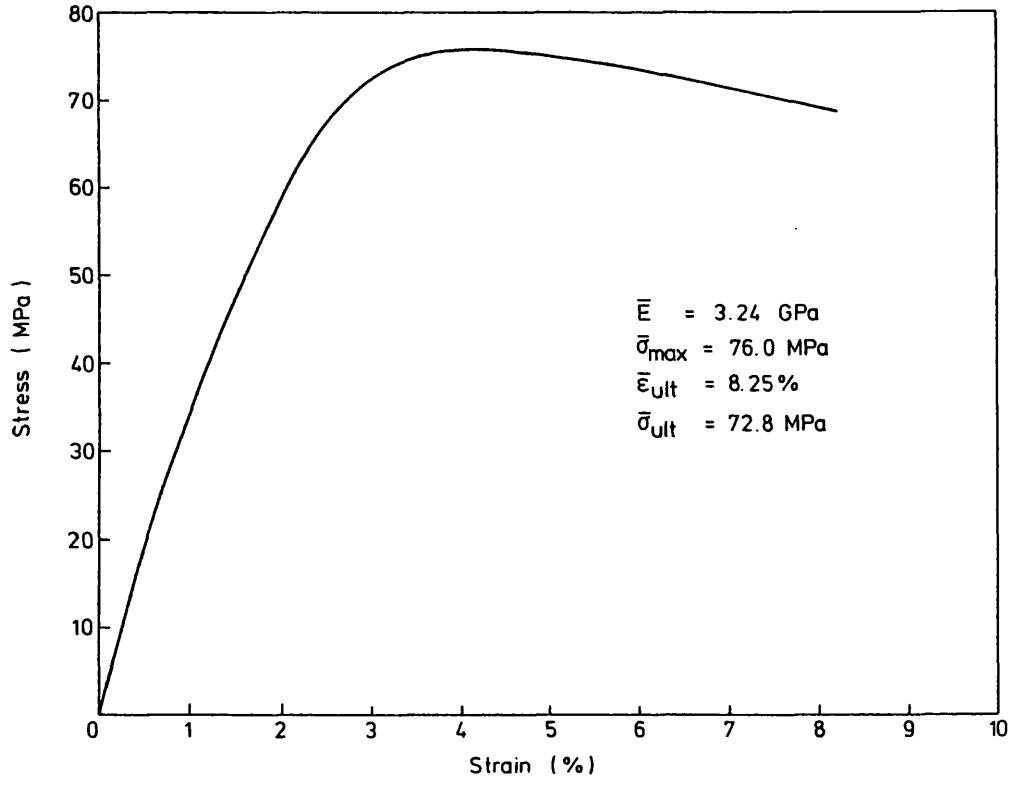

FIG. 65. Stress/strain response of 10% urethane neat resin.

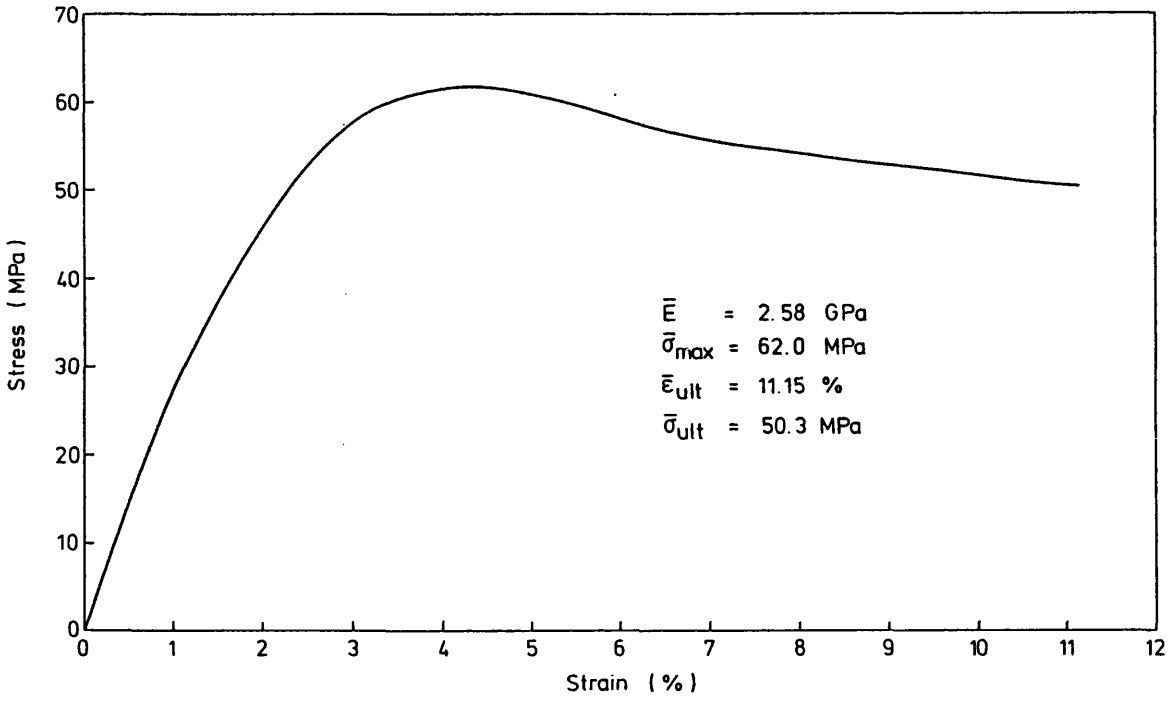

FIG. 66. Stress/strain response of 20% urethane neat resin.

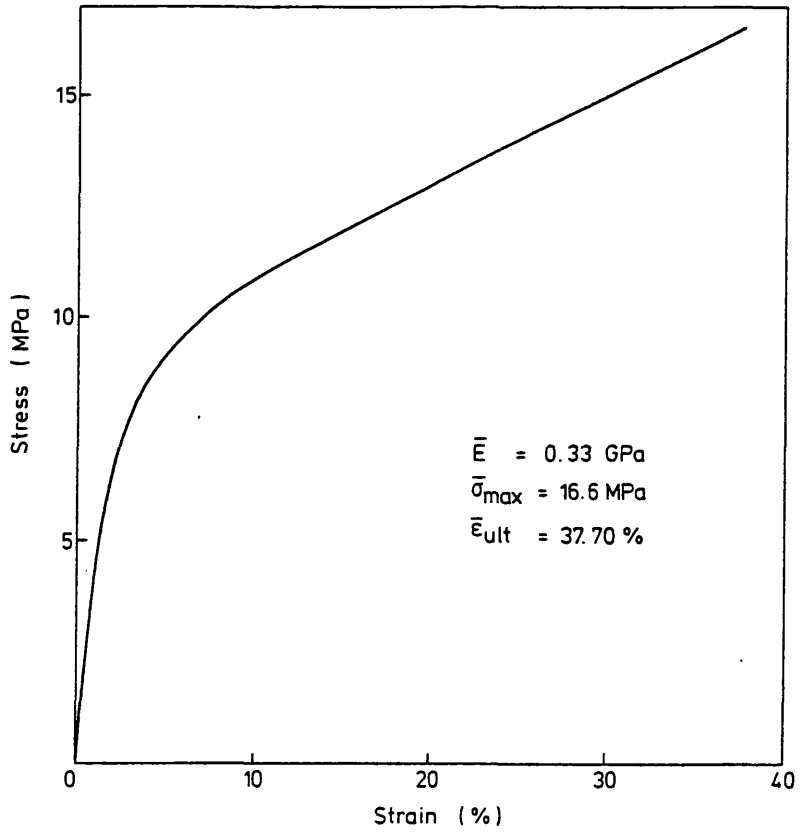

FIG. 67. Stress/strain response of 40% urethane neat resin.

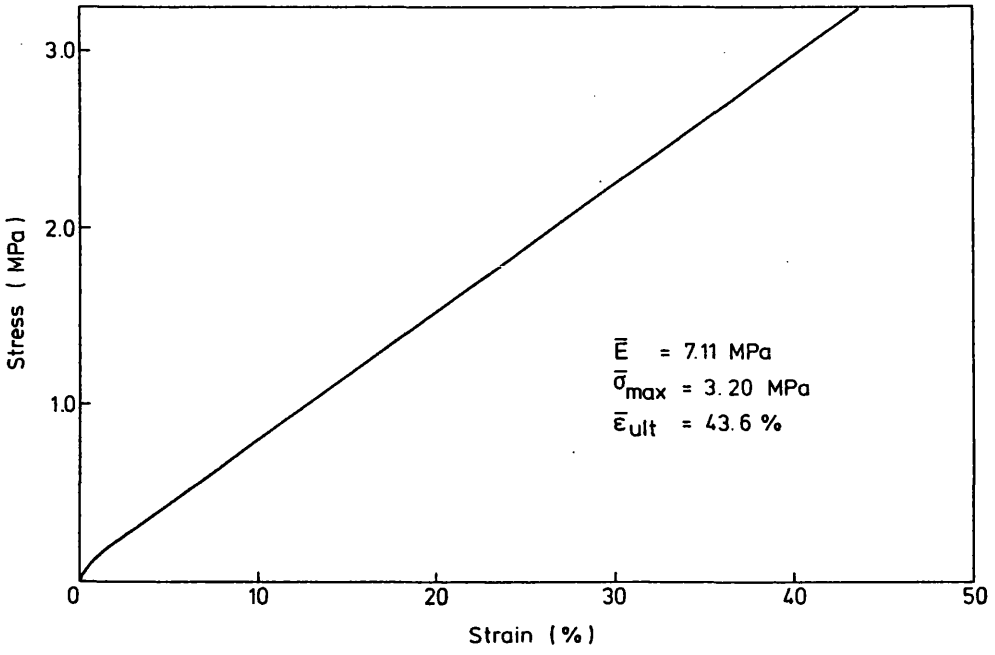

FIG. 68. Stress/strain response of 60% urethane neat resin.

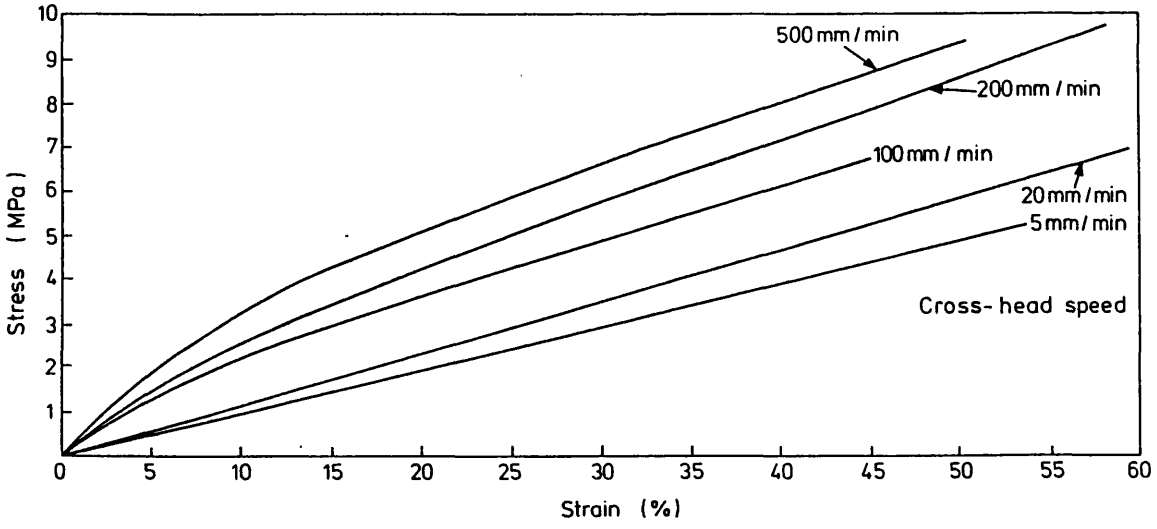

FIG. 69. Stress/strain response of 60% urethane neat resin at various testing speeds.

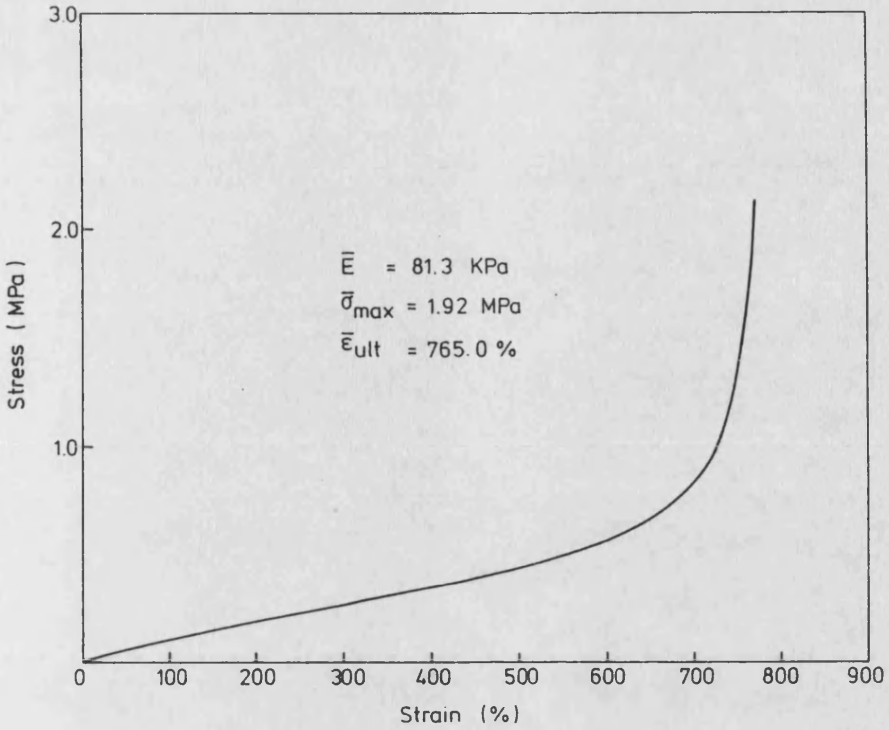

FIG. 70. Stress/strain response of 100% urethane neat resin.

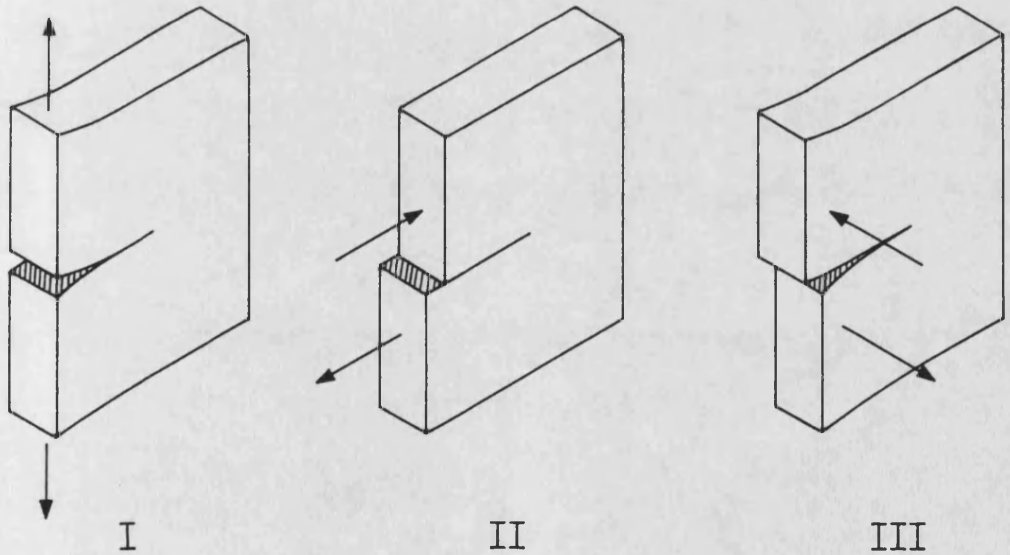

FIG. 71. The three modes of crack extension. (From Pascoe, ref 87).

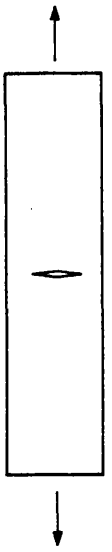

FIG. 72. Schematic of centre notched plate specimen in tension.

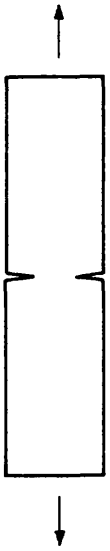

FIG. 73. Schematic of double edge notched plate specimen in tension.

FIG. 74. Schematic of single edge notched plate specimen in tension.

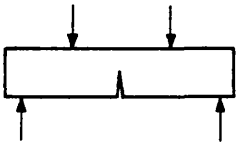

FIG. 75. Schematic of single edge notched specimen in 3-point bending.

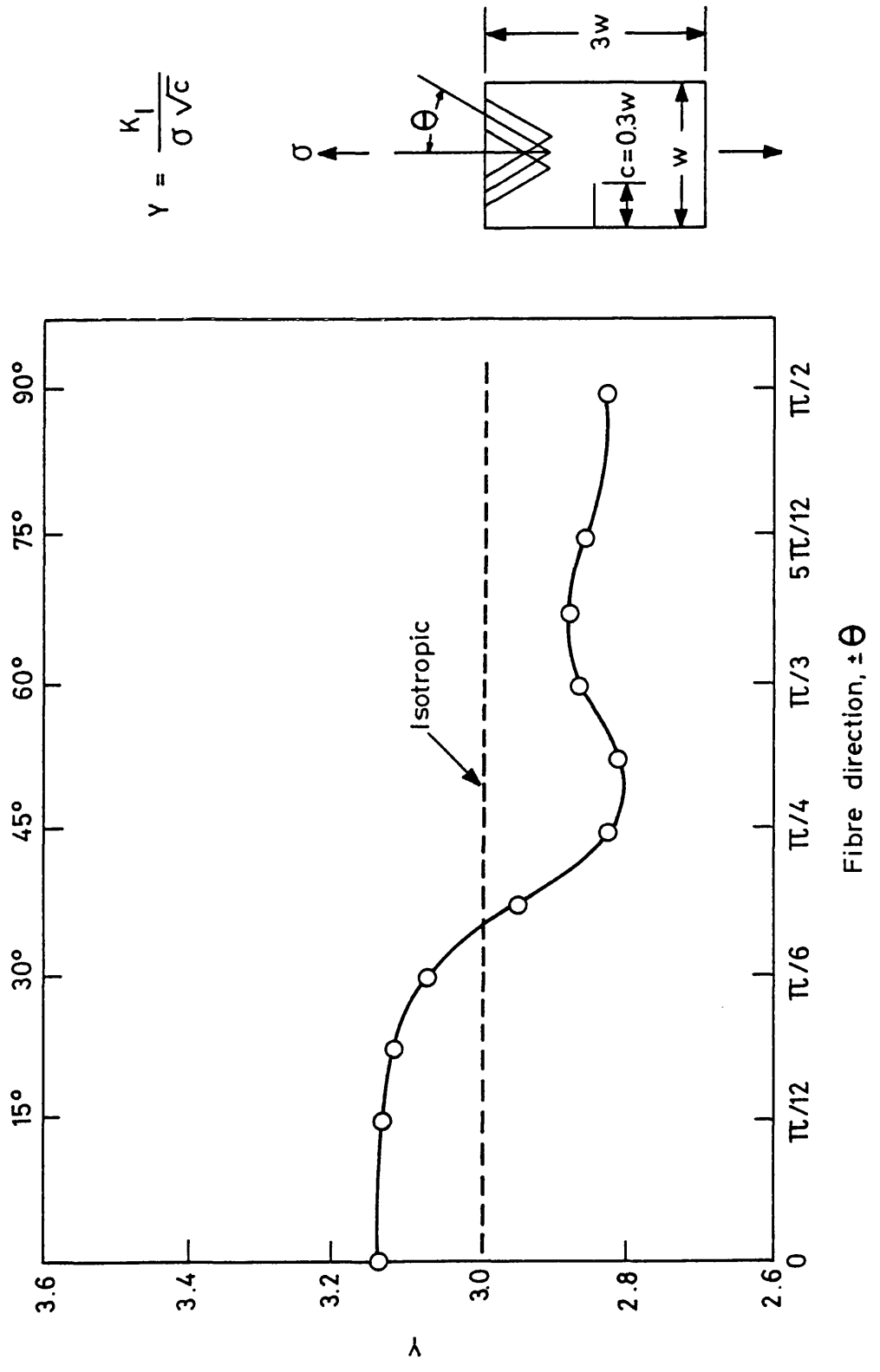

FIG. 76. Anisotropic finite width correction factors for various orientations of carbon fibre/epoxy single edge notched specimens. (From Mandell, McGarry, Wang and Im, ref 98).

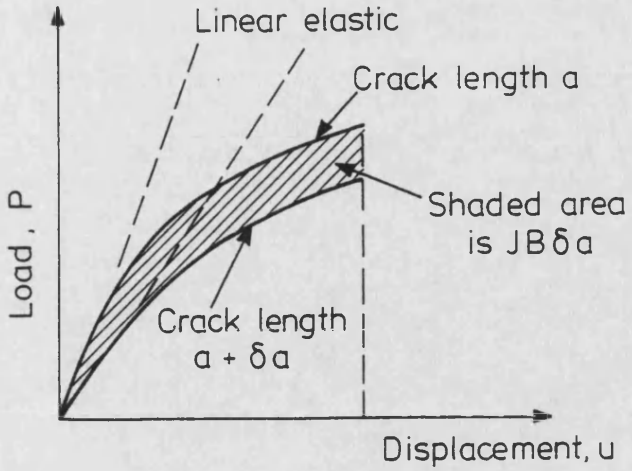

FIG. 77. Graphical description of the determination of J integrals. (From Knott, ref 89).

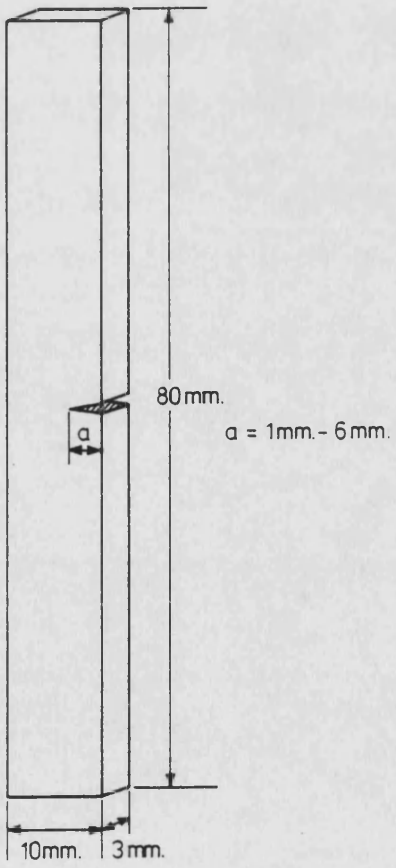

FIG. 78. Single edge notched specimen used for fracture mechanics tests on neat resin and transverse composite materials.

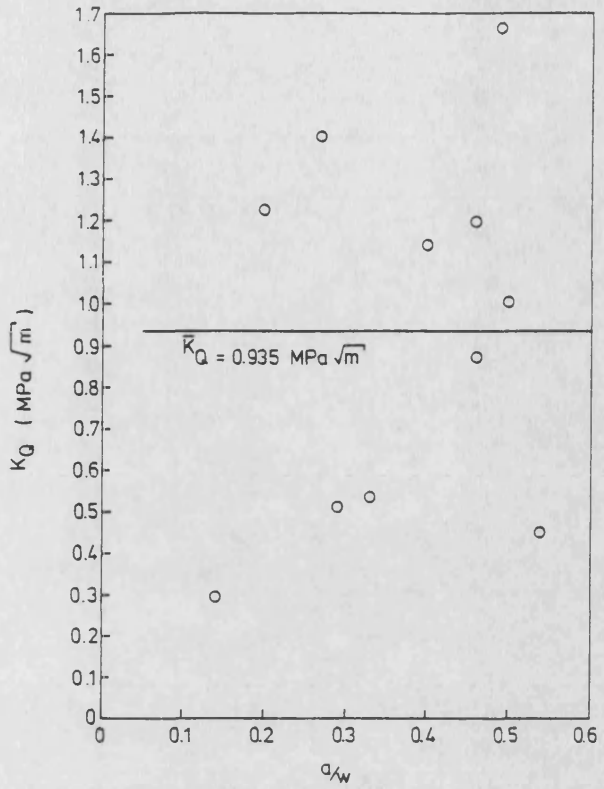

FIG. 79. Candidate fracture toughness (K_Q) against relative crack length for 0% urethane transverse composite.

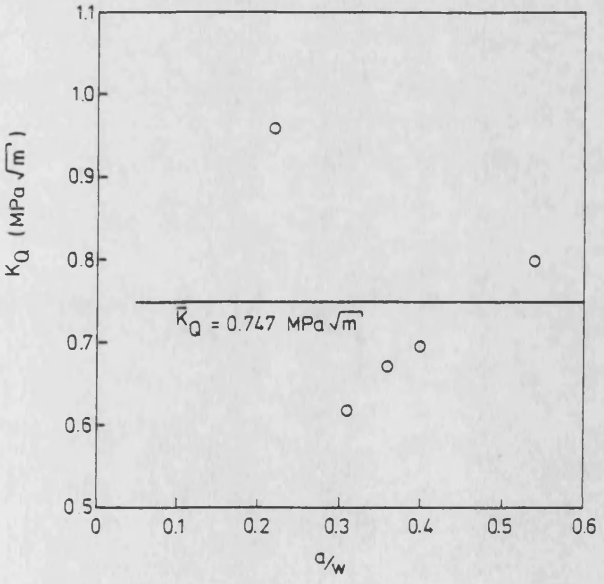

FIG. 80. Candidate fracture toughness (K_Q) against relative crack length for 10% urethane transverse composite.

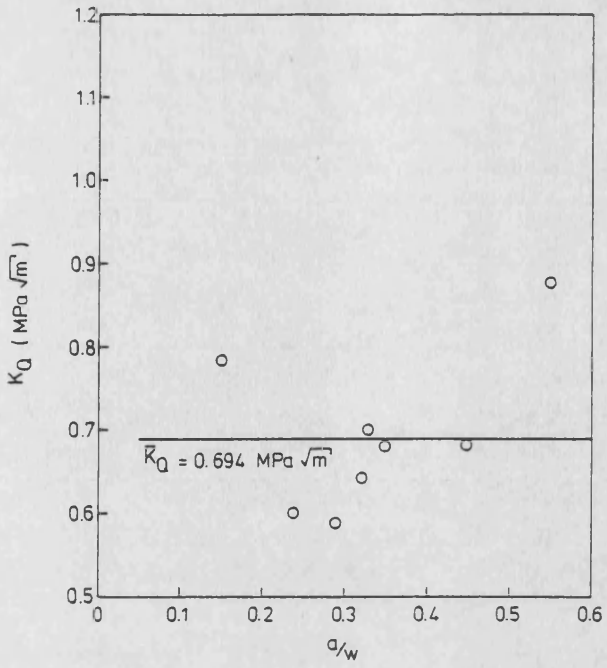

FIG. 81. Candidate fracture toughness (K_Q) against relative crack length for 20% urethane transverse composite.

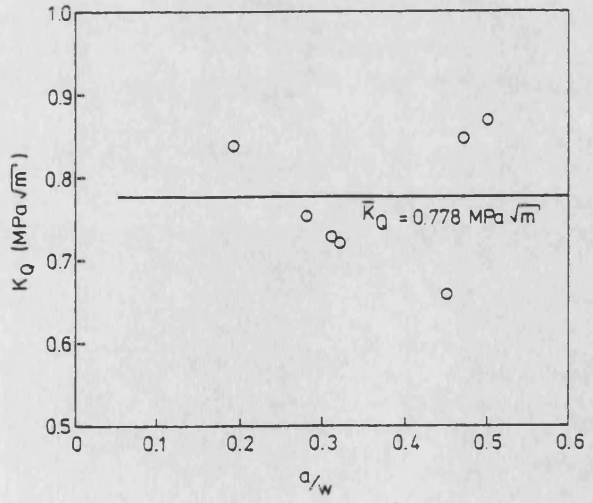

FIG. 82. Candidate fracture toughness (K_Q) against relative crack length for 40% urethane transverse composite.

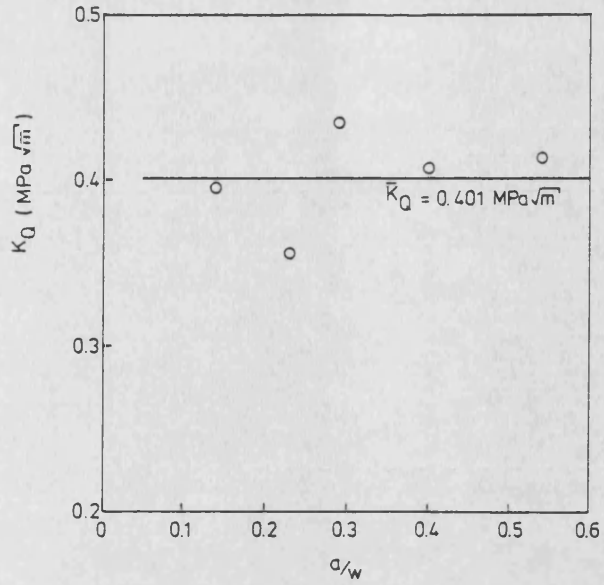

FIG. 83. Candidate fracture toughness (K_Q) against relative crack length for 60% urethane transverse composite.

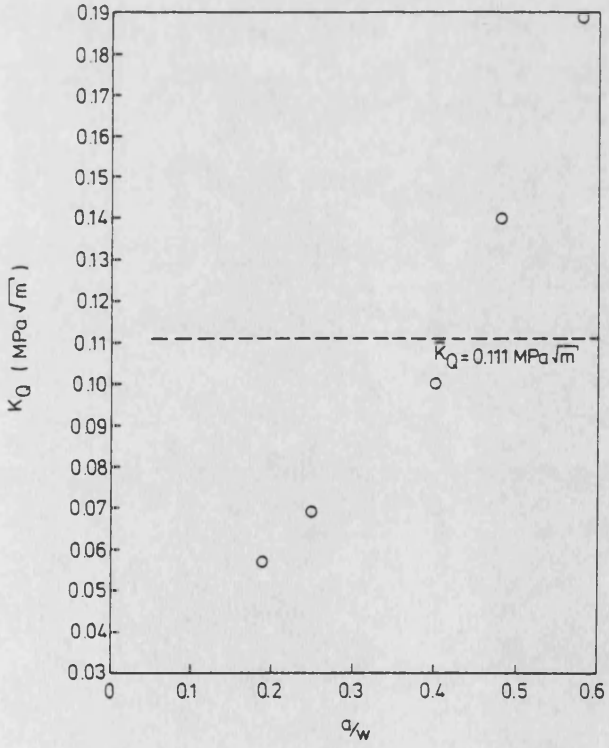

FIG. 84. Candidate fracture toughness (K_Q) against relative crack length for 100% urethane transverse composite.

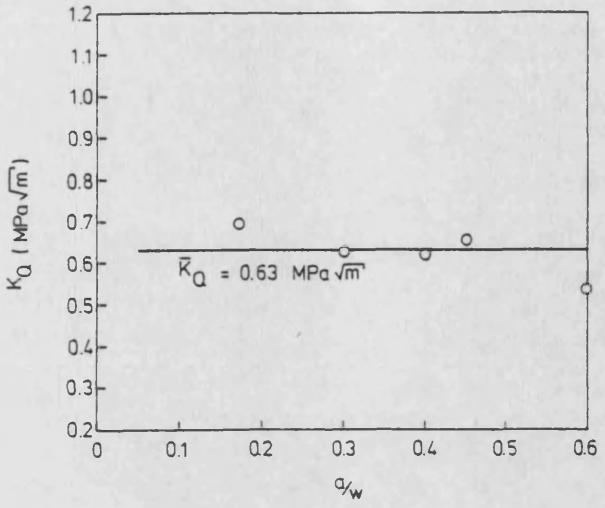

FIG. 85. Candidate fracture toughness (K_Q) against relative crack length for 0% urethane neat resin.

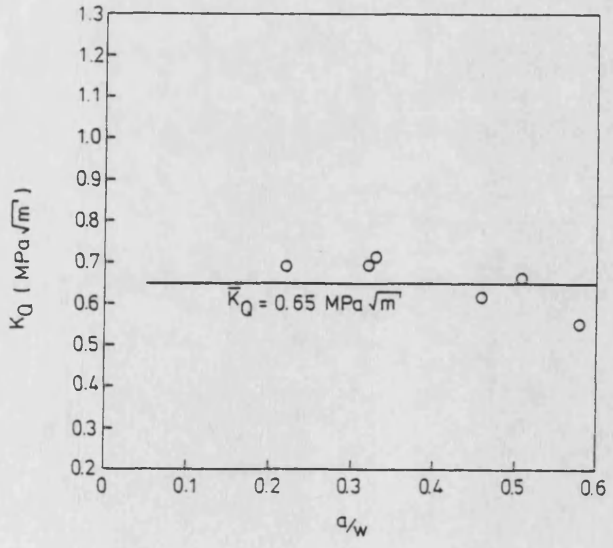

FIG. 86. Candidate fracture toughness (K_Q) against relative crack length for 10% urethane neat resin.

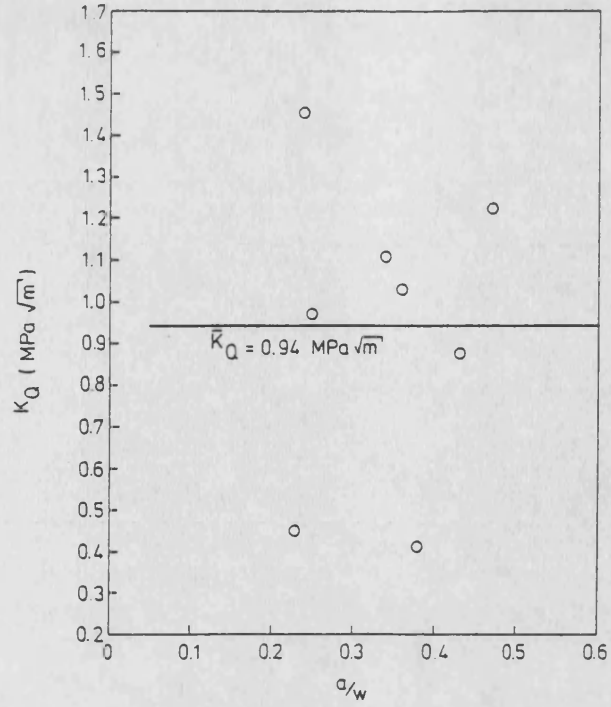

FIG. 87. Candidate fracture toughness (K_Q) against relative crack length for 20% urethane neat resin.

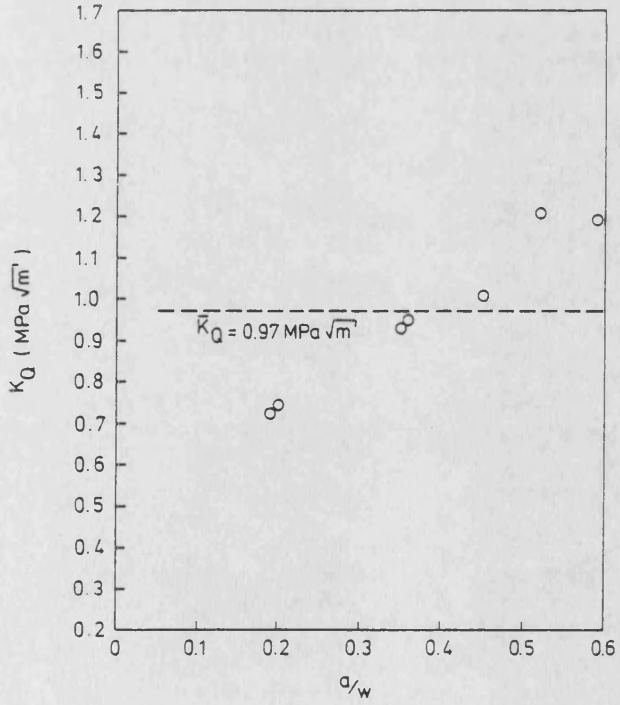

FIG. 88. Candidate fracture toughness (K_Q) against relative crack length for 40% urethane neat resin.

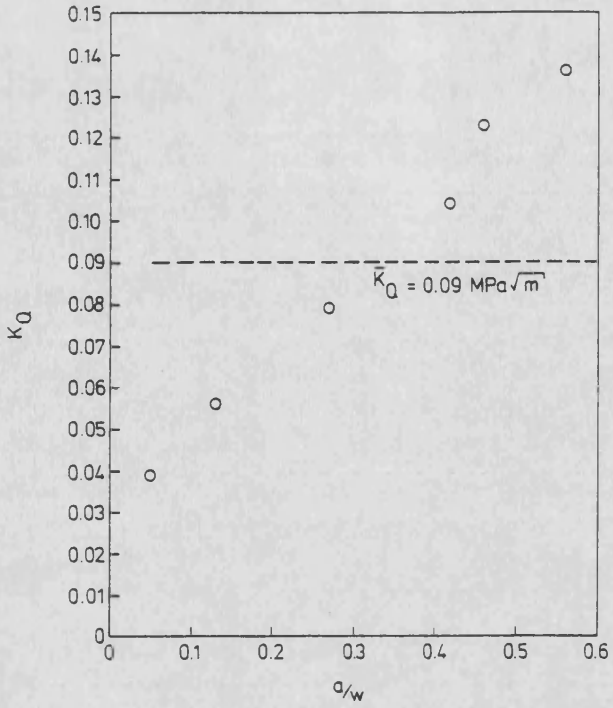

FIG. 89. Candidate fracture toughness (K_Q) against relative crack length for 60% urethane neat resin.

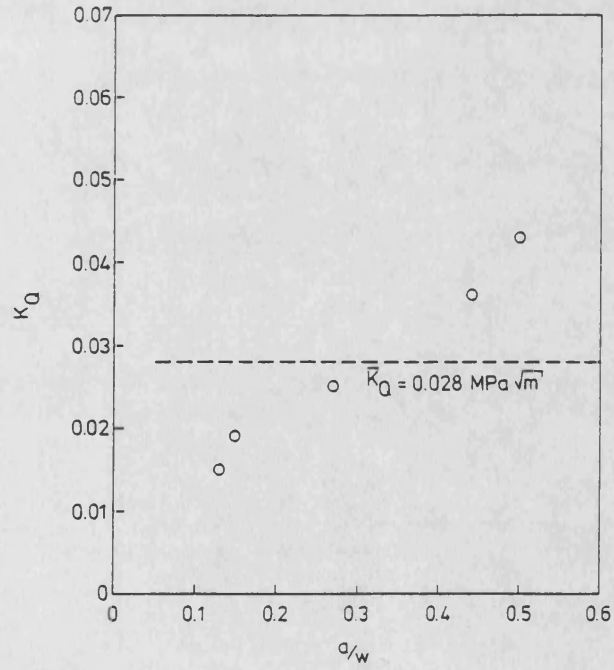

FIG. 90. Candidate fracture toughness values (K_Q) against relative crack length for 100% urethane neat resin.

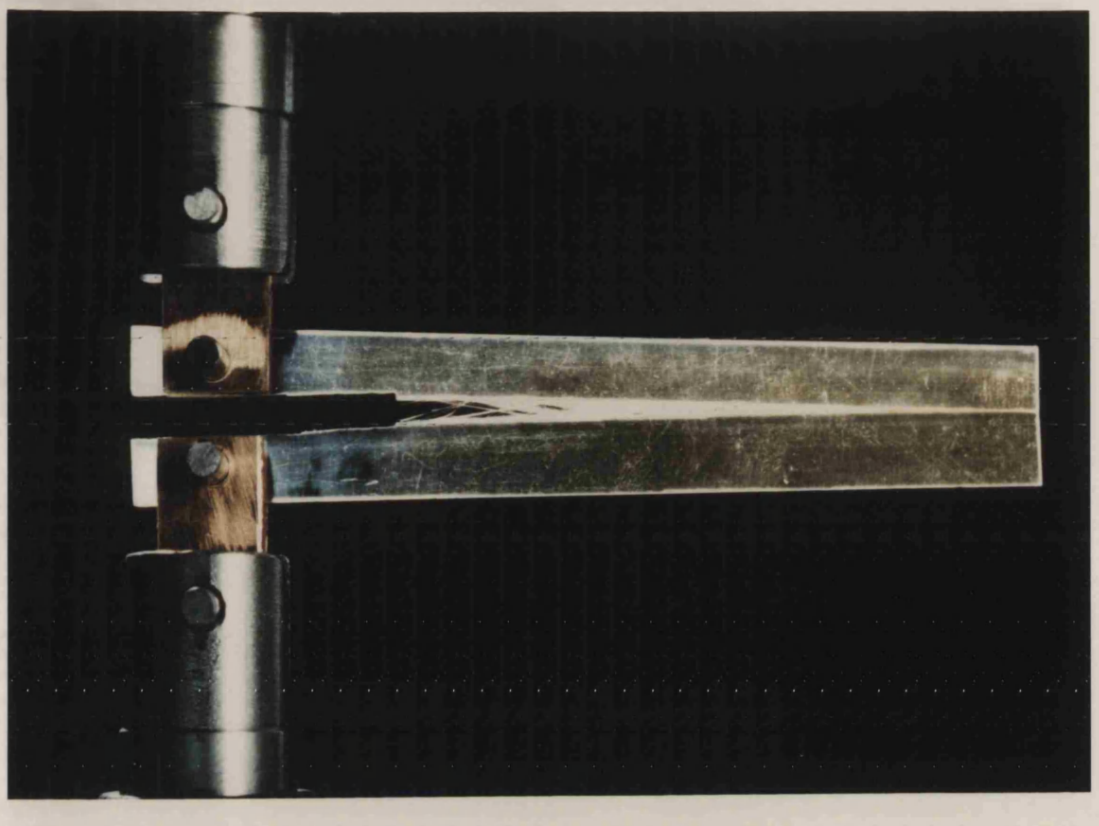

FIG. 91. Photograph of narrow double cantilever beam showing the tied zone of fracture face bridging stringers.

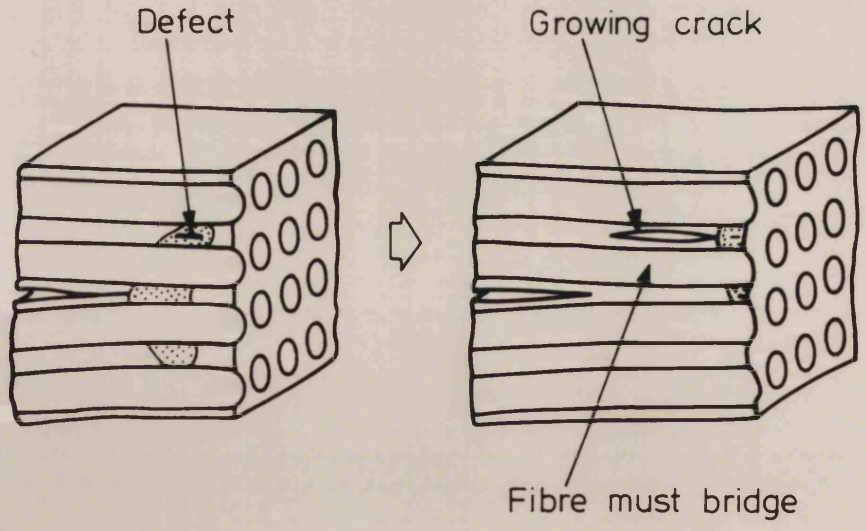

FIG. 92. Schematic of transverse crack propagation by nucleation of flaws ahead of a crack tip. (From Johnson and Mangalgiri, ref 62).

HARWELL LABORATORY
PHOTOGRAPHIC GROUP

HRC 38777

NOT FOR PUBLICATION

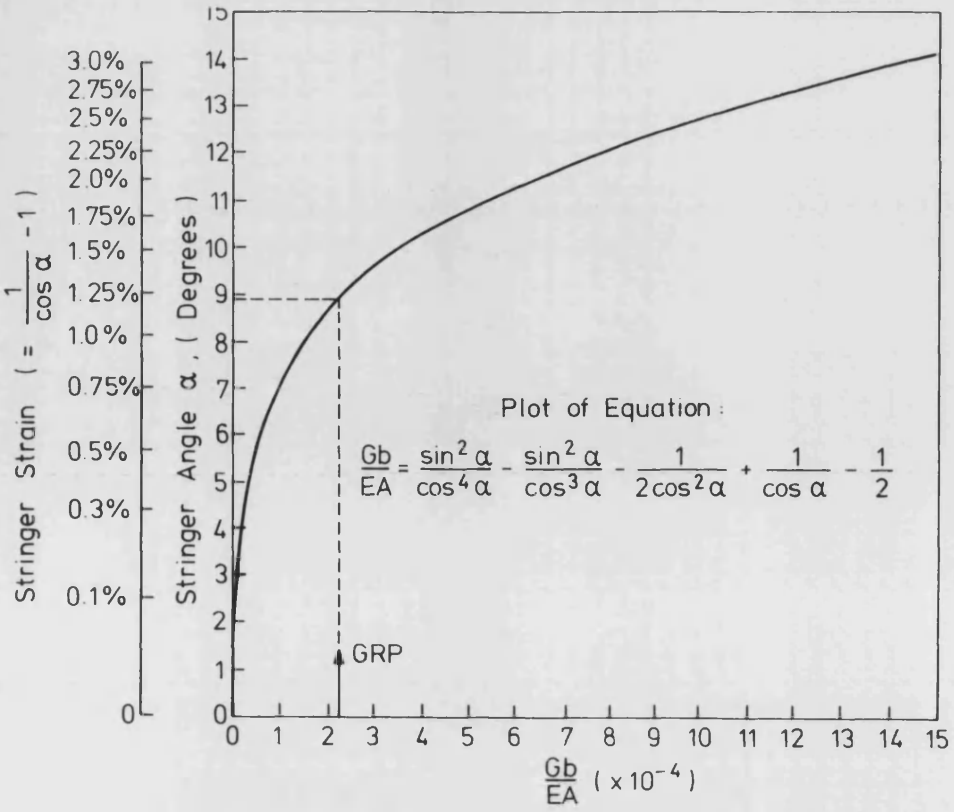

FIG. 93. Graph of the expression predicting equilbrium stringer angles and stringer strains.

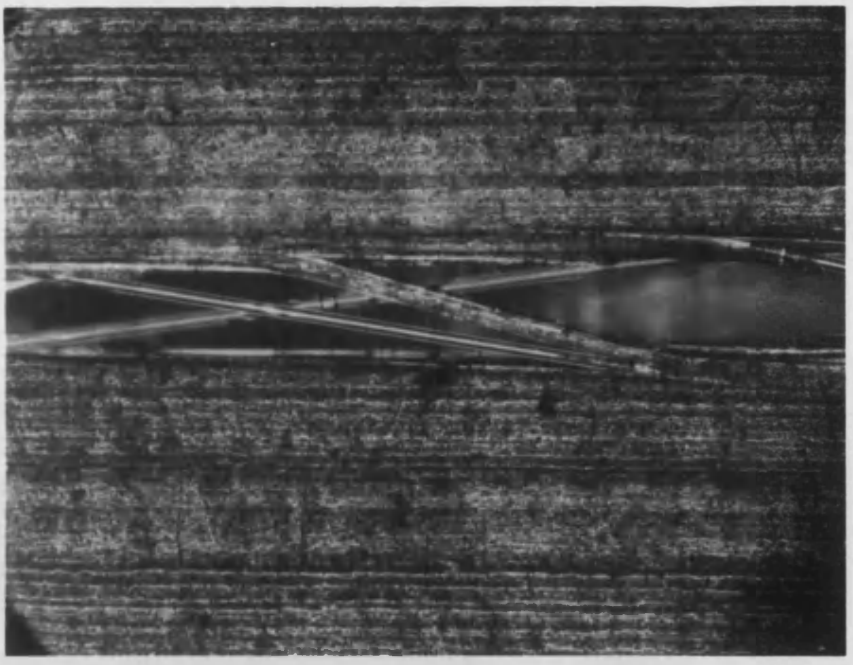

FIG. 94. Micrograph of the tied zone on a transverse double cantilever beam specimen.

HARWELL LABORATORY
PHOTOGRAPHIC GROUP

HR 38774

NOT FOR PUBLICATION

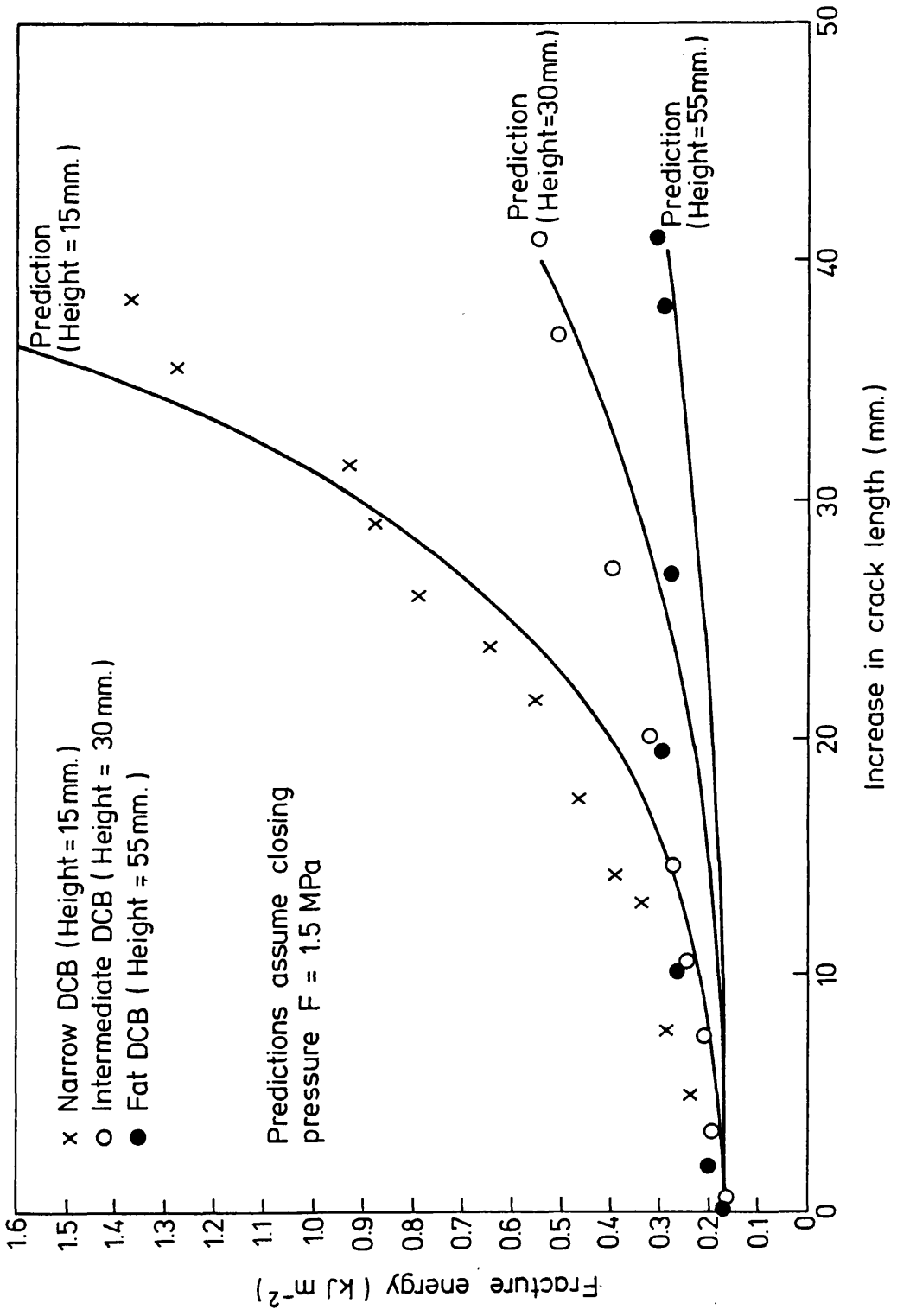

FIG. 95. Comparison of experimental results and theoretical predictions of the change of fracture toughness with crack length.

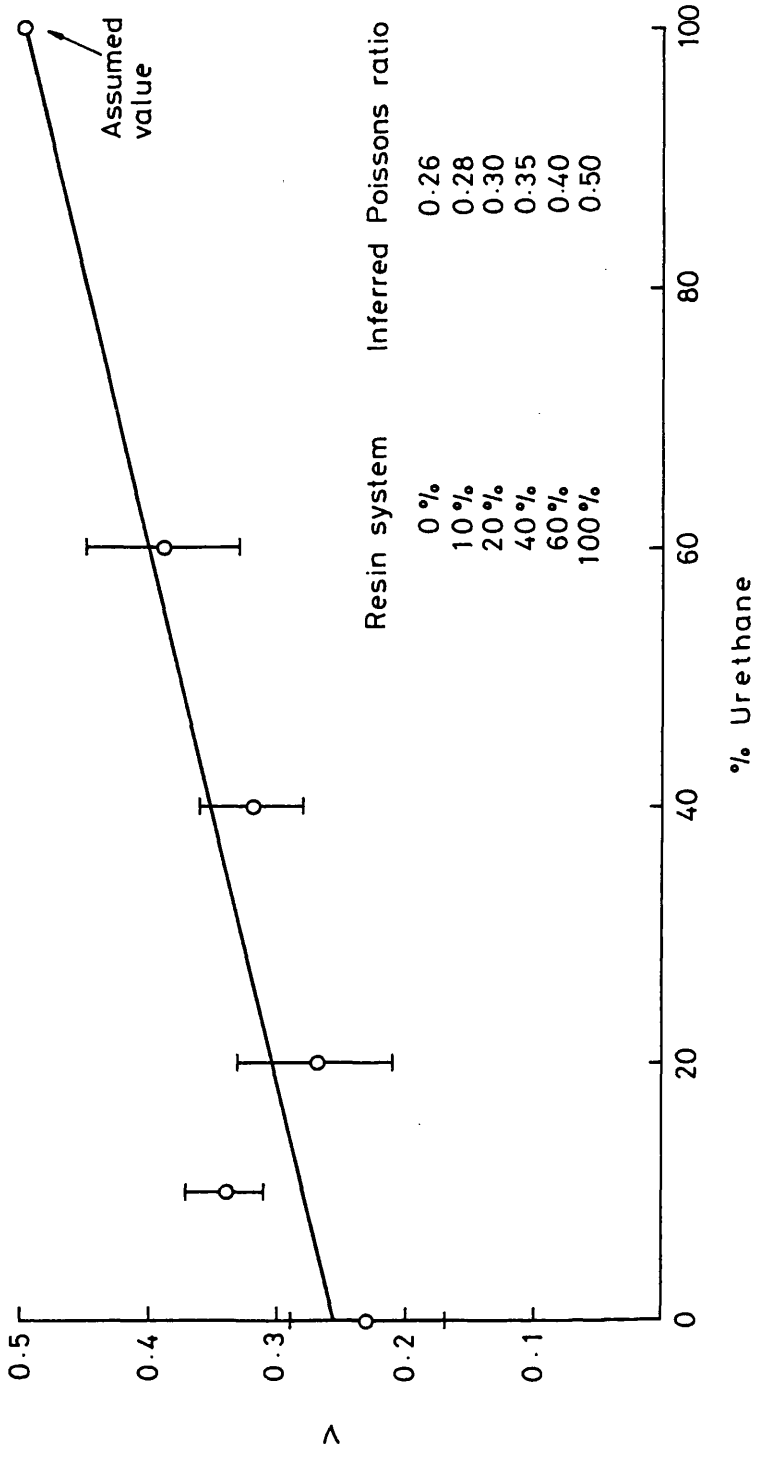

FIG. 96 Experimental results for Poisson's ratio versus urethane content in resin. The straight line identifies the Poisson's ratio value used in the models for transverse modulus prediction.

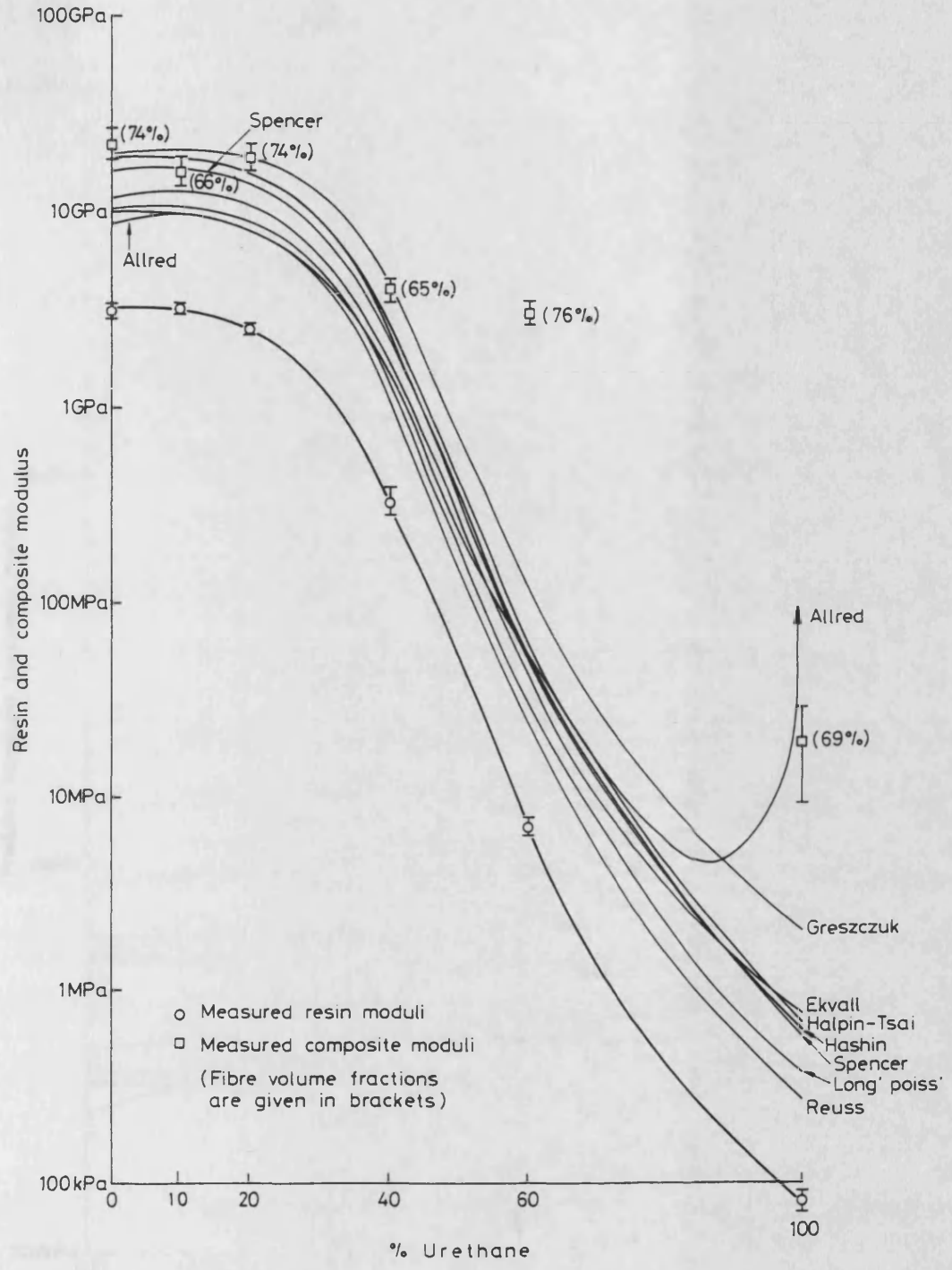

FIG. 97. Graph of the measured values of neat resin and transverse composite moduli against urethane content, together with transverse composite modulus predictions using various theoretical models.

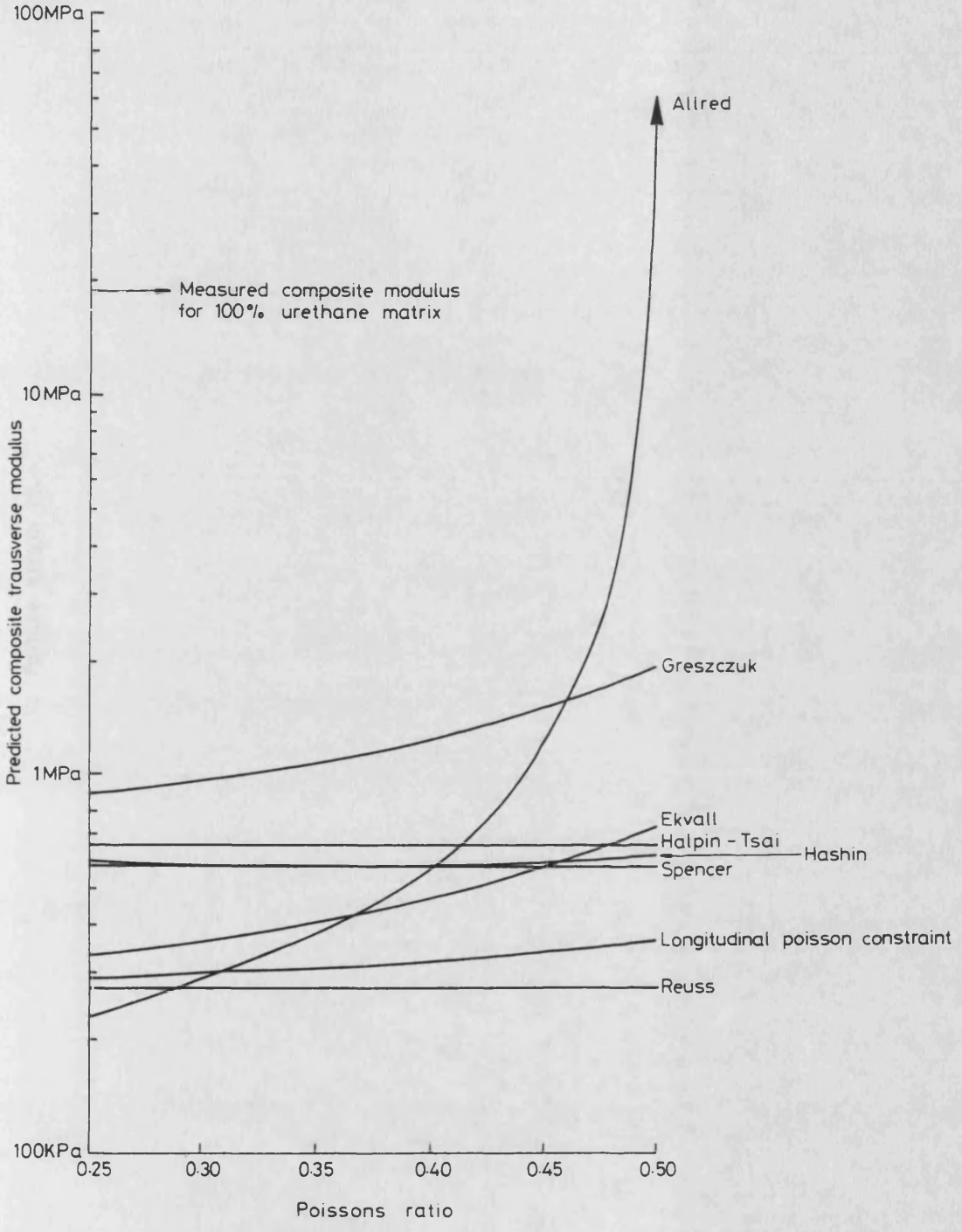

FIG. 98. Graph of predicted transverse 100% urethane resin composite moduli from several theoretical models versus Poisson's ratio.

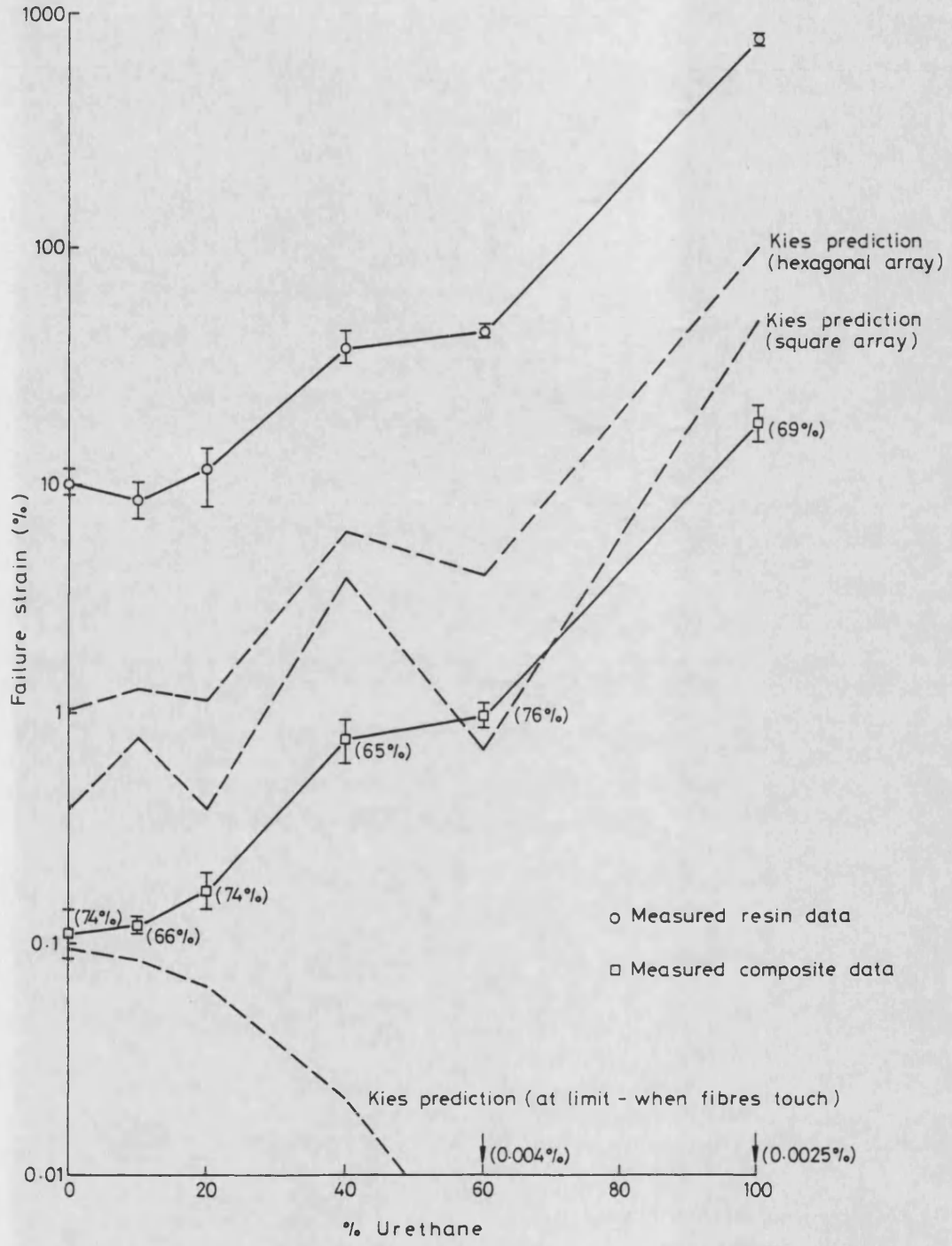

FIG. 99. Measured resin and transverse composite failure strains plotted against urethane content with predictions from Kies strain magnification theory.

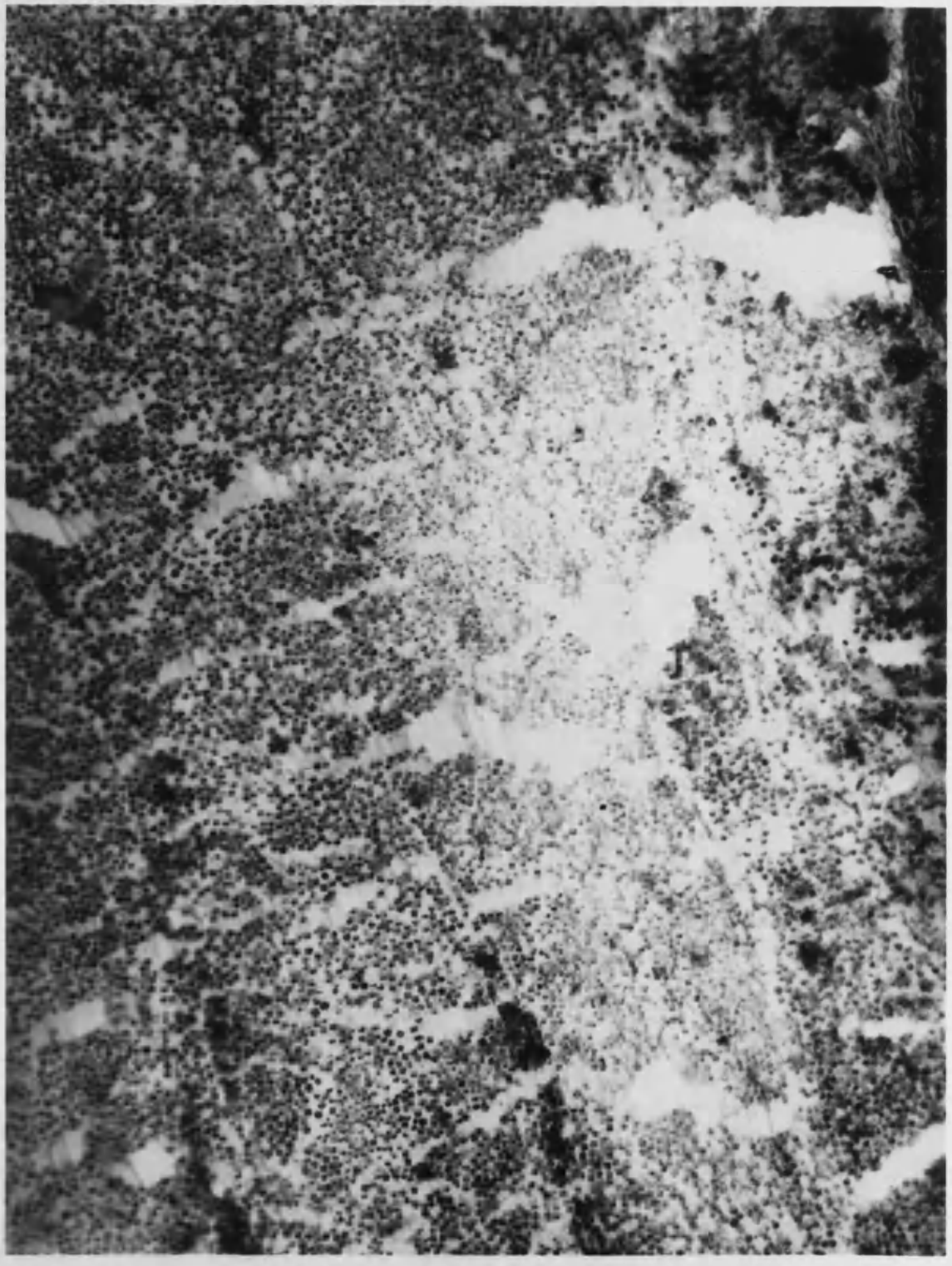

FIG. 100. Microsection of a cavitated region in 100% urethane transverse composite showing highly strained fibrils of pure rubber. Mag'92x.

HARWELL LABORATORY
PHOTOGRAPHIC GROUP

HR 38775

NOT FOR PUBLICATION

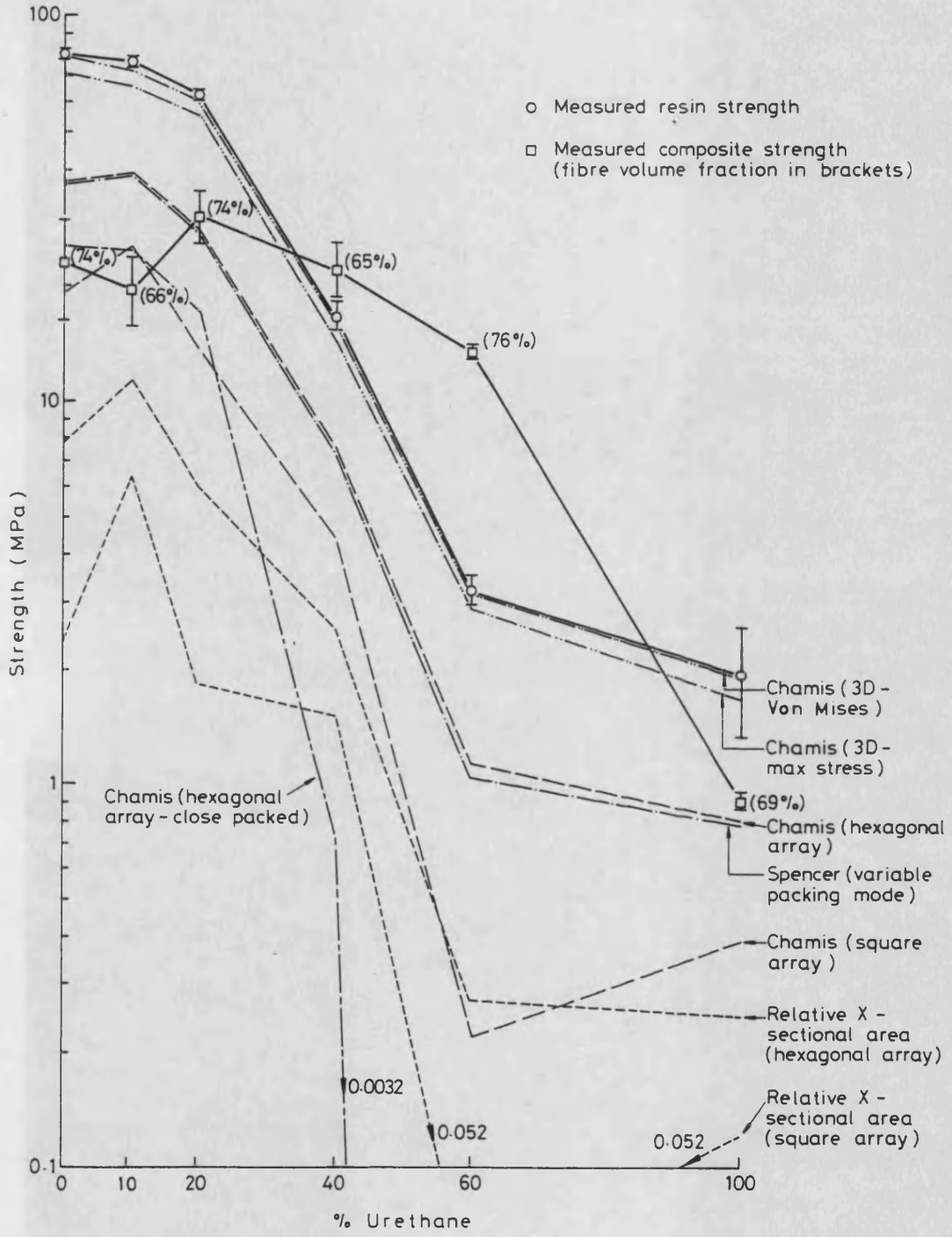

FIG. 101. Measured resin and transverse composite strengths plotted against urethane content, with predictions from stress magnification theories.

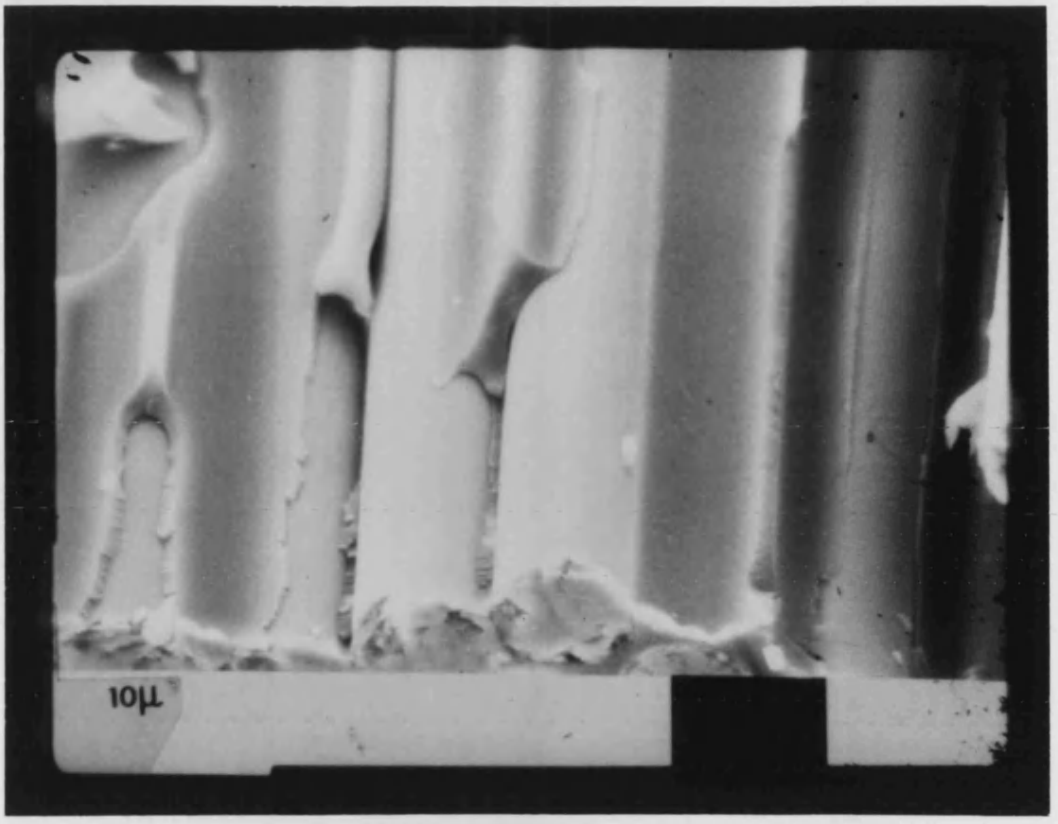

FIG. 102. Scanning electron micrograph of 0% urethane composite transverse fracture surface.

FIG. 103. Scanning electron micrograph of 10% urethane composite transverse fracture surface.

HARWELL LABORATORY
PHOTOGRAPHIC GROUP

HR 38773

NOT FOR PUBLICATION

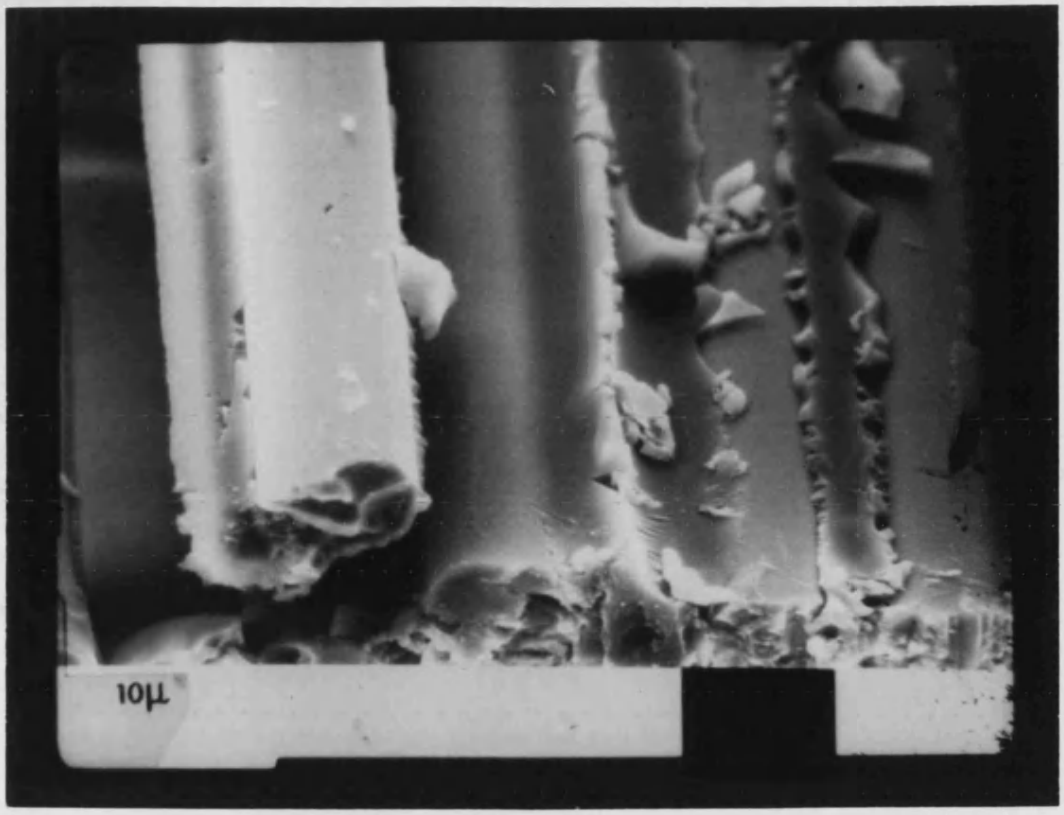

FIG. 104. Scanning electron micrograph of 20% urethane composite transverse fracture surface.

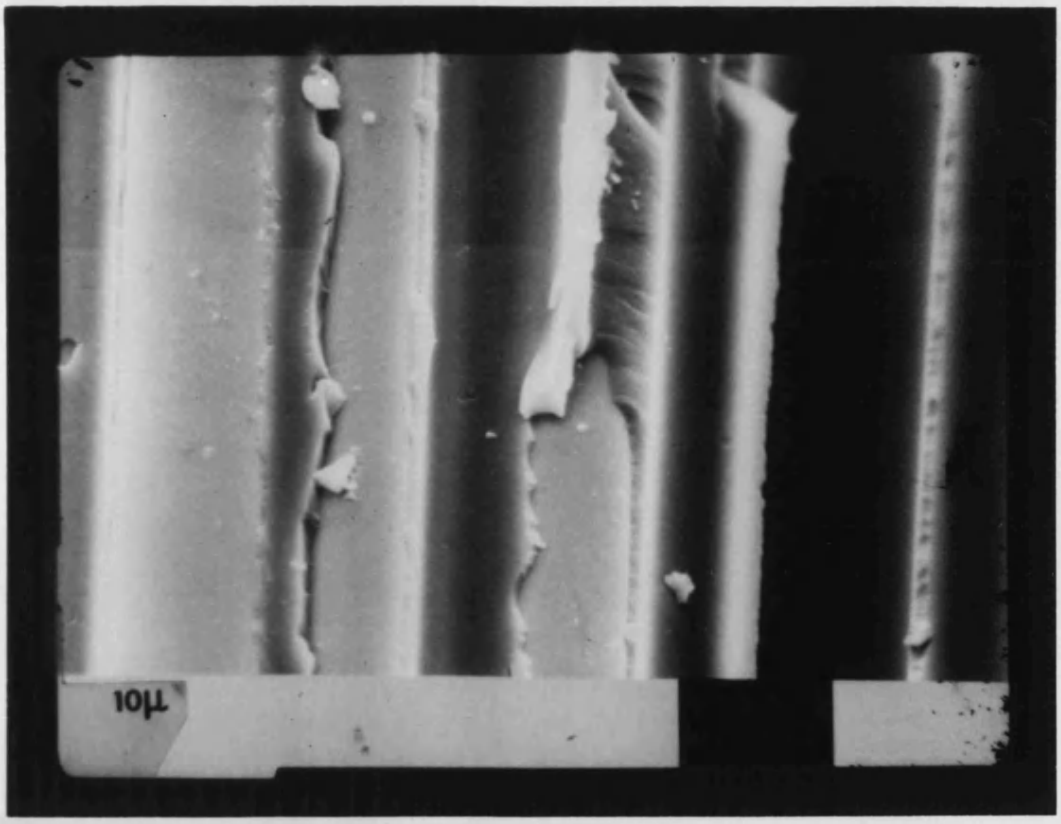

FIG. 105. Scanning electron micrograph of 40% urethane composite tranverse fracture surface.

HARWELL LABORATORY
PHOTOGRAPHIC GROUP

HR 38772

NOT FOR PUBLICATION

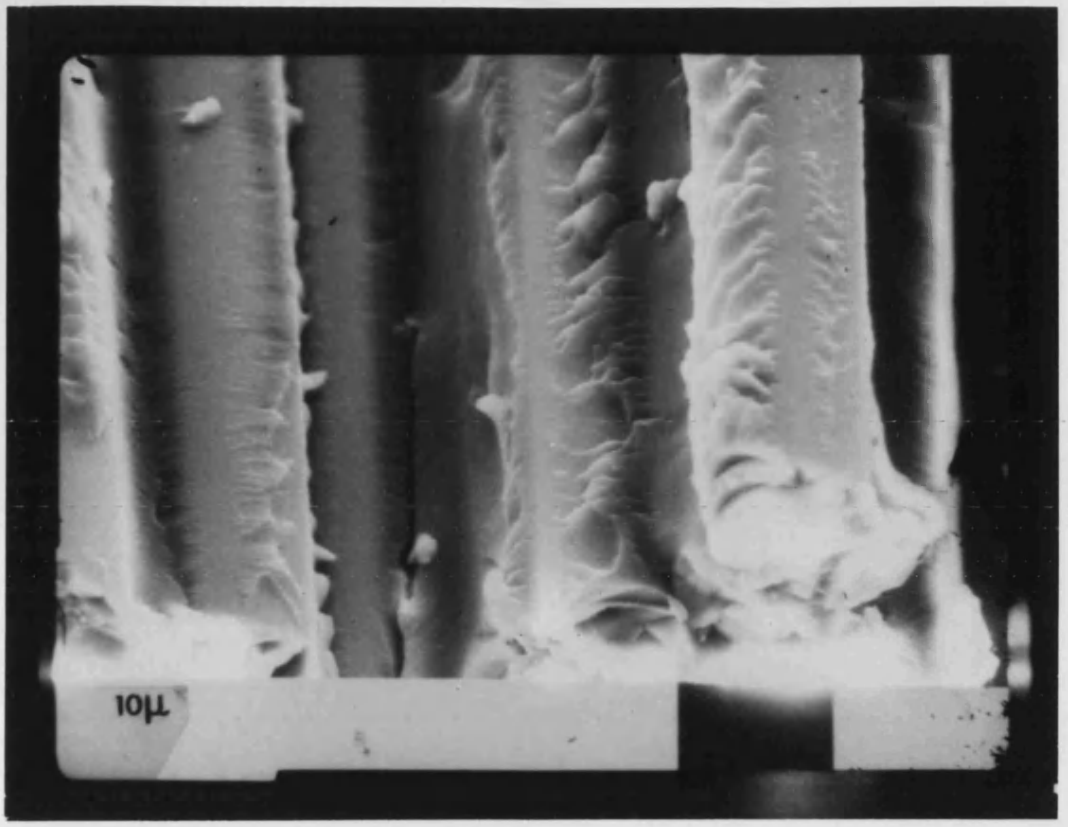

FIG. 106. Scanning electron micrograph of 60% urethane composite transverse fracture surface.

FIG. 107. Scanning electron micrograph of 100% urethane composite transverse fracture surface.

HARWELL LABORATORY
PHOTOGRAPHIC GROUP

HR 38771

NOT FOR PUBLICATION

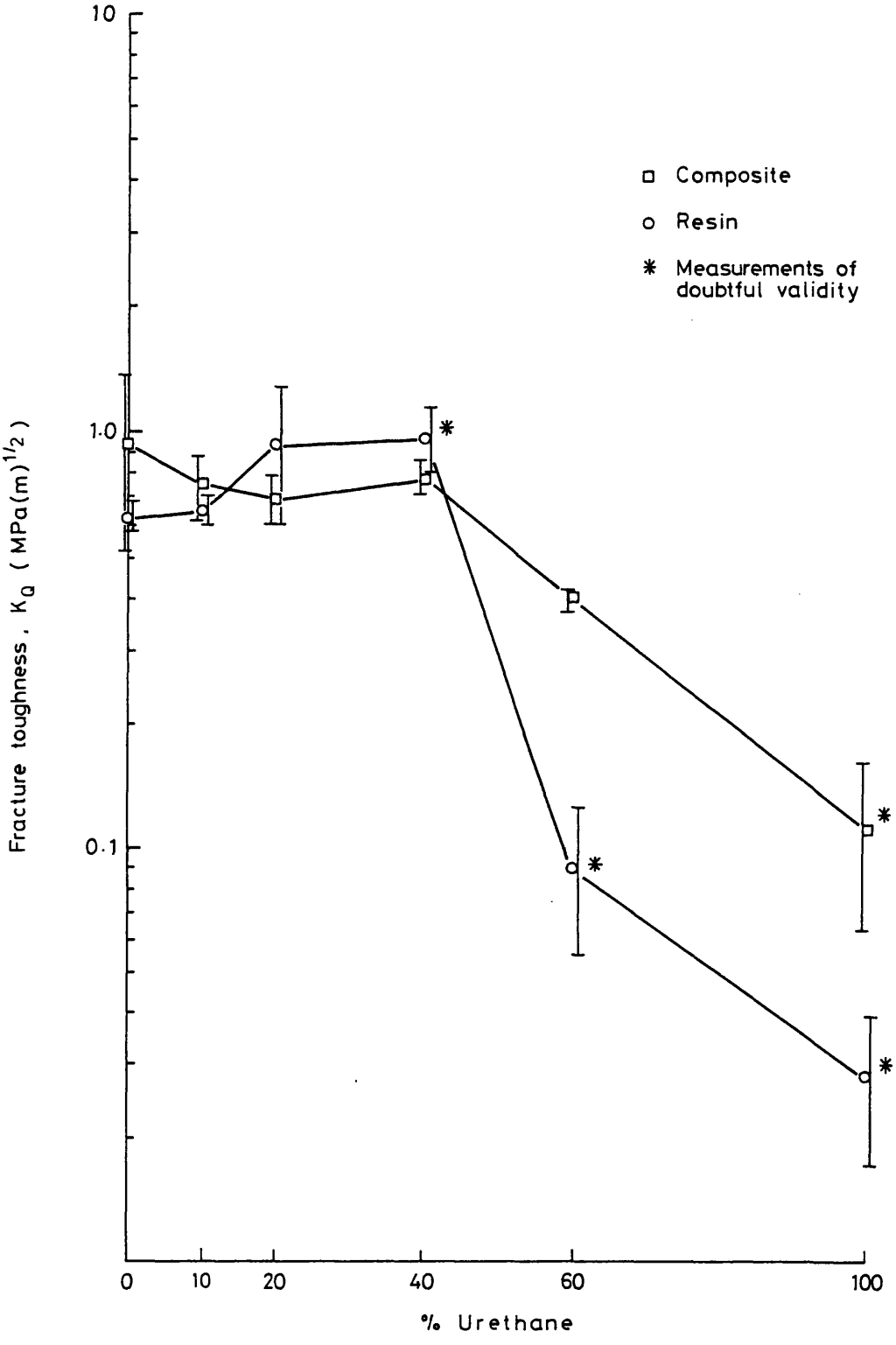

FIG. 108. Candidate critical stress intensity factors (K_Q) for neat resin and transverse composites plotted against urethane content of the resin.

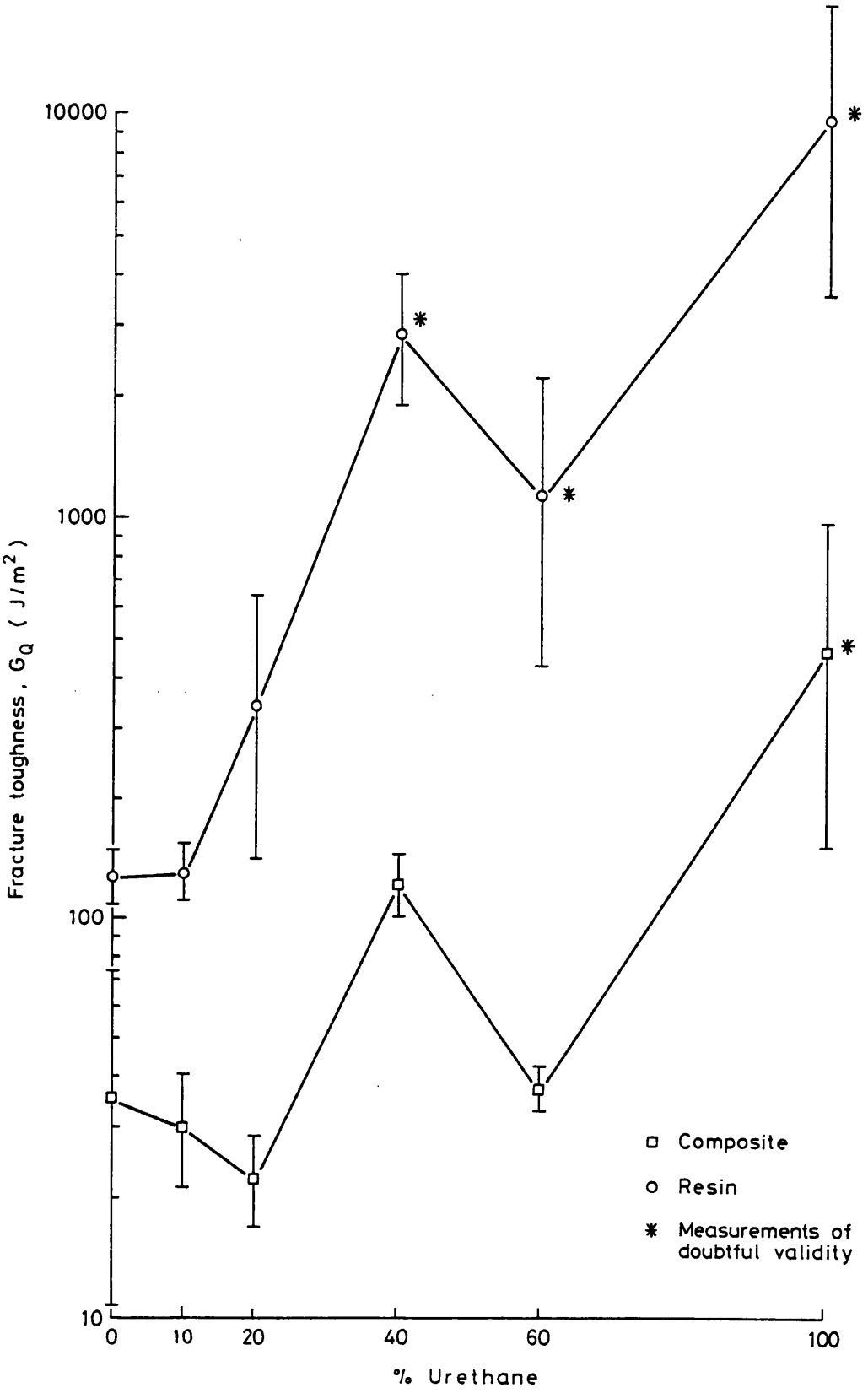

FIG. 109. Candidate critical rate of release of strain energies (G_Q) for neat resin and transverse composites plotted against urethane content of the resin.

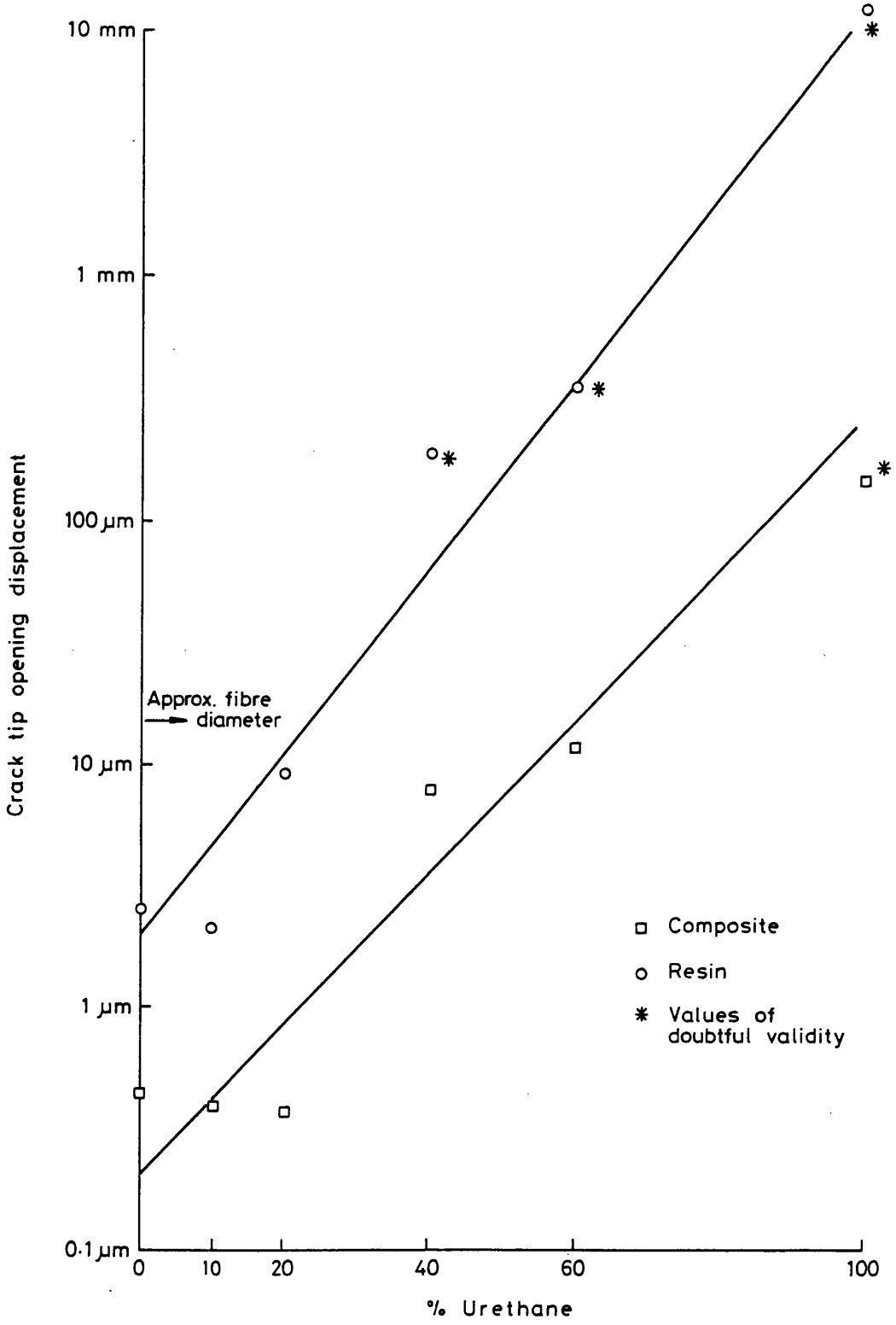

FIG. 110. Crack tip opening displacements for neat resin and transverse composites plotted against proportion of urethane.

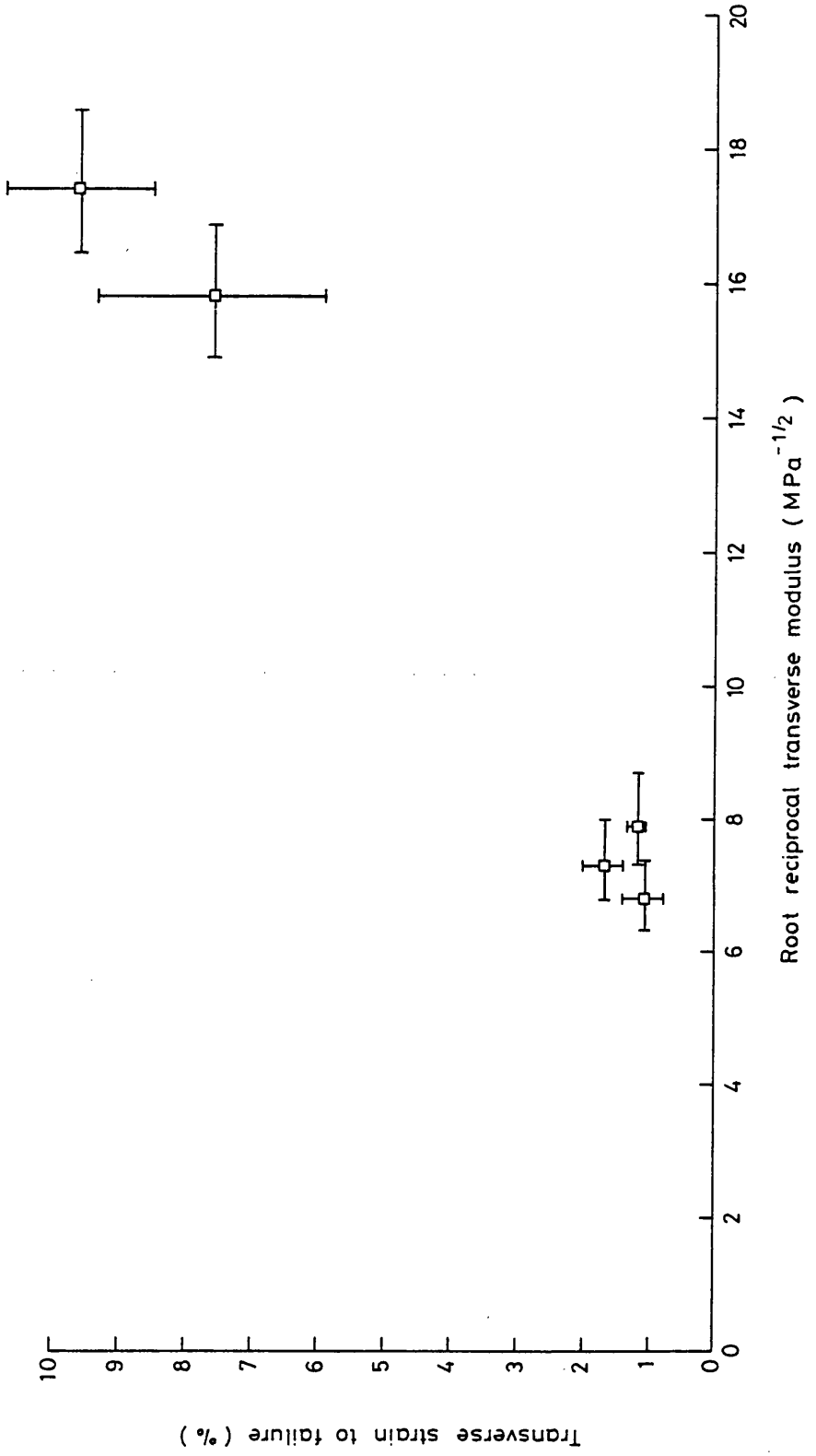

FIG. 111. Measured transverse failure strain plotted against root reciprocal of measured transverse modulus.

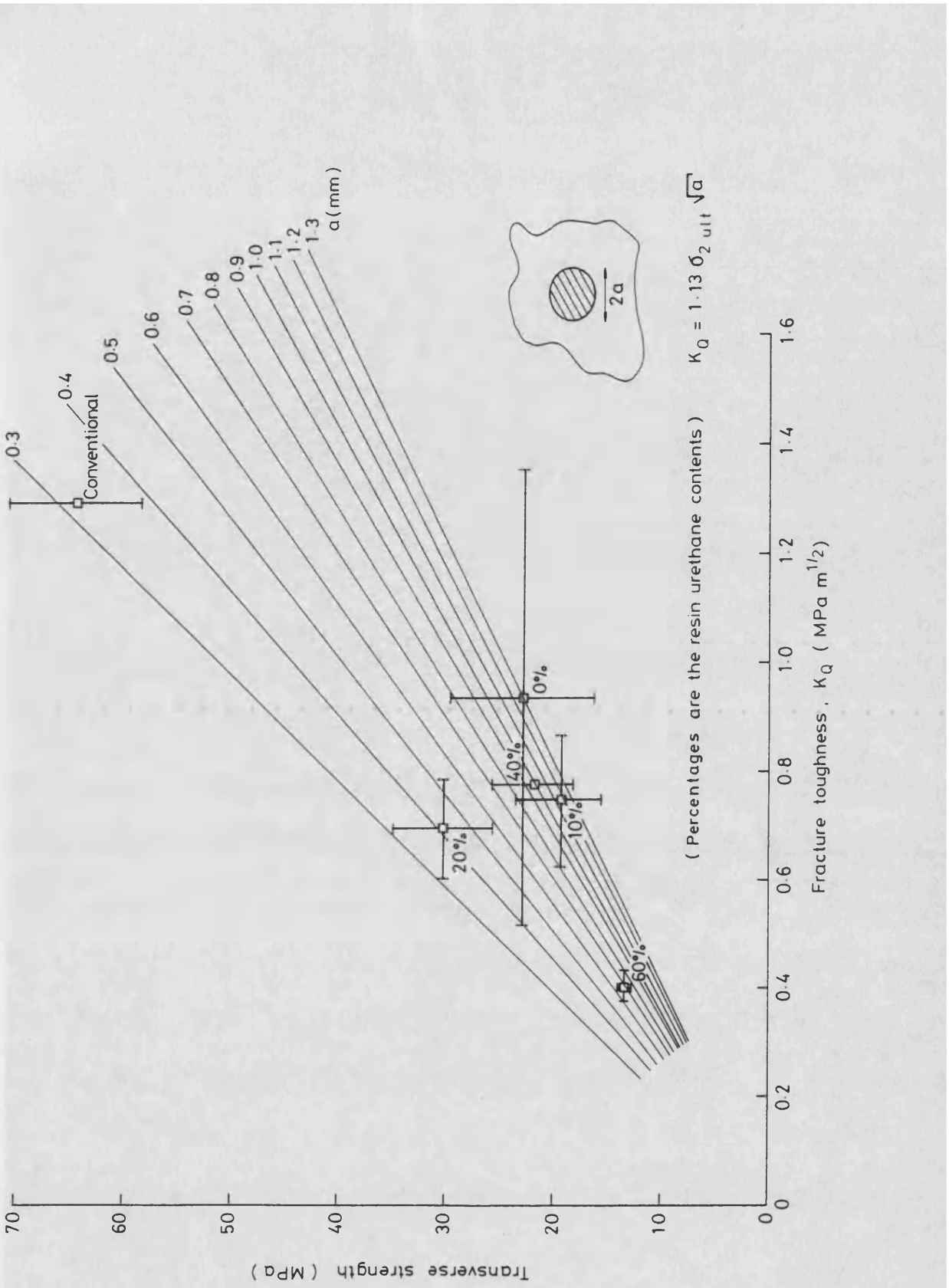

FIG. 112. Measured transverse strengths plotted against measured transverse toughness with various inherent defect sizes indicated.

FIG. 113. Optical micrograph of crack initiation location on the fracture surface of a 0% urethane neat resin strength specimen. Mag'92x.

HARWELL LABORATORY
PHOTOGRAPHIC GROUP

HR 38770

NOT FOR PUBLICATION

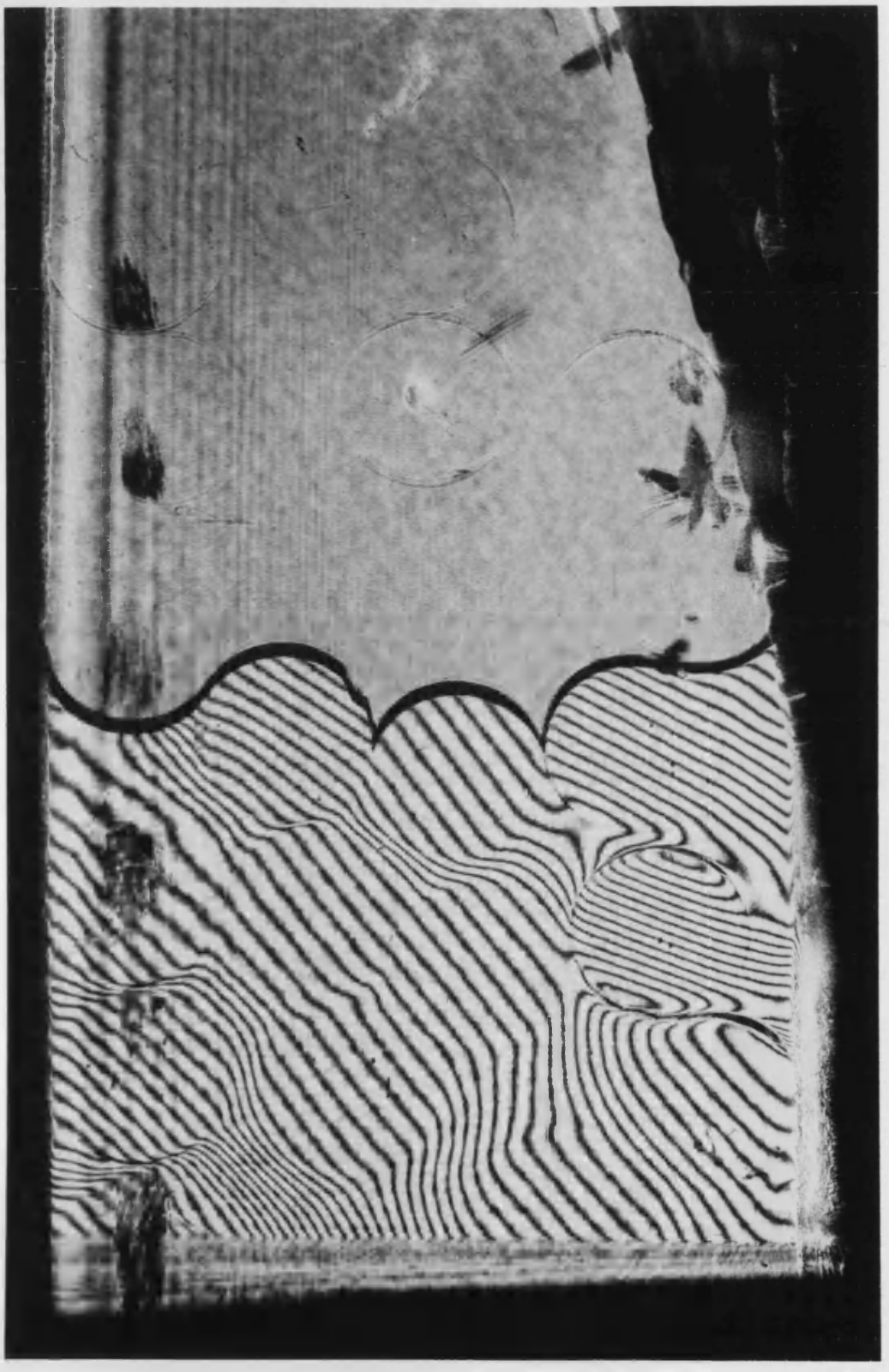

FIG. 114. Deformation map of a model transverse composite obtained by laser Moiré interferometry.

HARWELL LABORATORY
PHOTOGRAPHIC GROUP

HR 38767

NOT FOR PUBLICATION